

Experimentelle Untersuchung und Methodik
zur Konditionierung und Fertigung von
Aktor-Sensor-Systemen auf Basis von
Nickel-Titan Drähten

Dissertation

zur Erlangung des Grades
des Doktors der Ingenieurwissenschaften
der Naturwissenschaftlich - Technischen Fakultät
der Universität des Saarlandes

von

Dominik Scholtes

Saarbrücken

2024

Tag des Kolloquiums: 28.01.2025

Dekan: Prof. Dr.-Ing. Dirk Bähre

Berichtersteller: Prof. Dr.-Ing. Stefan Seelecke

Prof. Dr.-Ing. Dirk Bähre

Vorsitz: Prof. Dr.-Ing. Michael Vielhaber

Akad. Mitarbeiter: Dr.-Ing. Niklas König

Gut Ding will Weile haben und vortreffliche Sachen werden
ohne große Mühe und Arbeit nicht erworben.

- *Hans Jakob Christoffel von Grimmelshausen 1669*

Vorwort und Danksagung

Seit Februar 2015 war ich am Lehrstuhl für intelligente Materialsysteme (imsl) unter Leitung von Prof. Dr.-Ing. Stefan Seelecke in Saarbrücken angestellt. Der Tätigkeit als wissenschaftliche Hilfskraft folgte im Juni 2017, nach dem Fertigstellen meiner Masterthesis, die Anstellung als wissenschaftlicher Mitarbeiter. Aus den Inhalten und Ergebnissen diverser Forschungsprojekte, die ich in dieser Zeit bearbeiten konnte, entstand die vorliegende Dissertation in kumulativer Form. Sie wurde im Rahmen meiner Promotion an der Universität des Saarlandes angefertigt und besteht im Kern aus vier Veröffentlichungen in wissenschaftlichen Fachzeitschriften, welche ich als Erstautor verfasst habe. Die Veröffentlichungen sind in die Arbeit eingebunden. Abgerundet werden sie von einem Rahmen aus Einleitung mit Motivation, einer Einordnung der Themen und einer Schlussfolgerung mit einigen Anwendungsbeispielen.

An dieser Stelle möchte ich in erster Linie Stefan Seelecke danken, der mir den Weg zur Promotion erst vorgeschlagen hat. Ohne diese eindringliche Einladung seinerseits hätte es nie eine Dissertation mit meinem Namen auf dem Deckblatt gegeben. Ich bin auch dankbar für die großartige Zeit mit dem gesamten Team des Lehrstuhls. Hier entstanden, in einem mehr freundschaftlichen als kollegialen Umfeld, technische Lösungen und Forschungsergebnisse, die in der internationalen Smart Materials Community große Beachtung finden. Besonders hervorheben möchte ich die Unterstützung auf persönlicher sowie technischer Ebene von Rouven Britz, Yannik Goergen und Lukas Zimmer (aka. *SMA sozial*). Auch namentlich zu erwähnen ist Paul Motzki, der mich in vielen Situationen unterstützt hat. Mit ihnen sind über die berufliche Ebene hinaus Erinnerungen entstanden, die ich nicht vergessen werde.

Meinen Eltern Hans und Gertraud Scholtes bin ich sehr dankbar, denn sie sind dafür verantwortlich, dass ich überhaupt die Möglichkeit hatte zu studieren. Sie sind meine größte Stütze, auf die ich mich immer blind und ohne nachzudenken, verlassen kann. Meinen Opa Roland Taffner möchte ich hier ebenfalls erwähnen, denn er hat, neben meinem Vater, die Begeisterung für Technik in mir geweckt und gefördert. Auch meine sportlichen Erfolge, die er ursprünglich zu verantworten hat, haben mir geholfen, mich persönlich weiterzuentwickeln. Zum Abschluss kann ich mit ziemlicher Sicherheit erwähnen, dass ich ohne meine wunderbare Partnerin Leslie nicht die Motivation hätte aufbringen können, diese Arbeit fertigzustellen.

Saarbrücken, den 17.06.2024

Zusammenfassung

Die Dissertation gliedert sich in zwei Themenbereiche. Im ersten Block wird die Entwicklung eines multifunktionalen Prüfstands für Zugversuche und aktorische Tests an FGL-Mikrodrähten diskutiert. Er erlaubt präzise Messungen ihrer anwendungsrelevanten Eigenschaften. Damit werden Methoden entwickelt, um den Einfluss von Training auf das Verhalten der Drähte zu untersuchen. Es zeigt sich, dass elektro-thermisches Training bei hoher Last die Widerstandshysterese reduziert, das mechanische Verhalten beeinflusst und die funktionale Stabilität verbessert. Zusätzlich wird das Verhalten der FGL bei hohen Umgebungstemperaturen untersucht, wobei sich mit Training und Belastung das Hochtemperaturverhalten verändert.

Im zweiten Teil wird die Entwicklung eines Widerstandsschweißprozesses für die Herstellung von kompakten NiTi-Mikrodrahtbündeln beschrieben. Der Schweißprozess ermöglicht die zuverlässige Verbindung von NiTi-Drähten mit verschiedenen Legierungen und die Fertigung flacher Bündelaktoren. Die geschweißten Bündel zeigen eine schnelle Abkühlgeschwindigkeit und skalierbare Abtriebskraft.

Insgesamt ergänzen sich beide Bereiche, indem sie eine Brücke von der detaillierten Charakterisierung und Optimierung einzelner FGL-Mikrodrähte hin zur praktischen Fertigung und Anwendung von FGL-Aktor-Sensor-Systemen schlagen. Diese Herangehensweise ermöglicht es, theoretische Erkenntnisse in praxisrelevante Systeme zu überführen und somit die Einsatzmöglichkeiten von FGL-Aktuatoren zu erweitern.

Abstract

The dissertation is divided into two main thematic areas. In the first part, the development of a multifunctional test rig is discussed, enabling tensile and actuation tests on shape memory alloy (SMA) microwires. It allows precise measurements of the wires' properties that are relevant for applications. With it, methods are developed to investigate the influence of training on the wires' behavior. It is found that electro-thermal training under high load reduces the hysteresis of the resistance signal, influences the mechanical behavior, and improves functional stability. Additionally, the behavior of SMA at high ambient temperatures is examined, revealing that training and load significantly influence high-temperature behavior.

The second part describes the development of a resistance welding process for producing compact NiTi microwire bundles for actuator-sensor systems. The welding process ensures the reliable bonding of NiTi wires with various alloys and the manufacturing of flat bundle actuators. The welded bundles feature rapid cooling and scalable output force.

Overall, both topics complement each other by bridging detailed characterization and optimization of individual SMA microwires with the practical production and application of high-performance SMA actuator-sensor systems. This approach enables the direct transfer of theoretical insights into practical technologies, thereby expanding the application possibilities of the material.

Inhalt

1	Einleitung, Grundlagen und Motivation.....	1
2	Publikationen zur Charakterisierung und Fertigung von FGL Aktor-Sensor-Systemen	6
2.1	Zusammenfassung und Einordnung der Publikationen.....	6
2.2	A Multifunctional Characterization Test Bench for Shape Memory Alloy Micro-Wires – Design, Implementation and Validation	12
2.3	Electro-Thermo-Mechanical Characterization of Shape Memory Alloy Wires for Actuator and Sensor Applications – Part 1: The Effects of Training	38
2.4	Electro-Thermo-Mechanical Characterization of Shape Memory Alloy Wires for Actuator and Sensor Applications – Part 2: High Ambient Temperature Behavior	62
2.5	Dissimilar Resistance Welding of NiTi Microwires for High Performance SMA Bundle Actuators	76
3	Fazit und Ausblick	87
3.1	Abgeleitete Anwendungen	88
3.2	Ausblick	92
	Literaturverzeichnis	93
	Anhang.....	102
	Ergänzende Messdaten zu Veröffentlichungen	102
	Beitragsberichte zu den eingebundenen Veröffentlichungen	110
	Liste der eigenen Publikationen.....	114

1 Einleitung, Grundlagen und Motivation

Die Integration von zusätzlichen Funktionen sowie die Elektrifizierung von immer mehr Teilbereichen von technischen Systemen steigt unaufhörlich an. Dies führt einerseits zu nie dagewesener Automatisierbarkeit, Anpassbarkeit und einem Gewinn an Komfort. Andererseits werden vorhandene Systeme dadurch schwerer, komplexer und ihr Energieverbrauch steigt. Des Weiteren stoßen konventionelle elektrische Antriebssysteme, wie Elektromagnete und Elektromotoren, in den oft eng bemessenen Bauräumen, an ihre Grenzen. In dieser Nische können unkonventionelle Aktoren bzw. intelligente Werkstoffe ihre Vorteile als Antriebssysteme ausspielen und darüber hinaus dazu beitragen, die Energieeffizienz zu steigern und das Gewicht zu reduzieren.

Thermische Formgedächtnislegierungen (FGL) gehören zu dieser Klasse der intelligenten Werkstoffe (engl.: smart materials), welche dadurch gekennzeichnet sind, dass sie auf die Veränderung bestimmter Umgebungsbedingungen selbstständig reagieren. Im Falle der FGL führt eine Veränderung der Temperatur zur Umwandlung der kristallinen Gitterstruktur, was sich als makroskopisch sichtbare Formänderung äußert. Weitere Beispiele für intelligente Werkstoffe sind unter anderem magnetische Formgedächtnislegierungen, piezoelektrische Materialien, elektroaktive Polymere und magnetorheologische Flüssigkeiten [1]–[10].

Der Formgedächtniseffekt in einer Legierung wurde erstmals von Arne Ölander im Jahr 1932 beschrieben [11]. Die bis heute, aufgrund ihrer hohen Lebensdauer und reversibler Dehnung, kommerziell erfolgreichste FGL besteht aus Nickel-Titan (NiTi). Sie wurde in den sechziger Jahren, unter dem Namen „Nitinol“, von Buehler und Wang am Naval Ordnance Laboratory in den USA erforscht [12]–[14]. Beim Überschreiten einer kritischen Temperatur, der sogenannten Umwandlungstemperatur, verändert sich das NiTi-Kristallgitter von Martensit zu Austenit. Unter Verringerung der Temperatur wird dieser Prozess nach dem Durchlaufen einer Hysterese umgekehrt, und die Gitterstruktur wandelt sich wieder vollständig in Martensit um [15], [16]. Der Prozess geht mit einer reversiblen geometrischen Formänderung einher, wodurch der Begriff Formgedächtnis geprägt wird. Neben binärem NiTi finden sich auch weitere tertiäre und quaternäre Legierungen, nicht nur auf Nickelbasis, mit Formgedächtniseffekt. Als wichtige Beispiele lassen sich NiTiCu, NiTiHf, NiTiCuCo, eisenbasierte Legierungen wie FeSiMg und kupferbasierte Legierungen wie CuZnAl, nennen [17]–[21].

Durch die besonderen Eigenschaften sind FGL, insbesondere NiTi, in den unterschiedlichsten Anwendungsfeldern zu finden. Der größte Anwendungsbereich ist bis heute die Medizintechnik, wo die gute Biokompatibilität von NiTi sowie die superelastischen Eigenschaften des austenitischen Gefüges zum Tragen kommen [22]. In der Regel wird hierbei Nickel-reiches NiTi eingesetzt, welches sich durch eine niedrige Umwandlungstemperatur bei Raumtemperatur bereits in der austenitischen Phase befindet. Diese ist superelastisch und lässt sich bis zu 10% dehnen, ohne eine plastische Verformung zu hinterlassen [23]. Konkrete Anwendungen sind hier zum Beispiel Stents und Führungsdrähte zur minimalinvasiven Behandlung und Untersuchung des Herzens [24], [25].

Ein im Jahr 1980 durch Rodriguez und Brown eröffnetes Forschungsfeld im Bereich der FGL ist die Elastokalorik [26]. Das Phänomen basiert auf den latenten Wärmen, die bei der Phasentransformation von Austenit zu Martensit frei werden [27], [28]. Die Transformation wird durch gezielte mechanische Be- und Entlastung der FGL-Elemente herbeigeführt. Zur Anwendung kommt der Effekt in festkörperbasierte Wärmepumpen, die mit superelastischen FGL betrieben werden. Vorteile dieser Systeme sind, dass sie ohne klimaschädliche Kühlmittel auskommen und das Potenzial aufweisen, die Energieeffizienz, beziehungsweise den sogenannten „coefficient of performance“ (COP), deutlich zu steigern [29], [30]. Stand der Forschung sind aktuell erste Prototypen für kontinuierlich laufende Kühlmaschinen, beziehungsweise Wärmepumpen, und die Entwicklung von dauerfesten Werkstoffen [31]–[34]. Der eigentliche Formgedächtniseffekt, hervorgerufen durch thermisch induzierte Austenit-Martensit Transformation, wird hingegen hauptsächlich in der Antriebstechnik eingesetzt. Es kommen vorrangig Titan-reiche, binäre NiTi-Legierungen zum Einsatz, welche typischerweise eine Umwandlungstemperatur von circa 90° C aufweisen. Das bedeutet, dass sie bei Raumtemperatur in der quasiplastischen Martensitphase vorliegen. Am häufigsten werden FGL-Aktoren in Form von Drähten und Federn verwendet [35]–[40]. Durch ihre Kompaktheit, Flexibilität und gute Integrierbarkeit spielen FGL-Drähte in elektrischen Antrieben die größere Rolle, während FGL-Federn ihren Anwendungsbereich eher in passiv geheizten Systemen, wie Ventilen oder Thermostaten, finden. Der Draht funktioniert dabei ähnlich wie ein künstlicher Muskel. Elektrischer Strom, der durch den Draht fließt, führt aufgrund des Joule-Effekts zur Erwärmung. Dadurch kontrahiert der Draht um bis zu ca. 5% und es werden hohe Abtriebskräfte erreicht [41].

Die wichtigsten Eigenschaften von FGL-Aktoren sind ihre hohe Energiedichte und das sogenannte Self-Sensing [15], [42]–[45]. Dadurch lassen sich besonders kompakte und leichte

Aktor-Sensor-Systeme aufbauen. Unter Self-Sensing versteht man bei FGL die Korrelation von elektrischem Widerstand zur Geometrie. Mithilfe des Widerstandssignals lassen sich Rückschlüsse auf die Position und den Zustand des Antriebssystems ziehen, ohne zusätzliche Messtechnik einzusetzen.

Formgedächtnisantriebe finden sich bereits in einigen kommerziellen Produkten wie Ventilen für den automobilen Sitzkomfort sowie kleinen und größeren Linear- und Rotationsantrieben [46]–[48]. Die jüngste und aufsehenerregendste Entwicklung im kommerziellen Bereich sind optische Bildstabilisator- und Autofokusmodule für Smartphone Kameras, angetrieben mit FGL-Mikrodrähten [49]. Mit Ausnahme dieser Entwicklung sind kommerzielle Produkte auf FGL-Basis in der Regel simpel gehalten und mit großen Reserven konstruiert. Außerdem wird im Allgemeinen mit geringen Kräften gearbeitet, was hauptsächlich am dynamischen Verhalten von FGL-Aktuatoren liegt. Während die Aktivierung mittels kurzer Stromimpulse nahezu beliebig schnell vonstattengeht, hängt die Dynamik, aufgrund des thermischen Effekts, maßgeblich von der Abkühlgeschwindigkeit der FGL ab [50]. Übertragen auf Drähte lässt sich schlussfolgern, dass mit Durchmessern bis zu 100 μm Zykluszeiten von einer Sekunde und weniger erreicht werden. Da allerdings auch die Abtriebskraft über die Materialspannung mit dem Durchmesser skaliert, liegt die dann realisierbare Kraft in der Regel im Bereich von maximal 1,5 N [51].

Außer über die Bündelung, also das mechanische Parallelschalten mehrerer Aktordrähte, kann die Kraft eines FGL-Aktors also auch über die Materialspannung angepasst werden [52]–[56]. Kommerziell verfügbare NiTi-Drähte sind von den Herstellern auf eine maximale Materialspannung zwischen 150 MPa und 200 MPa trainiert. Das bedeutet, die Drähte sind thermo-mechanisch so behandelt, dass sie bei diesen Spannungen ein stabiles Verhalten zeigen. Der Hauptgrund diesen Spannungsbereich zu nutzen ist, dass bei moderaten Dehnungen von ca. 2% von einer Dauerfestigkeit des Materials ausgegangen werden kann [51], [57]–[59]. Da bei einigen Anwendungen aber keine Dauerfestigkeit gefordert ist, sondern durch die Produktlebensdauer lediglich fünf- bis sechsstellige Zyklenzahlen notwendig sind, ist eine Erhöhung der Materialspannung in diesen Fällen zielführend. Der Hauptvorteil liegt in der Möglichkeit, die Abtriebskraft zu skalieren, ohne den Bauraum oder das Gewicht zu verändern. Das bedeutet, dass die Arbeitsdichte des Antriebssystems dadurch erhöht wird [60]. Darüber hinaus schwankt die Umgebungstemperatur in einigen potenziellen Einsatzgebieten sehr stark. Ein bekanntes Beispiel ist der Automobilsektor, wo die maximale Einsatztemperatur von Aktuatoren bei über 80 °C liegt. Dies schränkt den Einsatz von thermisch aktivierten FGL-

Aktuatoren ein. Allerdings ist die Umwandlungstemperatur abhängig von der Materialspannung, sodass mit einer Erhöhung dieser nicht nur die Arbeitsdichte, sondern auch deren Einsatztemperatur erhöht werden kann.

Komplexere Systeme aus gebündelten, hochbelasteten Drähten und damit hoher Dynamik bei gleichzeitig hohem Kraftpotential sind, besonders in Verbindung mit Self-Sensing, bis dato jedoch noch Stand der Forschung [43], [61]–[68]. Gründe hierfür sind unter anderem, dass die exakten mechanischen und elektrischen Eigenschaften der FGL und das Verhalten bei den angesprochenen Bedingungen trotz jahrzehntelanger Forschung noch nicht in voller Gänze bekannt sind. Außerdem ist die herkömmliche Verbindungstechnik, das Crimpen, nicht geeignet, um kompakte Drahtbündel automatisierbar zu fertigen.

Ein Ziel dieser Arbeit ist es, die wichtigsten Aspekte zu untersuchen, um die FGL-Technologie auch in anspruchsvollen Anwendungen, mit hohen Kräften, sich verändernden Umgebungsbedingungen und mit funktionierendem Self-Sensing, in kommerziellen Produkten einzusetzen. Dazu wird eine anwendungsorientierte, experimentelle elektro-thermo-mechanische Untersuchung der aktorischen und sensorischen Eigenschaften unter unterschiedlichen Bedingungen durchgeführt. Der Fokus liegt dabei auf dem Einfluss der Konditionierung von kommerziell verfügbaren NiTi-Drähten zur Anwendung mit erhöhten Materialspannungen und der Erforschung und Optimierung des Widerstandsverhaltens. Diese Experimente werden bei Umgebungstemperaturen von 23 °C bis 100 °C, auf einem eigens für Mikrodrähte entwickeltem Prüfstand, durchgeführt. Die dabei entwickelte Methode lässt sich auf beliebige Legierungen und Drahtdurchmesser anwenden sowie um weitere Parameter ergänzen. Ein Hauptunterschied zu experimentellen Charakterisierungen von FGL, wie sie in der Literatur zu finden sind, liegt in der anwendungsorientierten, systematischen Vorgehensweise [69]–[74]. Hervorzuheben sind dabei die joulesche Erwärmung der Proben, die Durchführung mehrerer unterschiedlicher Messungen und Methoden an derselben Probe mit nur einer Aufspannung sowie die systematische Untersuchung des Zusammenhangs zwischen aktorischen Eigenschaften und Sensorverhalten.

Ein weiteres Ziel der Arbeit ist es, die entsprechend untersuchten und optimierten FGL-Mikrodrähte automatisierbar und zuverlässig zu kompakten, flachen und haltbaren Bündel-Aktuatoren zusammenzufügen. Dazu wird ein neuartiger Widerstandsschweißprozess entwickelt und untersucht. Die NiTi-Drähte werden stofffremd mit Blechen aus Stahl und Kupferlegierungen verschweißt und die Verbindungsqualität wird methodisch untersucht. Das Resultat sind flache, kompakte Mikrodraht-Bündel mit höherer Abkühlgeschwindigkeit als ein

vergleichbarer, dickere Einzeldraht. Im Vergleich zum Laserschweißen, welches bereits vielfältig für unterschiedlichste Anwendungsbereiche mit NiTi untersucht wurde, ist das Widerstandsschweißen kosteneffektiver, einfacher zu handhaben und, durch den robusten Prozess, gut automatisierbar [75]–[79].

Mithilfe der gefertigten Bündel sowie den Ergebnissen aus der Charakterisierungsstudie wurden bereits einige neuartige Anwendungen in Form von funktionalen Prototypen entwickelt und aufgebaut, welche am Ende der Arbeit vorgestellt werden.

Der Hauptteil der Dissertation beginnt im folgenden Kapitel. Die vier eingebunden Veröffentlichungen werden zu Beginn des Kapitels zusammengefasst und zueinander eingeordnet. In den Unterkapiteln folgen in thematischer Reihenfolge die Veröffentlichungen, die so abgedruckt sind, wie sie auch in den wissenschaftlichen Zeitschriften veröffentlicht sind. Im dritten Kapitel folgt ein Fazit der gesamten Arbeit sowie ein Ausblick über offen gebliebene Forschungsthemen. Außerdem werden, als weiteres Ergebnis der Forschungsarbeit, einige Anwendungsbeispiele vorgestellt, die durch die erarbeiteten Ergebnisse entwickelt werden konnten. Im Anhang sind ergänzende Ergebnisse zu den Veröffentlichungen, die Beitragsberichte zu jeder Veröffentlichung sowie eine Liste aller Publikationen des Autors zu finden.

2 Publikationen zur Charakterisierung und Fertigung von FGL Aktor-Sensor-Systemen

Im Folgenden werden die vier Veröffentlichungen, welche Grundlage und Inhalt der Dissertation bilden, in ihrer chronologischen Reihenfolge zusammengefasst und in Zusammenhang gebracht. Die chronologische Reihenfolge entspricht dabei auch der thematischen Reihenfolge, in der sie in dieser Arbeit eingebunden sind. Die Themen sind in zwei grundlegende Blöcke aufgeteilt: die methodische Charakterisierung von FGL-Mikrodrähten und die Fertigung von FGL-Bündelaktoren aus Mikrodrähten mittels Widerstandsschweißen. Dabei teilt sich die Charakterisierung wiederum in drei Veröffentlichungen auf: die Entwicklung und Validierung eines multifunktionalen Prüfstands für FGL-Mikrodrähte, die Untersuchung des Einflusses von Training sowie die Untersuchung des Hochtemperaturverhaltens auf dem vorgestellten Prüfstand. Die vierte Veröffentlichung behandelt die Entwicklung eines Widerstandsschweißprozesses für die Fertigung von kompakten NiTi-Mikrodrahtbündeln für Aktor-Sensor-Systeme auf FGL-Basis.

2.1 Zusammenfassung und Einordnung der Publikationen

FGL werden in der Literatur in der Regel mit thermo-mechanischen Verfahren, wie isothermen Zugversuchen oder isobarer thermischer Aktivierung, charakterisiert [69]–[71], [80]. Dabei wird meist nur ein einzelnes Verfahren zur Charakterisierung verwendet, was zum Beispiel den Vergleich der Ergebnisse zwischen Zugversuchen und thermischer Aktivierung erschwert. Außerdem wird häufig die dynamische Differenzkalorimetrie (DSC) zur Charakterisierung der thermo-mechanischen Eigenschaften eingesetzt [72]. Diese Verfahren stellen eine wichtige Säule dar, um die grundlegenden Eigenschaften von FGL-Materialien zu untersuchen. In technischen Anwendungen, jedoch werden FGL überwiegend elektrisch, mittels des Joule Effekts, geheizt und die anliegende Last ist nicht konstant. Um das Verhalten von FGL-Drähten in der Anwendung besser zu verstehen und den Einfluss diverser Parameter zu untersuchen, ist eine anwendungsorientierte Charakterisierung notwendig. Dazu wird in der ersten Veröffentlichung ein multifunktionaler Prüfstand entwickelt, aufgebaut und validiert. Wegen der Vorteile und der Verbreitung in technischen Anwendungen, wie in Kapitel 1 beschrieben, ist er für FGL-Mikrodrähte mit Durchmessern von 25 μm bis 100 μm ausgelegt. Dazu sind spezielle Bauteile nötig, die einerseits die Reibung minimieren und andererseits eine hohe Messgenauigkeit aufweisen. Hauptbauteile des horizontal ausgelegten Aufbaus sind eine

Kraftmessdose, eine Linearachse, zwei Luftlager, auf denen die Drahtklemmen montiert sind, sowie eine Vorrichtung zur spannungsgeregelten Drahtprobeninstallation. Die Drahtklemmen zur elektrischen und mechanischen Kontaktierung der FGL-Probe befinden sich in einer heizbaren Kammer. Diese verhindert auch, dass unkontrollierte Luftströmungen die Temperatur des Drahtes beeinflussen. Der Prüfstand ist multifunktional, was bedeutet, dass an einer einzelnen Drahtprobe Zugversuche sowie aktorische Versuche durchgeführt werden können. Dies geschieht durch die kraftgeregelte Ansteuerung der Linearachse. Dadurch können, mittels „Hardware-in-the-Loop“, Vorspannsysteme wie Federn, Massen und Endanschläge simuliert werden. Die Temperatur in der Kammer, die die Drahtprobe umgibt, kann währenddessen zwischen Raumtemperatur und 100 °C geregelt werden. Die elektrische Aktivierung erfolgt mit konstantem Strom oder konstanter elektrischer Leistung. Außerdem ist die Dehnrage, respektive die Heizrate, frei wählbar. In der Veröffentlichung wird auf die Konstruktion und die Messmittel detailliert eingegangen. Die Wiederholgenauigkeit der Probeninstallation wird gezeigt, um dann die einzelnen Funktionen des Prüfstands zu testen und validieren. Eine weitere Besonderheit ist hier die hochpräzise Strom- und Spannungsmessung, mit der sich auch bei niedrigen Strömen (<10 mA) verlässliche und präzise Widerstandssignale generieren lassen. Die Versuche zur Funktionsvalidierung werden mit verschiedenen Drahtdurchmessern durchgeführt, um den Umfang der Funktionalität zu zeigen. Am Ende wird die Möglichkeit der Durchführung von zyklischen Zug- und Aktorversuchen dargestellt, womit eine Drahtprobe trainiert werden kann. Diese kann dann ohne manuelle Manipulation mit Zugversuchen charakterisiert werden und in anwendungsnahen aktorischen Versuchen mit unterschiedlichen Vorspannmechanismen untersucht werden. Aus den Daten, die der entwickelte Prüfstand generiert, können viele wichtige Materialparameter sowie Systemparameter für aktorische und sensorische FGL-Anwendungen extrahiert werden. Dazu gehören: E-Modul von Austenit und Martensit, Resistivität der unterschiedlichen Phasen, die Hysteresebreite, remanente Dehnung nach Training, Hub-Kraft-Verhalten und Hub-Widerstand für diverse Vorspannsysteme. Durch den Ausschluss jeglicher Störgrößen sind Daten, die mithilfe des Prüfstands ermittelt werden, prädestiniert für die Parametrierung und Validierung von numerischen Modellen und Simulationen. In einem Artikel von Mandolino et al., bei welchem Autor dieser Dissertation als Coautor mitgewirkt hat, wurde das bereits gezeigt [81]. In der zweiten Veröffentlichung wird eine Methode erarbeitet, um die wichtigsten Eigenschaften von FGL Aktor-Sensor-Systemen, mithilfe des Prüfstandes, experimentell zu erforschen. Mit dieser Methode wird der Einfluss eines zusätzlichen Trainings auf

vorkonditionierte NiTi-Drähte untersucht. Ziel ist es, bei Materialspannungen bis zu 400 MPa ein stabiles Materialverhalten zu erreichen sowie das, aufgrund der R-Phase, stark hysteretische Verhalten des Widerstandssignals zu verbessern. Rein mechanisches Training mit zyklischen Zugversuchen wird einem elektro-thermischen Training mit konstanter Last gegenübergestellt. Verglichen werden die Proben anhand einer definierten Reihe an Zugversuchen mit definierten Heizleistungen sowie Aktor-Tests mit unterschiedlichen Lasten. Die Einflüsse der beiden Trainingsvarianten auf das Spannungs-Dehnungs-Verhalten im Zugversuch, den maximalen Hub in Aktortests, die funktionelle Stabilität und das jeweilige Widerstandsverhalten werden analysiert und bewertet. Als Ergebnis wird herausgestellt, dass das Training dem jeweiligen Lastfall anzupassen ist, weshalb das mechanische Training weniger effektiv ist. Mit dem elektro-thermischen Training bei 400 MPa Spannung wird die Hysterese des Widerstandssignals am besten reduziert. Der Hub bei geringer Last nimmt aufgrund der remanenten Dehnung allerdings ab. Die funktionale Stabilität kann, im Gegensatz zur unbehandelten Probe, bei bis zu 400 MPa nachgewiesen werden. Anhand der Leistungs-Dehnungs-Kurve, die der typischen Temperatur-Dehnungs-Kurve entspricht, wird gezeigt, dass die Trainings eine Veränderung der Umwandlungstemperatur des Materials bewirken. Die Umwandlung findet weniger diskret statt und ist über einen größeren Temperaturbereich verteilt. Mit den Ergebnissen der Veröffentlichung lassen sich im Verhalten optimierte Antriebssysteme mit Self-Sensing auf FGL-Basis entwickeln, die unter erhöhten mechanischen Lasten stabil funktionieren [82]. Die Daten der Widerstandsmessungen helfen bei der Verbesserung von Self-Sensing Algorithmen. Als Erklärung für das nicht lineare, hysteretische Verhalten des Widerstandssignals in Aktor-Anwendungen wird das Auftreten der R-Phase identifiziert.

Ein Ausschlusskriterium für den Einsatz von FGL als Antriebsmechanismus ist in vielen Anwendungen die zu erwartenden Betriebstemperaturen. Es gibt wenig Forschung im Bereich der Hochtemperaturanwendung von kommerziellen NiTi-Legierungen [62]. Die Grenzen des Machbaren basieren dabei auf Indizien, sind aber noch nicht hinreichend erforscht. In der dritten Veröffentlichung werden daher anwendungsorientierte Untersuchungen bei hohen Umgebungstemperaturen, auf demselben Prüfstand, mit den entwickelten Methoden angestellt. Bei Temperaturen von bis zu 100 °C wird der Einfluss des Trainings und der Last auf das Aktor-Sensor-Verhalten untersucht und die Limitierungen werden analysiert. Für niedrige (Konstant- und Feder-) Lasten, werden unbehandelte und thermisch trainierte FGL-Drähte mit Aktortests bei Umgebungstemperaturen bis zu 80 °C verglichen. Es wird gezeigt, dass die Änderung der

Umgebungstemperatur keinen Einfluss auf die Self-Sensing Eigenschaft hat. Außerdem wird herausgestellt, dass das Last-Profil und das Training die Hochtemperatur-Eignung eines FGL-Aktorsystems beeinflussen. Durch das Training sowie höhere Lasten verschiebt sich der maximale Arbeitspunkt in höhere Temperaturbereiche. Mithilfe von Lasten bis 400 MPa, bei denen durch das Training funktionale Stabilität herrscht, verschiebt sich die maximale Einsatztemperatur nochmals um etwa 20 °C nach oben. Zum Verdeutlichen der Anwendungsrelevanz wird auf dem multifunktionalen Prüfstand eine beispielhafte Anwendung untersucht. Diese wird mithilfe von „Hardware-in-the-Loop“ simuliert und es wird gezeigt, dass durch die wissensbasierte Systemauslegung ein Ventil mit funktionierendem Self-Sensing entwickelt werden kann, welches in einem weiten Temperaturbereich sicher und zuverlässig funktioniert.

Die erreichbaren Kräfte in solchen Systemen sind durch die Mikrodurchmesser in der Regel beschränkt. Mittels einer Bündelung der Drähte lässt sich die Kraft skalieren, ohne dabei signifikant an Dynamik zu verlieren [53]. Der Stand der Technik bei der Verbindungstechnik für NiTi-Drähte sind Quetschverbindungen, bestehend aus Messing-Crimps. Diese haben jedoch einige Nachteile. Durch das unedle Metall kann es zur Korrosion in der Verbindungsstelle kommen, was zu schlechter elektrischer Kontaktierung führt. Außerdem sind die Crimps im Vergleich zum Drahtdurchmesser groß, und zum Quetschen sind hohe Kräfte und eine Zugänglichkeit von mehreren Seiten während der Montage notwendig. In der vierten Veröffentlichung wird mit dem Widerstandsschweißen eine Verbindungstechnik für die Fertigung von Bündeln aus FGL-Drähten untersucht, die bisher wenig Beachtung in der Literatur findet. Dieser Schweißprozess hat die Vorteile, dass die Zugänglichkeit nur von einer Seite gegeben sein muss, die Fügekräfte gering sind und allgemein eine gute Automatisierbarkeit gegeben ist. Somit ist er prädestiniert für die automatisierte Montage von Aktor-Sensor-Systemen auf FGL-Draht Basis. In der Veröffentlichung wird das stofffremde Widerstandsschweißen von NiTi Mikrodrähten mit 100 µm Durchmesser an Stahl und Kupferlegierungen untersucht. Das Ziel ist die Fertigung von kompakten, flachen FGL-Drahtbündeln. Die Schweißergebnisse werden dazu methodisch evaluiert, um einen optimalen Parametersatz zu entwickeln. Während die Schweißverbindung von NiTi-Draht mit Bronze und Messing machbar ist, jedoch nicht in hinreichender Wiederholbarkeit und Festigkeit resultiert, zeigt sich bei der Verbindung zu Stahl eine zuverlässig hohe Festigkeit mit guter Wiederholbarkeit. Mit Lebensdauerversuchen und Mikroskopie Untersuchungen wird die Schweißverbindung genauer untersucht, bevor der Bündelungsprozess vorgestellt wird.

Mithilfe des Widerstandsschweißens werden flache FGL-Bündelaktoren gefertigt. Bis zu sieben NiTi-Drähte können auf rostfreie, 5 mm breite und 0,4 mm dünne Stahlbleche geschweißt werden. Aktortests zeigen, dass die Abkühlgeschwindigkeit im Vergleich zu einem dickeren FGL-Draht mit entsprechendem Durchmesser deutlich schneller ist, während die Kraft mit der Drahtanzahl skaliert.

Mithilfe der Ergebnisse aus den vier Veröffentlichungen kann der Anwendungsbereich von FGL-Aktuatoren deutlich erweitert werden. Nicht nur ist das Verhalten und die notwendige Konditionierung bei hohen Lasten mit experimentellen Daten belegt, auch sind die Grenzen der Einsatztemperatur eindeutig untersucht. Mithilfe des Trainings können Kraftausbeute, Umwandlungstemperatur und Widerstandssignal verbessert werden. Durch die geschweißten Bündel kann die Kraft von Aktoren aus dünnen Drähten nahezu beliebig skaliert werden und auch die Verbindung von Einzeldrähten, wird durch den entwickelten Widerstandsschweißprozess für viele Anwendungen erleichtert. Somit ergänzen sich beide Themenbereiche, indem sie eine Brücke von der detaillierten Charakterisierung und Optimierung einzelner FGL-Mikrodrähte hin zur praktischen Fertigung und Anwendung von FGL-Aktor-Sensor-Systemen schlagen. Diese Herangehensweise ermöglicht es, theoretische Erkenntnisse direkt in praxisrelevante Technologien zu überführen.

2.2 A Multifunctional Characterization Test Bench for Shape Memory Alloy Micro-Wires – Design, Implementation and Validation

Dominik Scholtes ^{1,2}, Marvin Schmidt ², Philipp Linnebach ², Stefan Seelecke ^{1,2},
Paul Motzki ^{1,2}

¹ Lehrstuhl für Intelligente Materialsysteme, Zentrum für Mechatronik und
Automatisierungstechnik, ZeMA gGmbH, Saarbrücken

² Lehrstuhl für Intelligente Materialsysteme, Fachrichtung Systems Engineering, Fachrichtung
Materialwissenschaft und Werkstofftechnik, Universität des Saarlandes, Saarbrücken

Veröffentlicht in MDPI Materials.

DOI: 10.3390/ma16134820

© 2023 by the authors.



Dieser Artikel ist lizenziert unter Creative Commons Namensnennung 4.0 International
(Creative Commons Attribution 4.0 International, CC BY 4.0).

Article

A Multifunctional Characterization Test Bench for Shape Memory Alloy Micro-Wires—Design, Implementation and Validation

Dominik Scholtes ^{1,2,*} , Marvin Schmidt ², Philipp Linnebach ², Stefan Seelecke ^{1,2}  and Paul Motzki ^{1,2} 

¹ Intelligent Materials Systems Lab, Center for Mechatronics and Automation Technology, ZeMA gGmbH, 66121 Saarbrücken, Germany; stefan.seelecke@imsl.uni-saarland.de (S.S.); paul.motzki@imsl.uni-saarland.de (P.M.)

² Intelligent Materials Systems Lab, Department of Systems Engineering, Department of Materials Science and Engineering, Saarland University, 66123 Saarbrücken, Germany

* Correspondence: dominik.scholtes@imsl.uni-saarland.de

Abstract: Most relevant to predicting the behavior of shape-memory-alloy (SMA)-based actuator-sensor applications activated by Joule heating are the electro-mechanical characteristics of the material under consideration. For a comprehensive characterization, a single setup that is able to provide all relevant data and information is desirable. This work covers the design, implementation and validation of such a high-end test bench for the holistic characterization of SMA micro-wires. In addition, the setup provides the possibility of application simulation experiments. Key elements of the design are the clamping mechanism guided on air bearings, a linear direct drive, a high-resolution load cell, a high-precision constant current source and a stress-controlled in-line wire sample installation. All measurements take place inside an isolated, temperature-controlled chamber. With the presented setup, the electro-mechanical and thermal characteristics of SMA wire samples with diameters from 20 μm to 100 μm can be determined. Via hardware-in-the-loop (HiL) implementation, the outputs with different biasing mechanisms and additional end-stops can be simulated even at high ambient temperatures. The generated results facilitate the prediction of the exact characteristics of SMA-driven actuator-sensor systems in a variety of applications and lead to a better general understanding of the alloy's properties. All functionalities and features of the setup are presented by discussing the results of exemplary experiments.

Keywords: shape memory alloy; nickel–titanium; NiTi; Nitinol; material characterization; actuator; superelastic; tensile test; high temperature; hardware-in-the-loop



Citation: Scholtes, D.; Schmidt, M.; Linnebach, P.; Seelecke, S.; Motzki, P. A Multifunctional Characterization Test Bench for Shape Memory Alloy Micro-Wires—Design, Implementation and Validation. *Materials* **2023**, *16*, 4820. <https://doi.org/10.3390/ma16134820>

Academic Editor: Junsong Zhang

Received: 1 June 2023

Revised: 28 June 2023

Accepted: 1 July 2023

Published: 4 July 2023



Copyright: © 2023 by the authors. Licensee MDPI, Basel, Switzerland. This article is an open access article distributed under the terms and conditions of the Creative Commons Attribution (CC BY) license (<https://creativecommons.org/licenses/by/4.0/>).

1. Introduction

Shape memory alloys (SMA) show, on the one hand, a great potential to reduce the weight, size and energy consumption of existing drive systems. On the other hand, they enable the integration of actuators in new areas, where spatial conditions typically prevent active elements from being implemented.

From an engineering perspective, SMA wires can be seen as electrical actuators in wire shape, and from a material science view, their thermo-mechanical behavior is of foremost interest, which is the reason for which much research concerning the thermo-mechanical behavior of SMA materials is being conducted. However, for the design of new SMA-driven systems, measurement data based on electrically heated wires and the characteristic of their electrical resistance are of high relevance. Based on this, the temperature dependency and, especially, methods to influence the transition temperatures of the material are of concern to investigate the limitations of SMA-driven actuators.

The fundamentals of thermal SMAs have been discussed extensively in research articles over the last decades [1–5]. Hence, in this work, the following paragraph gives only a short summary on the topic.

SMA have the highest known energy density as an actuator and combine this with resistance-based self-sensing capabilities [6–8]. They are often used in the form of wires and are commercially available in the form of binary nickel–titanium (NiTi). This is also called Nitinol. Nitinol was first investigated by researchers of the U.S. Naval Ordnance Laboratory in 1963 [9]. Depending on the alloy composition, the material shows varying thermo-mechanical behavior. Ni-rich NiTi is superelastic and can be stretched up to 10% at room temperature without permanent damage [10]. The Ti-rich variant, on the other hand, undergoes a (quasi-)plastic deformation if stretched at room temperature. When it is then heated to the so-called transformation temperature, it transforms back to its original geometry. This behavior is called shape memory effect, and strains of 5% or more can be fully recovered [3]. Both effects are based on a reversible rearrangement of the materials' crystal lattice structure, in which a phase transformation from martensite to austenite takes place. The composition of the lattice structure depends on the temperature and the material stress, which is why we talk about the thermo-mechanical behavior of NiTi [11]. To use SMAs as actuators, a Ti-rich NiTi wire is typically heated either by electrical power via Joule heating or passively by a high-temperature fluid in contact with the alloy [12,13]. Because of their high energy density, SMA wires are especially suitable for small and lightweight actuator systems, such as valves, small-size gripping systems and optical image stabilization [14–16]. Other fields of research include continuum robots for catheters and endoscopes as well as bionic applications [17–20]. In all these applications, the self-sensing feature of SMA wires is put to use, and externally positioned sensors are dispensable. The sensing is based on a change of the electrical resistance that can be observed when the SMA undergoes the austenite–martensite transformation. The resistance depends on the contemporary crystal structure, the SMA's length and cross-sectional area, as well as its temperature [12,21].

SMA actuators in the shape of thin wires have many benefits and are therefore the focus of this work, just as they are also the focus of many commercially available products and recent research and developments [14,22–25]. Due to their unique form factor, they create much freedom for design, and their surface-to-cross-sectional area ratio enables faster cooling compared to other forms. The implementation of these wires and electrical contacting are already well-understood, and they can be bundled to create muscle-like strands that exhibit high forces with unchanged dynamics [15,26,27]. As most technical applications have high requirements on the dynamics of the system, this work concentrates on wires with diameters of 100 μm and below, which are also referred to as microwires. These microwires have been shown to realize switching cycle times of 1 Hz to 35 Hz with natural convective cooling in air [2,28].

Dynamic mechanical analyzers (DMA) are used for the thermo-mechanical characterization of SMA wires, but they lack the electrical components necessary to characterize Joule-heated actuator wires as well as the required repeatable installation process [29,30]. To achieve significant and repeatable measurement data with which the behavior of Joule-heated SMA wires can be systematically investigated, a test bench is required that is designed to conduct a variety of experiments on a single sample. The goal of this work is the development and implementation of a fully adjustable setup for actuator simulations even at high ambient temperatures, on which tensile tests and SMA wire training procedures can also be performed. Fundamental measurements form the basis of SMA wire characterization; these enable the systematic comparison of different wire samples concerning their alloy composition and heat treatment, among other things. This enables the selection of the best specimen for a certain application and helps to increase the overall understanding of SMA wire behavior. The data are also used to parametrize and validate numerical SMA models and simulations, as was undertaken by Mandolino et al. with measurement data acquired on the setup described in this work [31]. For the design of sophisticated SMA-based actuator systems with uncommon load scenarios (e.g., high ambient temperatures, high material stress), it is important to investigate the SMA's characteristics

under the exact same conditions as they are in the application. This ensures that the system works exactly as intended.

The remainder of this paper is structured as follows. Section 2 covers the design and features of the test rig as well as the control and measurement system. In Section 3, all functions of the setup are validated and discussed on the basis of exemplary experimental results, and Section 4 finishes with a conclusion and an outlook for future publications.

2. Mechanical Design of the Test Bench, Data Acquisition and Measurement Setup

In this section, the mechanical design of the characterization setup is described in detail. All parts and functions are discussed, including the measurement setup and data acquisition. The goal is to create a test bench on which a multitude of experiments can be conducted on a single test specimen and on a single platform without manual manipulation of the SMA wire. Significant results as well as the ability to change the specimen in an easy way and to reinstall it with the highest repeatability are mandatory.

The setup is developed for wires with a diameter of 20 to 100 μm and a length of about 100 mm. Due to the delicacy of SMA microwires, a multitude of measurements have to be taken into account to achieve repeatable and significant experimental results. A schematic of the setup design and a photograph of the implemented test rig are presented in Figure 1.

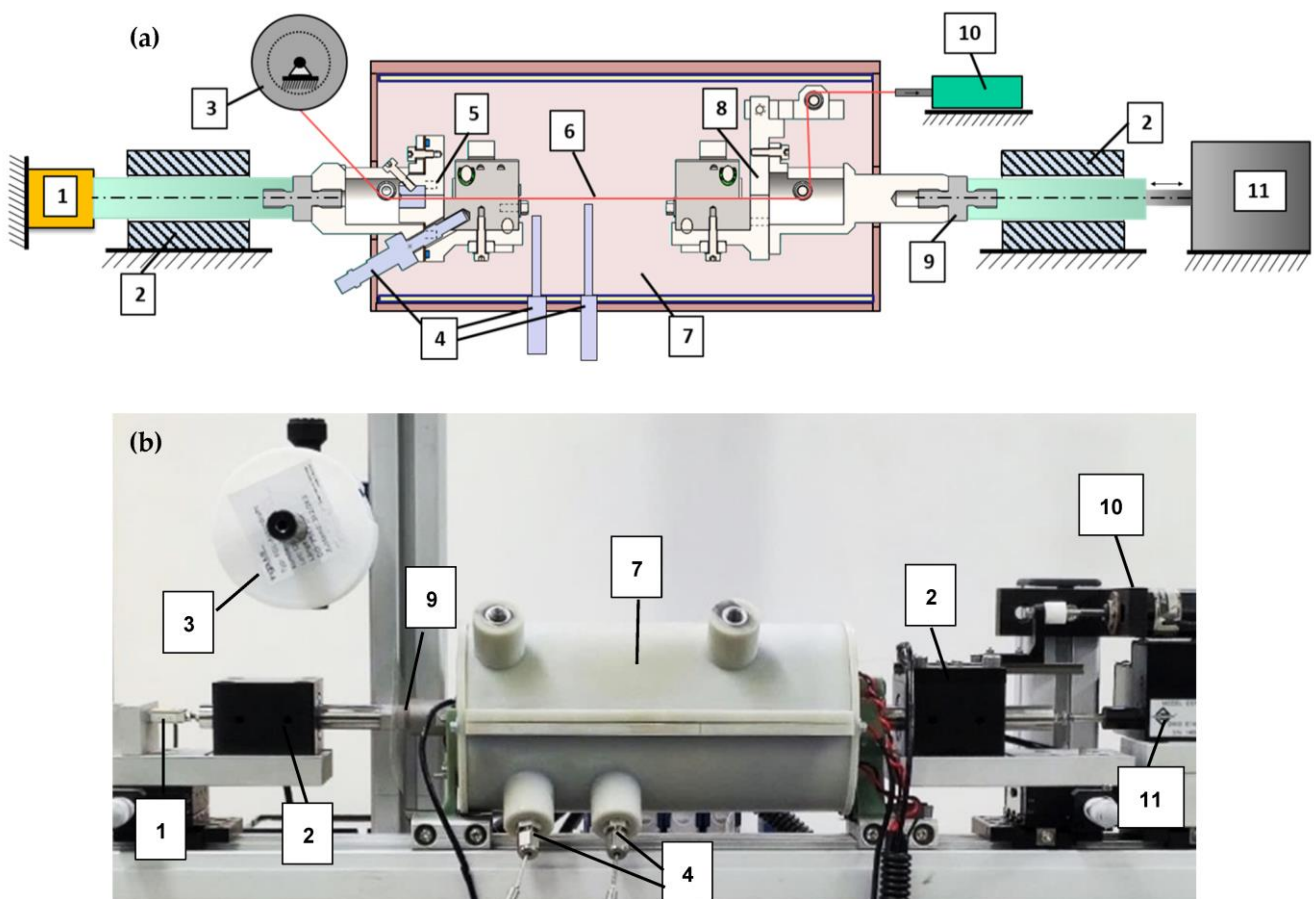


Figure 1. (a) Schematic design of the experimental setup. (b) Picture of the fully implemented test rig with closed heating chamber including the following components: 1: load cell; 2: air bearing; 3: SMA wire reel; 4: PT100 sensors; 5: fixed wire clamp (F); 6: SMA wire; 7: heating chamber; 8: moving wire clamp (M); 9: insulation adapter; 10: preload drive (P); 11: linear direct drive.

From a mechanical point of view, the key element of the whole setup is the clamping mechanism to fix the SMA wire specimen. The CAD assembly of the clamps can be seen in Figure 2a,b. These clamps fix the SMA wire mechanically, and all electrical supply and mea-

surement connections are attached, as can be observed in the picture of the implemented clamps in Figures 2 and 3. The clamps are an assembly of milled parts made from stainless steel. Two offset angled surfaces create a V-shape that defines the position of the SMA wire exactly in the center of the clamps and in line with the whole setup. The wire is clamped on the inner surface of the V-shape over a length of 10 mm. The clamps are tightened manually by spring-loaded hexagonal bolts (parts 1 and 4 in Figure 2). The spring is designed such that the required clamping force of the SMA wire is reached when it is fully compressed. Thus, the clamping force is repeatable, and the wire is held in place safely. Furthermore, the clamps feature guiding rollers and small holes to guide the SMA wire in and out of the isolating chamber they are placed in. They are electrically isolated from the rest of the test rig by PTFE adapters (Figure 1, part 9) in order to enable the electrical heating of the SMA wire without any short circuits.

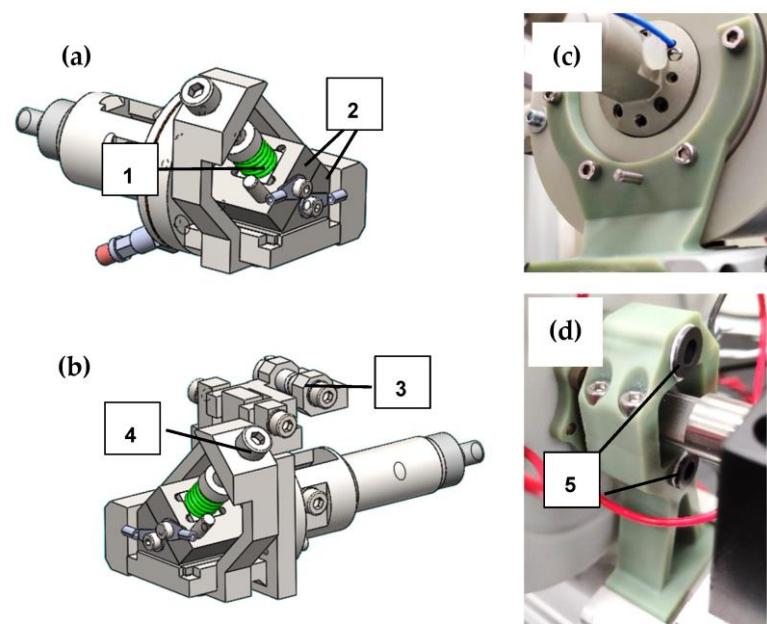


Figure 2. On (a,b), the CAD designs of both wire clamps are displayed. Image (c) shows the fixed bearing of the isolating chamber, and (d) illustrates the floating bearing, which allows for a thermal expansion. The following parts are displayed: 1: spring to load the clamps, 2: clamping jaws, 3: guiding rollers for the SMA wire, 4: bolt to manually tighten clamps, 5: linear guides for thermal expansion of isolating chamber.



Figure 3. Picture of the inside of the chamber with heating foil, both wire clamps with a SMA wire sample installed, electrical wiring and PT100 sensor tips.

Each clamp is mounted to an air bearing shaft, as shown in Figure 1 (2), with the goal of reducing friction losses as much as possible. This is crucial for meaningful micro-wire force measurements, due to the low absolute force level (0.1 N at 200 MPa for a 25 μ m

diameter wire). The bearing is also necessary to keep the lateral forces caused by the weight of the clamps from affecting the force measurement and the linear drive.

The fixed wire clamp (F) is connected via the air bearing to a “Futek LSB200 2 lbs” load cell with a measuring range of approx. ± 10 N. Knowing the SMA wire diameter, the material stress can be calculated with the force measurement data. The moving wire clamp (M) is attached to an “Aerotech ANT-25LA” linear direct drive. Its range of travel is 50 mm, and it is equipped with a sub-micrometer-resolution position encoder that is used as feedback to obtain the wire strain. Additionally, these two components set the base for a closed-loop force and position control, called hardware-in-the-loop (HiL). To ensure a consistent specimen length of 100 mm for each experiment, the distance between the clamps is precisely set using a gauge, and the linear drive is “homed” and in fixed-position mode. To install the SMA wire in a repeatable way, an additional stepper motor (Figure 1, part 10) is installed to pull the wire to a defined pre-stress before it is fixated with the clamps. This process will be discussed in detail in Section 3.

Microwires need to be shielded from irregular air flow and variable convection. Slight air streaming in a room, which occurs, for example, due to the air condition, influences the wire temperature and leads to irregular measurement results. For this reason, the developed setup features a cylindrical chamber with a diameter of 90 mm and a length of 200 mm, in which the wire sample as well as the clamps to fix it are placed. The upper half of the chamber (part 7 in Figure 1b) can be removed to access the wire and the clamps. Inside, a heating foil is attached to the chamber’s walls, which is depicted in Figure 3. In combination with PT100 temperature sensors, the temperature within can be precisely controlled and monitored to set points of up to 100 °C. To account for the expansion of the material when the chamber is heated, the mounting points are located close to the axial center of the cylinders faces, including a floating bearing on one end. With these measures, which are depicted in Figure 2c,d, blockage of the moving clamps due to thermal expansion of the chamber is prevented, and an annular gap for the clamps of less than 0.5 mm is set.

To achieve the highest possible repeatability and least handling effort, the wire is taken directly from the reel on which it is delivered by the supplier. It is guided into the chamber through the open fixed wire clamp (F), onto the featured guiding rollers, and then it exits on the opposite side, where it can be mounted to the pre-loading system (P) (Figure 1, part 10). This procedure is only necessary for the initial setup. After that, a fresh sample is installed by pulling a new part of the wire from the spool to the experimental chamber. This kind of controlled installation process has the benefit that no manual handling or cutting of the SMA wire is necessary to install a new specimen after the first setup.

The whole setup is mounted on a “ThorLabs” rail system (Figure 4) combined with milled custom adapters and positioning stages for a precise alignment of the setup. The outer measurements of the mechanical setup are 800 mm \times 350 mm \times 200 mm (l \times h \times w). The setup is installed on an optical table with air damping to keep shocks and vibrations in the environment of the setup from interfering with the highly sensitive force measurement.

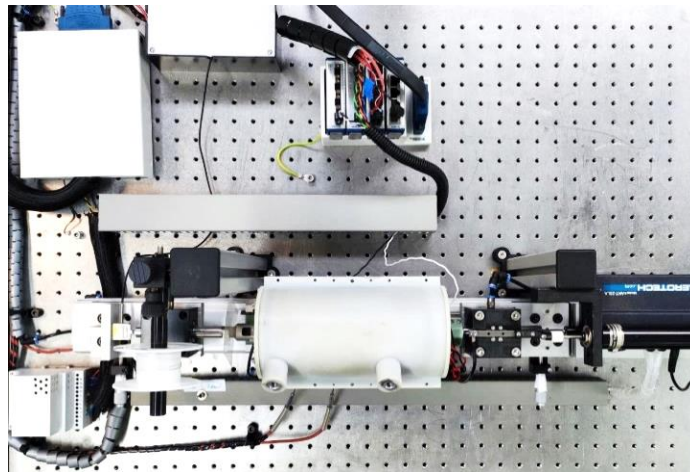


Figure 4. Top-view picture of the whole setup installed on an air damped table, including measurement equipment.

A “National Instruments NI PXI7852R” FPGA-based system and “LabVIEW” programming environment on a PC serve for the control unit as well as data acquisition. The system features several high-resolution analog and digital in- and outputs. The measured values are as follows: position of the moving wire clamp, force of the SMA wire, voltage and current of the wire, temperature inside the chamber. With these values, we can retrace the stress, strain, electrical resistance and electrical power of the SMA wire specimen. The ambient temperature in the heated chamber is measured with two PT100 sensors. They are placed in proximity to the wire: one is close to the fixed clamp, and the other is in the center of the chamber, as can be seen in Figure 3. Another temperature sensor can be added to measure either the temperature inside the fixed clamp or the ambient temperature of the room in which the setup is placed.

A temperature measurement of the wire specimen itself is omitted. A reliable and meaningful measurement can only be performed with a contactless measurement method, for example, an infrared camera. A sensor in physical contact with the wire works as a heat sink, which corrupts the result and does not acquire the temperature distribution over the wire length. Due to the necessary calibration, emission factors, curved wire surface, the small diameter of the SMA and the fact that the sample is enclosed in the chamber, an infrared measurement also proves to be challenging.

Feedback control loops are implemented on the FPGA real-time system for the temperature in the chamber, the electrical power to heat the SMA wire, as well as the force and position of the linear direct drive. With the latter, so-called HiL tests can be performed, which enable one to simulate a spring or constant load as a biasing element of the actuator wire. Position control modes enable the addition of arbitrary end-stops to the load scenarios.

Apart from heating the ambient air in the chamber, the wire is heated via Joule heating. Therefore, a custom current source with 24 V supply voltage is designed. An output current of 0–250 mA is set and controlled by a 0–10 V input signal from an NI module. It features three separate 0–10 V output channels with a different measurement range to measure the supplied current. For high electrical powers, in austenitic tensile tests, for example, the 0–250 mA channel is used. For acquiring precise resistance values close to zero power in the martensitic state, for ambient heating and when cooling down in HiL tests, the channels 0–25 mA and 0–6.25 mA are used for a better resolution. The current source is validated in preliminary work, and an absolute measurement error of 10 μ A is achieved. This kind of precision is necessary to receive significant resistance values.

All input parameters for the experiment are set on a user interface on the PC, where the experiments are started, and the measurement data are depicted. When an experiment is finished, the data are saved for post processing, plotting and analysis with “MATLAB”.

3. Result and Discussion of Validation Experiments and Functionalities

In this section, the functionalities and features of the test rig are proposed and validated with exemplary results on a variety of NiTi wire specimens. The full range of possible experiments and sample diameters is introduced by means of various wire manufacturers. The authors do not intend to compare the different manufacturers and companies to each other, which is why each experiment is performed with a number of varied parameters to place the focus on the capabilities of the test setup. The goal here is to present the options that are provided by the results generated with the help of the test rig, to evaluate and extract various parameters of interest and application relevant data.

Before each experiment, the test specimen needs to be installed in a precise and repeatable manner. As described in Section 1, the length of a SMA actuator is defined by its current temperature and stress as well as the stress-temperature history. In this article, we define the austenitic length of the SMA wire at 10 MPa stress as “zero length” L_0 . The required heating power can easily be acquired in preliminary experiments, by testing at which power level the specimen does not contract any further. The benefit of setting this length as zero is that a SMA wire cannot become any shorter than when it is 100% in the austenite phase, which makes it absolutely repeatable. The stress is chosen, so that the wire is straight without slack or bending, and the correct length is set. For a repeatable and defined length and crystal lattice composition of each SMA wire specimen to be tested, the installation procedure, presented in a flowchart in Figure 5, is performed.



Figure 5. Flowchart of the installation procedure of a SMA wire specimen in the test rig.

After all clamps are opened, the specimen is mounted to the fixed wire clamp (F) and the preloading drive (P) outside the chamber (Figure 1). The moving wire clamp (M) stays open, and the wire is only guided through it. The wire is pulled by the preloading drive, while it is electrically heated above A_f temperature, until the defined stress of 10 MPa is reached. Then, the bolt of clamp (M) is tightened to fix the specimen, and the installation process is finished. The heating current is switched off, and clamp (P) is opened. After this process, the SMA wire sample is known to have a L_0 of 100 mm, and it is ready for the following experiments.

Each experiment is started by conducting a so-called “reset test”, with the goal of having the same repeatable initial condition for every test and reducing the influence of the order in which different experiments are conducted on a specimen. To reset a wire sample to these initial conditions, it is heated to austenite and cooled back down to martensite under stress-free conditions.

In general, two different sorts of experiments can be conducted on the test rig: tensile tests, in which the wire is cycled mechanically, and actuator tests, in which the wire is cycled thermally via Joule heating. Both variants can be repeated any number of times, which is used for training experiments. SMA samples for tensile tests are heated with constant electrical power, constant current or via the ambient air temperature. The parameters that are variable are the maximum strain, the strain rate and the level of heating power/current/temperature. The actuator tests are conducted with the help of HiL. Biasing elements such as springs and masses can be simulated with the help of a closed-loop force and position control of the linear direct drive. The heating is achieved via triangular current signals, as a constant power supply is not common in actuator applications due to the complexity. Parameters that can be varied are the biasing force and spring stiffness, the activation signal duration, the maximum heating current and the ambient temperature. To limit the travel, as it is also often done in applications, arbitrary end-stops can be set.

The following resulting data are extracted from all experiments: time in s, force in N, position (of the linear drive) in mm, voltage over the SMA in V, current in A, ambient

temperature in °C. The diameter of each wire sample is measured in a cold state with a micrometer gauge to calculate the material stress. The change in the wire's cross-sectional area under strain or contraction is not considered.

In the following subsections, only stress–strain diagrams are presented instead of force elongations graphs, to have a common and comparable basis for varying diameters or wire lengths. Force and elongations can easily be calculated, as the necessary parameters are listed for each experiment. Electrical resistance and power are calculated from the voltage and current measured during the experiments.

3.1. Validation of Installation Process

To validate the previously described installation procedure of wire samples, a special test series is conducted. The goal is to check the repeatability of the procedure, so that wire samples can be changed, and the next experiment will have the same initial conditions as the one before. For the checkup, a “SAES Getters Smartflex 100” NiTi wire specimen with a measured diameter of 100 μm is used [32]. A specimen is installed in the defined manner, and a tensile test with 0.2% maximum strain and a constant power of 0.5 W is performed. The installation procedure and the following tensile test is repeated three times, of which the results are presented in Figure 6.

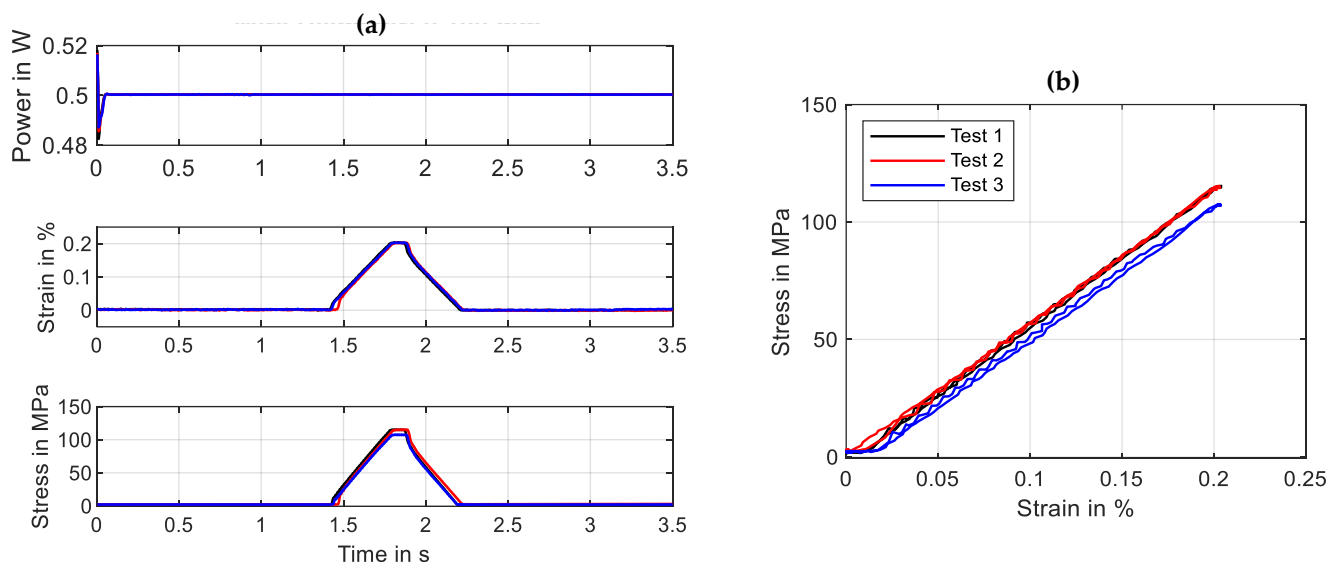


Figure 6. Results of the validation experiments for the wire installation process. Depicted are input and output parameters over time in (a) and stress over strain in (b). Test parameters: tensile test, max. strain 0.2%, strain rate 0.005 s^{-1} , wire specimen “SAES Getters Smartflex” 100 μm , electrical heating power 0.5 W, 3 iterations.

The results of the validation experiment show that the L_0 has a maximum variance of 0.015% strain, resulting in 7 MPa difference in stress at 0.2% strain. These values prove that a good repeatability of the installation process is provided.

3.2. Tensile Tests under Constant Electrical Power Heating

The first function of the test rig to be introduced are tensile tests in which the maximum strain, strain rate and heating method are variable parameters. The results are used for a basic characterization of actuator wires and allow for evaluation and comparison, for example, of different alloy compositions and transformation temperatures. For this exemplary experiment, the wire is heated with a constant electrical power and stretched to 5% strain with a strain rate of 0.01 s^{-1} . A “Dynalloy Flexinol LT (70 °C)” NiTi wire with a measured diameter of 49 μm is used [33]. To examine the tensile characteristics under different conditions, five tensile tests are performed in a certain order. Before the

experiment starts, the sample undergoes the previously introduced reset procedure, in which it is heated to full austenite and cooled down without tensile stress. The first tensile test is conducted with no power applied, but 5 mA of measuring current is used to calculate the resistance. This test is repeated once. Then, three more tensile tests are performed with high power (0.37 W), medium power (0.31 W) and low power (0.25 W). For evaluation, the acquired data are plotted over time and can be seen in Figure 7. In between each of these iterations, the reset procedure is omitted.

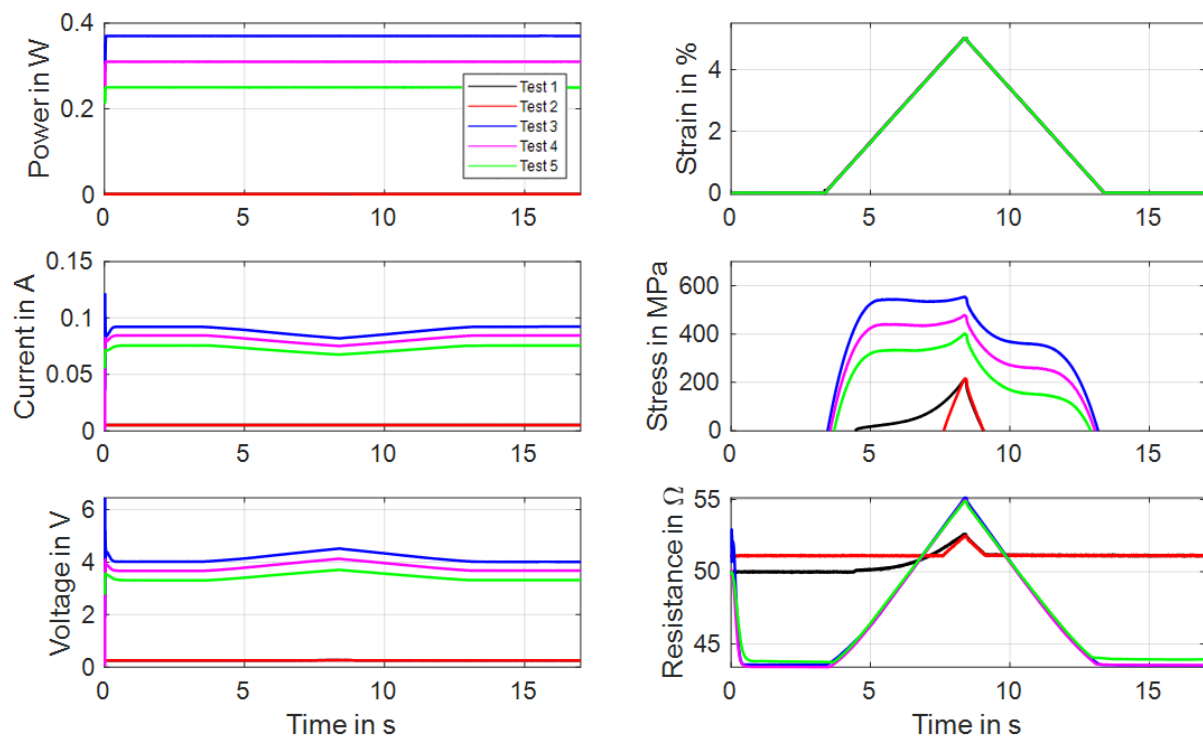


Figure 7. Results of tensile tests with wire specimen “Dynalloy Flexinol LT (70 °C)” of 49 μm diameter under varied constant power. All results are plotted over time. Test parameters: max. strain 5%, strain rate 0.01 s^{-1} , ambient temperature 22 °C.

The first two tests, in black and red color, show the martensitic material characteristics. In the first experiment, a detwinning of the martensite can be observed that builds under stress-free cooling from austenite to martensite. After the material is detwinned, the second tensile test shows the purely elastic behavior of martensite. In Figure 8, the results of stress and resistance are plotted over strain. Here, the martensitic detwinning and the elastic branch can be observed as well. In Figure 8a, the typical stress–strain hysteresis with varying transformation plateaus depending on the heating power is recognizable, and in Figure 8b, a linear change in resistance under a tensile load with constant heating power is evident.

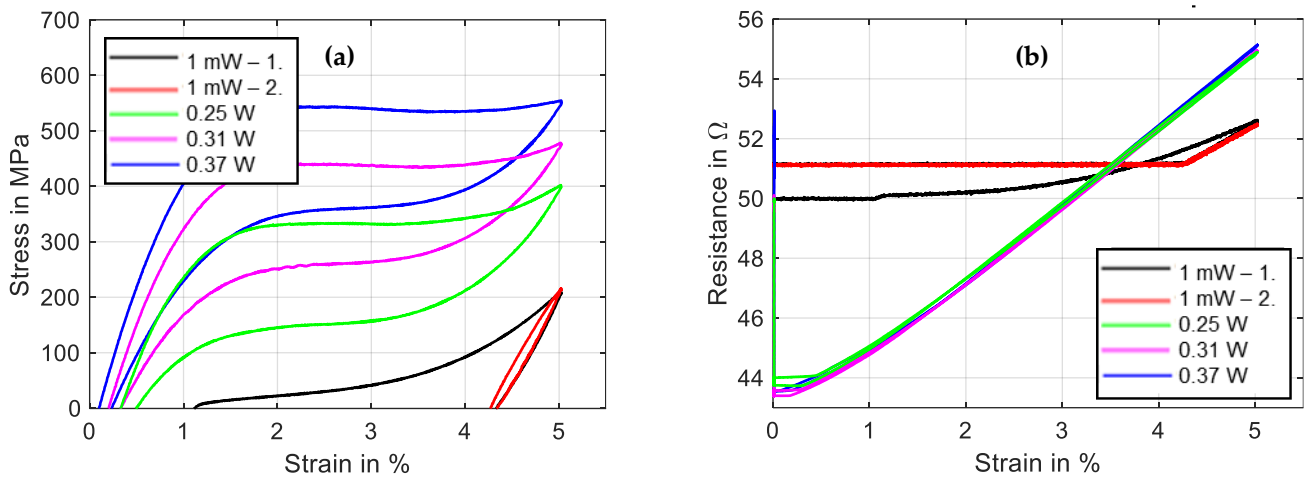


Figure 8. Results of tensile tests with wire specimen “Dynalloy Flexinol LT (70 °C)” of 49 μm diameter under varied constant power: (a) shows stress vs. strain, and (b) shows resistance vs. strain.

3.3. Tensile Tests under Constant Electrical Current Heating

A power-controlled electrical supply is uncommon in SMA applications due to the complexity and lack of benefits. For scientific tests, on the other hand, this is of interest, because a constant heating power equals a constant temperature if the strain rate and the rate of the change in power are sufficiently small [34]. As the main target of the setup is to provide measurement data that are of relevance for applications, experiments with constant current to heat the wire are also part of the test portfolio and are presented in the following. In the example depicted in Figures 9 and 10, a strain rate of 0.005 s⁻¹ at a maximum strain of 5% is chosen for a “Fort Wayne Metals NiTi #5” wire with a measured diameter of 73 μm [35].

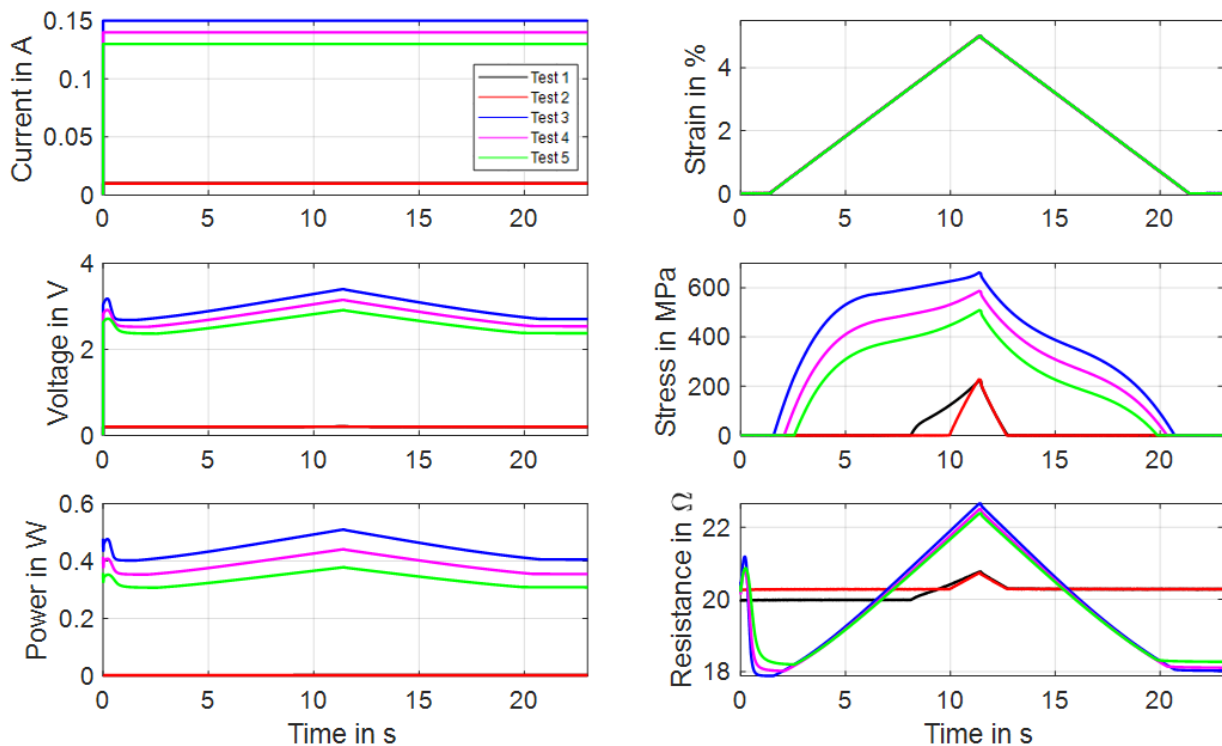


Figure 9. Results of tensile tests with wire specimen “Fort Wayne Metals NiTi #5” of 73 μm diameter under varied constant current heating. All results are plotted over time. Test parameters: max. strain 5%, strain rate 0.005 s⁻¹, ambient temperature 22 °C.

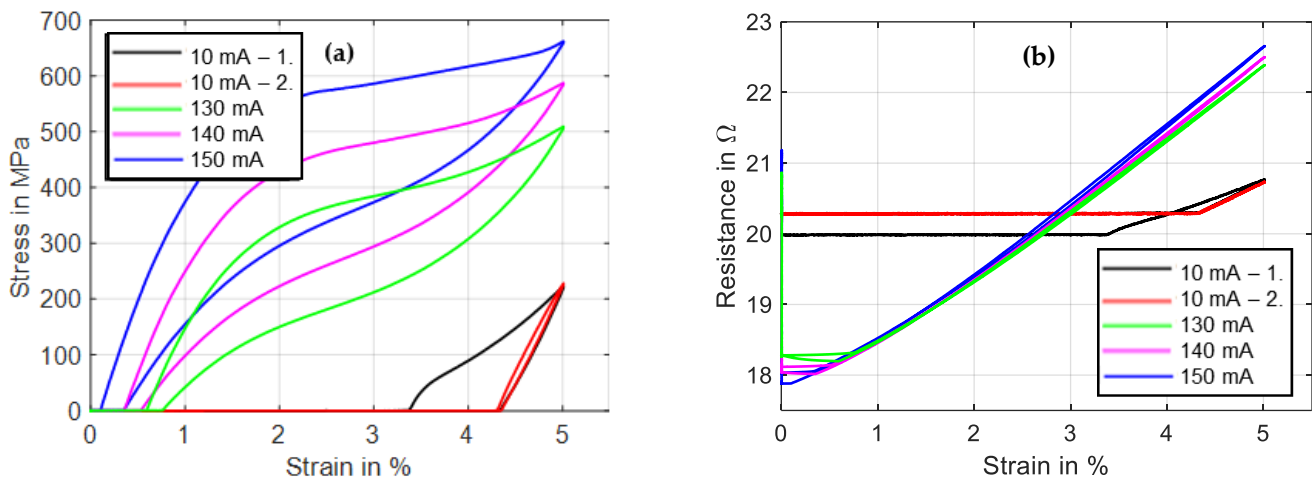


Figure 10. Results of tensile tests with wire specimen “Fort Wayne Metals NiTi #5” of 73 μm diameter under varied constant current heating: (a) shows stress vs. strain, and (b) shows resistance vs. strain. Test parameters: max. strain 5%, strain rate 0.005 s^{-1} .

The method of the experiments is the same as mentioned in Section 3.2, and the heating is controlled with a constant current instead of constant power. The first tensile test is conducted with 5 mA of measuring current to calculate the resistance. This test is repeated once. Then, three more tensile tests are performed with high current (150 mA), medium current (140 mA) and low current (130 mA). As can be observed in Figure 10a, the main difference from constant power heating is that the slopes of the transformation plateaus are steeper and less distinct, due to the increase in electrical power with increasing wire resistance. A detwinning of the martensite is also evident in this sample for the first tensile test. The amount of twinned martensite and, with it, the intrinsic two-way-effect of a SMA wire are varied in between samples. This depends on individual load history as well as the training and the alloy composition [36]. With the help of the austenite and martensitic branch of the stress–strain curves in Figure 10a, as well as the resistance–strain graph in Figure 10b, the first important tool for the design of a SMA actuator is available.

With these results, the maximum stroke and the force output of an actuator with a certain bias element can be estimated by a graphical/geometrical comparison of the austenite and martensite branches. The necessary electrical specifications can be estimated with the maximum and minimum values of austenitic and martensitic resistance values and the equivalent heating currents.

3.4. Tensile Tests under Ambient Temperature Heating

The chamber that isolates the specimen from the surrounding air can be used to passively heat the SMA wire, as described in Section 2. Therefore, a certain temperature setpoint is chosen, and the inside of the chamber is heated up to that level. In this subsection tensile tests with a passively heated wire are proposed. The outputs are used to check at which temperature a sample starts to build up austenite phase fractions and to compare electrically heated experiments with temperature-controlled tests for evaluating transition temperatures. For these tests, a NiTi wire sample provided by “Ingpuls GmbH” with a diameter of 73 μm is used [37]. For each temperature setpoint (22 $^{\circ}\text{C}$, 60 $^{\circ}\text{C}$, 80 $^{\circ}\text{C}$, 100 $^{\circ}\text{C}$), a tensile test with three iterations is performed. Before every set of tensile tests, the reset procedure is conducted. Thus, the first iteration of one set deviates from the second and the third, as can be observed in Figures 11 and 12. For the tensile tests of this subsection, the maximum strain is set to 6% with a strain rate of 0.005 s^{-1} . All tests are conducted with the same sample in order of rising temperature. The temperature control is based on the PT100 sensor placed in the middle of the chamber, and the measurement in proximity to the clamp provides information about the uniformity of temperature distribution inside the chamber. The temperature-over-time graph in Figure 11 makes this distribution visible. Meanwhile,

the air in the middle of the chamber is steady at the chosen setpoint. The temperature at the edge is slightly lower due to small air gaps in the surrounding and the clamp working as a heat sink.

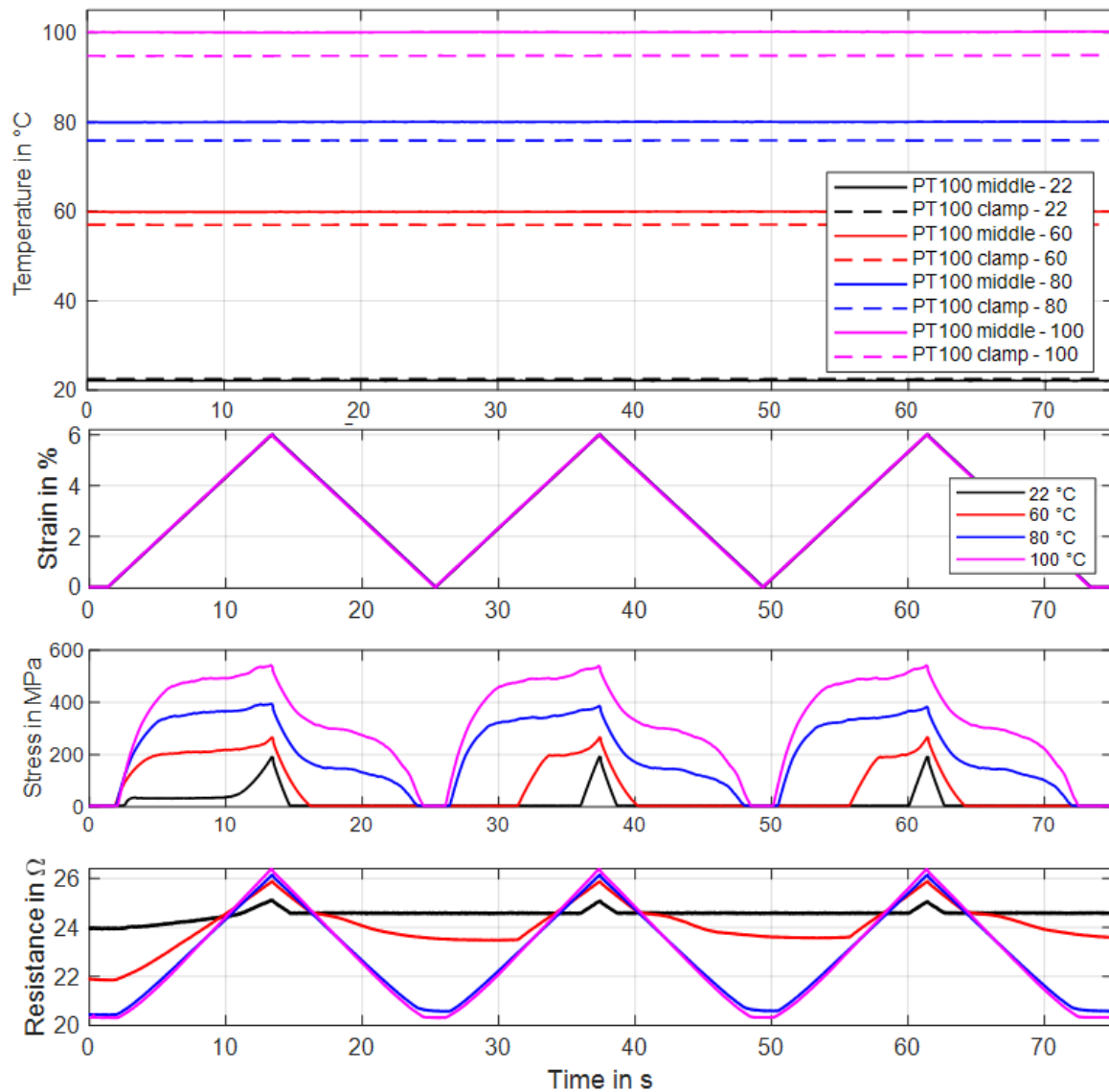


Figure 11. Results of tensile tests with a wire specimen by “Ingpuls GmbH” of 73 μm diameter with varied ambient temperature. Three iterations are performed for each temperature. All results are plotted over time. Test parameters: max. strain 6%, strain rate 0.005 s^{-1} , measurement current 10 mA.

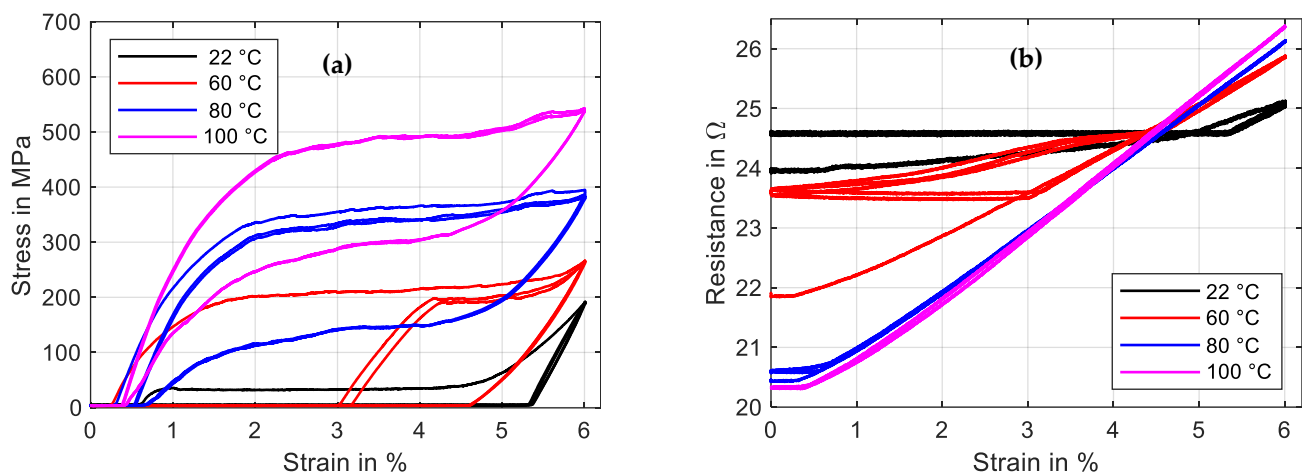


Figure 12. Results of tensile tests with a wire specimen by “Ingpuls GmbH” of 73 μm diameter with varied ambient temperature. Three iterations are performed for each temperature. (a) shows stress vs. strain, and (b) shows resistance vs. strain. Max. strain 6%, strain rate 0.005 s^{-1} .

The shape of the stress–strain hysteresis in Figure 12a, for temperatures of 80 °C and higher, shows the typical austenitic characteristics, as can be expected for an actuator wire. For the experiment at room temperature, the same detwinning effect in the first cycle as in the previous subsections can be observed. The set of tensile tests at 60 °C ambient temperature shows that the material is already partially transformed to austenite. To achieve the resistance values, a measurement current of 10 mA is applied during all experiments. The results of the resistance measurements are plotted over strain in Figure 12b. The typical linear behavior is observed at 22 °C, 80 °C and 100 °C. The 60 °C experiment shows a hysteretic characteristic, as the sample seems to partially transform back to austenite when it is fully relaxed.

3.5. Actuator Tests with Constant Load Bias

The so-called HiL function of the test rig enables the performance of actuator tests with the simulation of various biasing mechanisms. The linear direct drive is used in a force-control mode with a closed loop feedback of the force measurement provided by the loadcell. Constant load biasing with arbitrary levels, a variable linear bias spring with an adjustable force offset and freely selectable end stops are implemented. In this subsection, the constant load biasing function of the test rig is proposed with the example of a 100 μm “SAES Getters Smartflex” NiTi wire. The time sequence of the output data is depicted in Figure 13.

The test sequence is started with only the measurement current of 10 mA applied to achieve continuous resistance measurement results from the experiment’s start. The linear drive is moved to pull the wire to the preset force value of 1.48 N, which results in a material stress of 188 MPa. When the setpoint is reached, a triangular current signal with a maximum value of 220 mA and a signal duration of 60 s, as displayed in Figure 13, is run three times. This results in the wire contracting to a strain of 0.7% and releasing back to 5.7% of absolute strain. A difference between the initial cycle and the next cycles can be observed in the strain and stress signal in Figure 13 as well as in Figure 14a. The reason for this behavior lies in the detwinning of martensite in the first cycle. In the reset procedure that is performed before each set of experiments, martensite in a twin structure is generated because of the “load-free” condition in the experiment. In the last two cycles of the experiment, the biasing stress only allows for the formation of detwinned martensite.

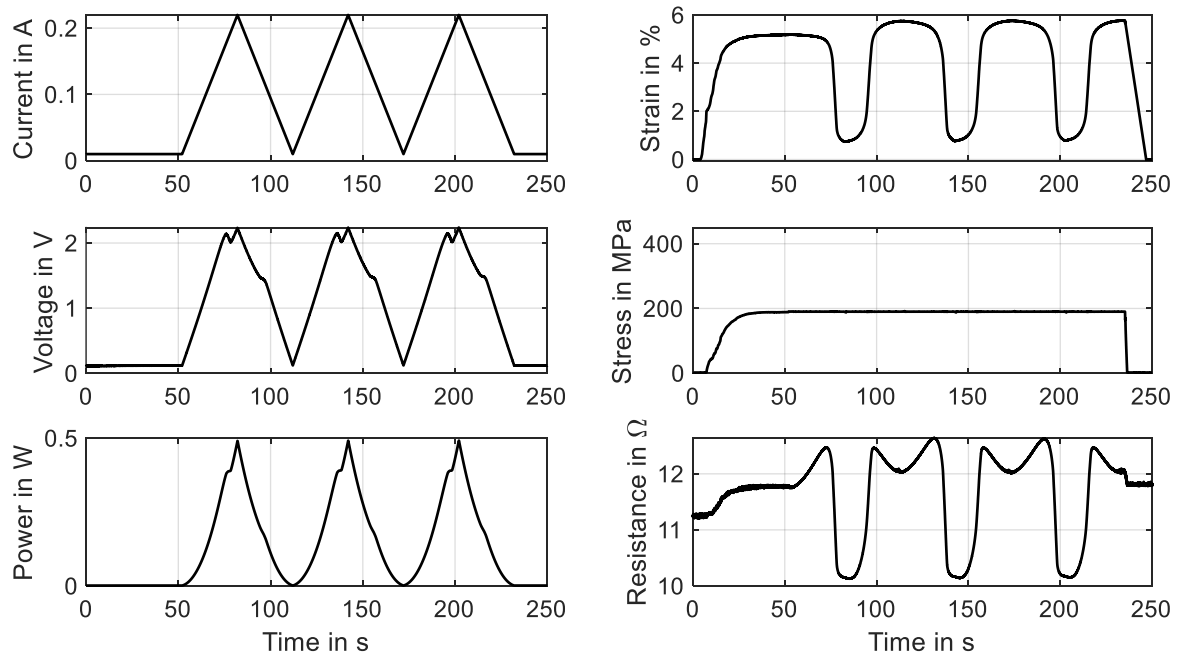


Figure 13. Results of actuator tests with wire specimen “SAES Getters Smartflex” of 100 μm diameter under constant load biasing of 188 MPa. A triangular current signal with an amplitude of 220 mA and a signal duration of 60 s are applied. Three iterations are performed for the experiment, of which all results are plotted over time.

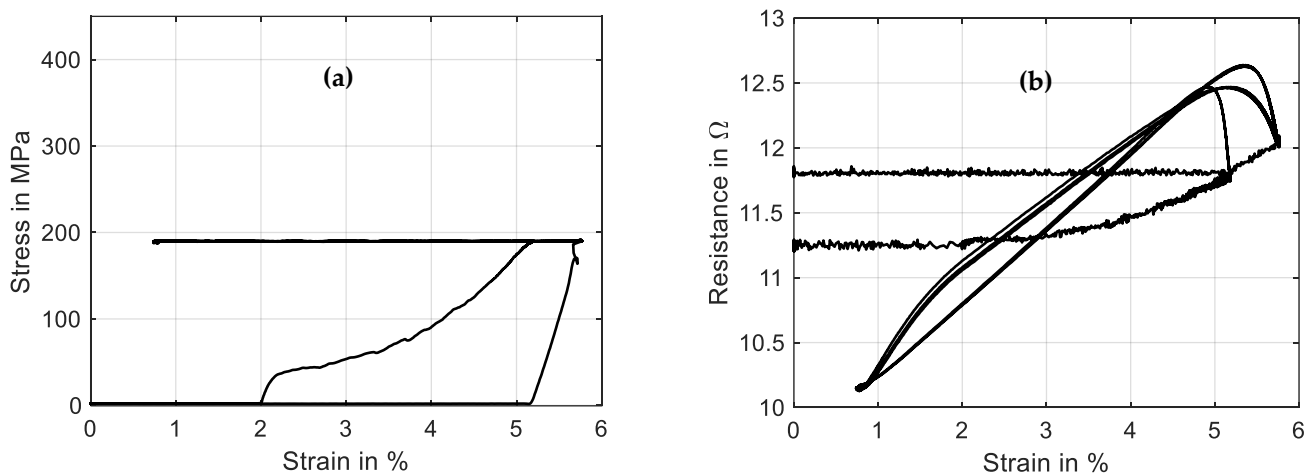


Figure 14. Results of actuator tests with wire specimen “SAES Getters Smartflex” of 100 μm diameter under constant load biasing of 188 MPa. A triangular current signal with an amplitude of 220 mA and a signal duration of 60 s are applied. Three iterations are performed for the experiment. (a) shows the stress vs. strain behavior, and (b) shows resistance vs. strain.

This difference due to the initial lattice structure of the NiTi is also observed in the resistance-over-strain graph in Figure 14b. The linear correlation between resistance and strain in tensile tests gives way to a hysteretic behavior. Taking into account the start of the second signal, when the behavior is stabilized, the resistance rises from 12 Ω to 12.7 Ω as the wire temperature rises, and only a minor change in geometry and the crystal lattice appears. In the phase transformation to austenite, accompanied by a contraction of about 4.8%, the resistance drops to 10.2 Ω . As the heating current is reduced again, a slight dip in resistance can be observed, which leads to the first loop in the hysteresis. This is due to the temperature outweighing the influence on the resistance. Then, the crystal

lattice transforms back to martensite, accompanied by a rise in resistance of up to 12.5Ω . Another loop is formed in the cooling process, as the slope of the resistance over strain is not monotonous and cuts the heating branch of the resistance–strain curve. Returning to full martensite and room temperature, the starting value of 12Ω is reached again.

The SMA wire is heated electrically and quantitative temperature measurements of micro wires cannot be performed in this test setup and neither can the wire temperature be measured in SMA-driven applications. The power–strain diagram is shown in Figure 15 and can be compared to a typical temperature-over-strain diagram. As the experiment is conducted in a quasistatic manner due to the slow heating rate, a correlation between electrical power and temperature is allowed [8]. The typical shape of a SMA temperature–strain hysteresis can be qualitatively observed in the power–strain plot as well. In systematic experiments, these plots can be used to achieve the austenite start and finish power of a wire sample for various loads. With the help of temperature-controlled experiments, a comparison is possible as well.

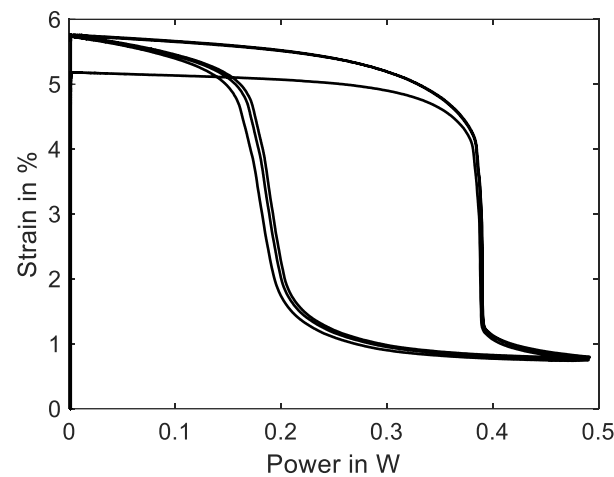


Figure 15. Results of actuator tests with wire specimen “SAES Getters Smartflex” of $100 \mu\text{m}$ diameter under constant load biasing of 188 MPa . A triangular current signal with an amplitude of 220 mA and a signal duration of 60 s is applied. Three iterations are performed for the experiment. The diagram shows the strain over electrical power behavior.

As soon as the electrical power is increased, the SMA sample starts to contract with a slow rate. After about 1.5% contraction, at 0.39 W , the main portion of the phase transformation takes place, and the wire contracts suddenly about 3% . The last 0.4% strain is reached at 0.5 W . The transformation back to martensite is less sudden, has a flatter slope and occurs mainly at about 0.2 W . From this hysteresis curve, we can extract the information about austenite and martensite start and finish power values and the width of the hysteresis, which helps to compare and evaluate different SMA samples for specific applications.

3.6. Actuator Tests with Spring Load Bias

In most cases, the biasing system for an SMA wire in technical applications includes linear springs. The stiffness and pretension of the spring influence the stroke output and resistance of SMA wires. To conduct a systematic study on this influence with variations in the parameters, it is possible to simulate any spring with any pretension with the test setup. Furthermore, we can test and investigate specific actuator configurations in detail before building the actual system. In this example, a “SAES Getters Smartflex” NiTi wire with $100 \mu\text{m}$ diameter is prestressed to the same level as in Section 3.5, and a spring stiffness of 0.2 N/mm is applied. The wire is heated with the same sequence as before, which is a triangular signal with 60 s duration and an amplitude of 220 mA . The results of three iterations of the experiment are shown in Figure 16.

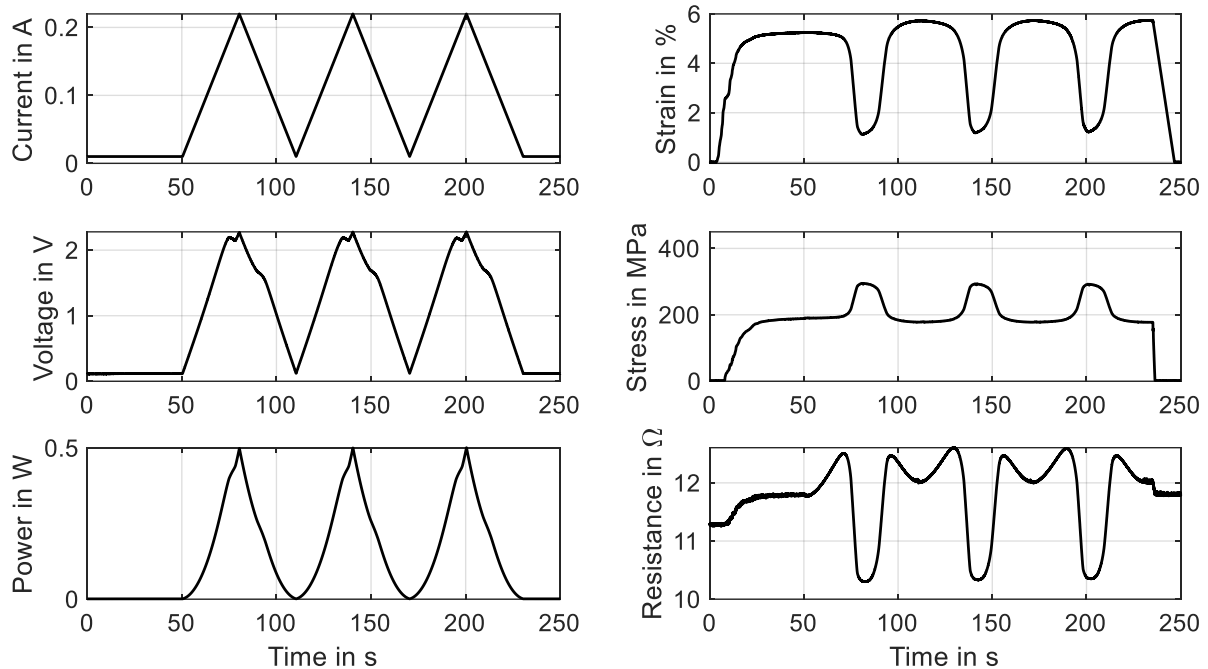


Figure 16. Results of actuator tests with wire specimen “SAES Getters Smartflex” of 100 μm diameter under spring load biasing of 0.2 N/mm and a pretension of 1.48 N. A triangular current signal with an amplitude of 220 mA and a signal duration of 60 s is applied. Three iterations are performed for the experiment, of which all results are plotted over time.

The results of stress and resistance plotted over strain are displayed in Figure 17. The same difference in the initial cycle can be observed as in Section 3.5 due to twinned martensite formed in the reset procedure before the actual experiment. The stress–strain curve follows the spring characteristic and exhibits a stroke of 4.5% in stable conditions after the first activation. The actuator cycles between 170 and 295 MPa. In the strain–time trend of Figure 16, it is observed that the maximum stroke is slightly reduced with ongoing cycling. The SMA behavior is not stable in the high-stress region, and a residual strain builds up.

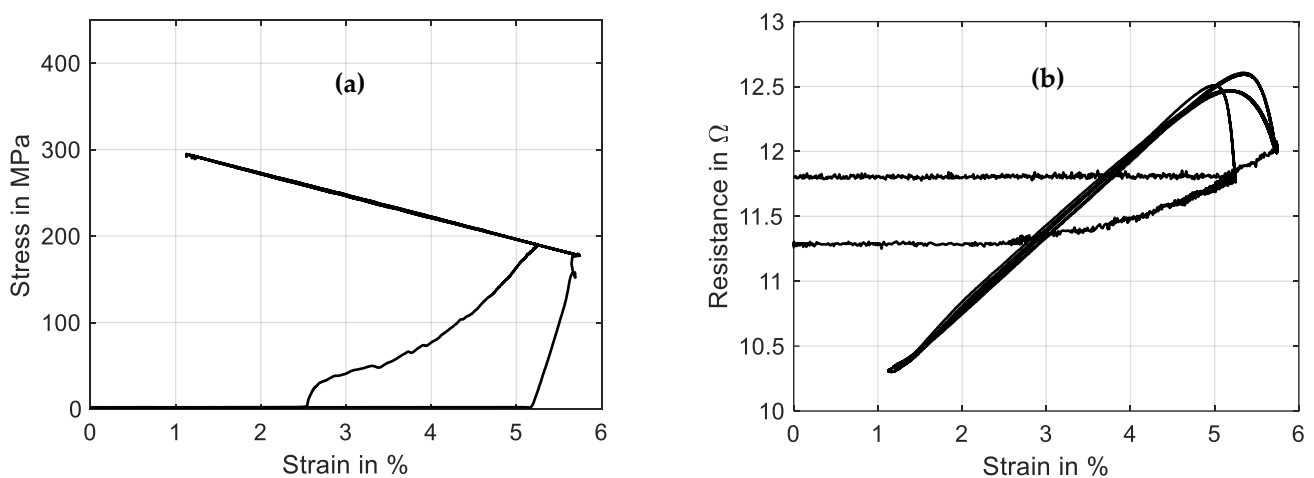


Figure 17. Results of actuator tests with wire specimen “SAES Getters Smartflex” of 100 μm diameter under spring load biasing. A triangular current signal with an amplitude of 220 mA and a signal duration of 60 s is applied. Three iterations are performed for the experiment. (a) shows the stress vs. strain behavior, and (b) shows resistance vs. strain.

Comparing the resistance–strain graph in Figure 17b to Figure 14b, the spring-loaded SMA wire shows a less hysteretic behavior but still shows similar crossing loops. This difference can be explained by the stress dependency in the transformation temperatures of the SMA materials. The stress increases with the wire contracting, and at the same time, this increases the transformation temperature. For SMA-driven technical systems, this means that the resistance signal of the self-sensing feature is easier to interpret and correlate with a certain actuator position.

The stress dependency of the phase transformation temperature also prostates in the strain–power hysteresis in Figure 18, where the shape of the hysteresis is changed compared to Figure 15. The transformation from austenite to martensite and back is less steep, as phase transformation temperature rises with increasing stress, and vice versa. The higher material stress makes higher heating powers necessary to fully transform the crystal lattice to austenite. By varying spring stiffness and preloading, their influence on heating power and resistance behavior can be studied systematically. The results can help to predict the necessary parameters for high load scenarios of SMA that are rather uncommon and to increase the performance of self-sensing-based control strategies for SMA actuators.

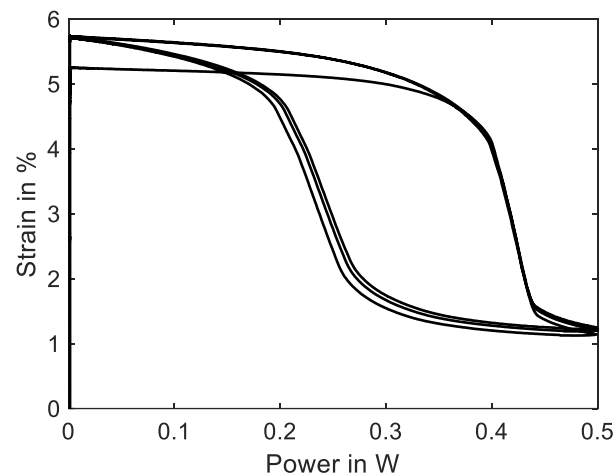


Figure 18. Results of actuator tests with wire specimen “SAES Getters Smartflex” of 100 μm diameter under spring load biasing. A triangular current signal with an amplitude of 220 mA and a signal duration of 60 s is applied. Three iterations are performed for the experiment. The diagram shows the strain vs. electrical power behavior.

3.7. Actuator Test with Spring Load Biasing, End Stops and 60 °C Ambient Temperature

The full potential of the test rig is put on display in this following subsection. For applications in commercial products, the automotive and the industrial environment, the ambient conditions change, and increased temperatures prove to be especially challenging for SMA actuator performance. Additionally, a defined movement of drive units is often supported by end stops. To investigate the capabilities of SMA wire actuators at high temperatures and the influence of the biasing force on the characteristics, several features of the test rig are combined for these experiments. Before the experiment is started, the chamber is heated to a stable temperature of 60 °C. The wire specimen is again a “SAES Getters Smartflex” with 100 μm diameter, which is prestressed to 188 MPa. Due to the increased ambient temperature, the amplitude of the triangular signal of the heating current is reduced to 180 mA to avoid overheating and damaging the sample. To simulate a realistic application, for example, a fluidic valve, two end stops at 1.5% and 4% strain are implemented. The experimental procedure is similar to Sections 3.5 and 3.6, and the end stops limit the range of travel. The results of all measurement data are presented over time in Figure 19. Temperature is not included, as it is held constant along the experiment.

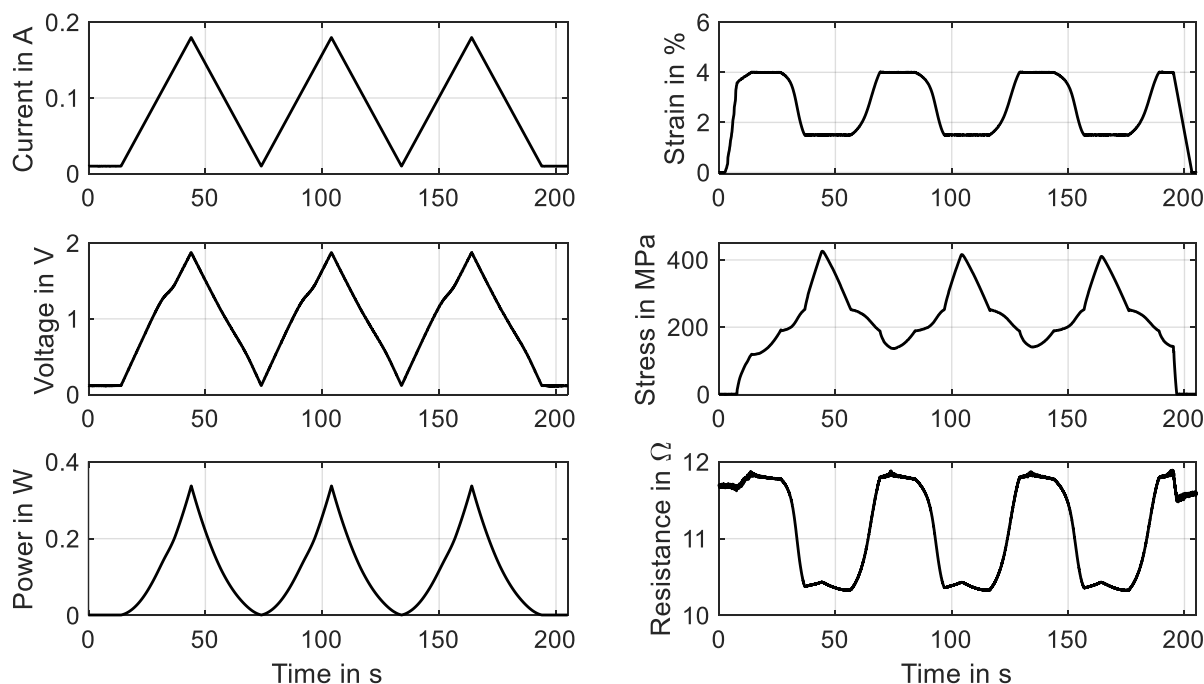


Figure 19. Results of actuator tests with wire specimen “SAES Getters Smartflex” of 100 μm diameter under spring load biasing with end stops and 60 °C ambient temperature. A triangular current signal with an amplitude of 180 mA and a signal duration of 60 s is applied. Three iterations are performed for the experiment, of which all results are plotted over time.

Due to the end stop at 4% strain, the movement of the SMA sample starts after the 188 MPa spring preload is overcome. This can be observed in a good manner in Figure 20a. As the second end stop is reached at 1.5% strain, the stress rises up to 420 MPa. This SMA sample is not trained for stresses higher than 200 MPa, and therefore, the maximum stress drops with each cycle, as can be observed in Figure 19. The strain output is not affected, as the end stops limit the travel beforehand.

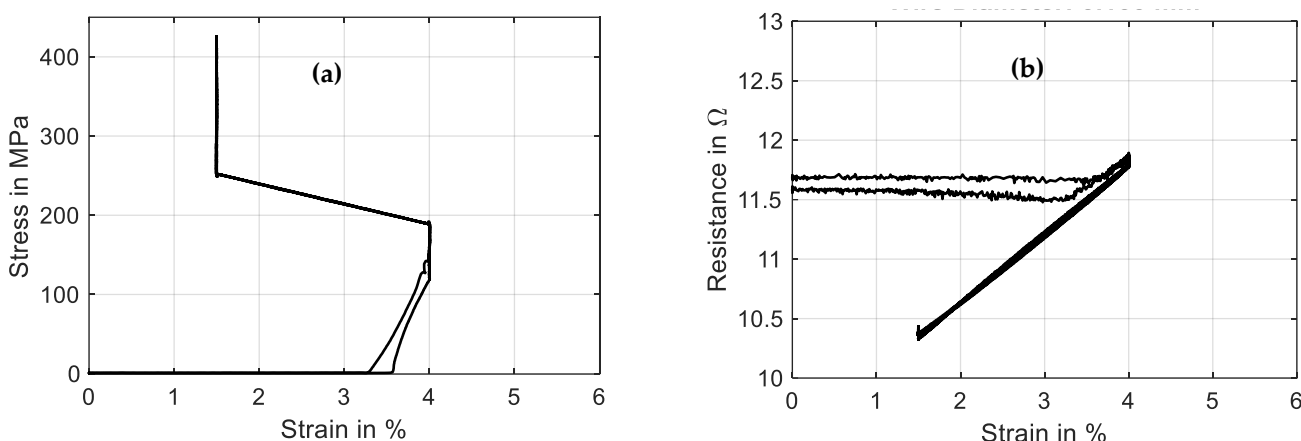


Figure 20. Results of actuator tests with wire specimen “SAES Getters Smartflex” of 100 μm diameter under spring load biasing with end stops and 60 °C ambient temperature. A triangular current signal with an amplitude of 180 mA and a signal duration of 60 s is applied. Three iterations are performed for the experiment. (a) shows the stress vs. strain behavior, and (b) shows resistance vs. strain.

The resistance (Figure 20b) is even less hysteretic than in the previous subsection, because of the ambient temperature being close to the austenite start temperature and the limited travel. Thus, loops at both ends are cut off as well. The bends in the resistance

signal in Figure 19 when the end stops are reached promise a good detectability with the help of resistance-based control strategies.

If these limits can be detected, the overshoot in material stress can be reduced, for example, with a feedback control. This can lead to better fatigue life and higher energy efficiency of SMA systems. When looking at the strain–power hysteresis in Figure 21, compared to Figure 18, it can be observed that it has moved towards the lower left corner and decreased in width and height. Because of the increased ambient temperature, the electrical power needed to start the transformation is reduced to under 0.2 W, and the end stops limit the strain. It is also evident that a maximum current of only about 150 mA is sufficient to reach full contraction in this configuration.

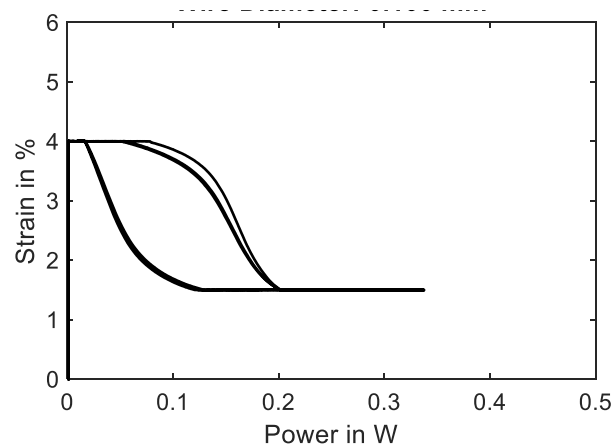


Figure 21. Results of actuator tests with wire specimen “SAES Getters Smartflex” of 100 μm diameter under spring load biasing with end stops and 60 $^{\circ}\text{C}$ ambient temperature. A triangular current signal with an amplitude of 180 mA and a signal duration of 60 s is applied. Three iterations are performed for the experiment. The diagram shows the strain over electrical power behavior.

3.8. Training—Cyclic Tensile and Actuator Tests

Commercially available NiTi actuator wires are usually trained and exhibit a stable behavior when used within a typical range of 200 MPa. As is shown in Sections 3.6 and 3.7, excessive material stress leads to instable stress–strain characteristics, and the stroke and force output degrade over time. This aspect and the residual strain can lead to the failure of a system in the very beginning. To avoid this, SMA wires in high-stress applications need to undergo an additional training procedure to achieve a stable and predictable behavior. A distinction can be made between two basic principles of training: thermal cycling and mechanical cycling. To investigate the influence of these training methods with different parameters, the data acquisition of the test rig is designed to handle large data sets of test series with up to 100 cycles. In the following, one example for each training method is described by means of two different wire samples. In Figure 22, the results of a training process of a “SAES Getters Smartflex” NiTi wire with 24 μm are presented by means of mechanical cycling. The heating power is held constant at 0.23 W for the procedure, and 50 tensile tests with a maximum strain of 5% and a strain rate of 0.005 s^{-1} are conducted.

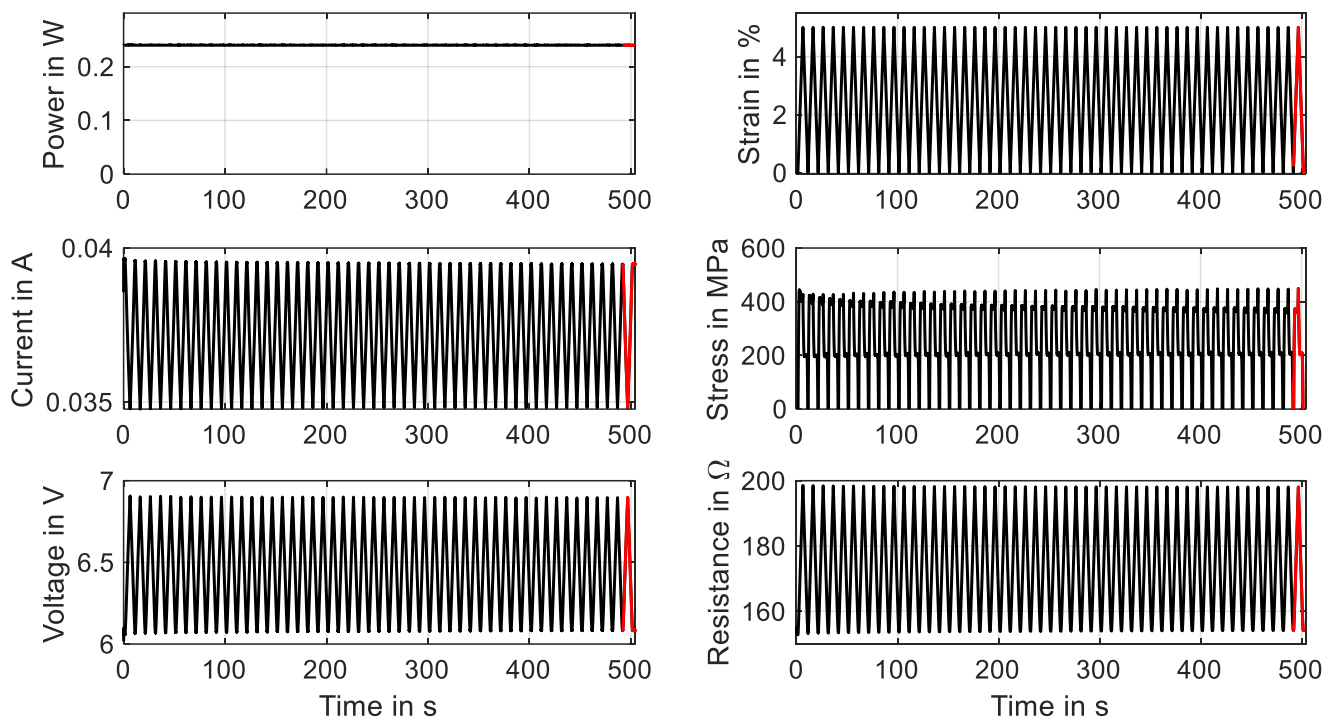


Figure 22. Results of cyclic tensile tests with wire specimen “SAES Getters Smartflex” of 24 μm diameter under constant power heating with 0.23 W, 5% maximum strain and a strain rate of 0.005 s^{-1} . The results of 50 cycles for a wire training are plotted over time. The final cycle is plotted in red.

It is observed that over time, the characteristics of stress and resistance change. Starting the experiment, the change is quite pronounced and then leads to a saturation. The stress–strain hysteresis, which is depicted in Figure 23a, undergoes a decrease in hysteresis width, as the upper-plateau stress decreases while the lower-plateau stress stays almost unchanged. Furthermore, the shape of the hysteresis is modified. The negative slope of the upper transformation plateau decreases and is almost constant in the last cycle. Evident is also the residual strain that is increased to 0.45%. In an application, this phenomenon leads to a reduced maximum stroke of the actuator, as is already indicated in Figure 16. The resistance, on the other hand, undergoes less changes. In Figure 23b, the residual strain manifests in a higher minimum resistance (154 Ω instead of 152 Ω), and the overall behavior changes only in a minor way. Parameters that can be varied for a systematic investigation of the training effect are the maximum strain, maximum stress, temperature level (electrical power), strain rate and number of cycles. Wire samples can be compared concerning the evolution of the hysteresis and the residual strain, which can help in the selection of the best-performing wire sample for applications with high material stress and can also give early insights into the fatigue behavior of the wire.

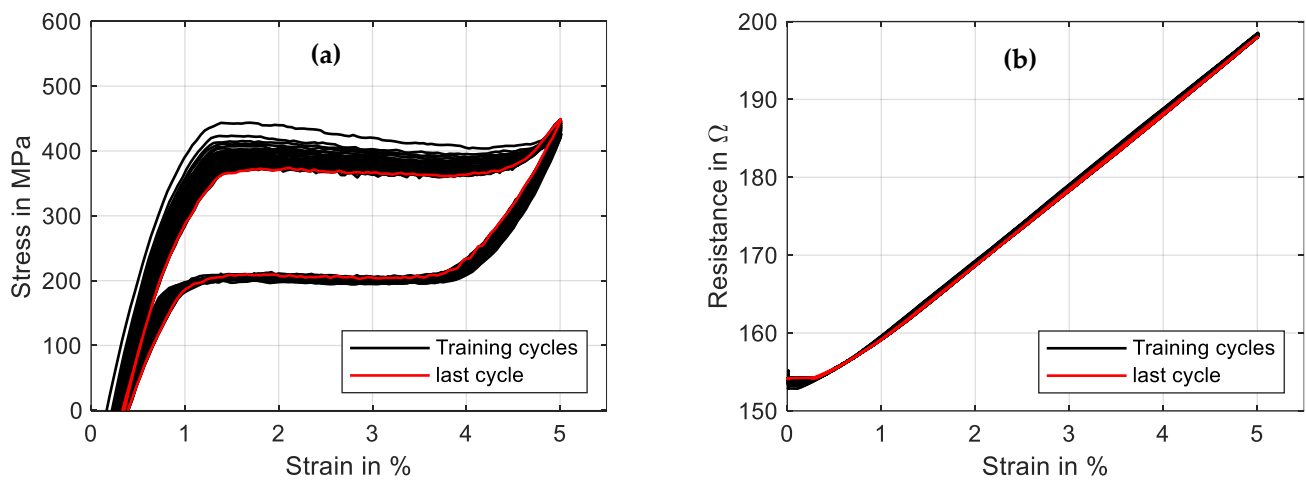


Figure 23. Results of cyclic tensile tests with wire specimen “SAES Getters Smartflex” of 24 μm diameter under constant power heating with 0.23 W, 5% maximum strain and a strain rate of 0.005 s^{-1} . The results of 50 cycles for wire training are plotted in a stress–strain plot (a) as well as a resistance–strain plot (b). The final cycle is plotted in red.

The second training method could also be performed with the wire in the actual application and is discussed in the example of a “Fort Wayne Metals NiTi #5” with a diameter of 73 μm and a constant stress of 320 MPa. The triangular current signal has a duration of 30 s and an amplitude of 160 mA. The experiment is performed with 50 cycles, of which the evolution of the results is shown in Figure 24. The main gradient in the characteristics of stress and resistance is visible in the first 10 to 20 cycles. A saturation is visible after that.

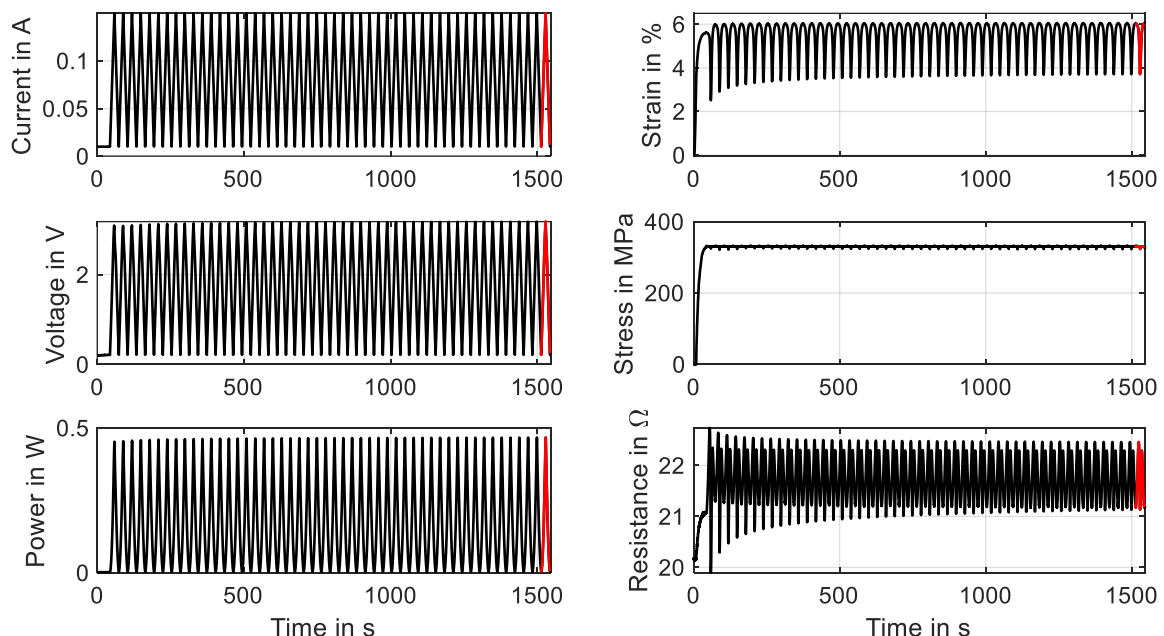


Figure 24. Results of a cyclic actuator test with wire specimen “Fort Wayne Metals NiTi #5” of 73 μm diameter under constant load biasing. A triangular current signal with an amplitude of 160 mA and a signal duration of 30 s is applied. Fifty activation cycles are for the training experiment, of which all results are plotted over time. The final cycle is plotted in red.

The change in characteristics of the resistance is more distinct than in mechanical cycling, which can be observed in Figure 25b. The minimum resistance increases from 19.9 Ω to 21.2 Ω , and the hysteretic shape and maximum value change as well.

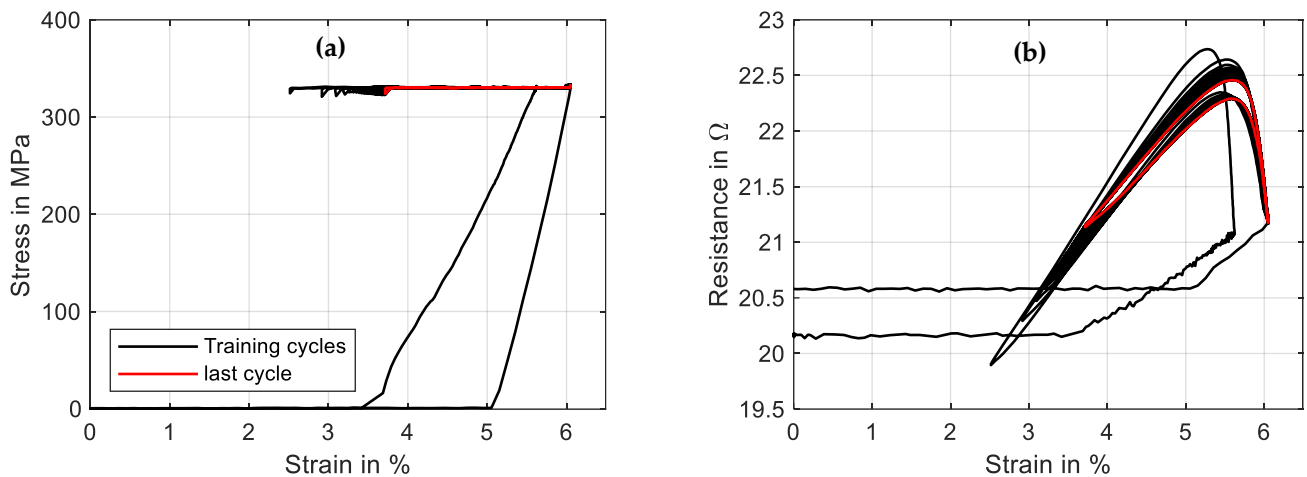


Figure 25. Results of a cyclic actuator test with a wire specimen “Fort Wayne Metals NiTi #5” of 73 μm diameter under constant load biasing. A triangular current signal with an amplitude of 160 mA and a signal duration of 30 s is applied. Fifty activation cycles are conducted for the training experiment, of which the stress–strain diagram is plotted in (a), and the resistance–strain behavior is plotted in (b). The final cycle is depicted in red.

The actuator stroke decreases from 3.5% strain to 2.3%, which can be observed in Figures 24 and 25a. In this case, investigations into how an increased heating current can reduce the effect are to be conducted. Of interest is also the influence of various stress levels and spring stiffnesses on the stabilization of the material characteristics. For both training methods, the minimum cycles needed for an effective training to new stress levels are of special interest. To evaluate the influence of various training methods and parameters, tensile tests for a basic characterization of the trained wire can be performed. From the outputs, the evolution of important data such as the residual strain, the intrinsic two-way effect and the hysteresis width can be extracted. The actual actuator performance can also be verified with actuator tests after the training series.

4. Conclusions and Outlook

In this work, the design and implementation of a SMA micro-wire characterization test bench are presented. With exemplary measurements of a variety of experiments, the multifunctionality of the setup is shown. On the presented test rig, with its unique properties and features, various application-oriented experiments and tests can be performed. The scope of functions is illustrated with a full range of wire diameters. Meaningful basic characterizations with differently heated tensile tests as well as actuator tests at adjustable ambient temperatures with variable biasing are performed, and the results are presented. Analyzing the results, we can extract, among other parameters, Young’s modulus of martensite and austenite, the hysteresis width, electrical resistivities, residual strains and functional fatigue after different training procedures. The setup helps to design actuator systems for many applications under difficult conditions such as high temperature and high stress. Due to the repeatable and significant results, the setup is well-placed for model and simulation validation. The most important lessons learned during the design and validation of the setup are the importance of reducing the friction with the help of air bearings, the necessity to isolate microwires from the surrounding air, as well as the precision needed to measure low electrical currents. In a future work, a systematic and application-oriented approach to measuring and characterizing a SMA wire sample on this test rig will be presented.

Author Contributions: Conceptualization, M.S. and P.L.; methodology, M.S., P.L. and D.S.; software, M.S. and D.S.; validation, D.S.; formal analysis, D.S.; investigation, D.S.; resources, P.L.; data curation, D.S.; writing—original draft preparation, D.S.; writing—review and editing, D.S., P.M. and S.S.; visu-

alization, D.S.; supervision, P.M. and S.S.; project administration, P.M. and S.S.; funding acquisition, P.M. and S.S. All authors have read and agreed to the published version of the manuscript.

Funding: This research has partially been funded by Alfmeier Präzision SE.

Institutional Review Board Statement: Not applicable.

Informed Consent Statement: Not applicable.

Data Availability Statement: Data is available within the manuscript.

Acknowledgments: The authors would like to thank Dynalloy, Fort Wayne Metals, Ingpus and SAES Getters for providing the NiTi materials used in this study. Additionally, the authors thank Thomas Würtz for technical advice and for sharing his knowledge on analog electronics.

Conflicts of Interest: The authors declare no conflict of interest. The funders had no role in the design of the study; in the collection, analyses or interpretation of data; in the writing of the manuscript; or in the decision to publish the results.

References

- Degeratu, S.; Rotaru, P.; Manolea, G.; Manolea, H.O.; Rotaru, A. Thermal characteristics of Ni–Ti SMA (shape memory alloy) actuators. *J. Therm. Anal. Calorim.* **2009**, *97*, 695–700. [CrossRef]
- Fumagalli, L.; Butera, F.; Coda, A. SmartFlex®NiTi Wires for Shape Memory Actuators. *J. Mater. Eng. Perform.* **2009**, *18*, 691–695. [CrossRef]
- Lagoudas, D.C. *Shape Memory Alloys*; Springer: Boston, MA, USA, 2008; Volume 1. [CrossRef]
- Miller, D.A.; Lagoudas, D.C. Thermomechanical characterization of NiTiCu and NiTi SMA actuators: Influence of plastic strains. *Smart Mater. Struct.* **2000**, *9*, 640–652. [CrossRef]
- Buehler, W.J.; Wang, F.E. A summary of recent research on the nitinol alloys and their potential application in ocean engineering. *Ocean Eng.* **1968**, *1*, 105–120. [CrossRef]
- Crews, J.H.; Buckner, G.D. Design optimization of a shape memory alloy-actuated robotic catheter. *J. Intell. Mater. Syst. Struct.* **2012**, *23*, 545–562. [CrossRef]
- Antonucci, V.; Faiella, G.; Giordano, M.; Mennella, F.; Nicolais, L. Electrical resistivity study and characterization during NiTi phase transformations. *Thermochim. Acta* **2007**, *462*, 64–69. [CrossRef]
- Furst, S.J.; Seelecke, S. Modeling and experimental characterization of the stress, strain, and resistance of shape memory alloy actuator wires with controlled power input. *J. Intell. Mater. Syst. Struct.* **2012**, *23*, 1233–1247. [CrossRef]
- Buehler, W.J.; Gilfrich, J.V.; Wiley, R.C. Effect of Low-Temperature Phase Changes on the Mechanical Properties of Alloys near Composition TiNi. *J. Appl. Phys.* **1963**, *34*, 1475–1477. [CrossRef]
- Janocha, H.; Bonertz, T.; Pappert, G. *Unkonventionelle Aktoren: Eine Einführung*; Oldenbourg Wissenschaftsverlag: München, Germany, 2013.
- Wang, T.; Ma, Z.; Rao, X.; Jiang, D.; Ren, Y.; Liu, Y.; Yu, K.; Cui, L. Temperature-dependence of superelastic stress in nanocrystalline NiTi with complete transformation capability. *Intermetallics* **2020**, *127*, 106970. [CrossRef]
- Lewis, N.; York, A.; Seelecke, S. Experimental characterization of self-sensing SMA actuators under controlled convective cooling. *Smart Mater. Struct.* **2013**, *22*, 094012. [CrossRef]
- Park, C.H.; Son, Y.S. SMA spring-based artificial muscle actuated by hot and cool water using faucet-like valve. In *Active and Passive Smart Structures and Integrated Systems 2017*; SPIE: Bellingham, WA, USA, 2017; Volume 10164, pp. 165–174. [CrossRef]
- Actuator Solutions GmbH. “Actuator Solutions GmbH”. Available online: <https://www.actuatorolutions.de/english/products/> (accessed on 12 May 2023).
- Scholtes, D.; Seelecke, S.; Rizzello, G.; Motzki, P. Design of a compliant industrial gripper driven by a bistable shape memory alloy actuator. In *Smart Materials, Adaptive Structures and Intelligent Systems*; American Society of Mechanical Engineers: New York, NY, USA, 2020. [CrossRef]
- Kazi, A.; Honold, M.; Rimkus, W.; Lokner, T.; Baeuml, M.; Koepfer, M. SMA actuator for optical image stabilization. In Proceedings of the ACTUATOR 2018—16th International Conference and Exhibition on New Actuators and Drive Systems, Bremen, Germany, 25–27 June 2018; pp. 375–378.
- Simone, F.; Rizzello, G.; Seelecke, S.; Motzki, P. A Soft Five-Fingered Hand Actuated by Shape Memory Alloy Wires: Design, Manufacturing, and Evaluation. *Front. Robot. AI* **2020**, *7*, 608841. [CrossRef]
- Uleru, G.-I.; Hulea, M.; Burlacu, A. Bio-Inspired Control System for Fingers Actuated by Multiple SMA Actuators. *Biomimetics* **2022**, *7*, 62. [CrossRef]
- Mandolino, M.A.; Goergen, Y.; Motzki, P.; Rizzello, G. Design and characterization of a fully integrated continuum robot actuated by shape memory alloy wires. In Proceedings of the 2022 IEEE 17th International Conference on Advanced Motion Control (AMC), Padova, Italy, 18–20 February 2022; Institute of Electrical and Electronics Engineers (IEEE): New York, NY, USA, 2022; pp. 6–11. [CrossRef]

20. Cheng, C.; Cheng, J.; Huang, W. Design and Development of a Novel SMA Actuated Multi-DOF Soft Robot. *IEEE Access* **2019**, *7*, 75073–75080. [[CrossRef](#)]
21. Takimoto, A. Relationship between Volume Fraction of Strain-Induced Martensite Under Tension and Electrical Resistivity in a Ti-Ni SMA Wire. *J. Phys. Colloq.* **1995**, *5*, C8-599–C8-604. [[CrossRef](#)]
22. Huang, X.; Kumar, K.; Jawed, M.K.; Nasab, A.M.; Ye, Z.; Shan, W.; Majidi, C. Highly Dynamic Shape Memory Alloy Actuator for Fast Moving Soft Robots. *Adv. Mater. Technol.* **2019**, *4*, 1–9. [[CrossRef](#)]
23. Mohd-Jani, J.; Leary, M.; Subic, A.; Gibson, M.A. A review of shape memory alloy research, applications and opportunities. *Mater. Des.* **2014**, *56*, 1078–1113. [[CrossRef](#)]
24. Britz, R.; Rizzello, G.; Motzki, P. High-Speed Antagonistic Shape Memory Actuator for High Ambient Temperatures. *Adv. Eng. Mater.* **2022**, *24*, 2200205. [[CrossRef](#)]
25. Cambride Mechantronics. Available online: <https://www.cambridgemechatronics.com/en/cml-technology/applications/> (accessed on 11 May 2023).
26. Britz, R.; Motzki, P. Analysis and evaluation of bundled SMA actuator wires. *Sens. Actuators A Phys.* **2021**, *333*, 113233. [[CrossRef](#)]
27. Kratz, R.; Stelzer, M.; von Stryk, O. Macroscopic SMA wire bundle actuator/sensor system: Design, measurement, control approach. *IFAC Proc. Vol.* **2006**, *39*, 1054–1058. [[CrossRef](#)]
28. Song, S.-H.; Lee, J.-Y.; Rodrigue, H.; Choi, I.-S.; Kang, Y.J.; Ahn, S.-H. 35 Hz shape memory alloy actuator with bending-twisting mode. *Sci. Rep.* **2016**, *6*, 21118. [[CrossRef](#)]
29. Casati, R.; Passaretti, F.; Tuissi, A. Effect of electrical heating conditions on functional fatigue of thin NiTi wire for shape memory actuators. *Procedia Eng.* **2011**, *10*, 3423–3428. [[CrossRef](#)]
30. Roy, D.; Buravalla, V.; Mangalgiri, P.; Allegavi, S.; Ramamurty, U. Mechanical characterization of NiTi SMA wires using a dynamic mechanical analyzer. *Mater. Sci. Eng. A* **2008**, *494*, 429–435. [[CrossRef](#)]
31. Mandolino, M.A.; Scholtes, D.; Ferrante, F.; Rizzello, G. A Physics-Based Hybrid Dynamical Model of Hysteresis in Polycrystalline Shape Memory Alloy Wire Transducers. *IEEE/ASME Trans. Mechatron.* **2023**. [[CrossRef](#)]
32. SAES Getters SMARTFLEX. Available online: <https://www.saesgetters.com/products-functions/products/shape-memory-alloys-nitinol/smartflex-brochure> (accessed on 31 May 2023).
33. Dynalloy. Technical Characteristics of Flexinol Actuator Wires. Available online: <http://www.dynalloy.com/pdfs/TCF1140.pdf> (accessed on 12 March 2019).
34. Talebi, H.; Golestanian, H.; Zakerzadeh, M.R.; Homaei, H. Thermolectric heat transfer modeling of shape memory alloy actuators. In Proceedings of the 22nd Annual International Conference on Mechanical Engineering-ISME2014, Ahvaz, Iran, 22–24 April 2014.
35. Fort Wayne Metals—Nitinol. Available online: <https://www.fwmetals.com/materials/nitinol/> (accessed on 31 May 2023).
36. Kneissl, A.C.; Mehrabi, K.; Bruncko, M.; McKay, B.J.; Uhlenhaut, D. Characterization and properties of NiTi(W) and CuAlNi shape memory alloys. *Int. J. Mater. Res.* **2009**, *100*, 1038–1045. [[CrossRef](#)]
37. Ingpusl SMA Components. Available online: <https://ingpusl.de/en/products-services/components/> (accessed on 31 May 2023).

Disclaimer/Publisher’s Note: The statements, opinions and data contained in all publications are solely those of the individual author(s) and contributor(s) and not of MDPI and/or the editor(s). MDPI and/or the editor(s) disclaim responsibility for any injury to people or property resulting from any ideas, methods, instructions or products referred to in the content.

2.3 Electro-Thermo-Mechanical Characterization of Shape Memory Alloy Wires for Actuator and Sensor Applications – Part 1: The Effects of Training

Dominik Scholtes ^{1,2}, Stefan Seelecke ^{1,2}, Paul Motzki ^{1,2}

¹ Lehrstuhl für Intelligente Materialsysteme, Zentrum für Mechatronik und Automatisierungstechnik, ZeMA gGmbH, Saarbrücken

² Lehrstuhl für Intelligente Materialsysteme, Fachrichtung Systems Engineering, Fachrichtung Materialwissenschaft und Werkstofftechnik, Universität des Saarlandes, Saarbrücken

Veröffentlicht in Wiley Engineering Reports.

DOI: 10.1002/eng2.12867

© 2024 by the authors.



Dieser Artikel ist lizenziert unter Creative Commons Namensnennung 4.0 International (Creative Commons Attribution 4.0 International, CC BY 4.0).

Electro-thermo-mechanical characterization of shape memory alloy wires for actuator and sensor applications—Part 1: The effects of training

Dominik Scholtes^{1,2}  | Stefan Seelecke^{1,2} | Paul Motzki^{1,2}

¹Intelligent Materials Systems Lab, Center for Mechatronics and Automation Technology - ZeMA gGmbH, Saarbrücken, Germany

²Intelligent Materials Systems Lab, Department of Systems Engineering, Department of Material Science and Engineering, Saarland University, Saarbrücken, Germany

Correspondence

Dominik Scholtes, Intelligent Materials Systems Lab, Center for Mechatronics and Automation Technology - ZeMA gGmbH, Saarbrücken 66121, Germany.

Email:

dominik.scholtes@imsl.uni-saarland.de

Abstract

So far shape memory alloys (SMA) are mostly characterized by their thermo-mechanical behavior due to the underlying thermal effect. In technical applications however, where their benefits like low weight and compact design become relevant, they are activated electrically. This work presents methods for a thorough and systematic characterization of SMA wire samples under Joule heating with the focus on aspects relevant for applications. The goal is to achieve a precise understanding of the sensor and actuator properties of SMA wire samples with different trainings under varying loads. All experiments are conducted on a custom designed test bench with a commercially available NiTi wire with 72 μm diameter, which enables the direct comparisons of tensile tests to actuation tests. The characterization consists of tensile tests and actuator tests with varying load and heating power for differently trained wire samples. The results vividly represent the influence of heating power, training and changing loads on stroke output, working point and the functional stability of SMA actuator wires. Especially, the evolution of the resistance signal and the influence of the R-phase on self-sensing is discussed. The proposed method enables to compare and choose the best suitable alloy with a fitting training for a desired application.

KEYWORDS

hysteresis, NiTi, resistance, R-phase, self-sensing, shakedown, two-way-effect

1 | INTRODUCTION

Shape Memory Alloy (SMA) wires hold remarkable promise in actuator and sensor applications owing to their unique electro-mechanical properties. These materials exhibit the ability to return to a predetermined shape after deformation when subjected to certain stimuli, such as temperature variations or mechanical stress. Their extraordinary characteristics, including high energy density and self-sensing capabilities, have positioned them as important components in various engineering fields.

However, despite their potential, the comprehensive understanding of SMA wire behavior remains an ongoing challenge. The existing knowledge gaps concern the complicated electro-thermo-mechanical interactions that determine their

This is an open access article under the terms of the [Creative Commons Attribution](https://creativecommons.org/licenses/by/4.0/) License, which permits use, distribution and reproduction in any medium, provided the original work is properly cited.

© 2024 The Authors. *Engineering Reports* published by John Wiley & Sons Ltd.

functionality, particularly in terms of their performance under varying loads and environmental conditions. Addressing these gaps is crucial to using the full potential of SMA wires in actuation and sensing, ensuring their reliability and optimizing their functionality in diverse applications.

This work has two main objectives: The presentation of a method for the thorough characterization of Joule heated SMA wires from application perspective and using this method to evaluate the effects of training on the actuator and sensor characteristics of SMA wires. The method includes tensile tests as well as a row of actuation experiments and their interpretation. With the results, a statement for the SMA's functional stability, the stroke output as well as the sensor characteristics for various loads is made.

The foundational aspects of SMA (Shape Memory Alloys) have been extensively discussed in scientific literature over recent decades.^{1–5} Hence, the following section offers a concise overview of the pertinent elements relevant to this study.

SMA's boast the highest known energy density among actuators and uniquely integrate resistance-based self-sensing capabilities.^{6–8} Commonly found in the form of commercially available wires, typically composed of binary Nickel-Titanium (NiTi), these alloys, also known as Nitinol, were first explored by researchers at the U.S. Naval Ordnance Laboratory in 1963.⁹ Exhibiting varied thermo-mechanical behavior contingent upon the alloy composition, these materials possess highly hysteric thermal and mechanical characteristics. NiTi with higher nickel content demonstrates superelasticity at room temperature, capable of being stretched up to 10% without sustaining permanent damage.¹⁰ Conversely, the titanium-rich variant undergoes (quasi-)plastic deformation when stretched at room temperature but regains its original geometry upon heating to the transformation temperature—a phenomenon known as the shape memory effect (SME), allowing for the complete recovery of strains of 5% and more.³ Both effects—superelasticity and SME—are rooted in a reversible rearrangement of the crystal lattice structure of the materials, involving a phase transformation from martensite to austenite and vice versa, where the lattice structure is contingent upon temperature and material stress.¹¹ Cooling down from austenite can lead to the emergence of a third intermediate phase called the R-Phase, intensifying the material's hysteresis in resistivity.^{12,13} SMA wires, typically consisting of titanium-rich NiTi, are commonly activated by either electrical power through Joule heating or passively through contact with a high-temperature fluid.^{14,15} Their exceptional energy density renders SMA wires particularly suitable for compact and lightweight actuator systems, such as valves, small-scale gripping systems, and optical image stabilization (OIS).^{16–18} Ongoing research delves into fields like continuum robots for catheters and endoscopes, as well as bionic applications.^{19–22} In these applications, the inherent self-sensing capability of SMA wires eliminates the need for external position sensors, relying instead on the electrical resistance changes observed during the austenite-martensite transformation. This resistance alteration is contingent upon the contemporary crystal lattice, wire dimensions, and temperature.^{14,23}

Basic material characterization of SMA is usually done with differential scanning calorimetry (DSC), temperature controlled tensile tests or thermally-induced phase transformation under a constant stress, which is extensively done by Churchill, Iadicola and Shaw as well as Miller and Lagoudas among others.^{4,24–26} Research is also presented on the thermal characteristics of the electrical resistance of NiTi.^{27–29} What most published data on SMA characterization has in common, is that the temperature of the specimen is controlled by a medium in contact with the wire, so that the temperature of the SMA is known. In contrast to that, the exact wire temperature is an unknown variable in real world applications. In the field of electrically heated SMA, Lewis et al. examined Joule heated wires under convective cooling, while Furst et al. studied the behavior and self-sensing capabilities of antagonistic Joule heated NiTi wires.^{14,30} This work complements previous research by presenting the following topics:

- An application-oriented method for the systematic characterization of SMA wires by Joule heating.
- The direct comparison between the tensile behavior and the actuator sensor characteristics under varying loads.
- The examination of the effects of two fundamental training methods on the mechanical and electrical properties.

Using wires as actuators has many benefits compared to other forms like strips or springs. Their flexibility allows for accommodation in tight spatial conditions, they can be bundled to scale the force with consistent dynamics, and they can easily be mounted and electrically connected.³¹ SMA wires react to an increase in electrical current respectively temperature in matter of milliseconds.³¹ Because of the fast cooling rate and thus possible dynamics of 1 Hz to 10 Hz and even up to 35 Hz, microwires (diameter smaller than 100 μm) have become essential in SMA driven products like OIS and valve systems.^{16,32–34} Therefore, this work is based on a commercially available NiTi wire with a diameter of 72 μm . The custom designed test rig used for the experiments, is presented in³⁵ by Scholtes et al. It features a stress-controlled

installation system for wire insertion directly from the reel without manual handling or cutting. The setup is designed to perform tensile tests as well as actuator tests with free to choose constant loads or springs on the same sample. For the experiments presented in this article, three differently trained wires are examined: as conditioned by the manufacturer, additional thermo-electrical training and additional mechanical training. The training of the SMA is also conducted on the test rig.

A commonly known limit for the application of SMA wire actuators is the ambient temperature. It is set by the transformation temperatures of the alloy, which lies typically at 80–90°C. It can be tuned for example by prestressing the wire and thus increasing the phase transformation temperatures.^{36,37} In “Part 2” of this research project, the actuator and sensor characteristics of Joule heated SMA wires in high ambient temperatures are examined. The impact of training and pre-stress on the shift of maximum operating temperature is investigated.

The subsequent sections of this paper are organized in the following manner: The experimental setup, the materials and measurement methods are described in Section 2. In Section 3 follows the presentation of the training procedures and their evaluation. In the subsections of 3, each of the differently treated samples is characterized by tensile tests and actuator tests with various constant loads and springs. The manuscript closes in Section 4 with a conclusion including a summary of the results and an outlook.

2 | EXPERIMENTAL SETUP, MATERIALS AND METHODS

All experiments discussed in the following are conducted on one setup, of which the design, implementation and validation is described exhaustively by Scholtes et al.³⁵ Refer to that publication for all details on the experiments and the test setup, which are not found in the following brief descriptions.

The test rig, displayed in Figure 1, consists of two clamps mounted on air bearings, that mechanically fix and electrically connect the SMA wire. One clamp is fixed to a load cell, while the opposing one is mounted on a linear drive. The clamps, as well as the wire sample, are positioned inside an isolating chamber to prevent ambient airflow from interfering with the measurements. The temperature inside the chamber is monitored with PT100 temperature sensors and can be controlled. An additional motor is accessible for directly extracting the wire from the reel and securely affixing it to the clamps in a stress-controlled manner. Herewith, after a swap of the SMA sample, repeatable measurement results are ensured. The test rig is multifunctional, which means that it is designed to conduct tensile tests, actuator tests and cyclic tests for shakedown experiments or training. All tests can be run on a single sample, without any further manual intervention, only by switching the software. This key feature enables the direct and precise comparison of the results of actuator tests and tensile tests, as they are performed in the exact same specimen. While the linear drive is run in position-control mode for the tensile tests, it is run in a closed-loop force-control mode for the actuator tests, where arbitrary loads can be mapped.

In general, all tests are run with a Joule heated wire, while it is possible to control either the electrical current or the electrical power. The isolating chamber is also temperature-controlled, but in this paper all experiments are run at room temperature of 23°C. It is designed to enable tests under high constant ambient temperatures but is not made to gradually cool or heat the air inside the chamber. The parameters electrical power or current, maximum strain and strain rate are adjustable for tensile tests. The force values are obtained by the loadcell, on which is the SMA wire is attached via a clamp mounted on an air bearing. The strain of the wire is measured by using the internal encoder of the linear drive. Actuator tests can be performed with an adjustable constant load or an arbitrary linear spring rate with settable pre-stress. Furthermore, the maximum heating current and the heating cycle time are configurable. The electrical supply for heating the SMA wire is provided by a custom designed constant current source with adjustable output currents of 0 mA to 250 mA and up to 24 V. A measurement error of only 10 μA allows, in combination with the measurement of the voltage drop over the wire, a precise resistance measurement also at low currents of 5–10 mA. The whole setup is controlled, and all data is acquired with a “National Instruments” FPGA based system and “NI LabVIEW”. An extensive discussion of the design of the test rig, the data acquisition, control and the conduct of experiments is given by Scholtes et al.³⁵

For all experiments in this work a “Dynalloy Flexinol HT” NiTi wire with a measured diameter d_0 of 72 μm (in twinned martensite) is used.³⁷ The initial wire length L_0 is always set to 100 mm in full austenite. For all following results, the wire strain ϵ is calculated with:

$$\epsilon = \frac{L - L_0}{L_0} \quad (1)$$

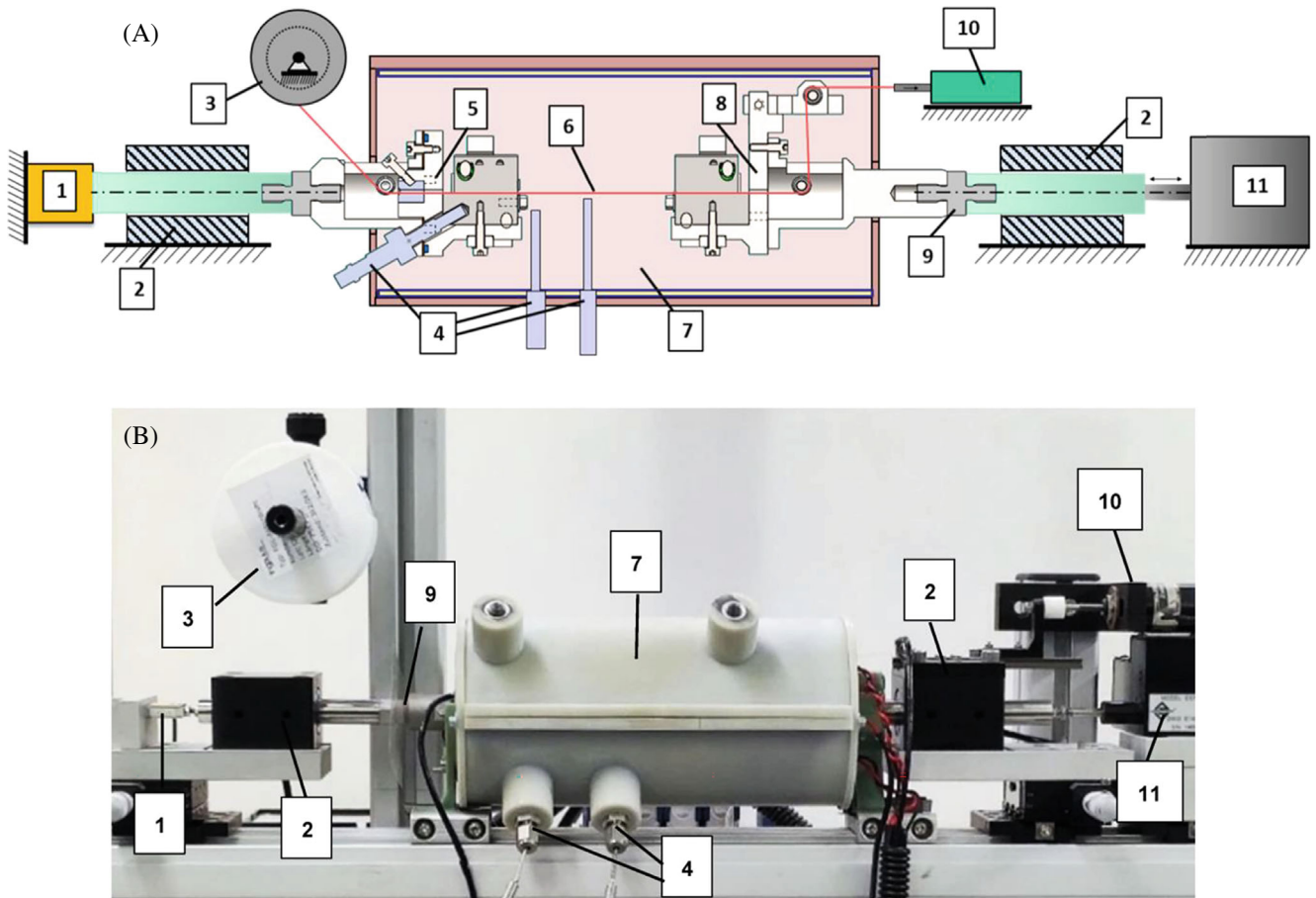


FIGURE 1 (A) Schematic design of the experimental setup. (B) Picture of the fully implemented test rig with closed heating chamber including the following components: 1: load cell; 2: air bearing; 3: SMA wire reel; 4: PT100 sensors; 5: fixed wire clamp; 6: SMA wire; 7: heating chamber; 8: moving wire clamp; 9: insulation adapter; 10: pre-stressing motor; 11: linear direct drive. (Reproduced under terms of the CC-BY license Copyright 2023, Scholtes et al., published by MDPI.)³⁵

The engineering stress σ is calculated with

$$\sigma = \frac{F}{A_0} \quad (2)$$

where F is the measured force and A_0 is the initial cross-sectional area of the wire at the length L_0 , which is calculated by

$$A_0 = \frac{\pi}{4} \times d_0^2. \quad (3)$$

For a better comparability, no absolute values for stroke or force are discussed. Also, if not described otherwise, a reset procedure is run on the NiTi wire before each experiment. For that, the wire is slack, heated to full austenite and cooled down under these stress-free conditions. This measure ensures that the wire is in the same initial state before every test.

3 | EXPERIMENTS AND RESULTS

The presented characterization method is used to examine the effects of different trainings on the actuator and sensor characteristics, as well as the basic material properties of NiTi wires. The “Dynalloy” wire comes conditioned and ready-to-use. It exhibits a stable material behavior at stresses of up to about 200 MPa, which is typical for commercially

available SMA actuator wires.^{36–38} This “as delivered” state of the wire is characterized as reference. With stress limited to 200 MPa, SMA actuators usually exhibit a good fatigue life, but there are some drawbacks. To achieve higher forces the installation space increases, because wire bundles or a transmission stage combined with longer wires are needed. A higher material stress results in a more compact and lightweight system with higher force output and can be used if a shorter lifecycle is acceptable. Therefore, the goal of this research is to achieve a stable stroke and resistance characteristics of the SMA wire at up to 400 MPa of material stress with additional training. It is expected that the thermal, mechanical and electrical characteristics of the SMA actuator wire change and loads above 200 MPa. A residual strain and a shift in working point are the most pronounced effects that are anticipated. Two different trainings are conducted on separate samples. In one method, the wire is thermally cycled, while a constant stress of 400 MPa is applied until it reaches a stable condition once more. The temperature is controlled with a triangular current signal run through the wire. The triangular current signal provides a varied and continuous input, allowing for a more comprehensive analysis of the SMA wire’s response across a range of stimuli compared to a square wave for example. It helps to understand the wire’s response under changing current levels, especially concerning stress, strain and resistance. The second method is a mechanical training, where the wire is activated by a constant electrical power and is repeatedly stretched with a constant strain rate of 0.01 s^{-1} to 5.5% strain until the residual strain no longer increases.

All three specimen then undergo a so called “basic characterization”, which consists of a set of five tensile tests with varying heating power and a certain strain. To paint the whole picture, two more tensile tests are added, where the NiTi wire is pulled in full austenite as well as full detwinned martensite up to 400 MPa. The results allow to extract many important material parameters and perform a first comparison of the training methods. To evaluate the actuator-sensor properties and validate the functional stability, four different actuator tests are performed with each sample: two sets with a constant load of 200 and 400 MPa as well as two sets with spring loads ranging from 100 to 200 MPa and 200 to 400 MPa. These loads are chosen due to their relevance for applications. With up to 200 MPa of stress it is possible to achieve more than one million activation cycles, while up to 400 MPa still enables an acceptable lifetime of the actuator-sensor system with a doubled force output.³⁶ Comparing spring loads of varying stiffnesses to constant loads, helps to grasp the influence of the slope of a load and enable inter- and extrapolation. The characteristics of loads significantly different than discussed in this paper need to be examined separately, which can be done with the methods introduced in this work.

The order in which the results are discussed does not correspond to the order in which the measurements are carried out. Also, they are not necessarily run on the exact same piece of NiTi material. Depending on the loads that the wire has to endure, a new sample is installed in the test rig and trained accordingly once again for the following experiments.

3.1 | Thermal training

In this subsection, the execution and results of the (electro-)thermal training procedure are discussed. The NiTi wire is loaded with 400 MPa of constant stress. A maximum current of 180 mA with a triangular signal shape and 40 s cycle time is run through the wire to heat it. The current does not fall below a threshold value of 10 mA to ensure a consistent resistance measurement. In Figure 2 the timings of current, voltage, electrical power, strain, stress and resistance are displayed for the first ten cycles of the training procedure. The training procedures shown here are also known as shakedown response.^{28,29,39} Especially in the first ten cycles, the typical ratcheting and plastic shakedown behavior for martensite-austenite transformation of NiTi is observed in the strain and the resistance data in Figure 2.

For all 100 cycles, the same ratcheting and plastic shakedown is displayed in Figure 3 in the strain versus power graph. “Ratcheting” describes the movement of the working range in positive strain direction. The maximum martensitic strain of the wire increases about 0.73% from 6.93% (1st cycle in Figure 3) to 7.65% (return point of the last cycle in Figure 3). This plastic shakedown can be seen in Figure 4 on the left. With 2.18% (from 1.08% to 3.26%), the increase of minimum strain in austenite is greater the change in martensite strain. The reason for these observations lies in microstructural changes within the SMA wire, induced by the repeated heating and cooling under load. This causes changed in the arrangement of the crystal lattice and leads to altered stress-strain curves, residual strain and changing transformation temperatures.

Here it should be noted, that due to the reset procedure before the experiment, the characteristics of the first actuation cycle always deviates from the rest of the results with a lower starting strain in martensite. As the wire is cooled down with

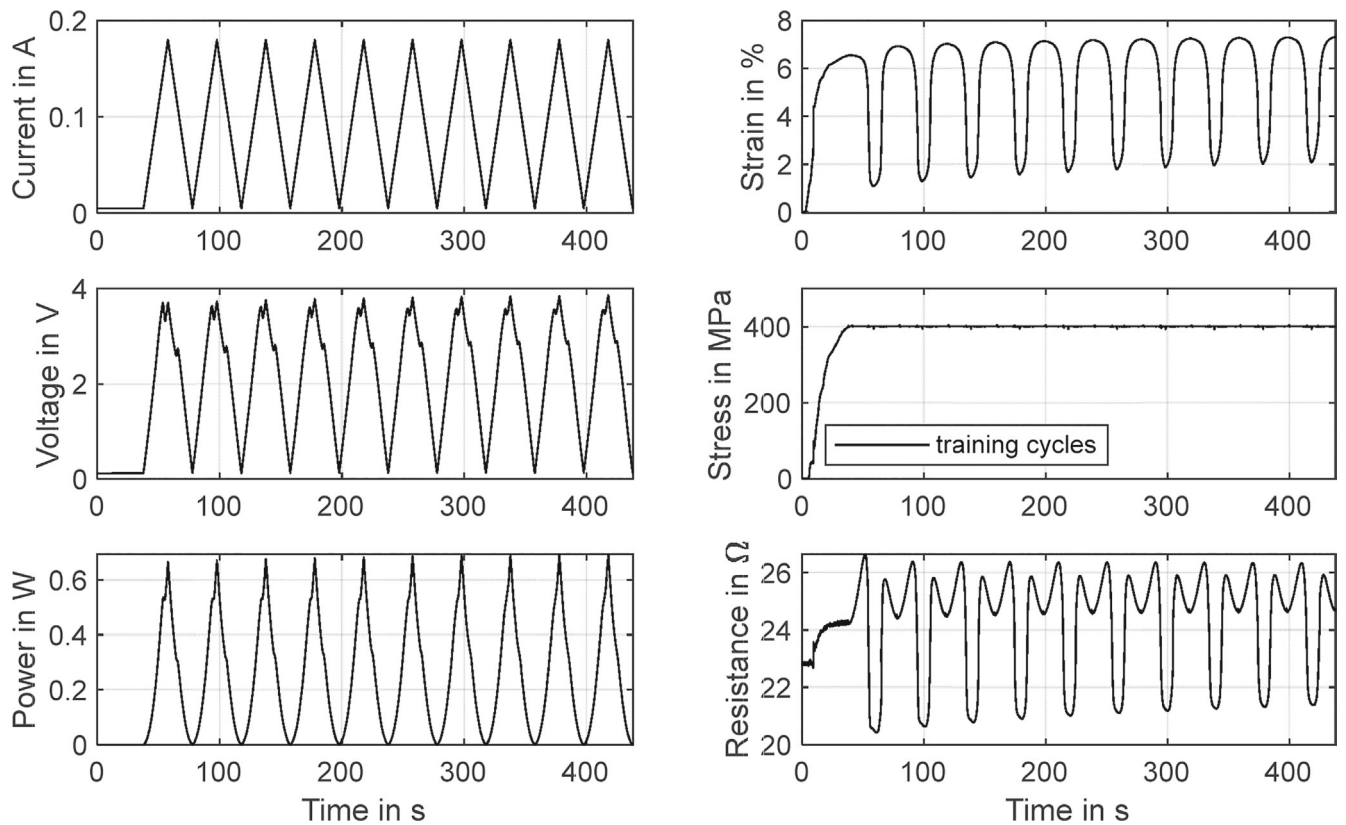


FIGURE 2 Measurement data of the first ten cycles of the thermal training plotted over time. Presented are the triangular activation current signal with an amplitude of 180 mA and a cycle time of 40 s as well as the resulting values of voltage, power, strain and resistance. The stress is held constant at 400 MPa.

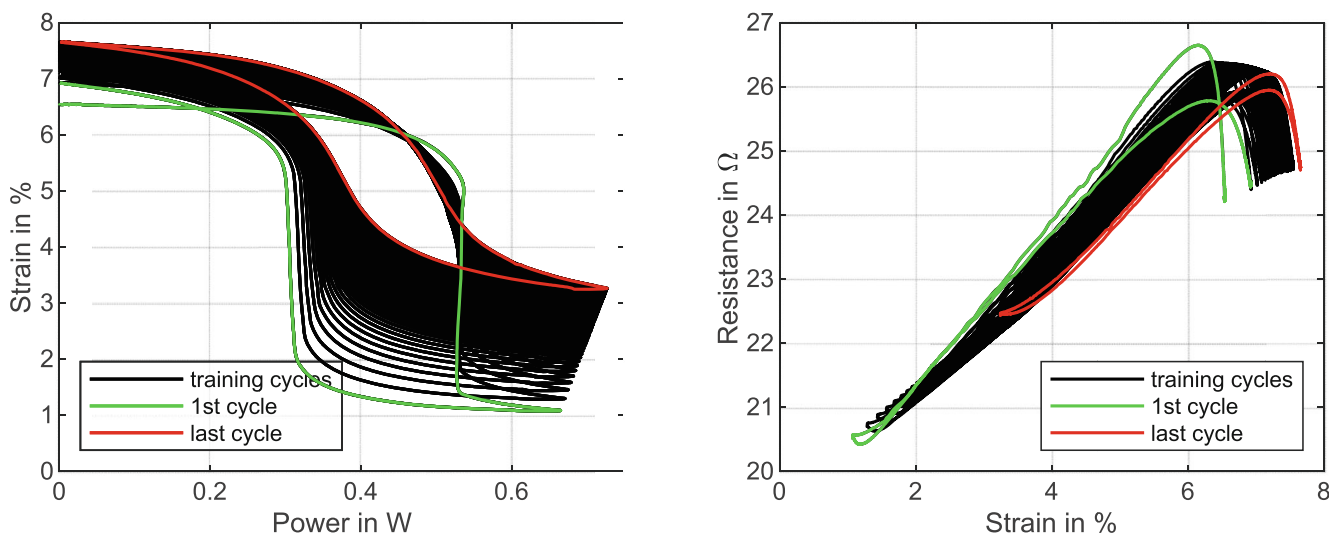


FIGURE 3 Results of the Joule heated thermal training experiment with 100 activation cycles. Illustrated are the evolution of strain versus power (left) and electrical resistance versus strain (right) with first and last cycle highlighted in color.

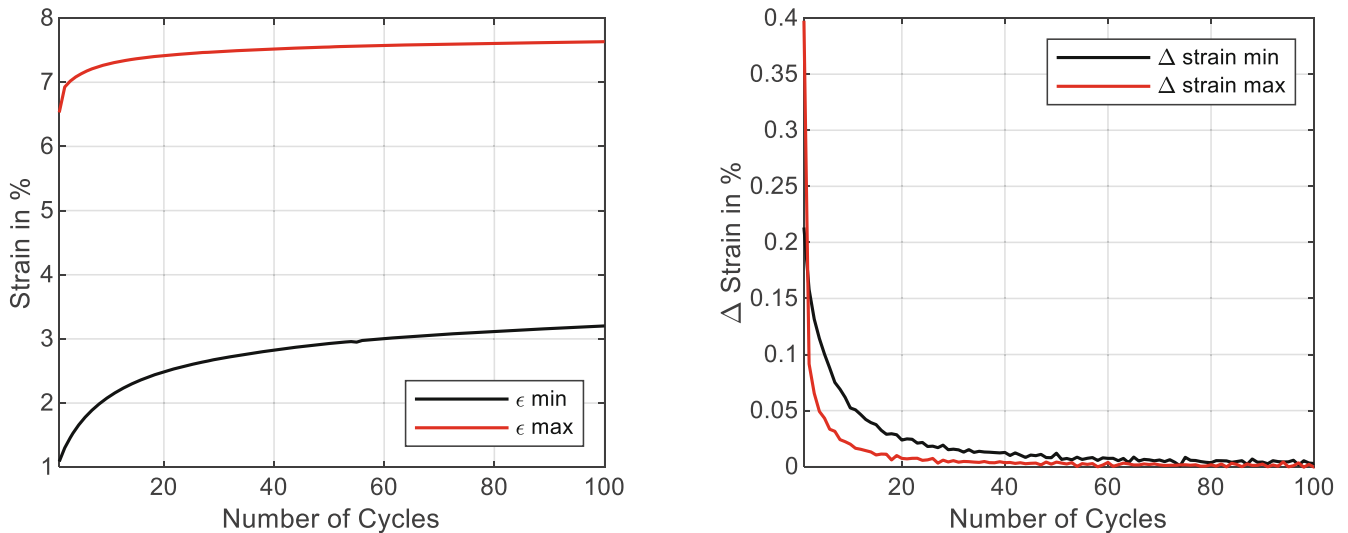


FIGURE 4 Outline of the stabilization of max. and min. strain of the NiTi wire under electro-thermal activation with 400 MPa load. The graph on the left shows the degradation of stroke (plastic shakedown) and the shift of the working point (ratchetting) of the sample. The graph on the right shows the difference in strain between each cycle and the preceding one (derivative) for max. and min. strain.

no stress applied, a certain portion of twinned martensite is formed because of the SMA wire's intrinsic two-way-effect (TWE) as described in.⁴⁰ A stable detwinned martensite is only formed after the first activation cycle when cooling under tensile stress. This is also evident in many results in the following subsections.

As criterion for the stability of the sample after the training, the derivative of strain Δ_{strain} is used. The evolution of the derivative for max. and min. strain with the training cycles is depicted in Figure 4 on the right. The chosen threshold value for Δ_{strain} for a functional stability is 0.005%, which is reached for the max. strain after 30 cycles and for the min. strain after 90 cycles. The result after 100 cycles is a $\Delta_{\text{strain max}}$ of 0.000% and a $\Delta_{\text{strain min}}$ of 0.003%.

The resistance evolves according to the strain, which is displayed in Figure 3 on the right. Neglecting the inconsistency of the first cycle (green), the martensite resistance starts at 24.4 Ω and rises to 24.7 Ω (red) with the training, due to the increased absolute length of the wire. Because of the reducing contraction, which leads to an increased minimum length, the austenitic resistance starts at 20.5 Ω (green) and ends up at 22.5 Ω (red) after 100 cycles. Before the start of phase transformation and after the transformation is finished, the temperature influence on the wire resistance predominates and the typical increase in resistance occurs, visible in Figure 3 on right and in the resistance signal in Figure 2. It is pronounced at the start of transformation as the martensite slowly heats to A_s temperature. Overheating does not occur, which is why the curvature in the resistance signal is not mirrored in the area of full contraction.

3.2 | Mechanical training

The mechanical training corresponds to cyclic tensile tests with a maximum strain of 5.5%. The wire is heated with controlled electrical power of 0.35 W to reach an initial upper plateau stress (UPS) of about 450 MPa. For low strain rates, leading to isothermal experiments, the wire temperature can be assumed as constant, when the electrical power is constant. In Figure 5, the timing of the first ten training cycles of the with a strain rate of 0.01 s⁻¹ is illustrated.

The values of voltage, current and resistance react to the deformation of the wire. The stress signal evolves with progressing cycles, and remanent strain as well as a drop in UPS are recognizable. The change in shape of the stress-strain-hysteresis over 100 tensile cycles is displayed in Figure 6 on the left. The cause, as already explained in Section 3.1 lies in the in microstructural changes within the SMA, which is in thus case induced by repeated loading and unloading in a high temperature state. The level of the UPS drops from about 455 MPa in the 1st cycle to 383 MPa (both at 3% strain) in the last cycle. While that happens the negative slope in the transformation plateau evolves to a constant one. The stress at 5.5% increases from 450 to 468 MPa.

The lower plateau stress (LPS) starts at 190 MPa (at 3%) and, also because auf an increase in slope, rises to 205 MPa. Overall, the hysteresis becomes narrower with the mechanical training. The plastic shakedown manifests in the remanent

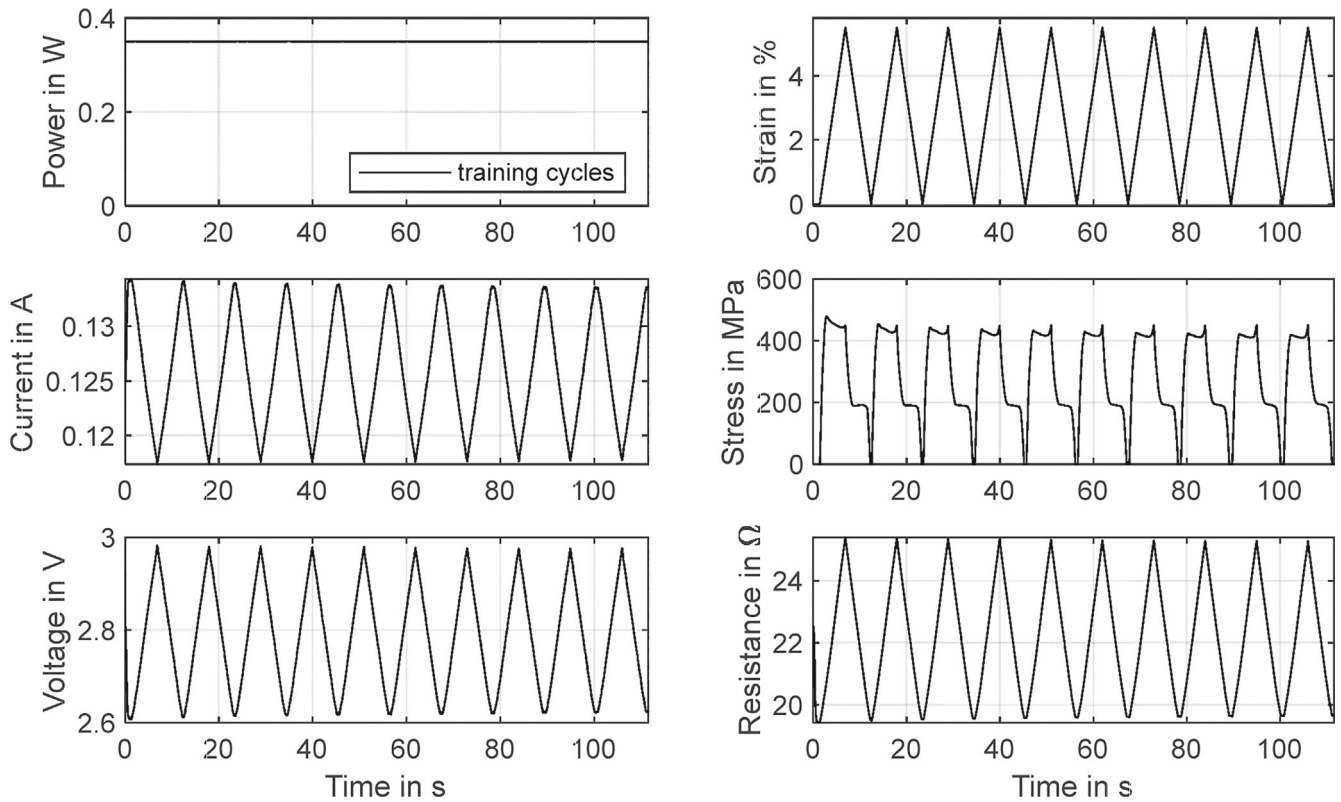


FIGURE 5 Measurement data of the first ten cycles of the mechanical training plotted over time. Presented are the loading and unloading signal with a strain rate of 0.01 s^{-1} at a constant electrical heating power of 0.35 W . Also, the resulting values of current, voltage, resistance and stress are depicted.

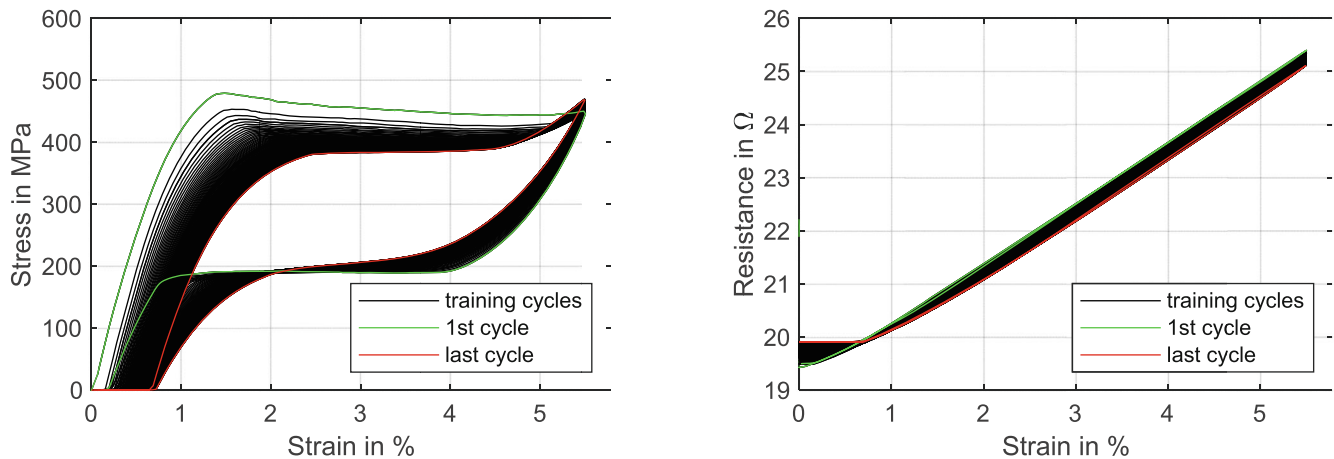


FIGURE 6 Results of the mechanical training with 100 cycles of 5.5% strain and 0.35 W heating power. The left plot illustrates the evolution of stress versus strain and the plot on the right the resistance versus strain behavior. First and last cycle are highlighted in color.

strain ϵ_{rem} that is represented in Figure 7 on the left, where the max. value of 0.72% is reached after 100 cycles. Equal to the thermal training, a Δ_{strain} of 0.005% is set as threshold of the stability criterion, which is reached after 77 cycles. The evolution of the derivative of remanent strain Δ_{strain} is displayed in Figure 7 on the right.

The resistance signal, represented in Figure 6 on the right, shows an almost linear behavior in relation to strain. In the 1st cycle the resistance starts at 19.5Ω in full stress-free austenite and increases to 25.4Ω at the end of the transformation plateau. After 100 tensile cycles to 5.5% strain, this maximum value drops to 25.1Ω , while the minimum value increases to 19.9Ω resulting from the remanent strain. In the area of the austenitic branch, the resistance signal shows

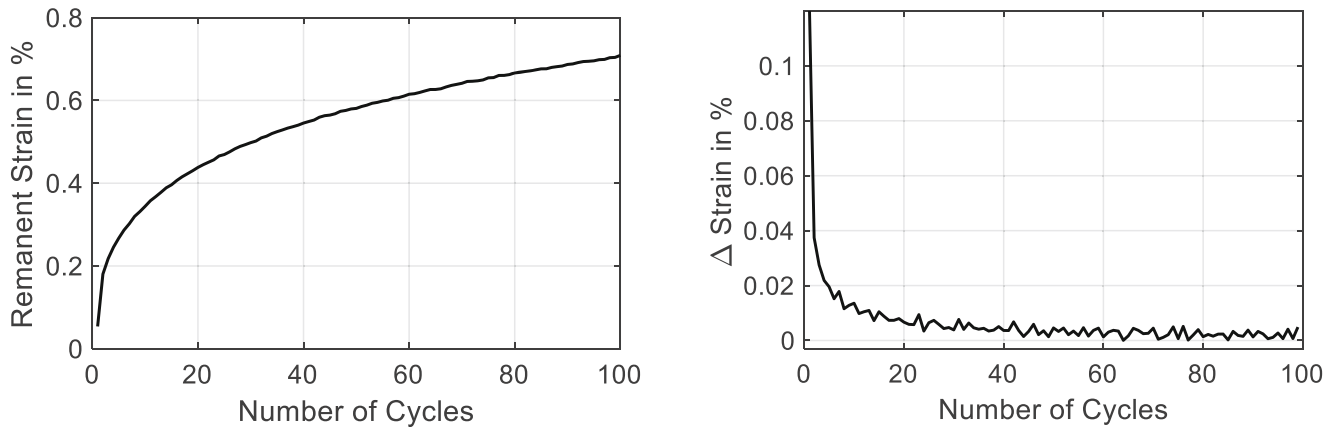


FIGURE 7 The graph on the left outlines the formation of remanent strain over the cycles of the mechanical training with a Joule heated wire sample. The graph on the right illustrates development the derivative of remanent strain over the training cycles.

a lower slope before the UPS is reached. In the linear region, a decrease in resistance between 1st and last cycle of 0.3Ω is observed.

3.3 | Characterization based on tensile tests

In the following, the execution and results of the first part of the characterization method are discussed. It is called “basic characterization” and consists of a set of several tensile tests with varying heating power and strain. With the experimental data, many material parameters like Young’s modulus, width of the mechanical hysteresis and resistivity are determined. The basic characterization is performed with each version of training: the untreated wire as it comes from the manufacturer, the wire with an additional mechanical training as described in Section 3.1 and the wire with an additional thermal training as described in Section 3.2. The results of stress and resistance in relation to strain for each sample are graphically displayed in Figure 8. The maximum strain ϵ_{max} results of the strain necessary to reach 200 MPa of stress in martensite at room temperature. No offset caused by remanent strain is subtracted, and every experiment starts at the position of L_0 as described in Section 2.

The basic characterization consists of five tensile tests with four different power values. The power levels are identified in preliminary tests of the untreated wire sample and are defined by the UPS of the tensile tests. The highest power is set to produce a UPS of around 550 MPa (± 20 MPa), with the UPS of medium and low power lying 100 MPa, respectively 200 MPa lower. Higher stresses result in plastic deformation of the NiTi wire and are not producing significant results from an application perspective because of low fatigue life. The strain rate is set to 0.01 s^{-1} for all tensile experiments. The experiments plotted over time can be found in the “Data S1” section. Two tests are run with only a measurement current of 10 mA applied, which produces a power of around 1 mW. That does not measurably affect the wire temperature. The sequence of the tensile tests for the basic characterization starts with these experiments with no electrical heating, aiming to measure the detwinning of the martensite (black curves in Figure 8) as well as the elastic branch of detwinned martensite (red curves in Figure 8). The power is then gradually increased to 0.29 W (green), 0.35 W (pink) and 0.41 W (blue).

For the untreated wire, a maximum strain of 5.5% is set. The first test with no heating power shows almost no intrinsic TWE, a transformation plateau with a stress starting at 30 MPa and rising to 80 MPa is recognizable. The stress slowly rises between 0.2% and 4%, where the slope increases and leads to 210 MPa at 5.5% strain. The usual explanation for this behavior is the reorientation from twinned martensite (of which the macroscopic geometry with no stress applied corresponds to that of austenite) to detwinned martensite. However, Churchill et al. and Gori et al. showed that “Flexinol”, as many other NiTi actuator wires as well, form R-phase fractions when cooling down from austenite at low stresses.^{27,28} The R-phase does not have a significant influence on the mechanical properties of NiTi, which is why it is often neglected. Although, when considering the resistance data of the untreated wire in Figure 8, its influence on the sensor characteristics becomes clear. When using a passive SMA actuator wire as a position sensor as can be done for example in an antagonistic wire

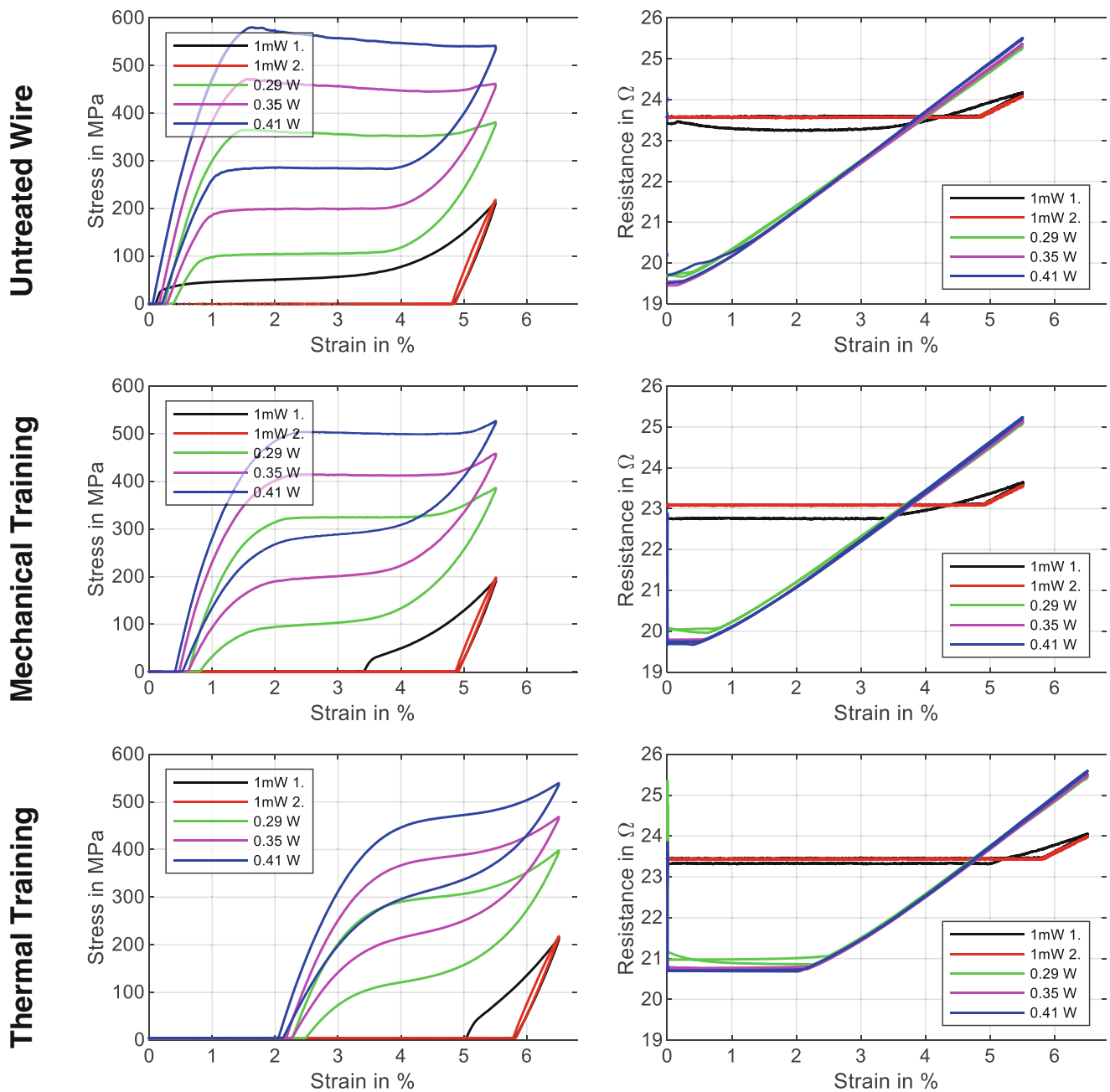


FIGURE 8 Results of the basic characterization tensile tests of three differently trained NiTi wire samples. The left column shows the stress versus strain hysteresis for heating powers from 1 mW to 0.41 W and the right column illustrates the corresponding resistance versus strain plot.

setup, a linear behavior of this wire is expected. In this case however, the hammock shaped resistance-strain curve makes the signal interpretation of a passive wire more difficult.

The initial value of the resistance of the “1 mW 1.” test is at a higher level than expected from martensite at L_0 . The explanation might be attributed to the heightened resistivity found within the partially present R-phase (ρ_R) of the alloy. After a small increase of the resistance from 23.4 to 23.5 Ω , the resistance signal forms a hammock shape where it drops to 23.2 Ω at 2.2% of strain, and then starts to slowly increase. The maximum value in elastically strained, detwinned martensite at 5.5% strain amounts to 24.2 Ω . The conclusion of these observations is that the crystal lattice of the NiTi wire transforms to a mixture of martensite phase in twinned configuration with a large portion of R-Phase when cooled down

from austenite under stress-free conditions. During the tensile test, the R-phase is detwinned and deformed to martensite phase, which is detwinned at the same time.

The second tensile test with no heating power results in a linear resistance behavior, starting at a constant resistance of 23.6 Ω as long as the wire is slack and reaching 24.1 Ω at the peak. The mechanical behavior of the twinned martensite is elastic, starting at 4.8% with a neglectable hysteresis. The low-, medium- and high-power experiments show properties similar to each other, while the mechanical hysteresis moves to higher levels with increased power, respectively wire temperature. The 0.29 W test results in a hysteresis width of 250 MPa. With increasing power, the hysteresis width increases slightly leading to a width of 258 MPa at 0.35 W and 273 MPa at 0.41 W. The width of the hysteresis, as well as UPS and LPS (displayed in Table 1) are measured at the strain value ϵ_{hyst} halfway through the loading cycle that calculates with

$$\epsilon_{hyst} = \frac{\epsilon_{rem} + \epsilon_{max}}{2}. \quad (4)$$

The resistance signals of these tensile tests appear to behave linear but feature a curvature change where the austenitic branch ends and at the end of the transformation plateau. The latter is not well pronounced in the experiments displayed here, as the tensile test does not fully enter the elastic branch of the stress induced martensite. The slope of resistance in the elastic branches of austenite and martensite differ from one another, due to their difference in resistivity. Both their slopes are lower than the slope in the region of the transformation plateau, which is to be observed on close inspection in Figure 8. The reason for this behavior can be found in the complex Poisson's ratio ν of NiTi.⁴¹ While the resistivity ρ of an SMA wire at a certain temperature is approximated by

$$\rho = R \times \frac{A}{L}. \quad (5)$$

where R is the measured resistance, L is the current wire length and A the current cross-sectional area of the wire, which is calculated with

$$A = \frac{\pi}{4} \times d_0^2 \times (1 - \nu \times \epsilon)^2 \quad (6)$$

and thus, depends on the variables strain ϵ and Poisson's ratio ν . The different resistivities of austenite ρ_A and martensite ρ_M do not explain a steeper slope in the transformation plateau. They are quite similar with martensite having a slightly

TABLE 1 Collection of the material properties extracted from the characterization by tensile experiments for 3 differently trained wire samples.

Value	Untreated wire	Mechanical training	Thermal training
ϵ_{max} in %	5.5	5.5	6.5
ϵ_{rem} in %	–	0.39	1.63
TWE in %	0.12	3.42	5.05
σ at ϵ_{max} in MPa	541	526	537
UPS in MPa	557	502	457
LPS in MPa	284	289	307
Hysteresis width in MPa	273	213	150
Hysteresis area in J	5.0	3.5	2.0
E_A in GPa	75.2	70.7	52.3
E_M in GPa	37.2	36.2	35.5
ρ_A in $10^{-7} \Omega\text{m}$	8.06	7.95	8.08
ρ_M in $10^{-7} \Omega\text{m}$	8.66	8.53	8.50
ρ_R in $10^{-7} \Omega\text{m}$	9.57	–	–
ΔR max. in Ω	6	5.5	4.9

higher value. The alloys resistivity gradually changes with the evolving phase fractions. However, an increased ν in the transformation plateau suits as an explanation, as Equations (5) and (6) demonstrate. For elastic deformation of metallic alloys ν is typically in the region of 0.33, while (quasi-)plastic deformation leads to isochoric behavior and a Poisson's ratio of 0.5. This indicates that the nonlinearity in wire resistance data under tensile loads results from the nonlinear Poisson's ratio of NiTi.⁴¹ The behavior can also be observed in the experimental results of Lewis et al.¹⁴ However, the assumption needs further investigation.

Also, it is to be observed in the measurement data that the mean slope of the resistance versus strain plot increases with increasing power, leading to a maximum resistance value of 25.5 Ω . In Figure 9 additional tensile tests for the evaluation of remanent strain ϵ_{rem} , Young's modulus of martensite phase (E_M) and austenite phase (E_A) as well as the estimation of actuation stroke are displayed. The tensile tests in the elastic region of full austenite and fully detwinned martensite are performed up to a stress of about 400 MPa. The untreated sample (Figure 9A) does not exhibit any remanent strain, as it is not cycled before the basic characterization. The quasi-plastic residual strain in martensitic phase detwinned with 400 MPa and 6.5% strain is 5.3%. The elastic moduli are displayed together with all other material properties in Table 1. They are calculated by a linear approximation of the slope of the elastic branches.

Examining the basic characterization of the mechanical training, an increase in intrinsic TWE to 3.5% can be found in Figure 8 in the middle row. With that the appearance of the R-phase also seems to be reduced, as the resistance is lower than in the previous experiment although the wire length is increased to 103.5 mm. The resistance levels in general are slightly lower compared to the untreated wire, except for the initial values with heating power, matching the results of the mechanical training. The results of mechanical hysteresis are also comparable to the results in Section 3.2, where the UPS decreases, and the slopes of the plateaus increase. The active strain, where the wire is actually loaded, in the basic characterization is reduced to a maximum of 5%. The residual strain extracted from the full austenite data in Figure 9B is 0.37%.

Moving to the results of the thermal training, it can be determined in Section 3.1 that the ratcheting and plastic shakedown move and reduce the working range of the SMA actuator wire. Therefore, the maximum strain of the basic characterization must be increased to 6.5%. The maximum active strain, where the wire is not slack, is reduced to 4.45% starting at 2.05% with a power of 0.41 W. The intrinsic TWE extracted from the first cold state experiment is 5.05%. The remanent strain is 1.6%, as visible in Figure 9C. The shape of the hysteresis is changed dramatically compared to the untreated wire, which is also reflected in the hysteresis area listed in Table 1. It is compressed in strain direction, the transformation plateaus are less pronounced and a more homogeneous transition from the austenite branch, through the transformation plateau to the stress induced martensite branch is observed. The hysteresis width is reduced to about 150 MPa.

There is no more evidence of the R-phase in the resistance results of cold state tensile tests. The initial resistance level is unchanged compared to the untreated wire, although the wire length is increased as a result of the training. The course of the resistance signal of the austenitic tests is shifted in the direction of positive strain and reaches a maximum value of 25.6 Ω . That corresponds almost to the maximum of the untreated wire with 1% lower strain. The reason can be found in the higher starting strain of the mechanical response and the increased nonlinearity of the resistance curve. This results from the changed transformation behavior, which also manifests in the mechanical hysteresis. When studying Figure 9

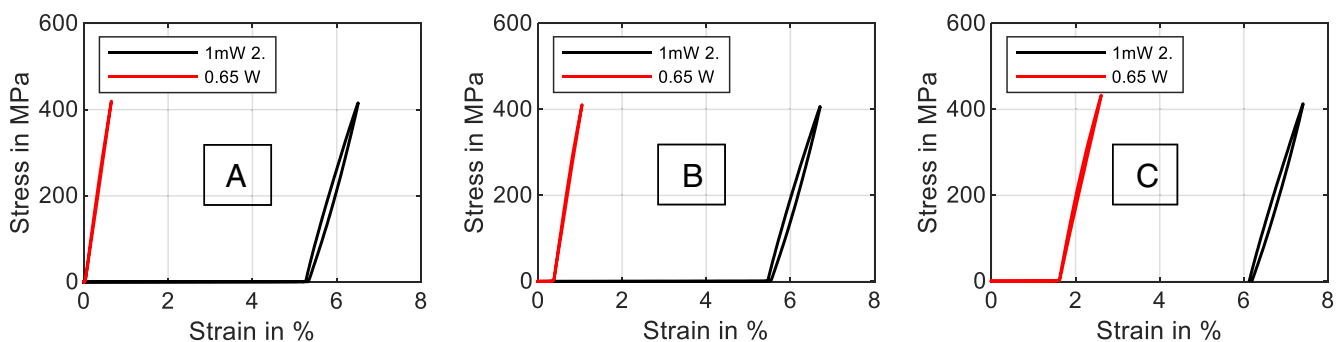


FIGURE 9 Results of tensile tests with maximum power (0.65 W) resulting in full austenite (red) and without heating power (1 mW) resulting in full detwinned martensite (black), while the stress is restricted to 400 MPa. The data for the three differently treated samples are depicted. “A”: untrained wire, “B” mechanically trained wire, “C” thermally trained wire.

and comparing the slopes of the elastic martensite and austenite branches, it is apparent that both training methods reduce the E_A , of which the exact values are displayed in Table 1.

To sum up, the results of the characterization with tensile tests leads to the conclusion, that training the wire with either of the proposed methods influences the sensor and actuator characteristics of an SMA wire. The stability of the R-phase is reduced with both training methods. This leads to easier signal interpretation on thermally passive wires, that are stretched to use as position sensors. The working point of the actuator shifts, especially after thermal cycling and the stroke is also reduced.

To design an SMA actuator system, the tensile tests up to 400 MPa in full austenite and fully detwinned martensite (Figure 9) are a proper tool to graphically estimate the maximum stroke that an SMA actuator generates in combination with a certain bias load. By drawing the characteristics of the bias system (e.g., a linear spring) in the stress–strain diagram, the stroke can easily be read from the intersection points with austenite and martensite curve. With the help of the resistance data, the necessary voltage and current supply can already be determined in an exact manner. The resistance range for self-sensing is also already known, which helps for the preliminary design of the electronics. For the exact behavior of the sensor signal however, the results of actuator tests, as discussed in the following paragraph, are necessary.

3.4 | Characterization of the actuator behavior

In this subsection, the results of actuation experiments with the introduced wire samples are discussed. The goal is to determine the influence of the different training methods on the actuator and sensor properties of the NiTi wire. These properties are the functional stability under high loads, the output stroke and the characteristics of the resistance signal. The characterization is performed with four different loads. In the low stress region, a spring load corresponding a pre-stress of 100 MPa and a max. stress of 200 MPa and a constant load corresponding a stress of 200 MPa are examined. In the high stress region, a spring load generating 200 to 400 MPa of stress as well as a constant load with 400 MPa are investigated. The experimental data plotted over time is displayed for one experiment in the main text. The remaining experimental data over time can be found in the “Data S1” section. The section is structured after the load used in the experiment, so that the characteristics of the samples can be compared to each other by means of the same load. For the evaluation of the actuation tests and the samples functional stability under a certain load, the activation cycle is repeated three times for each experiment. The first cycle usually defers from the remaining cycles due to the wires “load history”. In the following this is to be observed for constant load experiments only. Due to the experimental procedure, a preliminary actuation test is necessary for the spring force experiments to set the right pre-stress.

3.4.1 | Low stress actuation with spring load

For all following experiments a triangular signal with controlled current is used to heat the SMA wire and trigger the transformation. The amplitude of the electrical current is defined in preliminary tests to ensure a fully transformed austenite state for each stress level. For the experiments with low stress, the peak current is set to 160 mA. As displayed in Figure 10 the cycle time of the signal is 40 s to ensure a clean force control of the linear drive in the test rig and enough time for the wire to cool down at low currents. The current signal has an offset of 10 mA for a continuous resistance measurement. The pre-stressing and unloading path, visible in stress versus time in Figure 10, are not depicted in the strain and power plots discussed in the following, as they are not part of the actual experiment. The timing plots of all remaining experiments can be found in the “Data S1” section.

It is expected that the results of the low stress experiments show a good functional stability, and that no difference is to be observed between the first and third cycle. The stability is measured in the same manner as described in Section 3.1. In fact, these expectations are met by all three samples as is illustrated in Figure 11, where the three cycles cannot be distinguished in each case. No buildup of residual strain or shift in working point is observed. For one sample, the heating and cooling are indicated with arrows in the plot in Figure 11. This can be transferred to the rest of the data in this work, as the pattern stays the same.

The stroke of the untreated sample is 4.8% and is reduced by the plastic shakedown and ratcheting in both results of the trainings. The mechanically trained wire has an actuator stroke of 4.4% and the thermal training reduces the stroke to 4%. Here it is to be noted that the working range is moved by about 1% compared to the mechanical training, as was already observable in the basic characterization. Instead of strain versus temperature plots, in Joule heated experiments strain

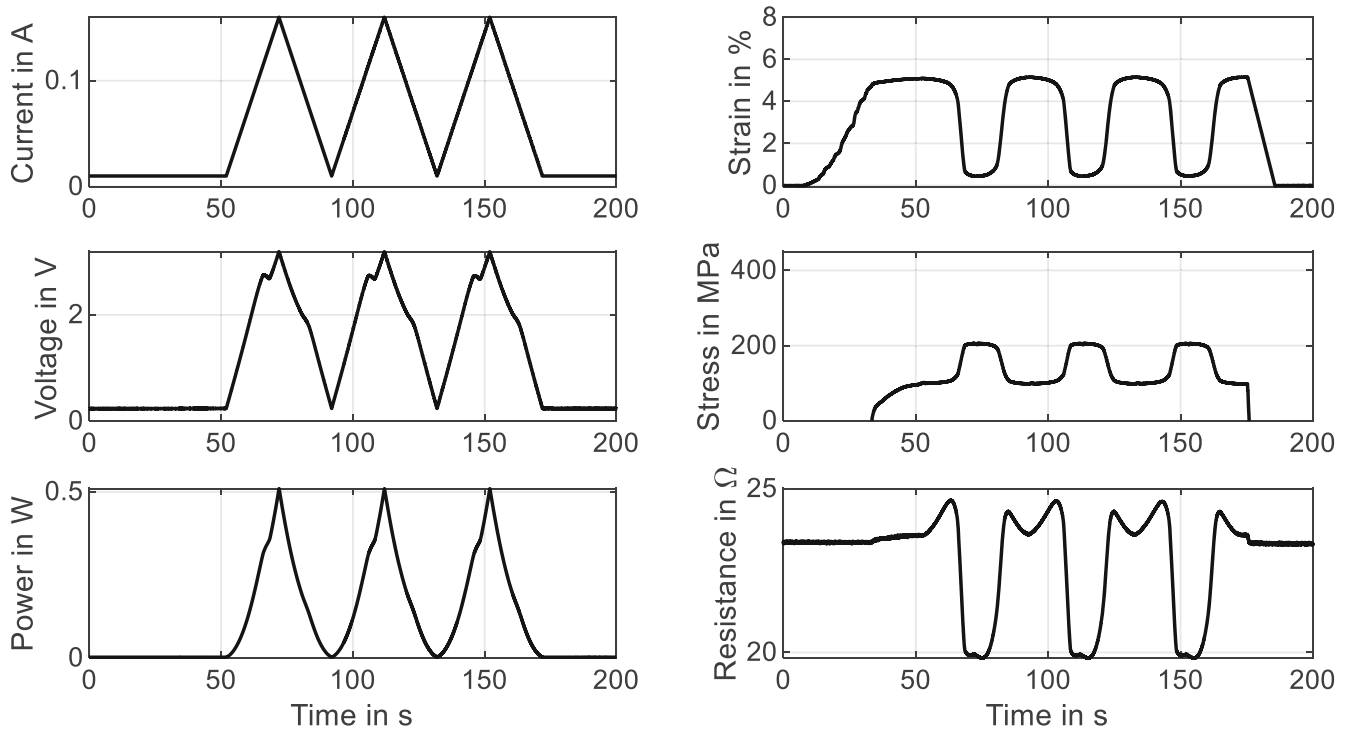


FIGURE 10 Timing of all measurements of the actuator experiment with controlled current in triangular shape, using the untreated wire sample. The bias is a linear spring load corresponding 100 MPa of prestress and 200 MPa maximum load.

versus electrical power plots are investigated. Without further ado, the electrical heating power cannot be correlated to a certain temperature. But due to the slow cycling the behavior is qualitatively very similar to strain versus temperature. In general, it is also possible to extract transformation powers as a replacement for the transformation temperatures. But as they strongly depend on the ambient temperature, this is neglected in this work.

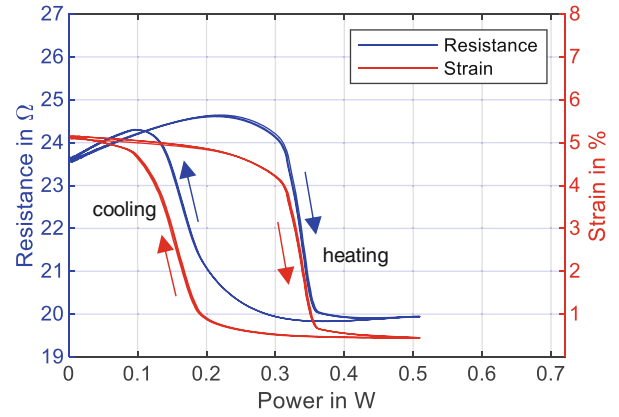
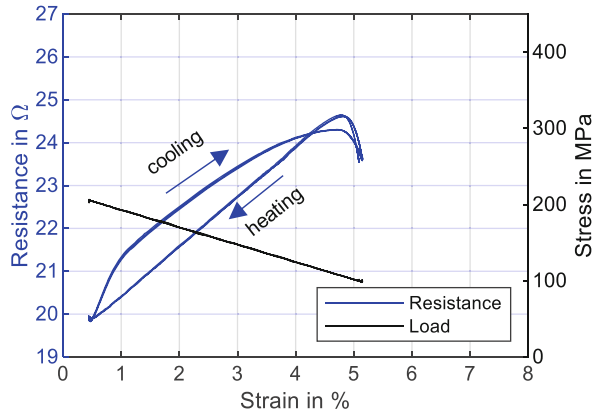
It can be observed in the strain-power hysteresis in Figure 11, is an analogy to the results of the mechanical hysteresis. The training reduces the hysteresis width and changes the slopes. The transformation points are less pronounced and especially the thermal training results in a homogeneous transition from martensite to austenite. While the untreated wire forms a curve parallel to the x-axis when in full austenite, the trained wires still have a downward slope. A higher power would lead to slightly increasing contraction.

Looking at the resistance over strain behavior in the left column of Figure 11, a distinct hysteresis is recognized. The resistance of the untreated wire starts at 23.5Ω in cold state and drops to 19.9Ω in full austenite. This corresponds to a change in resistance of 15%. The peak in resistance in the heating path results from the temperature influence before the main part of the phase transformation starts. After that, the heating path follows the strain in a linear manner until the minimum strain is reached and an increase in electrical power leads to another temperature related rise of the resistance. The course of the cooling is nonlinear and two changes in slope at about 1% and 4% of strain are recognizable. This hysteretic behavior in resistance is another evidence of the R-phase that forms when the NiTi wire cools down from austenite at low stresses. The influence of this intermediate phase on the resistance versus power plot can be observed in the first row and second column of Figure 11. The heating branch of strain and resistance both show distinct and overlapping characteristics in the area of the phase transformation. The cooling branch is different, and the resistance shows a round and homogenous shape, not directly following the strain of the wire.

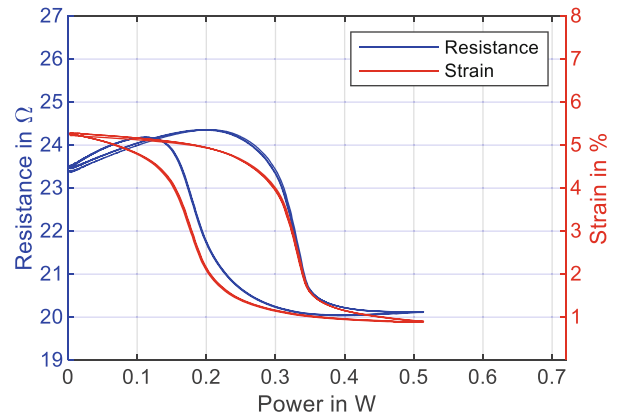
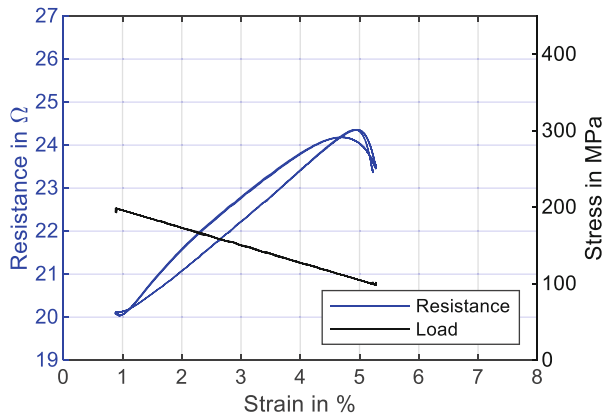
The results of the mechanical training show a reduced width of the resistance hysteresis related to strain and power. This means that the formation of R-phase is reduced, as can also be observed in Section 3.3. The thermal training reduces it even further, and the hysteresis is reduced to a max. width of 0.3Ω , coming from 1Ω for the untreated wire. Also, the course of the cooling branch of the resistance and strain versus power move closer together.

At this point, the conclusion for low stress actuation is, that a training reduces the maximum stroke that can be reached with the actuator and a thermal training also moves the working point due to the plastic deformation. This confirms the findings of the tensile tests. On the other hand, the decrease of the resistance-strain hysteresis is remarkable, especially

Untreated Wire



Mechanical Training



Thermal Training

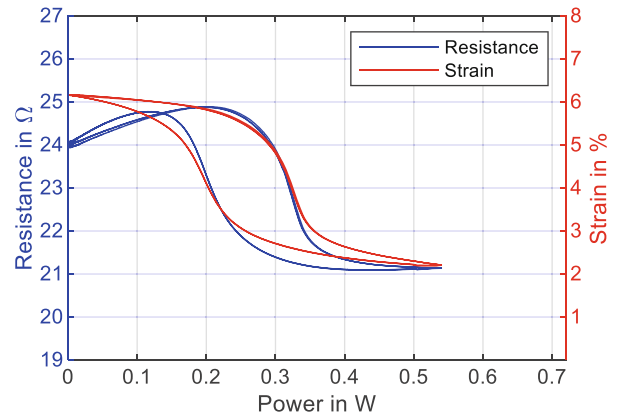
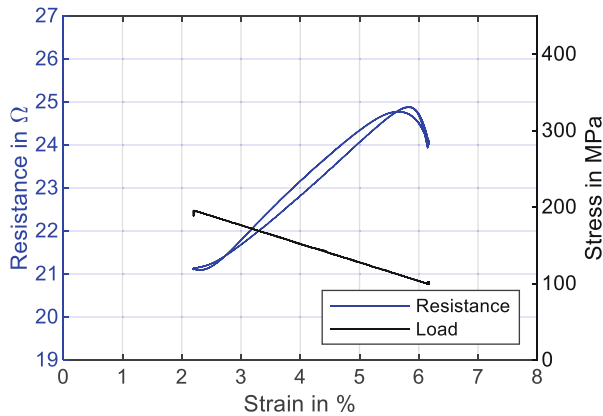


FIGURE 11 Actuator experiments with a linear spring load corresponding 100 MPa of pre-stress and 200 MPa of maximum load. Results for the three differently trained samples are depicted. The left column displays resistance and stress versus strain and the right column resistance and strain versus power.

due to the thermal training. It has a positive effect on the self-sensing capability, as complicated control algorithms to compensate the hysteresis are not necessary.

3.4.2 | Low stress actuation with constant load

The test parameters in this section are unchanged to Section 3.4.1, except for the load that is now kept constant at 200 MPa. The first cycle of each constant load experiments starts at a lower martensitic strain than the following cycles. This is because a tensile load of 200 MPa without thermal cycling does not fully re-orient the martensite crystal lattice and a small

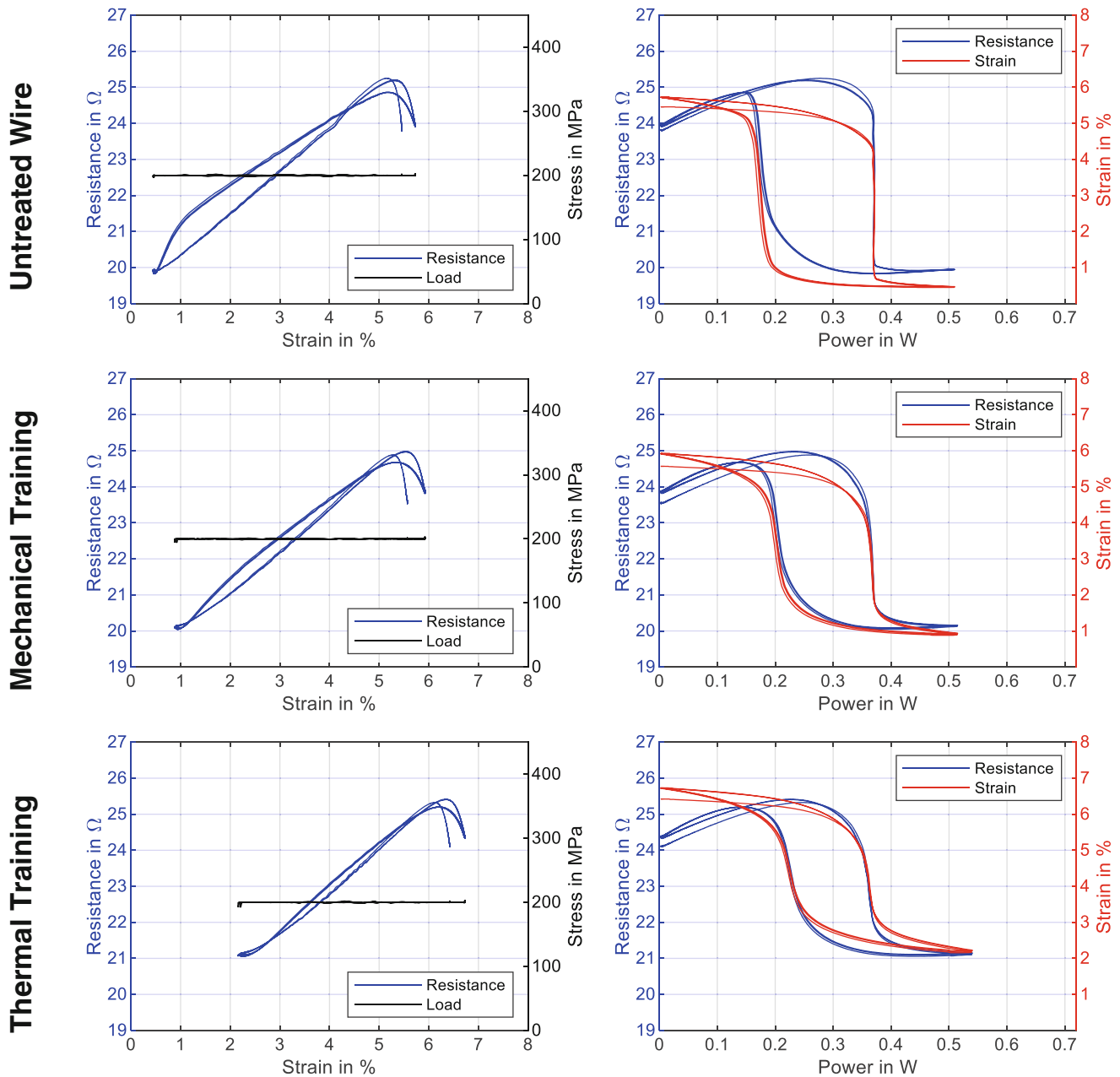


FIGURE 12 Actuator experiments with a constant load of 200 MPa. Results for the three differently trained samples are depicted. The left column displays resistance and stress versus strain and the right column resistance and strain versus power.

amount of twinned martensite is left. After the first heating cycle and cooling under stress, the crystal lattice transforms to a higher amount of detwinned martensite, and results in an increased strain.

This phenomenon has to be taken into account, when SMA driven systems are designed. Especially the mounting procedure of the SMA wires and commissioning of the final system is affected. None of the samples show stability issues. With the higher stress in martensite, the maximum strain of the SMA wire is increased and with that also the stroke of the actuator. As depicted in Figure 12, the stroke of the untreated wire amounts to 5.3%. The mechanical training reduces it to 5% and the thermally trained wire produces a stroke of 4.6%. This means that the stroke is increased by roughly 0.5% for all training variants due to the higher bias stress.

The slope of the strain versus power plot of the untreated wire is almost vertical when the phase transformation happens. Compared to a spring load, the stress-dependent transformation temperature stays the same and is not

depending on the strain. A spring load on the other hand, leads to a changing transformation temperature, increasing with decreasing strain. The shapes of the strain-power hysteresis change in the same manner as before. Their width decreases, transformation points evolve to transformation areas and the austenitic branch keeps a slight downward slope.

The general characteristics of the wire resistance relates to that of Section 3.4.1. The R-phase related resistance-strain hysteresis is recognizable in a similar way. However, the second curvature change at higher strains, that is observed with the spring load, is gone. This leads to a smaller hysteresis area, with a maximum width of 1Ω for the untreated wire. As before, both trainings reduce the hysteresis width and area. The thermally trained wire shows a max. hysteresis width of only 0.1Ω . The round shape of the cooling branch in the resistance-power plot, that does not follow the course of the strain is most pronounced in the results of the untreated wire in the first row and second column in Figure 12. Both trainings reduce this phenomenon. The training creates a less distinct transformation and a reduced R-phase proportion, the shape of the resistance-power hysteresis becomes smoother and moves closer to the strain-power plot.

3.4.3 | High stress actuation with spring load

As the goal of the training procedure is to reach a stable behavior of the SMA wire also under high stress, the following results show the necessity for this measure and the outcome for the two methods that are compared. For the high stress actuation experiments, the maximum heating current is increased to 180 mA, while the cycle time is unchanged at 40 s. The pre-stress of the linear spring corresponds to a stress of 200 MPa and the maximum stress is 400 MPa. The average stroke of the untreated SMA wire is 4.9% but reduces about 0.05% with each cycle. That is ten times higher than the stability criterion defined in Section 3.1.

As expected, the untreated wire, as conditioned by the manufacturer, is not stable at this stress level. The mechanical training improves the stability to 0.02% strain difference between the cycles at an average stroke of 4.6%, while the thermal training shows a stable behavior with 4.1% of stroke.

As displayed in the left column of Figure 13, the hysteresis of resistance in relation to strain is reduced drastically with the higher stress in all three samples. What stays recognizable are the loops at the beginning of the activation and at the end of the transformation. They are a result of the thermal hysteresis and the difference between martensite and austenite transformation temperatures. Neglecting these loops, the main course of the resistance signal behaves linear with almost no hysteresis. An exception is made by the untreated wire sample, where a slight hysteresis due to an increase in resistance is observed starting at 4.5% of strain and 250 MPa. The increased material stress suppresses the formation of the R-phase, while both trainings additionally reduce the effect. A stable behavior of the SMA wire with the examined spring tension is only achieved by prior thermal training. The mechanical cycling does unfortunately not create a sufficiently stable actuator. Having future production lines in mind, where actuator need to be trained for their specific application, the mechanical training would have been beneficial due to faster and easier implementation. It should be examined in further research, if a prior thermal training with the exact load as used in the actuator application (in this case 200–400 MPa spring load), would lead to the same stable behavior and better stroke output. Then, also the influence of the applied training load on the reduction of the R-phase is of interest.

Looking at the data in the power domain on the right column of Figure 13, the linear spring force leads to a similarly angled behavior in the transformation region like in Section 3.4.1. As before, training increases this angle, and the transformation start is less pronounced. A higher stress increases the quality of the resistance signal for self-sensing by eliminating the hysteresis almost to full extend. This makes the data easier to interpret but comes with the cost of reduced stroke and a training procedure for a stable behavior is required.

3.4.4 | High stress actuation with constant load

The final experiments discussed in this article are the actuation tests with 400 MPa of constant load. As before, the wire is Joule heated by a current controlled triangular signal with 180 mA of amplitude and 40 s cycle time. The results for all

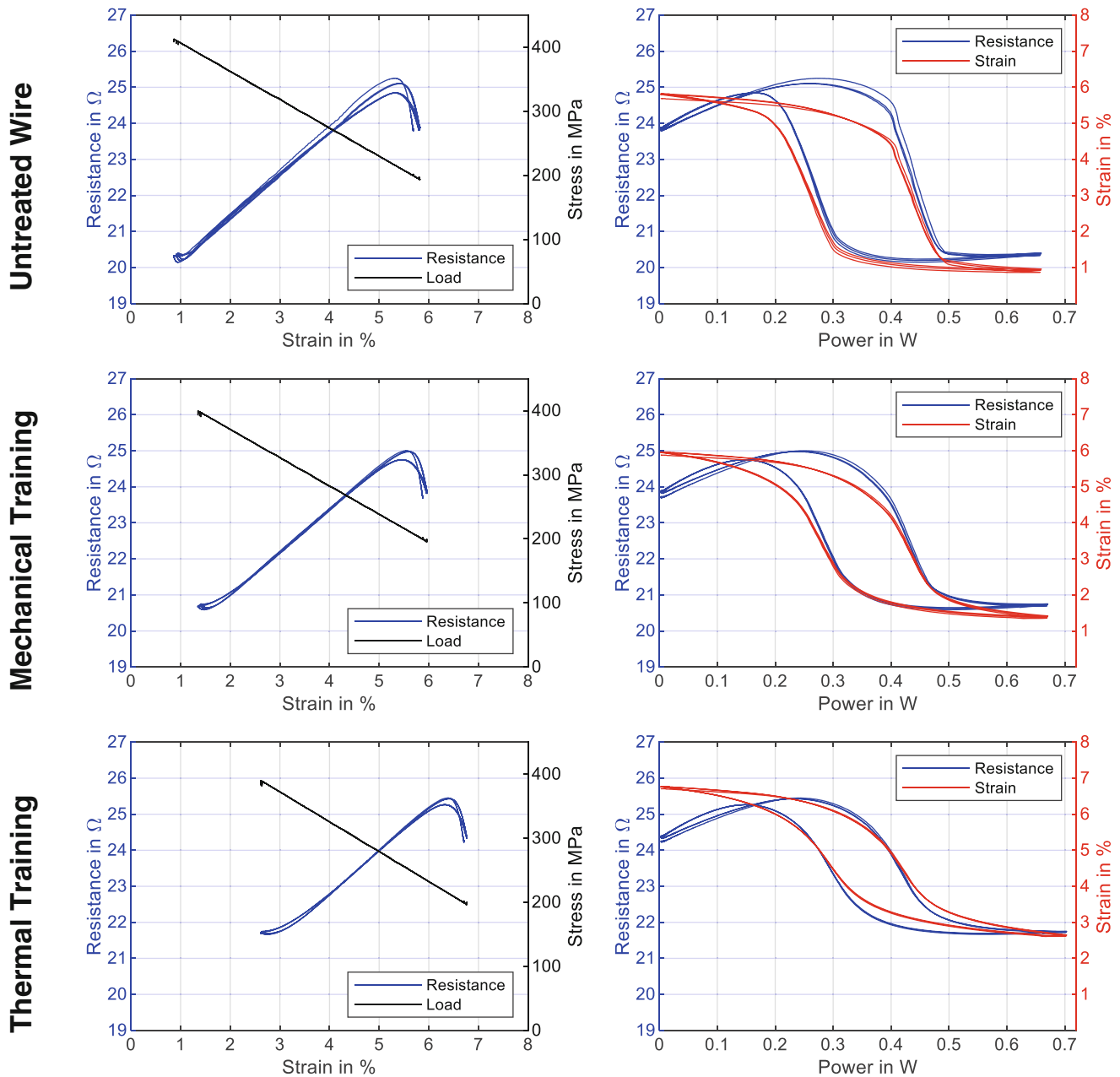


FIGURE 13 Actuator experiments with a linear spring load corresponding 200 MPa of pre-stress and 400 MPa of maximum load. Results for the three differently trained samples are depicted. The left column displays resistance and stress versus strain and the right column resistance and strain versus power diagrams.

samples are displayed in Figure 14 in the strain and power domain. It can be deduced from the previous sections that the untreated wire sample is not stable and basically the first three cycles of the training method displayed in Section 3.1 are to be observed here as well.

Pre-stressing the untreated SMA wire in twinned martensite to 400 MPa results in a strain of 6.6%. After the first activation cycle the martensitic strain increases to roughly 7% and an average stroke of 5.7% for the untreated wire is there. The trained variants behave similarly with 5.4% of stroke resulting from the mechanical training and 4.8% from the thermal training.

The mechanical training does not create a functional stability at 400 MPa actuation stress, as can be expected from the experiments discussed in previous sections. The thermally trained wire can on the other hand be expected to behave

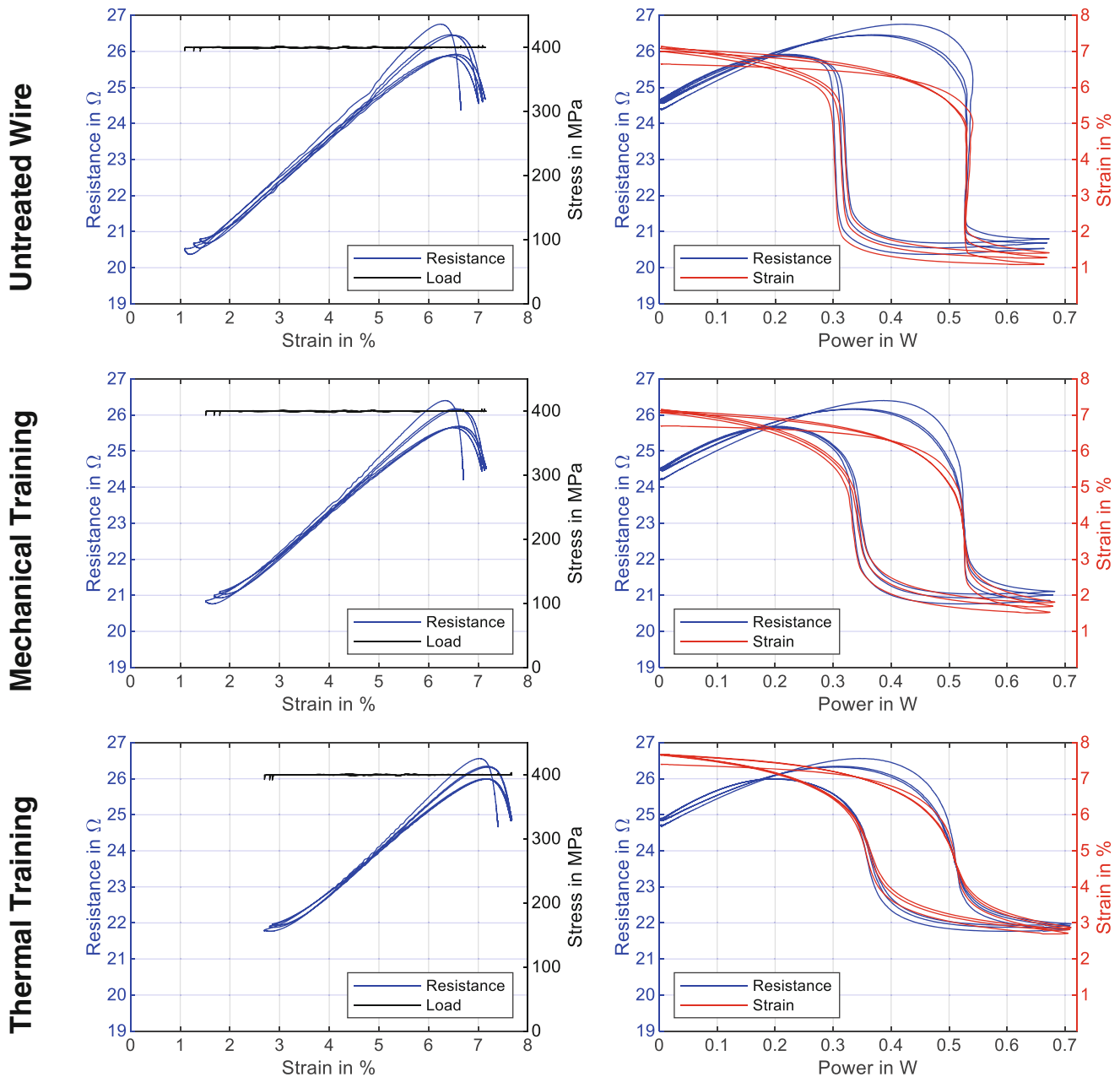


FIGURE 14 Actuator experiments with a constant load of 400 MPa. Results for the three differently trained samples are depicted. The left column displays resistance and stress versus strain and the right column resistance and strain versus power.

stable. The experiments discussed here have equal parameters like the thermal training, which met the stability criterion after 100 cycles. Therefore, only the first cycle of the actuation test of the thermally trained SMA wire shows the typical gap, known from the other experiments discussed in the previous sections.

In the first cycles of all three samples the resistance peak at the start of activation is higher than the following two. An explanation can be, that fractions of the R-phase with higher resistivity are present. It is apparent that for all three wire samples, the resistance versus strain behavior is still less hysteretic than these of the low stress experiments. However, the loops at the start and end of the heating phase are more pronounced than with 200–400 MPa of stress in Section 3.4.3.

The shape and behavior of the resistance and strain hysteresis in the power domain are similar to those in Section 3.4.2, with almost vertical course in the transformation for the untreated sample and the same evolution with the training as

described previously. Different than in the low stress results, the resistance follows the strain in a close manner, which leads to the small hysteresis in the strain domain.

It can be derived, that increasing the material stress reduced the resistance hysteresis only so far. The experiments with a constant load of 400 MPa show again slightly larger hysteresis for resistance strain, that are not due to the R-phase. The load profile plays a large role in designing SMA-actuator sensor systems and the maximum load is no sufficient information.

4 | CONCLUSION AND OUTLOOK

The article presents a new application-oriented method to characterize SMA wires for their use as Joule heated actuators with self-sensing. By means of the proposed procedures the exact behaviors of resistance and strain for arbitrary loads and different heating powers are investigated. With the help of a custom designed test-rig, all tests are run on the same sample and tensile tests can be compared to actuation tests. Prior to that, various trainings can be performed on the wire sample. The method is not restricted to the parameters used in this work and it is possible to examine any kind of thermal SMA actuator wire from 20 to 100 μm diameter with respect to their suitability for a certain application. Additionally, the tensile tests give us the basic material parameters to compare alloys and trainings.

In this work, the influence of mechanical and thermal training on the material and actuator-sensor properties on the example of “Dynamalloy Flexinol HT” are investigated. It can be concluded that the training of an SMA wire should be adapted to the load in the target application. That means that thermal training is to be preferred for an optimal utilization of the stroke. The thermal training reduces the hysteresis in the resistance signal and enables a stable material behavior at loads up to the training stress. Higher bias stresses in an application suppress the R-phase and lead to a more linear resistance curve, which makes the interpretation of the sensor signal easier. With higher stress, a more efficient use of space is enabled. When the actuator force is scaled by wire bundling or transmission stages instead, the installation space does increase. In recent research on soft and bending SMA actuators the findings of this work is able to help improving the actuation performance of the wire, by supporting the choice of the right training.^{42–44} Also, the findings of the proposed research can be transferred to these kinds of actuators to improve the understanding and utilization the self-sensing capabilities better.⁴⁵

The proposed methods are to be used in future work to further investigate how to tune certain properties of SMA wires by using specific training parameters. Examining the training with additional waveforms such as square waves, longer cooling periods and also different load profiles will be an essential part of it. Further research on the resistivity and its dependency on the Poisson's ration is also of interest. Therefore a precise and continuous measurement of the wire diameter during the phase transformation is necessary. In general, a manifold of other studies on various parameters and stimuli can be done. Due to its multifunctionality, the utilized test platform will be at the core of several research topics to come.

In “Part 2” of this work the limits for SMA actuators in high ambient temperatures and how to push them with training and increased material stress are investigated. An exemplary actuator is designed and tested by means of the hardware-in-the-loop feature of the test rig under high ambient temperatures.

AUTHOR CONTRIBUTIONS

Dominik Scholtes: Conceptualization; data curation; formal analysis; investigation; methodology; project administration; resources; software; validation; visualization; writing – original draft; writing – review and editing. **Stefan Seelecke:** Formal analysis; funding acquisition; investigation; methodology; project administration; supervision; writing – original draft; writing – review and editing. **Paul Motzki:** Formal analysis; funding acquisition; methodology; project administration; resources; supervision; writing – original draft; writing – review and editing.

ACKNOWLEDGMENT

Open Access funding enabled and organized by Projekt DEAL.

CONFLICT OF INTEREST STATEMENT

The authors declare no conflict of interest.

PEER REVIEW

The peer review history for this article is available at <https://www.webofscience.com/api/gateway/wos/peer-review/10.1002/eng2.12867>.

DATA AVAILABILITY STATEMENT

The data that support the findings of this study are available from the corresponding author upon reasonable request.

ORCID

Dominik Scholtes  <https://orcid.org/0009-0008-5515-4636>

REFERENCES

1. Degeratu S, Rotaru P, Manolea G, Manolea HO, Rotaru A. Thermal characteristics of Ni–Ti SMA (shape memory alloy) actuators. *J Therm Anal Calorim*. 2009;97(2):695–700. doi:10.1007/S10973-009-0215-0
2. Fumagalli L, Butera F, Coda A. SmartFlex® NiTi wires for shape memory actuators. *J Mater Eng Perform*. 2009;18(5–6):691–695. doi:10.1007/s11665-009-9407-9
3. Lagoudas DC. *Shape Memory Alloys*. Vol 1. Springer US; 2008. doi:10.1007/978-0-387-47685-8
4. Miller DA, Lagoudas DC. Thermomechanical characterization of NiTiCu and NiTi SMA actuators: influence of plastic strains. *Smart Mater Struct*. 2000;9(5):640–652. doi:10.1088/0964-1726/9/5/308
5. Buehler WJ, Wang FE. A summary of recent research on the nitinol alloys and their potential application in ocean engineering. *Ocean Eng*. 1968;1(1):105–120. doi:10.1016/0029-8018(68)90019-X
6. Crews JH, Buckner GD. Design optimization of a shape memory alloy-actuated robotic catheter. *J Intell Mater Syst Struct*. 2012;23(5):545–562. doi:10.1177/1045389X12436738
7. Antonucci V, Faiella G, Giordano M, Mennella F, Nicolais L. Electrical resistivity study and characterization during NiTi phase transformations. *Thermochim Acta*. 2007;462(1–2):64–69. doi:10.1016/j.tca.2007.05.024
8. Furst SJ, Seelecke S. Modeling and experimental characterization of the stress, strain, and resistance of shape memory alloy actuator wires with controlled power input. *J Intell Mater Syst Struct*. 2012;23(11):1233–1247. doi:10.1177/1045389X12445036
9. Buehler WJ, Gilfrich JV, Wiley RC. Effect of low-temperature phase changes on the mechanical properties of alloys near composition TiNi. *J Appl Phys*. 1962;1475:2–5. doi:10.1063/1.1729603
10. Janocha H, Bonertz T, Pappert G. *Unkonventionelle Aktoren: eine Einführung*. Oldenbourg Wissenschaftsverlag; 2013.
11. Wang T, Ma Z, Rao X, et al. Temperature-dependence of superelastic stress in nanocrystalline NiTi with complete transformation capability. *Intermetallics*. 2020;127:106970. doi:10.1016/J.INTERMET.2020.106970
12. Ling HC, Kaplow R. Stress-induced shape changes and shape memory in the R and Martensite transformations in Equiatomic NiTi. *Metall Trans A, Phys Metall Mater Sci*. 1981;12(12):2101–2111. doi:10.1007/BF02644180
13. Duerig TW, Bhattacharya K. The influence of the R-phase on the Superelastic behavior of NiTi. *Shape Mem Superelasticity*. 2015;1(2):153–161. doi:10.1007/s40830-015-0013-4
14. Lewis N, York A, Seelecke S. Experimental characterization of self-sensing SMA actuators under controlled convective cooling. *Smart Mater Struct*. 2013;22(9):094012. doi:10.1088/0964-1726/22/9/094012
15. Park CH, Son YS. SMA spring-based artificial muscle actuated by hot and cool water using faucet-like valve. 2017;10164:165–174. doi:10.1117/12.2257467
16. Actuator Solutions GmbH. Actuator Solutions GmbH. <https://www.actuatorolutions.de/english/products/> (accessed May 12, 2023)
17. Scholtes D, Seelecke S, Rizzello G, Motzki P. Design of a Compliant Industrial Gripper Driven by a Bistable shape memory alloy actuator. *Proceedings of the ASME Conference on Smart Materials, Adaptive Structures and Intelligent Systems*. 2020. doi:10.1115/SMASIS2020-2204
18. Kazi A, Honold M, Rimkus W, Lokner T, Bäuml M, Köpfer M. SMA actuator for optical image stabilization. ACTUATOR 2018 - 16th International Conference and Exhibition on New Actuators and Drive Systems, Bremen: VDE. 2018 375–378.
19. Uleru GI, Hulea M, Burlacu A. Bio-inspired control system for fingers actuated by multiple SMA actuators. *Biomimetics*. 2022;7(2):62. doi:10.3390/BIOMIMETICS7020062
20. Mandolino MA, Goergen Y, Motzki P, Rizzello G. Design and characterization of a fully integrated continuum robot actuated by shape memory alloy wires, in 2022 IEEE 17th International Conference on Advanced Motion Control, Institute of Electrical and Electronics Engineers (IEEE). 2022, pp. 6–11. doi:10.1109/AMC51637.2022.9729267
21. Cheng C, Cheng J, Huang W. Design and development of a novel SMA actuated multi-DOF soft robot. *IEEE Access*. 2019;7:75073–75080. doi:10.1109/ACCESS.2019.2920632
22. Bevilacqua D, Soletti G, Naso D, Rizzello G, Motzki P. Bio-inspired flapping wing antagonist actuation with SMA wires. *ACTUATOR 2022; International Conference and Exhibition on New Actuator Systems and Applications*. VDE; 2022:81–84.
23. Takimoto A. Relationship between volume fraction of strain-induced Martensite under tension and electrical resistivity in a Ti–Ni SMA wire. *J Phys IV*. 1995;05(C8):C8–C599. doi:10.1051/JP4/199558599
24. Churchill CB, Shaw JA, Iadicola MA. Tips and tricks for characterizing shape memory alloy wire: part 1 – Differential Scanning Calorimetry & Basic Phenomena. *Exp Tech*. 2009;33(1):51–62. doi:10.1111/J.1747-1567.2008.00460.X

25. Shaw JA, Churchill CB, Iadicola MA. Tips and tricks for characterizing shape memory alloy wire: part 2—fundamental isothermal responses. *Exp Tech*. 2008;32(5):55-62. doi:10.1111/J.1747-1567.2008.00410.X
26. Churchill CB, Shaw JA, Iadicola MA. Tips and tricks for characterizing shape memory alloy wire: part 4 - Thermo-mechanical coupling: experimental characterization of active materials series. *Exp Tech*. 2010;34(2):63-80. doi:10.1111/j.1747-1567.2010.00619.x
27. Gori F, Carnevale D, Doro Altan A, Nicosia S, Pennestrì E. A new hysteretic behavior in the electrical resistivity of flexinol shape memory alloys versus temperature. *Int J Thermophys*. 2006;27(3):866-879. doi:10.1007/s10765-006-0060-3
28. Churchill CB, Shaw JA. Shakedown response of conditioned shape memory alloy wire. *Behav Mech Multifunct Compos Mater*. 2008;6929:69291F. doi:10.1117/12.778726
29. Churchill CB, Shaw JA. Thermo-electro-mechanical shakedown response of conditioned shape memory alloy wires. *Proc ASME Conf Smart Mater Adapt Struct Intell Syst, SMASIS2009*. 2009;1:137-148. doi:10.1115/SMASIS2009-1306
30. Furst SJ, Crews JH, Seelecke S. Stress, strain, and resistance behavior of two opposing shape memory alloy actuator wires for resistance-based self-sensing applications. *J Intell Mater Syst Struct*. 2013;24(16):1951-1968. doi:10.1177/1045389X13486715
31. Britz R, Motzki P. Analysis and evaluation of bundled SMA actuator wires. *Sensors Actuators A Phys*. 2021;1-2:113233. doi:10.1016/J.SNA.2021.113233
32. Song SH, Lee JY, Rodrigue H, Choi IS, Kang YJ, Ahn SH. 35 Hz shape memory alloy actuator with bending-twisting mode. *Sci Rep*. 2016;6(February):1-13. doi:10.1038/srep21118
33. Cambridge Mechatronics - Actuators. <https://www.cambridge-mechatronics.com/en/cml-technology/actuators/> (accessed Aug. 21, 2023)
34. Kirsch SM, Welsch F, Bevilacqua D, et al. SMA antagonistic-micro-wire bundle: first measurement results, SMASIS 2020 - Conference on Smart Materials, Adaptive Structures and Intelligent Systems. 2020. doi:10.1115/SMASIS2020-2261
35. Scholtes D, Schmidt M, Linnebach P, Seelecke S, Motzki P. A multifunctional characterization test bench for shape memory alloy micro-wires—design, implementation and validation. *Mater*. 2023;16(13):4820. doi:10.3390/MA16134820
36. SAES Group. SmartFlex Springs and Wires. <https://www.saesgetters.com/sites/default/files/SMARTFLEXSPRINGSANDWIRES.pdf> (accessed Jul. 06, 2018)
37. Dynalloy. Technical characteristics of Flexinol actuator wires. Dynalloy Inc. <http://www.dynalloy.com/pdfs/TCF1140.pdf> (accessed Mar. 12, 2019)
38. Fort Wayne Metals - Nitinol. <https://www.fwmetals.com/materials/nitinol/> (accessed May 31, 2023)
39. Auricchio F, Constantinescu A, Menna C, Scalet G. A shakedown analysis of high cycle fatigue of shape memory alloys. *Int J Fatigue*. 2016;87:112-123. doi:10.1016/j.ijfatigue.2016.01.017
40. Scherngell H, Kneissl AC. Generation, development and degradation of the intrinsic two-way shape memory effect in different alloy systems. *Acta Mater*. 2002;50(2):327-341. doi:10.1016/S1359-6454(01)00342-1
41. Muslov SA, Lotkov AI, Timkin VN. Poisson ratio of TiNi. *Inorg Mater Appl Res*. 2022;13(2):306-317. doi:10.1134/S207511332202030
42. Kennedy S, Vlajic N, Perkins E. Cosserat modeling for deformation configuration of shape memory alloy unimorph actuators. *J Intell Mater Syst Struct*. 2023;34(6):642-652. doi:10.1177/1045389X221109256
43. Lalegani Dezaki M, Bodaghi M, Serjouei A, Afazov S, Zolfagharian A. Adaptive reversible composite-based shape memory alloy soft actuators. *Sensors Actuators A Phys*. 2022;345:113779. doi:10.1016/J.SNA.2022.113779
44. Goergen Y, Rizzello G, Motzki P. Systematic methodology for an optimized Design of Shape Memory Alloy-Driven Continuum Robots. *Adv Eng Mater*. 2023;26:2301502. doi:10.1002/ADEM.202301502
45. Kennedy S, Shougat MREU, Perkins E. Robust self-sensing shape memory alloy actuator using a machine learning approach. *Sensors Actuators A Phys*. 2023;354:114255. doi:10.1016/j.sna.2023.114255

SUPPORTING INFORMATION

Additional supporting information can be found online in the Supporting Information section at the end of this article.

How to cite this article: Scholtes D, Seelecke S, Motzki P. Electro-thermo-mechanical characterization of shape memory alloy wires for actuator and sensor applications—Part 1: The effects of training. *Engineering Reports*. 2024;e12867. doi: 10.1002/eng2.12867

2.4 Electro-Thermo-Mechanical Characterization of Shape Memory Alloy Wires for Actuator and Sensor Applications – Part 2: High Ambient Temperature Behavior

Dominik Scholtes ^{1,2}, Stefan Seelecke ^{1,2}, Paul Motzki ^{1,2}

¹ Lehrstuhl für Intelligente Materialsysteme, Zentrum für Mechatronik und Automatisierungstechnik, ZeMA gGmbH, Saarbrücken

² Lehrstuhl für Intelligente Materialsysteme, Fachrichtung Systems Engineering, Fachrichtung Materialwissenschaft und Werkstofftechnik, Universität des Saarlandes, Saarbrücken

Veröffentlicht in Wiley Advanced Engineering Materials.

DOI: 10.1002/adem.202400432

© 2024 by the authors.



Dieser Artikel ist lizenziert unter Creative Commons Namensnennung 4.0 International (Creative Commons Attribution 4.0 International, CC BY 4.0).

Electro–Thermo–Mechanical Characterization of Shape Memory Alloy Wires for Actuator and Sensor Applications, Part 2: High-Ambient-Temperature Behavior

Dominik Scholtes,* Stefan Seelecke, and Paul Motzki

The typical phase transformation temperatures of commercially available shape memory alloys (SMA) for actuator applications are in the region of 80–90 °C for austenite finish and around 60 °C for martensite start. That limits the areas of application for SMA actuators, as increased ambient temperatures restrict their functionality. Especially in the industrial and automotive sectors, operational temperatures of 80 °C and higher are commonly required. This article discusses the limits of operation temperatures for commercially available SMA actuator wires. Also, methods to increase this critical temperature limit, at which the SMA actuation strain falls below a certain threshold, are proposed. By means of electrothermal actuation experiments, the influence of the variation of bias loads and an additional training method are investigated. Supported by these results, an exemplary valve actuator system is designed, which exhibits consistent stroke in a wide range of ambient temperatures. All experiments and measurements are conducted on a custom designed test bench with the same commercially available SMA wire. The test bench is in the following used again to evaluate the designed SMA valve actuator.

1. Introduction and Fundamentals

A commonly known limit for the application of shape memory alloys (SMA) wire actuators is the ambient temperature. It is set by the transformation temperatures of the alloy, which lie typically at 80–90 °C. This article covers the investigation of the sensor and actuator characteristics of SMA wires at high ambient

temperatures up to 100 °C. The study's goal is to examine the limits of operational temperature for an SMA actuator system and how to push those limits and optimize the actuator and sensor performance. The proposed specific data helps to better tune and design SMA wires for applications, where increased ambient temperatures are of concern.

In the published article “Part 1: The Effects of Training” of this research project, an application-oriented characterization method for SMA actuator wires is discussed.^[1] That article is focused on the influence of two fundamental training methods and the influence of different loads on the stroke and resistance behavior of SMA actuator wires made from nickel–titanium (NiTi). The experiments are performed at a constant ambient temperature of 23 °C.


Building on that, the methods and experimental parameters introduced in the previous part are also utilized in the following sections. With this, the research is consistently continued and supplemented. The general idea is to develop a basic understanding and approach of how to design an actuator–sensor system that features an increased range of operational temperature and stable characteristics at high material stress. To achieve this, specific data of resistance, stroke and stress are proposed. The article is written to be comprehensive as a standalone work, with some repetition from the previous articles. Nonetheless, the whole picture with all facets is painted by also taking into account the previous articles on the characterization method^[1] and the custom designed test rig.^[2]

The basics of thermal SMA actuators are discussed widely in research articles since their discovery.^[3–7] A summary of these is already given in “Part 1.” However, according to the focus of this research, a brief overview of important fundamentals is discussed here as well.

SMAs are often used in the form of wires, which are commercially available mostly made of binary nickel–titanium (NiTi). The material shows high phase transformation temperatures accompanied by highly hysteretic thermal and mechanical characteristics. NiTi actuator wires are Ti rich and undergo a (quasi-) plastic deformation when a load is applied at room temperature. When the wire is then heated to the phase transformation temperature, it returns to its original geometry. This response

D. Scholtes, S. Seelecke, P. Motzki
Intelligent Materials Systems Lab
Center for Mechatronics and Automation Technology
ZeMA gGmbH, 66121 Saarbrücken, Germany
E-mail: dominik.scholtes@imsl.uni-saarland.de

D. Scholtes, S. Seelecke, P. Motzki
Intelligent Materials Systems Lab
Department of Systems Engineering
Department of Material Science and Engineering
Saarland University
66123 Saarbrücken, Germany

 The ORCID identification number(s) for the author(s) of this article can be found under <https://doi.org/10.1002/adem.202400432>.

© 2024 The Authors. Advanced Engineering Materials published by Wiley-VCH GmbH. This is an open access article under the terms of the Creative Commons Attribution License, which permits use, distribution and reproduction in any medium, provided the original work is properly cited.

DOI: 10.1002/adem.202400432

is called shape memory effect and strains of 5% and more can be fully recovered.^[5] It is based on a reversible rearrangement of the material's crystal lattice structure, where a phase transformation from martensite to austenite and vice versa takes place. Characteristic temperatures are austenite start (A_s) and austenite finish (A_f) temperature, as well as martensite start (M_s) and finish (M_f) temperature. They are determined by the strain over temperature diagram under a constant load (typically around 200 MPa), which can be observed in **Figure 1**. These transformation temperatures are crucial to determine the approximate maximum operation temperature for an SMA actuator. Not only a high A_f temperature is required for applications at increased ambient temperatures, but also high M_f , which results in a narrow hysteresis. The transformation temperatures and the width of the temperature hysteresis mostly depend on the alloy composition and grain structure, but they are also influenced by the material stress, according to the Clausius–Clapeyron relation.^[4,8]

In technical applications, SMA actuator wires are typically heated either by electrical power via Joule heating or less commonly by a high-temperature fluid in contact with the alloy.^[9,10] Because of their high energy density, SMA wires are especially suitable for small and lightweight actuator systems, such as valves, small-sized gripping systems, and optical image stabilization (OIS).^[11–13] These applications, especially in the industrial sector, must work under a wide range of ambient temperatures. Examples for possible SMA-driven applications in manufacturing processes are active valves for injection molding, valves for tempered media, and small gripping solutions at soldering stations, to name some.^[14] For automotive applications in exterior and interior, operational temperatures typically go up to 80 °C to ensure functionality in all climates and operating states. Even if the expected operation conditions are around room temperature, the functionality of actuation systems is required to be robust. Therefore, a certain safety to ensure functionality at varying ambient conditions must be complied with.

Also, the self-sensing feature of SMA wires is taking up an important role as it makes external position sensors dispensable.^[15] This sensing is based on a change of the electrical resistance, which is observed when SMAs undergo

the austenite–martensite transformation or a change in geometry.^[16] Their resistance depends on the contemporary crystal lattice, the wire length, and cross-sectional area as well as the temperature.^[9,17]

Material characterizations of SMA are usually performed with differential scanning calorimetry, temperature-controlled tensile tests, or thermally induced phase transformation under a constant stress, which is extensively done by Churchill, Iadicola, and Shaw as well as Miller and Lagoudas among others.^[6,18–20] Research is also presented on the thermal characteristics of the electrical resistance of NiTi.^[21–23] In the field of electrically heated SMA, Lewis et al. investigated the response of Joule-heated wires subjected to convective cooling, while Furst et al. explored the characteristics and self-sensing capabilities of antagonistic Joule-heated NiTi wires.^[9,24] The influence of training on the thermal characteristics of NiTi is investigated and the results suggest an increase in transformation temperature by the measure.^[25–27] In “Part1” of this research, however, the effects of two fundamental training methods on stroke output and the resistance characteristics of Joule-heated NiTi microwires are examined.^[1]

With the learnings from that study, the behavior of SMA actuators under increased ambient temperatures is investigated in this article. The objective of the investigation is the optimization of performance under high ambient temperatures, by combining training and the variation of prestress. The examined thermoelectrical training method promotes consistent material behavior under loads up to 400 MPa. Higher material stress means a higher force output of the actuator, which also leads to a higher work density^[28] and suppresses the formation of the R-phase in the NiTi crystal lattice, resulting in a more linear and less hysteretic resistance curve. As existing research based on thermomechanical experiments suggests the additional training is also expected to increase the operational temperature range of SMA actuators.

Due to their rapid cooling rate, small-diameter wires have become important in SMA-driven products like OIS and valve systems.^[11,29–31] Consequently, this study is centered on a commercially available NiTi wire measuring 72 μm in diameter. The experimental setup, detailed in another study^[2] by Scholtes et al. is purpose built for these microwires. In this article's experiments, two differently conditioned wires are investigated: one conditioned by the manufacturer and another subjected to additional thermoelectrical training.

In the following sections, the impact of training and prestress on the shift of maximum operating temperature of Joule-heated SMA wires is investigated. Based on the results, an exemplary actuator sensor system, which is required to function in a large range of ambient temperatures is conceived and simulated in the test rig. The dynamics of SMA microwires at elevated temperatures is not considered in this study, as it is focused on the effects of load and training on the stroke and resistance characteristics. Future work will be conducted looking into this important field.

The remainder of this article is structured as follows. The experimental setup, the materials and measurement methods, known from the author's prior publications, are described in Section 2. In the subsections of Section 3, the data of the actuation results at temperatures between 23 and 100 °C is presented and discussed for various bias stresses and trained as well as

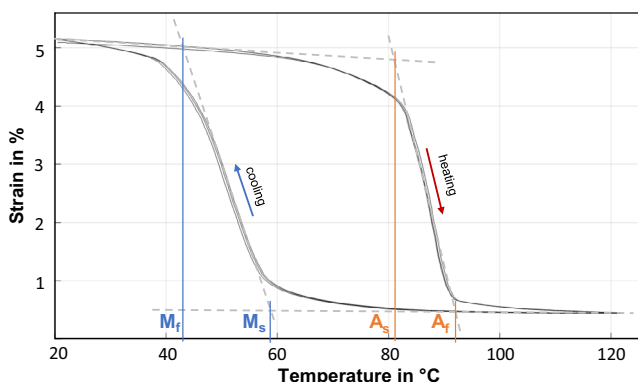


Figure 1. Example of a typical strain versus temperature diagram of a NiTi actuator wire. Depicted are the martensite start (M_s) and martensite finish (M_f) as well as the austenite start (A_s) and austenite finish (A_f) temperatures.

untrained wire samples. Section 4 features the conceptual design and evaluation of a SMA-driven valve suitable for high-ambient temperature operation. The manuscript closes in Section 5 with a conclusion including a summary of the results and an outlook.

2. Experimental Section

The experiments described in the following were carried out using a single setup meticulously detailed by Scholtes et al.^[2] For comprehensive information regarding the experiments and test setup beyond the descriptions provided here, please refer to that publication for exhaustive details on design, implementation, and validation.

The custom designed setup, displayed in **Figure 2**, was laid out horizontally. It consisted of two clamps equipped with air bearings that mechanically fixed the SMA wire and established the electrical connections. While one clamp was affixed to a load cell, the other was attached to a linear drive. To avoid any interference from external airflow during measurements, both the clamps and the wire sample were positioned within an isolated chamber. The temperature within the chamber was monitored and could be regulated in a range from 23 to 100 °C.

Additionally, a secondary motor was accessible to install the wire directly from the reel and fixed to the clamps in a stress-controlled regime. This process ensured consistent and repeatable measurement outcomes upon replacing the SMA sample. The test rig was multifunctional, which means that it was designed to conduct tensile tests, actuator tests, and cyclic tests for shakedown experiments or training. The linear drive was run in a closed-loop force-control mode for the actuator tests, where

arbitrary loads as well as end stops can be mapped, to simulate real-world applications.

All tests conducted in this article utilized a Joule-heated wire powered by controlled electrical current. The temperature-regulated isolating chamber played a pivotal role in this research, specifically in creating high ambient temperatures. The actuator tests were conducted within this chamber under increased temperatures, applying either a constant load or a linear spring rate alongside a defined prestress.

To facilitate the electrical heating of the SMA wire, a custom-designed constant current source was used, offering adjustable output currents ranging from 0 mA to 250 mA and a voltage of up to 24 V. The precise measurement of the voltage drop across the wire and the electrical current enabled accurate resistance measurement. The setup was controlled using a “National Instruments” FPGA based system and “NI LabVIEW”.

For all experiments in this work, a “Dynalloy Flexinol HT” NiTi wire with a measured diameter d_0 of 72 μm (in twinned martensite) was used.^[32] The initial wire length L_0 was always set to 100 mm in full austenite at a stress of 10 MPa. This length, set on a virgin wire, was used as the reference value in all experiments. For all following results, the wire strain ε was calculated with

$$\varepsilon = \frac{L - L_0}{L_0} \quad (1)$$

The mechanical stress σ is calculated with

$$\sigma = \frac{F}{A_0} \quad (2)$$

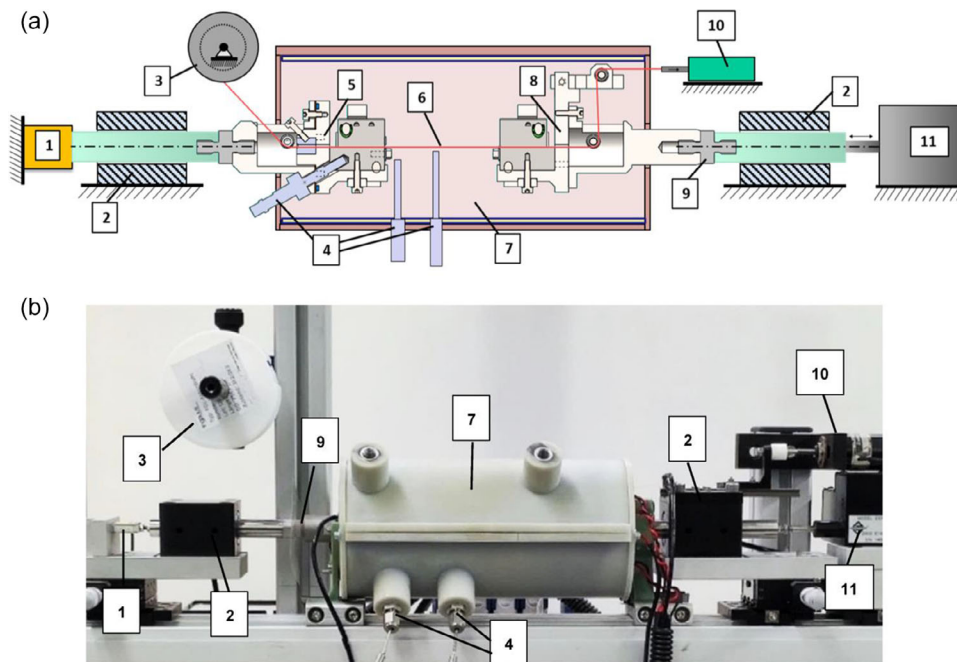


Figure 2. a) Schematic design of the experimental setup. b) Picture of the fully implemented test rig with closed heating chamber including the following components: 1: load cell; 2: air bearing; 3: SMA wire reel; 4: PT100 sensors; 5: fixed wire clamp; 6: SMA wire; 7: heating chamber; 8: moving wire clamp; 9: insulation adapter; 10: prestressing motor; 11: linear direct drive. (Reproduced under terms of the CC-BY license Copyright 2023, Scholtes et al. published by MDPI).^[2]

where F is the force acquired by the loadcell and A_0 is the initial cross-sectional area of the wire, which is calculated by

$$A_0 = \frac{\pi}{4} * d_0^2 \quad (3)$$

Additionally, a reset procedure was performed on the NiTi wire before each experiment. With this measure, uniform initial conditions for the wire specimen were ensured in every test.

3. Experiments and Results

In “Part 1” of these SMA actuation studies, tensile tests as well as actuator tests are performed, to evaluate the influence of training and different loads on the actuator and sensor properties of NiTi wires. The main learnings are that the wire in the “as-delivered” state is stable up to 200 MPa as intended by the manufacturer and shows good stroke outputs at low stresses. A wide hysteresis in the resistance versus strain signal is observed, indicating the presence of R-phase fractions in the crystal lattice. An additional training with 100 actuation cycles at 400 MPa proved to be superior to the also examined pure mechanical training. It leads to a stable actuator behavior at up to 400 MPa and a decreased resistance–stroke hysteresis. These effects come with the cost of a reduced stroke, a shift in operational range, and a general change in thermomechanical behavior, compared to the as-delivered wire.

The objective is to investigate the actuator and sensor properties at increasing ambient temperatures, pushing the limits for designing temperature stable actuator systems. The focus also lies on optimizing the performance concerning stroke and force in a wide range of operational temperature. Four bias systems relevant for applications are examined. As the continuation of the study in “Part 1”, the same load parameters are used. In the following, both samples, untreated and additionally trained, are actuated under a constant stress of 200 MPa as well as a linear bias spring ranging from 100 to 200 MPa. The sample with thermal training is also investigated under 400 MPa constant stress and a spring load of 200–400 MPa. The “as-delivered” wire is not tested under the higher loads, as the previous study already demonstrated its instability and the need for a prior training of the sample.

The range of loads is chosen due to the relevance for applications. Apart from the influence of different stress levels, it also creates a better understanding of how different slopes of the load profiles affect the actuator and sensor performance of the NiTi wire. The prestress of the spring configuration is set at room temperature and is retained at the high-temperature experiments. The expected contraction of the SMA wire due to the ambient condition leads to increased prestresses of the spring, being observed in the high-temperature stress–strain diagrams presented in the following subsections.

The experiments are conducted under temperature conditions ranging from room temperature to 100 in 10 °C steps. When 80 °C is reached and the stroke is less than 1%, the temperature is not increased further. For each test series, only the data of the five highest temperatures is proposed in the following sections. Additionally, the 23 °C experiment, which is also discussed in “Part1,” is added as basis for comparisons. For the interpretation

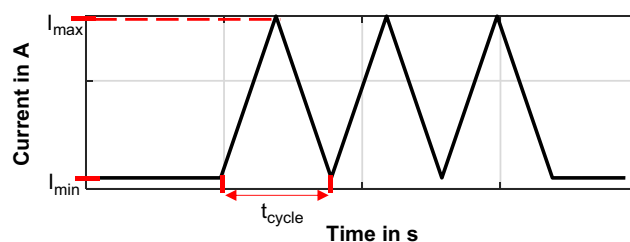


Figure 3. Triangular current input signal for actuation tests with the parameters cycle time t_{cycle} , minimum current I_{min} , and maximum current I_{max} .

and discussion, resistance and stress are displayed over strain for each ambient temperature. The Joule-heated activation of the SMA wire is controlled with a triangular current signal and three repetitions, as displayed in **Figure 3**. With the repetitions, the stability of the behavior can be confirmed, and the possible difference of the first cycle is observable. The triangular current signal offers a varied and continuous input, enabling a thorough examination of the SMA wire’s reaction to a spectrum of stimuli compared to, for instance, a square wave. It helps to understand the wire’s response under changing current levels, especially concerning stress, strain, and resistance.

Typically for SMA actuators, the first cycle differs from the following cycles due to different starting conditions. In this case, they are caused by the reset test. This reset test is run before each experiment to ensure the same starting conditions for every measurement. For the reset, the wire is slack, heated to full austenite, and then cooled down to ambient conditions with no load applied.

The input parameters of the current signal are cycle time t_{cycle} , minimum current I_{min} , and maximum current I_{max} , as illustrated in **Figure 3**. The measuring current I_{min} is set to 5 mA for all temperatures, ensuring a consistent resistance measurement. t_{cycle} and I_{max} are adjusted according to the temperature level to guarantee a repeatable and full cooldown of the SMA sample as well as prevent overheating. In **Table 1** the test parameters for the low-stress experiments (100–200 MPa spring load and 200 MPa constant load) are shown. **Table 2** includes the

Table 1. Test parameters depending on the ambient temperature for the low-stress experiments.

Temperature in °C	23	40	50	60	70	80
I_{max} in mA	160	155	140	135	125	120
t_{cycle} in s	40	60	80	80	120	120

Table 2. Test parameters depending on the ambient temperature for the high-stress experiments.

Temperature in °C	23	50	60	70	80	90	100
I_{max} in mA	180	160	155	150	145	140	130
t_{cycle} in s	40	60	80	80	120	120	120

input parameters for the high-stress experiments (200–400 MPa spring load and 400 MPa constant load).

The parameters are identified in preliminary tests. With increasing temperatures, the heating current is reduced to avoid overheating and damaging the NiTi wire. The cycle time is increased accordingly, to ensure a full cooldown at the applied ambient temperature.

3.1. Results of the Untreated Wire Sample under Low Stress

At low material stresses, which in this case means a maximum of 200 MPa, the transformation temperatures are low as well. Thus, a drop in actuator stroke at relatively low ambient temperatures is expected. Using linear springs to bias the SMA wire has the effect that the material stress rises with increasing actuator stroke. Therefore, also the phase transformation temperature of the NiTi wire is not constant but strain dependent.

In **Figure 4**, the results of actuation experiments with a spring prestressed to 100 MPa at 23 °C are displayed for temperatures between 23 and 80 °C. The stress rises to 200 MPa due to the wire's contraction and the spring stiffness. It is observed that with increasing ambient temperature, the minimum strain in austenite stays constant at 0.5%, but the martensitic strain decreases. For an application this means that the initial

position cannot be reached after the temperature increases. In a normally closed valve application, for example, the valve would not close properly when a certain ambient temperature is exceeded. Addressing the SMA stroke at significant temperature values, the overall stroke at 23 °C amounts to 4.7%, reduces to 2.2% at 60 °C, and then drops fast to 0.3% at 80 °C.

The resistance curve, displayed in **Figure 4** for six different ambient temperatures, shows the typical hysteretic shape evoked by the existence of R-phase portions, which is described in detail in “Part 1.”^[1] In short, it can be explained by the significant difference in resistivity of the R-phase compared to that of austenite and martensite. As the R-phase only occurs when cooling from austenite to martensite (due to the similarity in lattice structure of R and A), the curves of the heating and cooling path are different.^[15,21]

With increasing ambient temperature, the hysteretic behavior remains in place and inner loops of the hysteresis are observed. The slightly lower minimum resistance value of 19.8 Ω for the 23 °C experiment comes from the installation of a new sample for the remaining experiments. With increasing temperature, the minimum resistance values decrease minimally from 20.1 Ω at 40 °C to 20 Ω at 80 °C. Otherwise, the ambient temperature has no significant influence on the resistance characteristics. With increasing temperature, inner loops

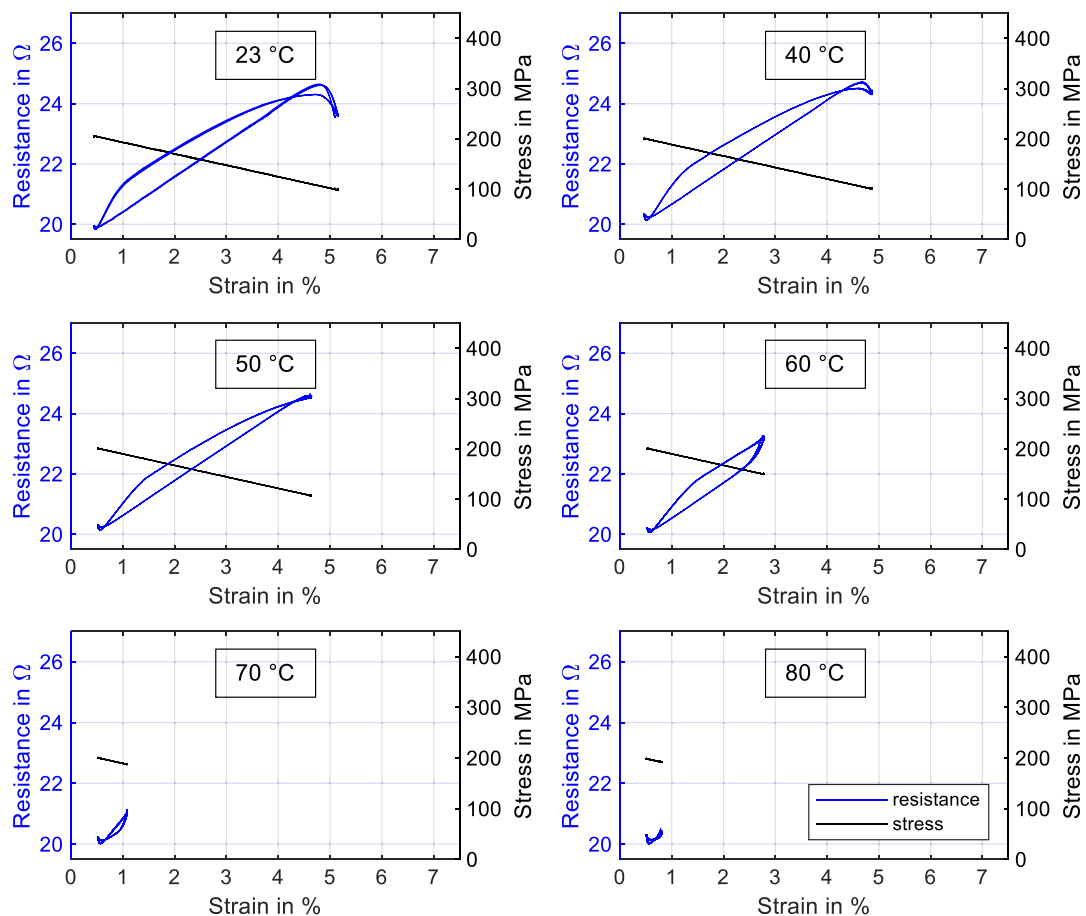


Figure 4. Data of Joule heated actuation experiments with a “Dynalloy Flexinol” NiTi wire of 72 μm diameter under a spring load ranging from 100 MPa (at 23 °C) to 200 MPa at varying ambient temperatures. Displayed are stress and resistance over strain for each temperature.

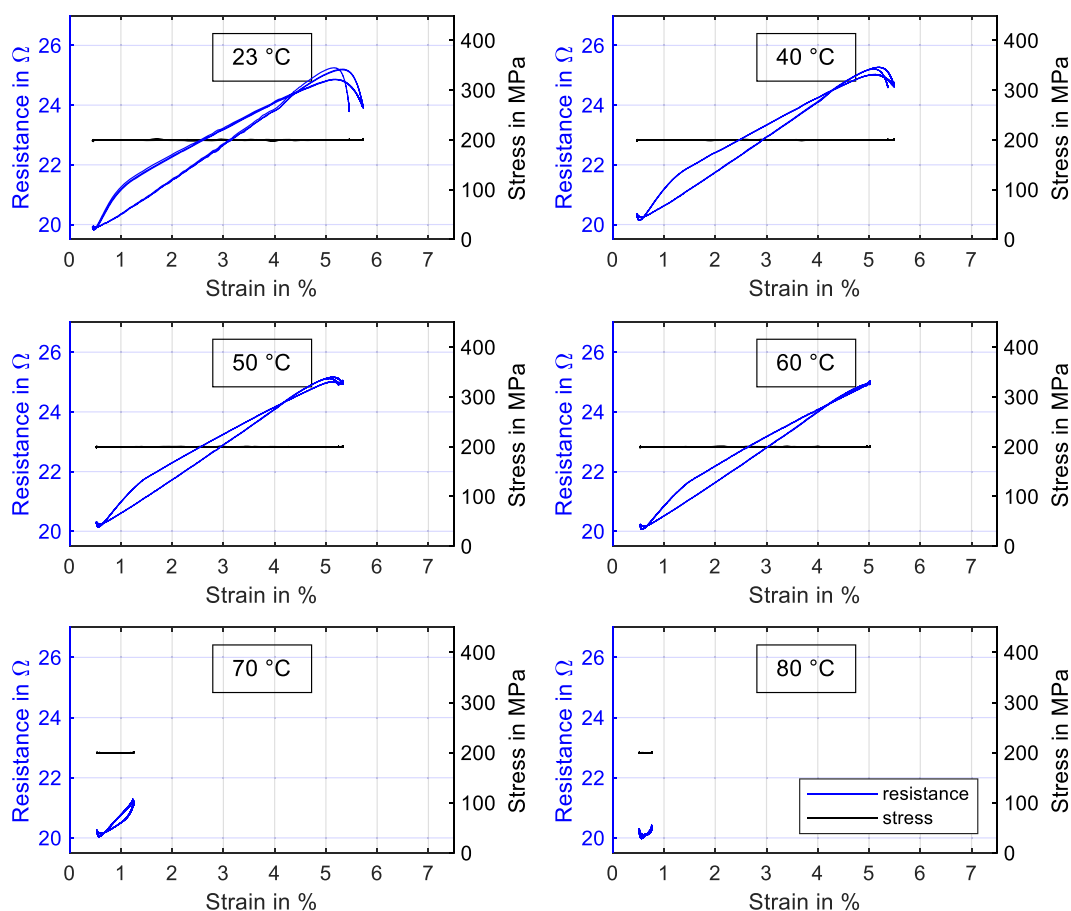


Figure 5. Data of Joule heated actuation experiments with a “Dynalloy Flexinol” NiTi wire of 72 μm diameter under a constant load of 200 MPa at varying ambient temperatures. Displayed are stress and resistance over strain for each temperature.

are formed due to the incomplete retransformation to martensite.

The experimental data of actuator tests with 200 MPa of constant stress are displayed in **Figure 5**. The temperatures of the experiments range from 23 to 80 °C.

Constant loads are less relevant for most technical applications but nonetheless important to understand the influence of the load profile on transformation temperatures. Because of it corresponding to a spring stiffness of zero, the ability to interpolate between the two presented experimental data sets is constituted.

Compared to the spring load, where 200 MPa of stress are applied at full contraction of the actuator only, the material stress is constantly high at all strains and not depending on the wire strain. This leads to increased transformation temperatures of the NiTi, which is most pronounced when looking at the 60 °C results where the stroke ranges at 4.5%. That is a decrease of only 0.8% in relation to the maximum stroke at 23 °C. Compared to that, the low-stress spring load exhibits a stroke of only 2.2% at 60 °C. The stroke then drops more suddenly upon increasing the temperature than with the spring load and ends up at 0.3% at 80 °C. As expected, that is the same value as generated by the spring load with maximum 200 MPa. The resistance hysteresis is, also with the increased overall stress, well

pronounced and inner loops are observed with increasing temperature. The width of the hysteresis depends on the material stress, as increased stresses suppress the R-phase. Therefore the width is similar where the stress level of the two experiments is almost equal. At higher strains, the hysteresis of the constant load is reduced compared to the spring load due to the larger stress difference.

Under spring loads, the changing stress influences the transformation temperatures of the material. This leads to a less discrete temperature where the crystal lattice changes configuration. In a strain–temperature diagram, like displayed in **Figure 1**, this results in less vertical and more angled transformation areas. Due to the constant stress in the data displayed in **Figure 5**, the material’s transformation temperatures are discrete. A rather sudden and more defined drop in actuation strain after exceeding 60 °C is therefore evident.

Combined with the larger overall stroke of the 200 MPa experiment, several lessons can be learnt for SMA-driven applications. When focusing on high stroke outputs and increased operational temperatures, a higher stress leads to larger stroke outputs and better functionality at high ambient temperatures. Accordingly, a spring with low stiffness and high pretension, resembling a constant load, is to be preferred as a biasing mechanism for better functionality at elevated ambient temperatures.

3.2. Results of the Thermally Trained Wire Sample Under Low Stress

The wire sample used in this and the following subsection is thermally trained with 100 cycles under a constant load of 400 MPa, by Joule heating the NiTi wire repeatedly. This procedure and the results are discussed in detail in “Part 1.”^[1] The goal is to create mechanical stability at increased actuation stresses, benefiting in higher force outputs and increased range of operational temperature of an SMA actuator wire. The training furthermore leads to a shift in working point as well as a reduced maximum stroke of the actuator, apparent when comparing the stress–strain curve in **Figure 6** to the same of **Figure 4**. Also, it is indicated that the resistance hysteresis is reduced by the treatment. The electrical power versus strain diagrams of “Part 1,” which can be compared to temperature–strain diagrams, suggest that the slope between A_s/A_f and M_s/M_f is less steep, and the phase transformation is spread over a wider range of temperature.^[1] The results of the low-stress spring load actuation experiments under increased ambient temperatures are displayed in **Figure 6**. Except for the additional training of the SMA wire, the experimental parameters are identical to those in **Section 3.1**.

It is observed that the width of the resistance hysteresis is smaller than of the untrained wire. The maximum martensitic length (23 °C) is shifted to 6.1% and the largest stroke is reduced to 4%. These are the accompanying effects of the thermal training, as they are mentioned previously. A significant decrease in stroke when reaching temperatures over 50 °C is evident but less pronounced than with the untreated wire. At 70 °C a stroke of 1.4% is still available and 0.7% are maintained at 80 °C. That means, that although the stroke at low temperatures is reduced due to the training, the effect is turned upside down at higher ambient temperatures, indicating that the goal of the training is met. Therefore, the actuator wire is better suited for high-temperature applications after undergoing thermal training. Additionally, the quality of the sensor signal is improved, due to the smaller resistance hysteresis.

The results for the experiments with 200 MPa of constant stress, similar to **Section 3.1**, are presented in **Figure 7**. Due to the higher material stress over the larger part of the strain curve, the resistance hysteresis is reduced further, compared to the low-stress spring results.

Most importantly to observe is that, due to the training, the stroke at 70 °C lies at 2.3%. This is contrasted by the as-delivered wire (**Figure 5**), where less than 1% of stroke is remaining.

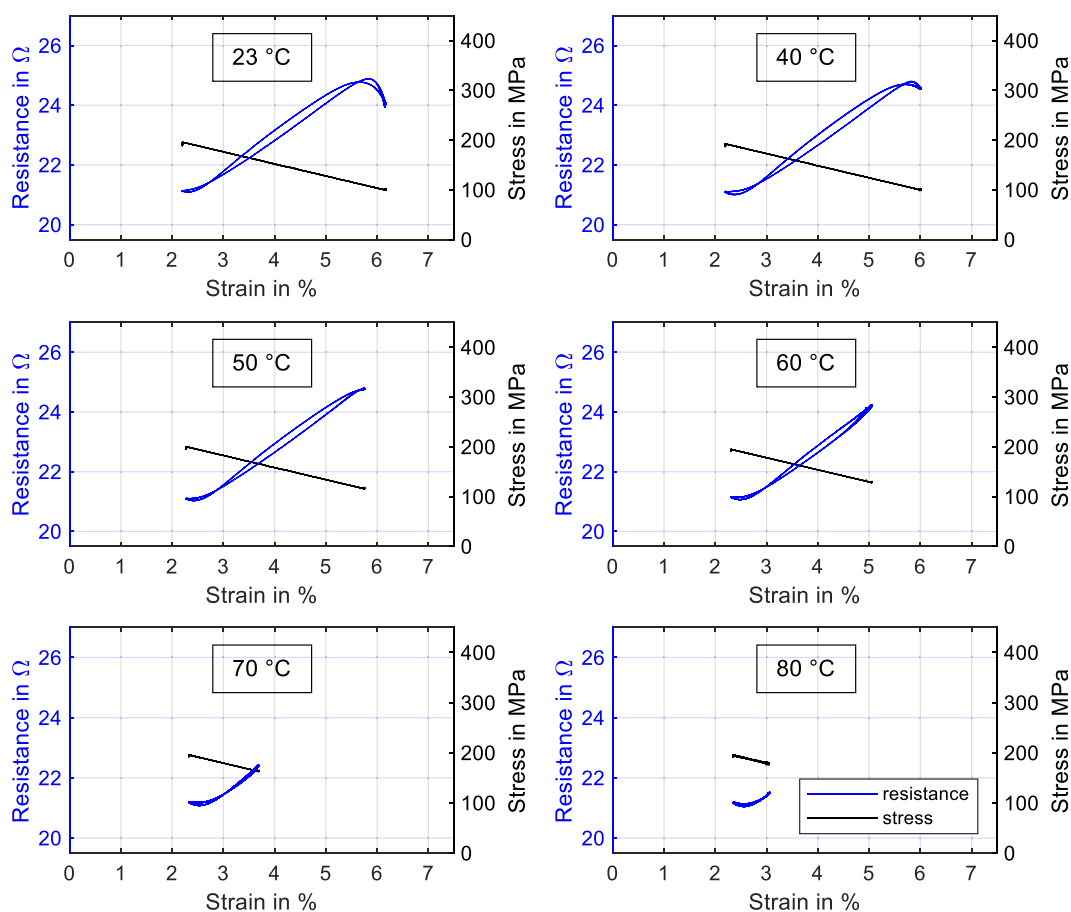


Figure 6. Data of Joule-heated actuation experiments with a “Dynalloy Flexinol” NiTi wire of 72 μm diameter with additional thermal training. It is biased with a spring load ranging from 100 MPa (at 23 °C) to 200 MPa. The experiments are run at varying ambient temperatures. Displayed for each temperature are stress and resistance over strain.

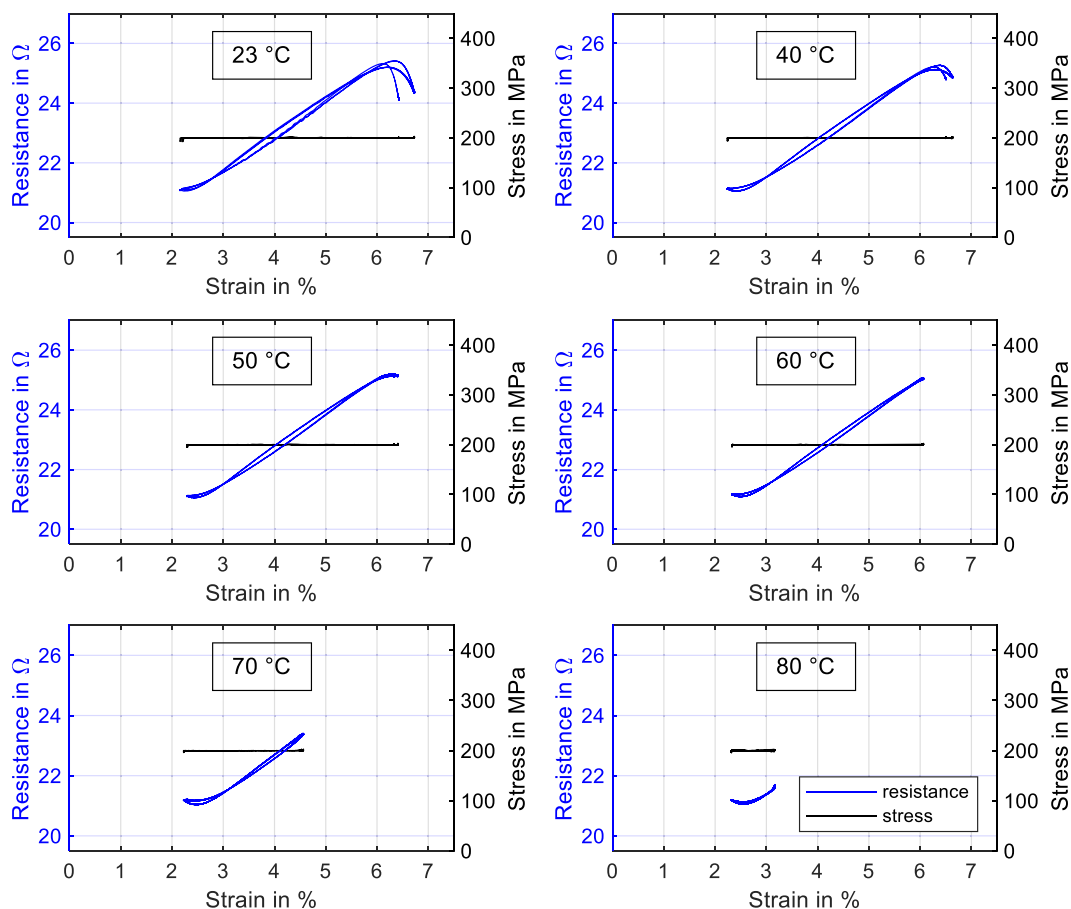


Figure 7. Data of Joule-heated actuation experiments with a “Dynalloy Flexinol” NiTi wire of 72 μm diameter with additional thermal training. It is biased with a constant load of 200 MPa. The experiments are run at varying ambient temperatures. Displayed for each temperature are stress and resistance over strain.

A stroke of over 2% is well utilizable for most application designs and comes with a good fatigue life. However, the threshold of operational temperature where the stroke decreases to slightly under 1% is still under 80 °C.

At this point a first conclusion for low stress actuation at high ambient temperatures can be drawn: The required operational temperatures are an important parameter when designing SMA-driven applications. The results of the discussed experiment for low stresses show that, depending on the stress level and profile, SMA wires in untreated condition feature stroke outputs of 4% and above up to ambient temperatures of 50 to 60 °C. These findings are graphically illustrated in **Figure 8**. It is observed, that under spring load, the phase transformation spreads over a wider range of temperature than the constant load.

Compared to the as-delivered samples, the thermally trained SMA wire exhibits a reduced stroke at low temperatures. At a threshold of about 60 °C, however, the beneficial outcomes of the training become evident. As displayed in **Figure 8**, the stroke of the trained wire drops less suddenly and a higher stroke at ambient temperatures above about 60 °C is the consequence.

As to be expected due to the Clausius–Clapeyron ratio, a higher stress increases the range of operational temperature. When comparing the spring load to the constant load in

Figure 8, the importance of the load profile of the SMA biasing system becomes clear. For applications, a spring with high prestress and low stiffness is to be preferred, for reaching high operational temperatures of the actuator system.

The relation of strain to resistance is not shifted by changing ambient temperatures. This indicates a good robustness of the self-sensing against altering ambient conditions.

3.3. Results of the Thermally Trained Wire Sample Under High Stress

Due to the instability of the as-delivered NiTi wire above 200 MPa of material stress, the experiments with 400 MPa and a spring load resulting in 200–400 MPa are only performed with thermally trained wire samples. The results of stress and resistance over strain for the spring load are displayed in **Figure 9**. The maximum ambient temperature for the experiments is increased to 90 °C due to the higher material stress.

The maximum stroke at 23 °C amounts to 4.2%. Up to 70 °C, the stroke output is slightly higher compared to the 200 MPa constant stress experiment, but the difference is not distinctly pronounced. This is caused by the stress increasing only slightly to about 240 MPa at 70 °C.

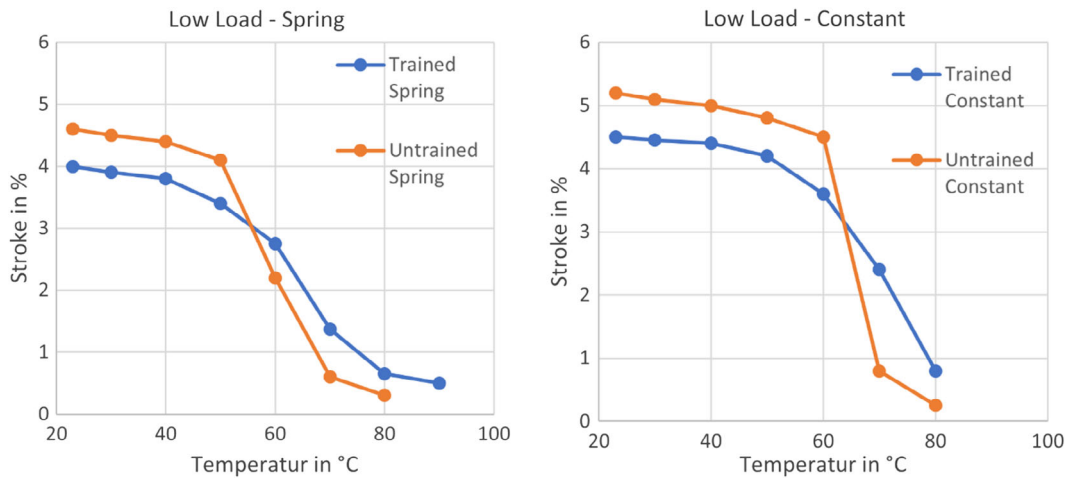


Figure 8. Diagrams of the evolution of the actuation stroke of a 72 μm NiTi wire under increasing ambient temperature. A comparison between the as-delivered wire (orange) and the thermally trained wire sample (blue) is displayed. Left: spring load with maximum 200 and 100 MPa at 23 $^{\circ}\text{C}$; right: constant load of 200 MPa.

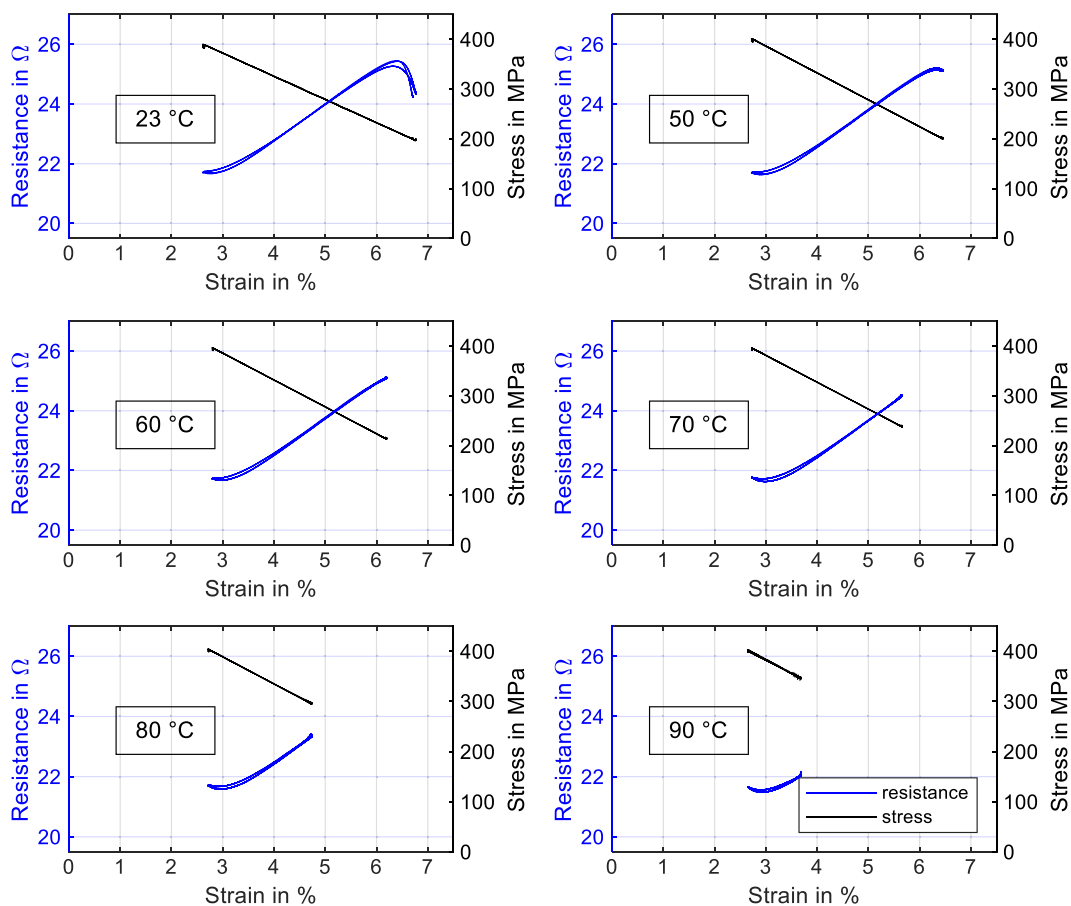


Figure 9. Data of Joule-heated actuation experiments with a “Dynalloy Flexinol” NiTi wire of 72 μm diameter with additional thermal training. It is biased with a spring load ranging from 200 MPa (at 23 $^{\circ}\text{C}$) to 400 MPa. The experiments are run at varying ambient temperatures. Displayed for each temperature are stress and resistance over strain.

The impact of the higher stress on the resistance hysteresis is however significant. It is reduced to a minimum, resulting from the combination of the training effect and the high stresses suppressing the formation of R-phase portions in the crystal lattice. This effect is independent from the ambient conditions, so that no significant hysteresis is observed in these experiments also at high temperatures.

At 70 °C, an actuator stroke of 2.9% is evident, reducing to 2% at 80 °C. At 90 °C, a strain difference of 1% is measured. Starting at a value of 70 °C, the difference to the 200 MPa constant stress experiment is well pronounced, as the spring rate leads to increasing stress.

From an application perspective it can be derived, that if 2% of strain is set as a minimum requirement for actuator applications, an SMA system with the here-presented parameters can be operated up to 80 °C ambient temperature.

Looking to assess the limits of operational temperatures of SMA wires, the highest overall stress investigated in this research is discussed in the following sections. The resulting data for various ambient temperatures of the actuation experiments with 400 MPa of constant load are presented in **Figure 10**. With such a high stress and the preceding training, it is possible to obtain a working actuator system generating over 2% of stroke at 90 °C.

With a maximum stroke of 4.9% at 23 °C, an increase in ambient temperature to 70 °C results in a loss of only 0.5% of stroke, while 4% of stroke can be utilized at 80 °C.

Compared to the data of the high-stress spring load, displayed in **Figure 9**, the hysteresis in the resistance curve increases slightly due to the higher stress in the beginning of the contraction. A small intersecting loop, with a crossing point in roughly half of the stroke, is observed. This can be explained by the increased influence of temperature, elevating the resistance before the A_s at 400 MPa is reached. The observation underlines the importance of the load profile when targeting a linear and well-interpretable self-sensing signal for a system design.

As expected, the highest load of this investigation exhibits the highest range of operational temperatures. To compare the spring load to the high constant load, the evolution of stroke output over the ambient temperature is shown in **Figure 11**. As shown, the higher overall load results in a larger stroke over the full temperature span. A decisive benefit of the 400 MPa of strain is evident at 80 °C ambient temperature, as the stroke of the spring load amounts to 2%, while the constant load leads to 4% of strain. As already mentioned in the introduction, 80 °C is a crucial value when it comes to applications in the automotive industry for example.

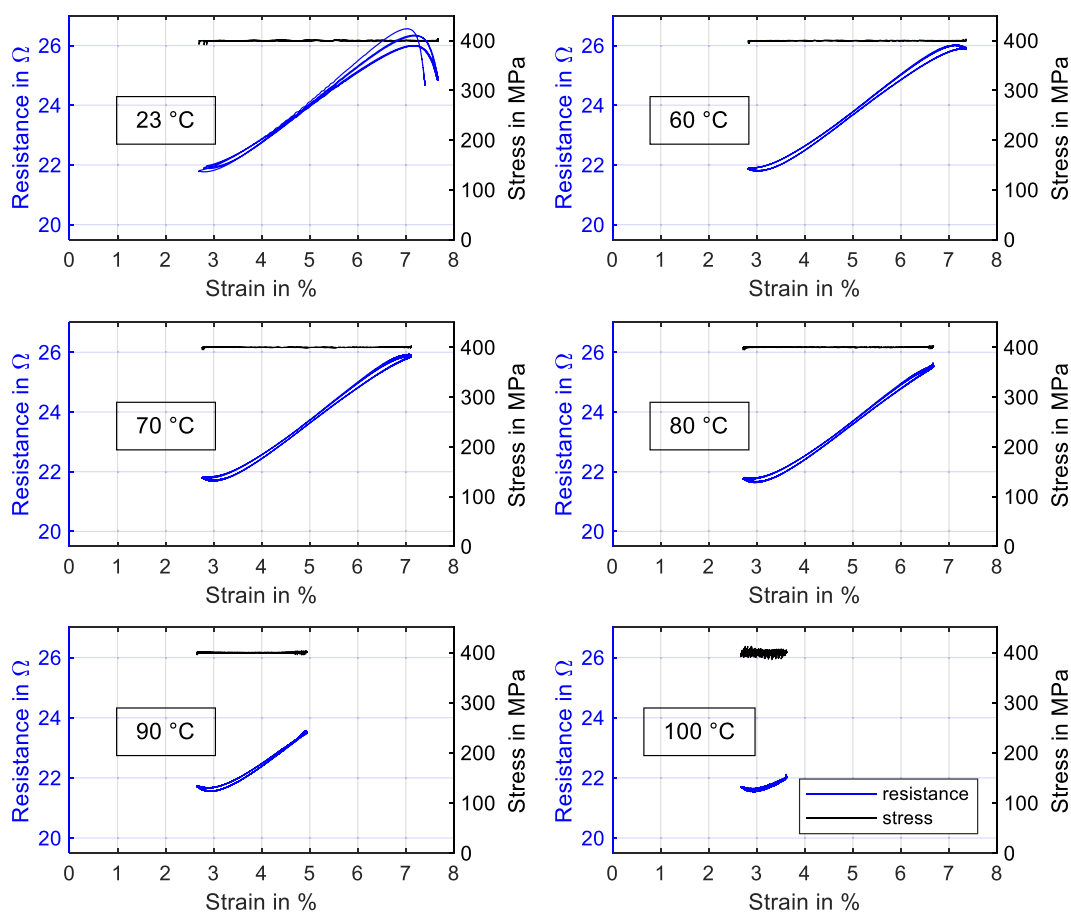


Figure 10. Data of Joule-heated actuation experiments with a “Dynalloy Flexinol” NiTi wire of 72 μm diameter with additional thermal training. It is biased with a constant load of 400 MPa. The experiments are run at varying ambient temperatures. Displayed for each temperature are stress and resistance over strain.

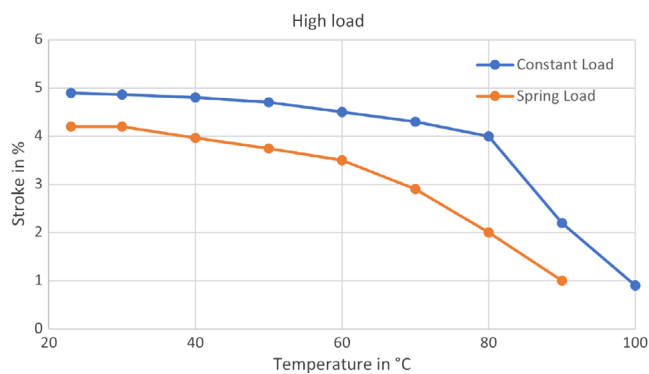


Figure 11. Diagram of the evolution of the actuation stroke of a thermally trained 72 μm NiTi wire under increasing ambient temperature. A comparison between the spring load ranging from 200 to 400 MPa (orange) and the constant load of 400 MPa (blue) is made.

When comparing the results of the high stress in Figure 11 to the evolution of stroke in the low-stress results in Figure 8, the increase in operational range, achieved by thermal training and increased material stress, is obviously recognizable. Although the untrained wire with 200 MPa of constant stress exhibits the largest stroke at room temperature, its performance drops sharply after reaching 60 °C. The 400 MPa constant stress experiments with the additionally trained SMA sample feature almost the same stroke at room temperature but can be run with 4% strain at up to 80 °C. Naturally, increased material stress, alongside with high strains, reduces the lifespan of SMA actuators. Wire stresses of 200 MPa and below are in the region of high-cycle-fatigue life in a Woehler diagram and cycle numbers over 1 million are common.^[4,33,34] With stress increased to 400 MPa and strains of 3%, only finite life fatigue is to be expected.^[33,34] The strain, on the other hand, also plays an important role in fatigue life of NiTi actuator wires.^[4,34] Reducing the wire strain to 1%, for example, and ensuring the stroke by using a longer SMA wire or utilizing transmissions can lead to better fatigue life also under high stresses for operation at increased ambient temperatures. For the application design this means that many parameters must be weighed up against each other to meet the requirements for the task at hand.

4. Application Design for Wide Temperature Range

To showcase the application relevance, the findings and results of the experimental investigation are transferred to an exemplary application concept design. This emphasizes the focus of the research and its relevance for the implementation of SMA-driven systems. As the multifunctional test rig can be used to test SMA microwires against arbitrary loads, the actuator design is tested and validated without having to manufacture a prototype. This makes the evaluation of the SMA system design very fast, as detailed mechanical design and construction are not needed at this early state of a concept phase. The measurements for actuator performance and for the suitability of the resistance signal are precise and meaningful as they are not disturbed by potential problems in the mechanical design of a prototype. As an

exemplary application, we choose a small, normally closed valve, with a simple design of an SMA wire working against a bias spring. Valves are a common application for SMA actuators, their detailed design is discussed widely in literature and a variety is already commercially available.^[35–37] Britz et al. presented a working prototype of a high-temperature SMA valve.^[14]

Under standard conditions, the conceptualized valve works at room temperature, and the pressure p does not exceed 1000 hPa. Under these conditions, the closing time of the valve is to be less than 1 s. Due to the restricted installation space and the necessary stroke of the valve tappet, the required SMA stroke amounts to 3%. The small and lightweight valve has an expected lifetime of 10,000 cycles, which is in the area of finite life fatigue of NiTi at elevated stresses.^[33,34,38,39] Although the data of SMA wire manufacturers suggest higher cycle numbers and are supported by first results with high-stress fatigue of SMA actuators, the actuator service life needs to be evaluated in detail inside the actual application.^[34,38] The main features of the valve, which are normally closed with SMA opening stroke of 3%, need to stay intact at ambient temperatures of up to 60 °C. At that temperature, the maximum pressure p , against which the valve tappet is required to remain closed, is 250 hPa. For reliable functioning, also after unpredictable events created by environmental influences, a safety factor needs to be taken into account.

A sketch of the valve design is displayed in Figure 12. With this sketch, the general functionality of the actuator design in the exemplary application is displayed. The normally closed state is enabled by a spring sitting on the valve tappet, which is biasing the SMA wire as well. The movement of the valve tappet is on one end restricted by the valve seat and on the other side by an end stop. The pressurized circular area of the valve tappet has a diameter of 1 mm. Applying the Equation (1) and (2), it becomes evident that the spring force to hold the valve closed against the pressure p corresponds to 200 MPa of material stress of a

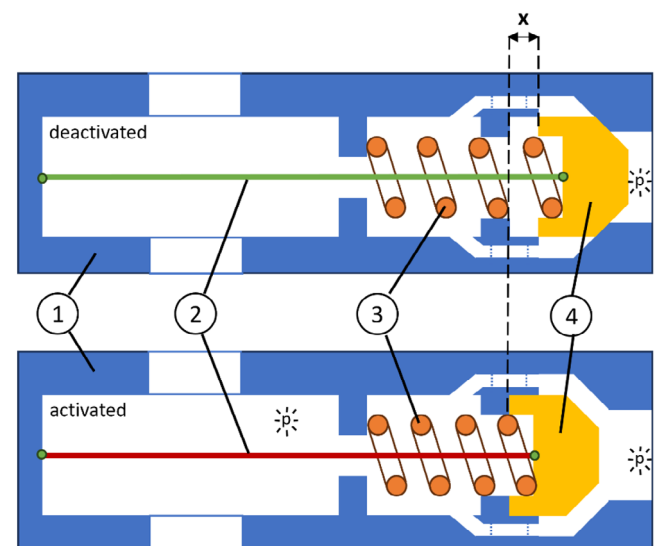


Figure 12. Sketch of the SMA-driven valve in deactivated (upper) and activated (bottom) state. The stroke x between the end stops is marked. The main parts of the design are as follows: 1: valve body; 2: SMA wire; 3: compression spring; 4: valve tappet.

72 μm wire. As by opening the valve, the wire stress increases to over 200 MPa, a thermally trained NiTi wire, as introduced in this study, is used. For reasons of consistency, the already investigated bias spring system ranging from 200 to 400 MPa is utilized. For the actuator test, the two endstops of the design shown in Figure 12 are added at a strain of 6% and 3% to the load profile, resulting in a valve stroke x of 3%. Due to this measure, a constant opening stroke is ensured over a wide temperature range. Design alterations to the valve to manage the flow of fluids, for example, do not influence the working principle of the SMA. However, the dynamics of the SMA wire inside the application are influenced by some additional factors. The forced convection and temperature of the medium, when in contact to the wire, as well as friction of the valve tappet, can play an important role for example.

The start of transformation reduces the load on the end stop (valve seat), as shown in Figure 13, but the valve does not open, due to the high prestress of the spring. Even at a temperature of 60 °C a delta in wire stress ΔF of 50 MPa is resting on the valve seat, as displayed in Figure 13 on the right. That corresponds to a force, high enough to hold the valve closed at 250 hPa of pressure p . With the endstop being positioned at 3% of strain (see Figure 13), the full stroke potential of the SMA wire is not used on purpose. If overloads due to friction or wear result in additional residual strain, the actuator system does not fail immediately thanks to that buffer zone.

The dynamics of the SMA wire will be naturally reduced by the increased ambient temperature. Although the activation time is unaffected and could happen in milliseconds, the convective heat transfer to the surrounding air is slower due to the smaller temperature difference. This can be counteracted by active cooling of the SMA wire, submerging the wire in a liquid or choosing an alloy with a higher M_f .^[40]

To not electrically overheat the SMA wire in the open position end-stop and take the changing ambient temperatures into account, a feedback control for the Joule heating is needed in such an application. As a feedback, the resistance value of the SMA wire is suitable. In the here-proposed application design, the resistance changes by about 3 Ω between the maximum values. Choosing a fitting algorithm, the end-stops can be detected via the inconsistencies in the evolution of the resistance signal. These inconsistencies are observable in the resistance–strain data of Figure 13 at 3% and 6%, where the endstops are reached.

5. Conclusion and Outlook

In the presented work, the characteristics of Joule-heated SMA microwires at elevated ambient temperatures are investigated. The focus lies on the intricate influence of varying actuator loads combined with additional training on the stroke output and resistance signal. As the second part of a coherent work, the findings from the previous article are developed further and are supplemented.

Various experiments on the as-delivered NiTi wire as well as the thermally trained wire with spring loads and constant loads, each with a low and high stress level, are discussed. The temperature range lies between room temperature and 100 °C. The resulting data implies that increasing the material stress of the SMA actuator from a usual range of 100–200 to 400 MPa raises the operational temperature range about 30 °C. This magnitude is to be expected due to the Clausius–Clapeyron ratio of the material. The additional thermal training, necessary to generate a stable characteristic at elevated material stress, also influences the phase transformation temperature, as existing research also suggests. This reflects on the utilizable stroke at high ambient temperatures as well. Even with low material stresses, the actuator characteristics at 60 °C and above are improved by the measure. However, it is observed that there is a complex relation between training and wire stress, which does not necessarily lead to improved actuator performance. For the examined training process and load parameters, this must be considered when the ambient temperature stays under 60 °C. For the design of actuator sensor systems it needs to be taken into account that the fatigue life of SMA actuators is reduced by increasing the wire stress.^[41,42] The hysteretic resistance signal also benefits from the training and from the higher actuation stress. The ambient temperature on the other hand does not influence or shift the resistance–strain characteristic. From this it can be concluded that the SMA's self-sensing feature is robust toward altering ambient conditions.

The results are used to conceive an exemplary SMA-driven application, that is then tested by HiL on the multifunctional test rig. A small, normally closed valve, actuated by a 72 μm NiTi wire, is designed. It features a stroke of 3%, working pressures of 250–1000 hPa, and an operational temperature range up to 60 °C.

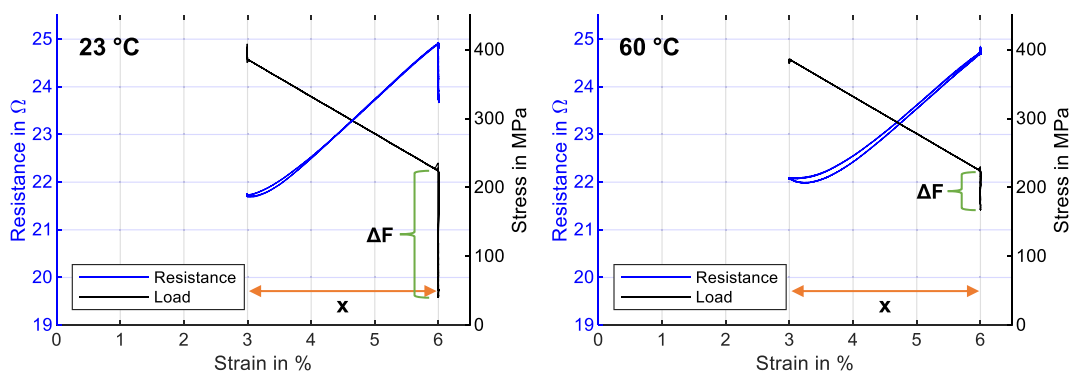


Figure 13. Actuator and sensor characteristics of the SMA wire for the application design. Two distinct operational temperatures are displayed: room temperature on the left and 60 °C on the right.

Next steps to be taken in this field of research are the examination of the dynamics of SMA actuators under high ambient temperatures. Therefore, different excitation waveforms like square waves are utilized for Joule heating to then being able to monitor the cooling time. Furthermore, the influence of other load profiles and stress levels is to be investigated, looking for a sweet spot in stroke utilization. As expected, the cooling time of the SMA increases at elevated ambient temperatures. This behavior can be counteracted by replacing the air surrounding the wire with oil or water.^[40] Currently research is being conducted on a specific application with fluid-submerged SMA actuator wires. The same is true for algorithms to compensate the resistance hysteresis and thus read distinct position values from the self-sensing data. Promising high-temperature SMA materials like NiTiHf show the ability to solve many of the issues that come with binary NiTi at high ambient temperatures in the future.^[43,44]

Acknowledgements

Open Access funding enabled and organized by Projekt DEAL.

Conflict of Interest

The authors declare no conflict of interest.

Data Availability Statement

The data that support the findings of this study are available from the corresponding author upon reasonable request.

Keywords

ambient conditions, hysteresis, limits, NiTi, resistances, self-sensing, two-way effects

Received: February 19, 2024

Revised: April 9, 2024

Published online:

- [1] D. Scholtes, S. Seelecke, P. Motzki, *Eng. Rep.* **2024**, e12867.
- [2] D. Scholtes, M. Schmidt, P. Linnebach, S. Seelecke, P. Motzki, *Materials* **2023**, *16*, 4820.
- [3] S. Degeratu, P. Rotaru, G. Manolea, H. O. Manolea, A. Rotaru, *J. Therm. Anal. Calorim.* **2009**, *97*, 695.
- [4] L. Fumagalli, F. Butera, A. Coda, *J. Mater. Eng. Perform.* **2009**, *18*, 691.
- [5] D. C. Lagoudas, in *Shape Memory Alloys*, vol. 1, Springer, Boston, MA **2008**.
- [6] D. A. Miller, D. C. Lagoudas, *Smart Mater. Struct.* **2000**, *9*, 640.
- [7] W. J. Buehler, F. E. Wang, *Ocean Eng.* **1968**, *1*, 105.
- [8] C. Velmurugan, V. Senthilkumar, S. Dinesh, D. Arulkirubakaran, *Mater. Today Proc.* **2018**, *5*, 14597.
- [9] N. Lewis, A. York, S. Seelecke, *Smart Mater. Struct.* **2013**, *22*, 094012.
- [10] C. H. Park, Y. S. Son, SMA spring-based artificial muscle actuated by hot and cool water using faucet-like valve," in *Active and Passive Smart Structures and Integrated Systems 2017*, SPIE **2017**, 10164T, <https://doi.org/10.1117/12.2257467>.
- [11] Actuator Solutions GmbH, <https://www.actuator-solutions.de/english/products/> (accessed: May 2023).
- [12] D. Scholtes, S. Seelecke, G. Rizzello, P. Motzki, in *ASME 2020 Conf. on Smart Materials, Adaptive Structures and Intelligent Systems, SMASIS 2020*, American Society of Mechanical Engineers Digital Collection **2020**.
- [13] A. Kazi, M. Honold, W. Rimkus, T. Lokner, M. Bäuml, M. Köpfer, in *ACTUATOR 2018 - 16th Int. Conf. and Exhibition on New Actuators and Drive Systems*, VDE, Bremen **2018**, pp. 375–378.
- [14] R. Britz, G. Rizzello, P. Motzki, *Adv. Eng. Mater.* **2022**, *24*, 2200205.
- [15] J. J. Zhang, Y. H. Yin, J. Y. Zhu, *Sensors* **2013**, *13*, 12958.
- [16] V. Antonucci, G. Faiella, M. Giordano, F. Mennella, L. Nicolais, *Thermochim. Acta* **2007**, *462*, 64.
- [17] A. Takimoto, *J. Phys. IV* **1995**, *05*, C8.
- [18] C. B. Churchill, J. A. Shaw, M. A. Iadicola, *Exp. Tech.* **2009**, *33*, 51.
- [19] J. A. Shaw, C. B. Churchill, M. A. Iadicola, *Exp. Tech.* **2008**, *32*, 55.
- [20] C. B. Churchill, J. A. Shaw, M. A. Iadicola, *Exp. Tech.* **2010**, *34*, 63.
- [21] F. Gori, D. Carnevale, A. Doro Altan, S. Nicosia, E. Pennestri, *Int. J. Thermophys.* **2006**, *27*, 866.
- [22] C. B. Churchill, J. A. Shaw, *Behav. Mech. Multifunct. Compos. Mater.* **2008**, 6929, 69291F.
- [23] C. B. Churchill, J. A. Shaw, in *Proc. ASME Conf. Smart Mater. Adapt. Struct. Intell. Syst. 2009, SMASIS2009, Oxnard 2009*, pp. 137–148.
- [24] S. J. Furst, J. H. Crews, S. Seelecke, *J. Intell. Mater. Syst. Struct.* **2013**, *24*, 1951.
- [25] P. E. Thoma, A. M. Blok, M.-Y. Kao, *MRS Proc.* **1991**, *246*, 321.
- [26] D. A. Hebda, S. R. White, *Smart Mater. Struct.* **1995**, *4*, 298.
- [27] K. C. Atli, I. Karaman, R. D. Noebe, D. Gaydosh, *Mater. Sci. Eng. A* **2013**, *560*, 653.
- [28] W. Kim, B. M. Barnes, J. E. Luntz, D. E. Brei, *J. Mech. Des.* **2011**, *133*, 111010.
- [29] S. H. Song, J. Y. Lee, H. Rodrigue, I. S. Choi, Y. J. Kang, S. H. Ahn, *Sci. Rep.* **2016**, *6*, 21118.
- [30] Cambridge Mechatronics – Actuators, <https://www.cambridge-mechatronics.com/en/cml-technology/actuators/> (accessed: August 2023).
- [31] S. M. Kirsch, F. Welsch, D. Bevilacqua, D. Naso, S. Seelecke, G. Rizzello, P. Motzki, in *SMASIS 2020 - Conf. on Smart Materials, Adaptive Structures and Intelligent Systems 2020*.
- [32] Dynalloy, <http://www.dynalloy.com/pdfs/TCF1140.pdf> (accessed: March 2019).
- [33] G. Scirè Mammano, E. Dragoni, *Int. J. Fatigue* **2014**, *69*, 71.
- [34] SAES Group, <https://www.saesgetters.com/sites/default/files/SMARTFLEXSPRINGSANDWIRES.pdf> (accessed: July 2018).
- [35] A. Czechowicz, S. Langbein, in *Shape Memory Alloy Valves: Basics, Potentials, Design*. Cham: Springer International Publishing, **2015**, <https://doi.org/10.1007/978-3-319-19081-5>.
- [36] M. Tiboni, A. Borboni, M. Mor, D. Pomi, *Proc. Inst. Mech. Eng.* **2011**, *225*, 443.
- [37] S. Nalbach, P. Motzki, S. Seelecke, in *ASME 2015 Conf. Smart Mater. Adapt. Struct. Intell. Syst. SMASIS 2015, Colorado Springs 2016*.
- [38] J. Mayer, P. Molitor, Y. Goergen, P. Motzki, in *Proc. ASME 2022 Conf. Smart Mater. Adapt. Struct. Intell. Syst. SMASIS 2022, Dearborn 2022*.
- [39] G. Scire Mammano, E. Dragoni, *Proc. Eng.* **2011**, *10*, 3692.
- [40] A. Pathak, D. Brei, J. Luntz, *Smart Mater. Struct.* **2010**, *19*, 035005.
- [41] G. Eggeler, E. Hornbogen, A. Yawny, A. Heckmann, M. Wagner, *Mater. Sci. Eng. A* **2004**, *378*, 24.
- [42] D. C. Lagoudas, D. A. Miller, L. Rong, P. K. Kumar, *Smart Mater. Struct.* **2009**, *18*, 085021.
- [43] F. Gantz, M. T. Wall, M. L. Young, D. J. Forbes, *Shape Memory Superelasticity* **2022**, *8*, 439.
- [44] E. Benafan, G. S. Bigelow, A. Garg, L. G. Wilson, R. B. Rogers, E. J. Young-Dohe, D. F. Johnson, D. A. Scheiman, J. W. Lawson, Z. Wu, *Shape Memory Superelasticity* **2024**, *10*, 55.

2.5 Dissimilar Resistance Welding of NiTi Microwires for High Performance SMA Bundle Actuators

Dominik Scholtes ^{1,2}, Ralf-Kilian Zäh ¹, Benedikt Faupel ³, Stefan Seelecke ^{1,2},
Paul Motzki ^{1,2}

¹ Lehrstuhl für Intelligente Materialsysteme, Zentrum für Mechatronik und
Automatisierungstechnik, ZeMA gGmbH, Saarbrücken

² Lehrstuhl für Intelligente Materialsysteme, Fachrichtung Systems Engineering, Fachrichtung
Materialwissenschaft und Werkstofftechnik, Universität des Saarlandes, Saarbrücken

³ Hochschule für Technik und Wirtschaft des Saarlandes (HTW), Saarbrücken

Veröffentlicht in MDPI Actuators.

DOI: 10.3390/act13100400

© 2024 by the authors.



Dieser Artikel wird lizenziert werden unter Creative Commons Namensnennung 4.0
International (Creative Commons Attribution 4.0 International, CC BY 4.0).

Article

Dissimilar Resistance Welding of NiTi Microwires for High-Performance SMA Bundle Actuators

Dominik Scholtes ^{1,2,*} , Ralf-Kilian Zäh ¹, Benedikt Faupel ³, Stefan Seelecke ^{1,2} and Paul Motzki ^{1,2,*} 

- ¹ Intelligent Material Systems Lab, Center for Mechatronics and Automation Technologies—ZeMA gGmbH, 66121 Saarbruecken, Germany
- ² Intelligent Material Systems Lab, Department of Systems Engineering, Department of Material Science and Engineering, Saarland University, 66121 Saarbruecken, Germany
- ³ School of Engineering, University of Applied Sciences Saarbruecken (HTW), 66117 Saarbruecken, Germany
- * Correspondence: dominik.scholtes@uni-saarland.de (D.S.); paul.motzki@uni-saarland.de (P.M.); Tel.: +49-681-302-71360 (D.S.)

Abstract: Shape memory alloys (SMAs) are becoming a more important factor in actuation technology. Due to their unique features, they have the potential to save weight and installation space as well as reduce energy consumption. The system integration of the generally small-diameter NiTi wires is an important cornerstone for the emerging technology. Crimping, a common method for the mechanical and electrical connection of SMA wires, has several drawbacks when it comes to miniaturization and high-force outputs. For high-force applications, for example, multiple SMA wires in parallel are needed to keep actuation frequencies high while scaling up the actuation force. To meet these challenges, the proposed study deals with the development of a resistance-welding process for manufacturing NiTi wire bundles. The wires are welded to a sheet metal substrate, resulting in promising functional properties and high joint strengths. The welding process benefits from low costs, easy-to-control parameters and good automation potential. A method for evaluating the resistance-welding process parameters is presented. With these parameters in place, a manufacturing process for bundled wire actuators is discussed and implemented. The welded joints are examined by peel tests, microscopy and fatigue experiments. The performance of the manufactured bundle actuators is demonstrated by comparison to a single wire with the same accumulated cross-sectional area.



Citation: Scholtes, D.; Zäh, R.-K.; Faupel, B.; Seelecke, S.; Motzki, P. Dissimilar Resistance Welding of NiTi Microwires for High-Performance SMA Bundle Actuators. *Actuators* **2024**, *13*, 400. <https://doi.org/10.3390/act13100400>

Academic Editor: Wei Min Huang

Received: 5 August 2024

Revised: 13 September 2024

Accepted: 25 September 2024

Published: 5 October 2024



Copyright: © 2024 by the authors. Licensee MDPI, Basel, Switzerland. This article is an open access article distributed under the terms and conditions of the Creative Commons Attribution (CC BY) license (<https://creativecommons.org/licenses/by/4.0/>).

Keywords: actuator; joining; sensor; shape memory alloy; welding

1. Introduction

Shape memory alloys (SMAs) have many beneficial attributes, especially in the form of thin wires made of nickel–titanium (NiTi). Among those are a high energy density, a high actuation frequency, a self-sensing capability and a unique form factor [1–4]. On the other hand, there are applications that would benefit from SMA technology, with reduced weight and smaller installation space, but requirements like high forces combined with short cycle times cannot be met by usual designs of SMA actuators. As the force scales with the cross-sectional area of the SMA wire, the thermal effects of the volume to surface ratio result in long cooling periods.

Efficient product design requires a small number of parts and simple assembly processes. Of course, this is also true for SMA actuators. The state of the art joining technology for SMA wires is crimping. The crimp itself is an additional part, which needs to be clamped on the wire. Compared to an SMA microwire, the crimp is heavy and large, and it needs to be accessible from at least two sides for assembly. Additionally, high forces are needed to fix the crimp.

For both issues with SMA wire technology there are solutions available. High forces combined with high dynamics are achieved by bundling many small-diameter SMA wires in parallel so that their force output adds up but the volume to surface ratio is

consistent [3,5,6]. The difficult crimping process, on the other hand, can be replaced by substance-to-substance bonds like glueing, soldering or welding, where the latter shows most promising results.

The SMA phenomenon in NiTi alloys was discovered in the 1960s, and a lot of research has been conducted on the topic since then [7,8]. Today, NiTi is still the commercially most successful SMA material. Depending on the alloy composition, it behaves either as superelastic or quasiplastic at room temperature. The superelastic alloys are by far the most common and are widely used for medical applications like stents, guidewires, braces and other devices [9]. They can fully recover strains up to 7% [10,11]. Rather new developments based on superelastic alloys are the so-called elastocalorics, where superelastic SMAs are used as solid-state heat pumps [12–15], and SMA-based stretchable electronics with auxetic structures [16,17]. The titanium-rich, quasiplastic variant of NiTi can be plastically deformed at room temperature by applying a load. When subsequently heated above the phase transformation temperature, however, the deformation of about 5% is fully recovered in conjunction with high-force outputs. Both effects are based on a phase transformation of the crystal lattice structure between austenite (high-temperature phase) and martensite (low-temperature phase), while in superelastic alloys, the martensitic transformation is induced by stress and the transformation between austenite and martensite in actuator applications is thermally induced.

NiTi has a high electrical resistivity that changes significantly depending on the composition of the crystal lattice, the geometry, and the temperature. This effect, called self-sensing, is used to generate a position feedback signal of an SMA actuator by measuring its resistance during operation. SMA microwires (diameter smaller 100 μm) feature cooling times around one second and below under natural convection at air and room temperature; furthermore, their unique form factor allows them to be fitted in tight spatial conditions.

Welding of NiTi and similar alloys is an extensive field of research [18,19]. It is mostly concentrated on the similar and dissimilar laser welding of superelastic material for medical applications, where good results of joint strength and material properties are achieved. Laser welding has also been investigated for NiTi actuator wires down to diameters of 100 μm [20]. It has been shown that joints between NiTi and stainless steel as well as copper are feasible [21,22]. Welded joints of NiTi and stainless steel have been proven to show good mechanical properties. Other welding technologies like electron beam welding, friction stir welding, TIG welding, impact welding and resistance welding have also been investigated [23–25]. Published work on resistance welding, however, is not found in great numbers but suggests promising results for micro-dimensions [26–29]. The previous work of Scholtes et al. suggests that NiTi actuator wires with diameters between 100 μm and 25 μm can be welded to stainless steel sheet metal by spot welding, keeping 80 to 90% of the material's break load [30].

This research article discusses the dissimilar resistance spot welding of NiTi wires with 100 μm diameter from an engineering perspective. Most previous research on microwire welding focuses on superelastic alloys and joining two wires for medical applications or welding a single wire to a substrate. This work concentrates on joining NiTi actuator microwires to a suitable substrate for manufacturing a bundle actuator having high-force output and dynamics. The main targets are high joint break loads, good fatigue life and the development of an automatable and cost-efficient welding and bundling process. A detailed microstructural investigation of the samples is not part of this work. Welding parameters are evaluated by pull-off tests as well as peel tests. The welded samples also undergo an actuation fatigue test. The discussed welding process is faster, cheaper and more durable than the commonly used methods to join NiTi wires. Due to the easy-to-control parameters, the process is automatable, and wire bundles with small dimensions and few individual parts can be manufactured.

SMA wire bundles are investigated due to the need to achieve high actuation frequencies while also scaling up the force [3,31,32]. Bundling large-diameter wires enables high force outputs of several kilonewtons, which is otherwise only possible by using SMA

rods or bars [5,33]. These bundles are typically manufactured by clamping and wrapping, which usually comes with the disadvantages of many individual parts, relatively large clamp sizes and inconsistent electrical connections of the single wires. Welded bundles, however, need only two substrates for the wires to be joined to. If these are sheet metal parts, the bundles are very flat and feature an ideal installation space. However, they are not restricted to that formfactor, and SMA wire bundles based on a tubular or rectangular design are also possible. With these new bundles, systems with better performance, which means higher force output with fast cycle times, can be realized. The fields of applications for SMA actuators are broadened.

The rest of the article is split into three sections followed by a conclusion with an outlook. Section 2 covers the setup of the welding machine and the experimental methods to evaluate the welding parameters. In the first part of Section 3, the results of the parameter studies are discussed and complemented by actuation and fatigue tests. The second part of the section deals with the process of manufacturing welded SMA wire bundles and the evaluation of the same by actuation experiments.

2. Materials and Methods

Resistance spot welding is a process where electrical current and pressure are used to join two metallic alloys by melting them together at the point of contact, where a weld nugget is formed [34]. It is commonly used in the automotive industry to join metal sheets of a car body. Compared to laser welding, resistance welding is more cost efficient, and the process is easier to control.

In usual spot-welding applications, two opposing electrodes clamp the workpieces, which makes accessibility from two sides necessary. As it is beneficial from a manufacturing and assembly perspective to perform the joining process from only one side, this work is utilizing a gap-welding machine. As displayed in Figure 1, both electrodes are aligned with a small gap in between them. The lower work piece, in this case a piece of sheet metal, rests on a support, while the upper workpiece, the NiTi wire, is held in place by the pressure of either two electrodes (series or gap welding) or one electrode, while the second electrode contacts the sheet metal (step welding). By passing a current through the workpieces, their interface is heated to melting temperature by the Joule effect. After solidification, the pressure of the electrodes is released.

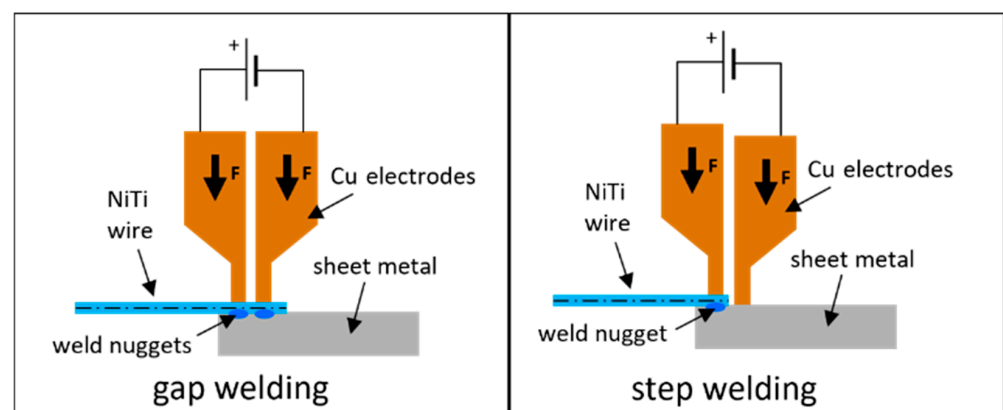


Figure 1. Schematic of resistance gap welding (left) and resistance step welding (right) of NiTi wires to a sheet of metal. Displayed are the two copper-based electrodes, pressing down on the work pieces.

The generated heat H is calculated by

$$H = I^2 * R * t * K \quad (1)$$

where I is the welding current, R is the overall resistance, t is the welding time and K is a thermal constant that depends on the geometry material and welding force. The

resistance is the sum of the individual resistances of the workpieces and the electrodes as well as the contact resistances between them. When studying Figure 2, it can be derived that the highest individual resistance is required at R4, the contact resistance between the weld partners.

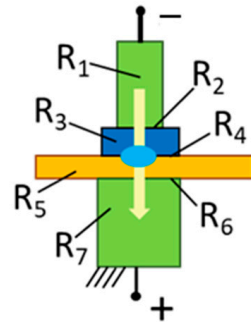


Figure 2. Schematic of the distribution of the overall resistance in a resistance welding process. R2 R4 and R6 are contact resistances. R1 and R7 are the bulk resistances of the electrodes. R3 and R5 are the bulk resistances of the weld partners.

The welding machine used in this work is a resistance gap welding head (Unitek, Thin-Line, Monrovia, CA, USA) with spring-loaded electrodes and adjustable force up to 100 N. The spring loading allows the weld head to follow the collapsing of the weldment when melting. The welding transformer Mac Gregor (Mildenhall, UK) DC 1000 supplies a current of up to 1000 A (DC) in a double pulse with adjustable durations of 1 ms to 100 ms and ramp up/down. For all experiments, electrodes made of CuCr1 with a tip area of 0.64 mm² are used.

The SMA wire used for the experiments is a commercially available SAES Getters (Milan, Italy) SmartFlex NiTi actuator wire with 100 µm diameter and a thin amber-colored oxide layer [35]. For the sheet metal substrate to which the wire is to be welded, a sample geometry of 5 mm × 10 mm with a 3 mm hole is designed. This allows for easy installation and fixation in the welding setup, the testing setups and in possible applications.

From an application perspective, copper and copper alloys are highly interesting as a welding partner for the NiTi wires, as the electrical wiring can be soldered with common methods. Furthermore, the next step with copper alloys could be a direct integration of SMA actuator wires onto PCBs for micro-actuators. However, difficulties with good welding results are expected, as relevant material parameters like electrical and thermal conductivity, displayed in Table 1, differ greatly between NiTi and Cu alloys [36]. While the resistivity of copper alloys is about tenfold smaller than that of NiTi and the thermal conductivity is the same amount larger, SS offers similar parameters compared to NiTi. Differences in those two parameters lead to an unfavorable shift in the resistance and heat distribution of the weld partners. Therefore, good weldability of NiTi to steel is expected. A feasibility study by Scholtes et al. confirms this assumption and presents promising results with SMA wire diameters down to 25 µm [30]. With special flux and solder (e.g., DIN EN 29453 (solder): S-Sn96Ag4 and DIN EN 29454.1, 3.2.2.A (F-SW11) (flux)), copper wires can also be joined to stainless steel with low process temperatures. This enables the integration of steel substrates to circuit boards and in general an easy electrical connection of the welded SMA actuators without using copper alloys as welding partners.

Table 1. Material parameters relevant for resistance welding of NiTi, stainless steel and copper alloys [37–40].

	NiTi	Steel	CuSn6	CuZn30
Resistivity (20 °C) in Ω·mm ² /m	0.86	0.75	0.11	0.06
Thermal conductivity (20 °C) in W/m·K	10	15	75	121

For investigating the resistance welding of NiTi to copper alloys, CuSn6 (DIN 2.1020) and CuZn30 (DIN 2.0265) are used. Alloying with zinc or tin increases the resistivity of copper and reduces the thermal conductivity. The samples have a thickness of 0.4 mm. With X6CrNiMoTi17-12-2 (DIN 1.4571) and X2CrNiMo17-12-2 (DIN 1.4404), two similar steel alloys are used in this study. They both feature particularly good weldability and corrosion resistance, while the 1.4571 is additionally alloyed with a small amount of titanium. The main difference for the experiments lies in the sample thickness (1 mm for 1.4571, 0.3 mm for 1.4404).

The welding procedure used in this work is displayed in Figure 3 in four steps. The sheet metal sample is positioned in the workpiece holder. The NiTi wire, guided through a small funnel, is placed on top of the welding partner. The weld head with two copper electrodes is moved down, pressing on the wire and sheet metal with 100 N, as is displayed in Figure 3(2). Then, the welding current is run through the weld partner, while the NiTi wire is slack. On close inspection of Figure 3(3), the red-hot metal between the tips of the electrodes is recognizable. After a short cooling time, the weld head is moved upwards, as is depicted on Figure 3(4), and the NiTi wire is joined to the steel sample.

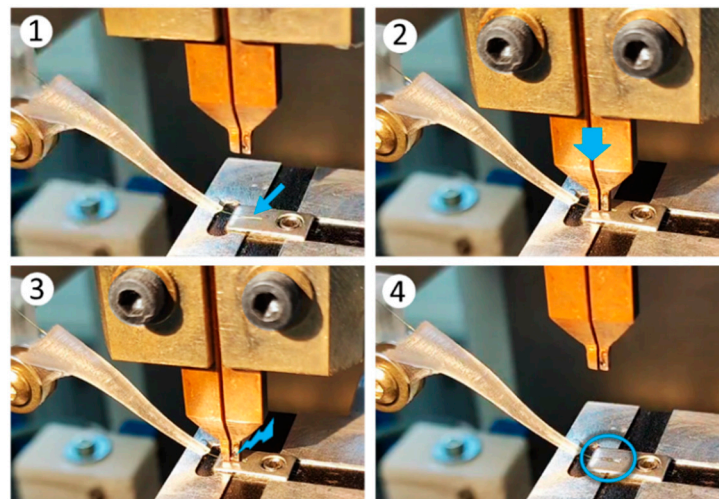


Figure 3. Step by step pictures of the resistance welding process: (1) placement of sheet metal sample and NiTi wire under weld head; (2) weld head moved down, applying pressure on SMA wire with both electrodes; (3) welding current is run through workpieces via copper electrodes; (4) weld head is moved up and NiTi wire is joined to steel substrate.

As stated in Equation (1), the influence of the welding current is squared, while the welding time has a linear effect on the generated heat. This work therefore focuses on the variation in the welding current, because it has the greatest influence on the results. The welding time is set to a constant value of two pulses with a 15 ms holding time and an additional 5 ms for ramping up and down. The delay between the pulses is set to 10 ms.

For evaluating the welded samples with pull-off tests, a custom-designed test bench (Figure 4) is used. It is mainly made to measure the break loads and joint strength of the NiTi microwires. Two different pull-off tests are applied to examine the quality of the weld. In a straight pull, the joint is loaded with a shear stress, which corresponds to the load in an actuator application. For a better identification of the best process parameters, a peel test is applied, where the NiTi wire is pulled off under an angle of 45°.

The most promising result is afterwards examined by optical as well as SEM microscopy of microsections and undergoes fatigue testing in cyclic actuator tests. The test setup for fatigue testing is presented by Mayer et al. [41] and can also be used for basic spring-biased SMA actuator characterization. The SMA wire bundles, which are manufactured with the elaborated welding parameters, are built by using an X-Y stage and a stress-controlled installation of the NiTi wires. The actuator characteristics of the high-

performance SMA bundles are examined on the same test rig. Therefore, a comparison of force and dynamics with equal-length SMA actuators is carried out. A bundle of four parallel 100 μm NiTi wires is compared to a 200 μm diameter wire. The actuators have the same accumulated cross-sectional area and thus deliver the same force output at equal material stress.

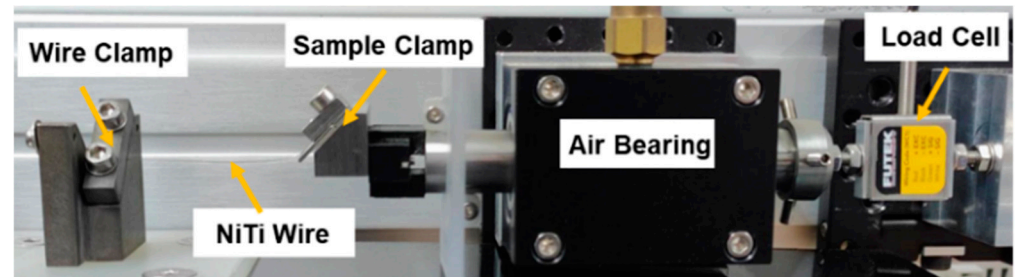


Figure 4. Picture of the test setup for pull-off and peel tests of the welded samples. The sample clamp is replaceable according to the type of experiment.

3. Results and Discussion

3.1. Parameter Study: Evaluation and Discussion

The first feasibility tests of resistance welding NiTi wires in various micro-diameters to stainless steel quickly lead to good results [30]. The thermo-mechanical characteristics in a stress–strain diagram show no measurable difference between the welded samples and clamped or crimped samples. It is expected that the welding heat affects the properties of the NiTi in the welding area and leads to brittleness and a loss of shape memory effect in the heat-affected zone. The brittleness is to be expected due to the intermetallic compounds that are formed [29]. This could potentially have a negative influence on the material properties such as strength, transformation strain and fatigue life, among others. However, as displayed in Figure 5 on the left, the thermal mass of any wire-mounting element in comparison to a microwire is so large that the SMA does not undergo phase transformation in proximity to the fastener [5]. Due to this uneven heat distribution, welding does not alter the functionality of SMA actuator wires. This also manifests in the actuator tests, where the stroke does not change with the used joining technology (clamping or welding). As illustrated in Figure 5, the heat-affected zone is smaller than the non-activated length at the edges of an SMA microwire.

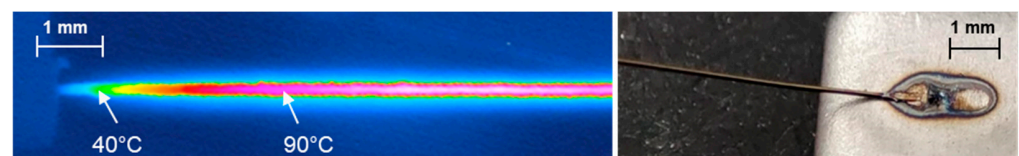


Figure 5. (Left): thermography of a crimped 76 μm NiTi wire, where the influence of the heat sink on the temperature distribution in the activated SMA wire is visible. (Right): the heat-affected zone of a resistance-welded 100 μm NiTi wire to stainless steel is recognized by the tempering colors.

Welding experiments with the introduced copper alloys are more challenging, and satisfying results are not as easily achieved compared to steel joints. Due to the low resistivity of CuSn6 and CuZn30, the contact resistance between the welding partner and NiTi is similar to the contact resistance to the copper electrodes. This results in unsuccessful welds, where the NiTi wire sticks to the electrodes of the weld head instead of the copper alloy sample. The CuZn30 additionally tends to create an electric arc in the welding process as the zinc evaporates, resulting in unusable welds. The most promising results are achieved with gap welding, where the electrodes only contact the NiTi wire, and welding currents of 400 A. The welded joint strength is significantly weaker than the joints to steel with 300 A, which is displayed in Figure 6. The straight pull-off tests are conducted

with five samples for each test. Because of the reasons discussed previously, more than five welding attempts with the copper alloys are necessary to obtain five usable samples.

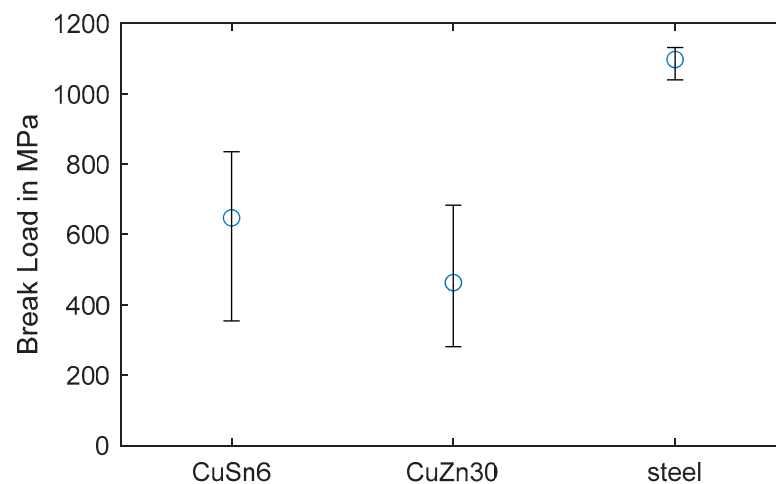


Figure 6. Comparison of the joint break loads of a 100 μm NiTi wire welded to CuSn6, CuZn30 and stainless steel. The results for average value and the spread of the straight pull-off tests are displayed.

The rupture of the NiTi wire usually happens in the heat-affected zone, which is to be expected. The NiTi weld bead stays joined to the sheet metal. However, welded samples with the copper alloys that result in weak joint strengths mostly feature a full separation of the NiTi wire and sheet metal. The welding results with stainless steel are repeatable, consistent and show high pull-off strength levels. The spread in the samples of both already pre-selected copper alloys is four to five times higher than that of steel with about half the average break load. Due to these factors, the investigation is continued with stainless steel samples only.

The joint break loads in straight pull-off tests of samples with varied welding currents with NiTi and 1.4571 exhibit values from 1000 MPa to 1200 MPa, and the differences are hardly recognized. Therefore, the parameters for the optimal welding current are evaluated by peel tests, which is a common testing method for resistance-welded sheet metals for car body parts in the automotive industry. The test series starts with a current of 150 A and is increased in 100 A steps up to a welding current of 550 A.

With each current, five samples are manufactured by step welding. The mean values and spreads of the peel test results are displayed in Figure 7. As a sweet spot around 250 A and 350 A is recognizable, a further test series with a 300 A welding current is added. Standard deviation is not displayed. Because of the relatively small number of samples, the spread is more meaningful. The data show a noticeable trend, where the average joint break load of the 300 A welding current is at a maximum with 417 MPa under peel load. Increasing and decreasing the welding current level leads to a drop in the average break load. It can also be determined that the spread of the peel break loads increases with increasing welding current. From the results of the straight pull-off tests, as well as the peel tests, it can be derived that resistance step welding of NiTi wires in micro-diameters to stainless steel sheets is a robust and easy-to-control process. This is promising for the application of an automated process for the manufacturing of SMA wire bundles and the direct wire integration by resistance welding in SMA-driven systems. Compared to laser welding, the proposed resistance welding process is cheaper and easier to control, and the positioning of the wire on the weld partner is simplified. A laser-welding process of NiTi microwires needs an additional fixation for the wire in the weld zone, and a special treatment of the SMA prior to welding can be necessary.

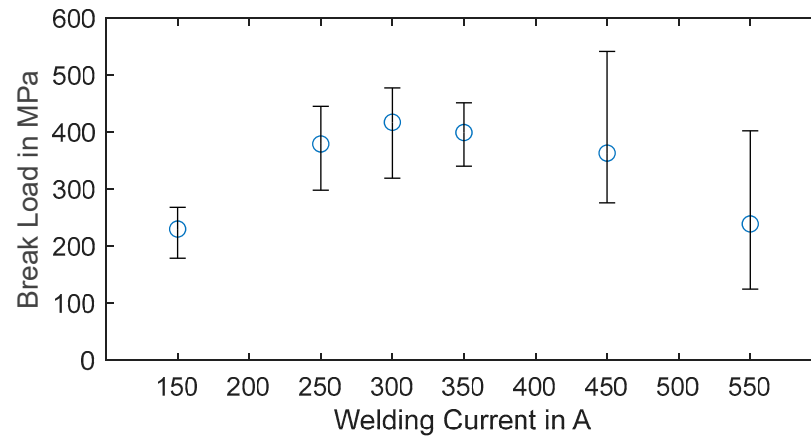


Figure 7. Average values and spread for the joint break loads achieved by peel tests with 100 μm NiTi wire resistance step welded to 1.4571 steel sheet metal.

As other parameters are known to influence the weld quality as well, the following additional tests are performed with a 300 A current:

- Gap welding;
- Welding with a negative electrode, step welding;
- Pressure force reduced to 35N, step welding;
- Sample 1.4404 with 0.3 mm thickness, step welding;
- Thicker oxide layer on NiTi wire, step welding.

The data of these added tests are displayed in Figure 8, with the 300 A step welding result as a reference value. It is recognizable that changing the welding method to gap welding and a different steel alloy with smaller thickness does not measurably influence the joint break load under peel stress. Reducing the force of the electrodes from 100 N to 35 N results in slightly lower strength.

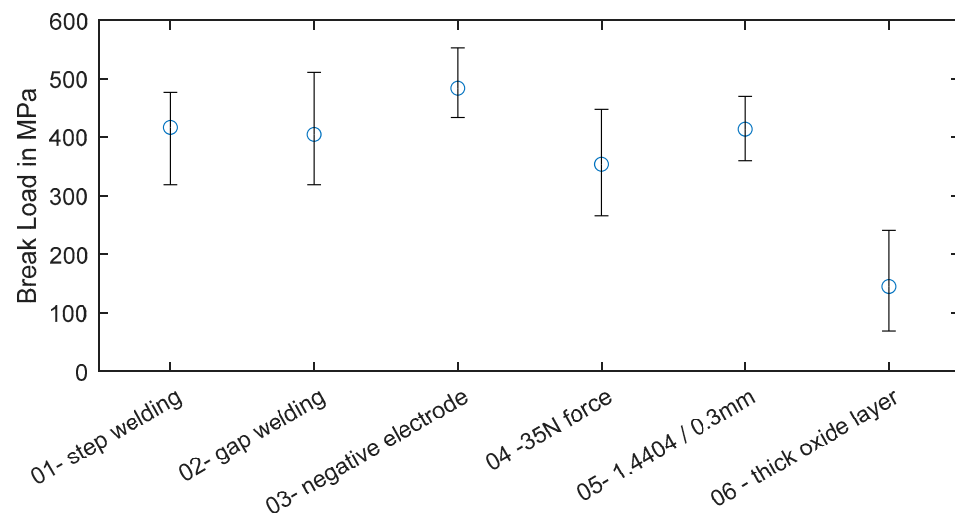


Figure 8. Average values and spreads of joint break loads of peel tests with various parameters and 300 A of welding current.

The Peltier effect is known to influence the formation of the weld bead in resistance welding of small dimensions [41,42]. The heat transfer in the thermoelectric effect occurs with the direction of the current, which is why the negative electrode should be placed on the smaller or thinner weld partner. A positive result on the weld strength by changing the electrode polarity is seen in this study as well. Placing the negative electrode on the NiTi microwire increases the joint break load of the peel tests slightly, as can be read from the

data displayed in Figure 8. During the manufacturing of NiTi wires, an oxide layer, mostly consisting of titanium oxide, is formed. Commercially available NiTi actuator wires come with oxide layers of different thicknesses. In general, it can be determined that a darker wire surface corresponds to a thicker oxide layer.

As the oxide layer is expected to influence the contact resistance in a negative way, the tests in this study are performed with a wire having a thin oxide layer. To compare both versions, in Figure 8 the peel tests results of a 100 μm wire with a thick dark oxide layer are displayed. The joint break load is significantly decreased. This indicates that the oxide layer must be reduced or removed for proper resistance welding strength. The experimental parameter identification for a dissimilar resistance welding process results in a robust parameter set. With 300 A, a 100 μm NiTi wire with a thin (amber colored) oxide layer can be welded to SS substrates with high joint strength and good repeatability. The exact steel alloy and thickness and the electrode configuration have only minor influences on the results. Common actuator applications work with up to 200 MPa of material stress, which corresponds to a safety factor of over five when the wire is not loaded under an angle.

For further investigations, microsections of the weld bead are prepared and microscopically examined. The sample is embedded in resin and cut down to where the weld bead begins. After that, the sample is basically sliced, and microsections are prepared approximately every 100 μm . The sections of the weld bead are etched and examined with optical microscopy, and the fusion zone is investigated by SEM and EDS, of which the results are displayed in Figure 9. The radial cuts through the NiTi wire on the left side in Figure 9 show the deformation of the NiTi under the influence of welding heat and pressure. The wire is flattened out and is pushed into the steel, which also softens due to the welding heat. Resistance welding can join two materials by a solid-state bond as well as a fusion bond. The first is known to show little strength under peel loads and can be identified by a clear separating line in microscopical images. Additional to the high peel strength, Figure 9a–c suggest that a fusion bond is evident. Based on the SEM (see Figure 9b) and the added EDS of a microsection of a sample with the same welding parameters, the fusion bond can be verified. A transition zone between the NiTi and 1.4571 steel is visible. The data of a line in the EDS through this zone, displayed in Figure 9c, shows a gradual distribution of the main alloying elements of the two joining partners. This suggests a melting of steel and NiTi in the welding area resulting in a strong fusion bond.

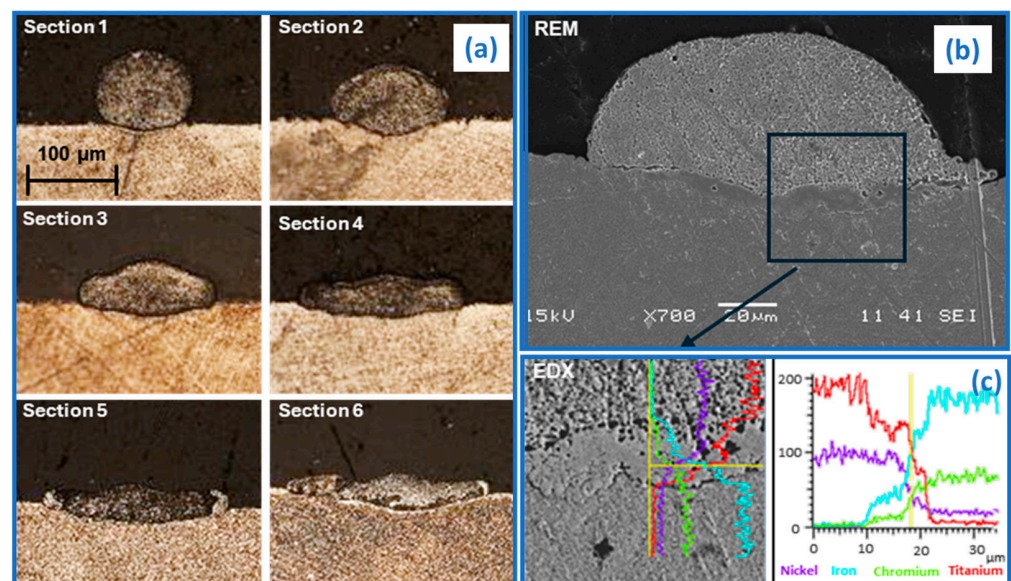


Figure 9. Microscopic analysis of resistance-welded NiTi to stainless steel. (a) shows microscopic pictures of samples cut radial to the wire with distances of 100 μm in between. In (b), an SEM picture of a different sample is displayed with the results of an EDS in (c).

For fatigue tests with the elaborated parameters, three samples with a 70 mm SMA wire welded on both ends to 1.4404 sheet metal are manufactured. The NiTi wire is welded on one side via step welding with the positive electrode, and the opposite side is joined to the steel by step welding with the negative electrode towards the load. This is because of the design of the setup of the welding machine and the workpiece holder on an X-Y stage, which is also explained in the following section. Each sample is installed on a lifetime test bench for fatigue testing detailed by Mayer et al. [43]. An in-depth discussion of the test bench including sketches and pictures can be found in the dedicated publication. The layout of the setup is horizontal and consists of three identical measurement stages aligned beside each other. The SMA actuators are biased with a tension spring. For each activation cycle, the maximum and minimum values for stroke as well as force are recorded. The samples are preloaded with 300 MPa (2.35 N) and heated with an electrical current of 300 mA until 3% of stroke is reached, which leads to increase in stress due to the spring characteristic of 400 MPa (3.14 N). After the specified stroke is reached, the samples cool for 3 s. The activation is repeated until failure of the sample. The results of the fatigue tests are illustrated in Figure 10, where the evolution of the stroke over the cycles is displayed. This behavior is typical for the high stress actuation of SMA wires. The failure of all three samples was due to breaking of the wire in 30% to 50% of the wire length from the weld spot. Sample Nr. 1 failed after 26,208 cycles, sample Nr. 2 after 26,362 cycles and sample Nr. 3 after 33,407 cycles.

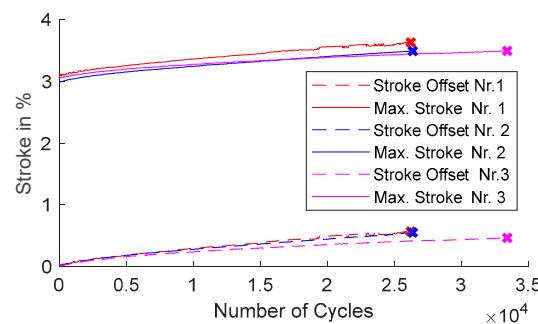


Figure 10. Fatigue test of three samples of 100 μm NiTi wire welded to steel sheet metal. Displayed is the maximum and minimum stroke of each cycle until failure.

The slight differences in stroke are due to differences in friction in the test setups as well as deviations in spring stiffness and pretension of up to 5%.

The results indicate that resistance welding does not affect the fatigue strength of NiTi actuator wires in a negative way. With the joint strength under a straight pull of 80% to 90% of the NiTi break load and fatigue strength in the same region as unwelded SMA wires, the welding process is a promising joining technology for actuator applications. Because of the material-to-material bond, the electrical connection is superior to clamping or crimping, which can lead to enhancement of the resistance signal quality for self-sensing applications. Derived from the proposed results, a large process window is at hand. While an optimum can be shown, the welding current can be set in a range of 250 A to 350 A with different weld partners, electrode configurations and polarities. With the exception of thick oxide layers on the NiTi wire, sufficient weld strength is always achieved.

3.2. Welded SMA Bundle Actuators

To scale the force of an SMA actuator wire, the straightforward method is to increase the wire diameter. However, this measure reduces the dynamics of the actuator drastically because the cooling time increases. The cyclic dynamics of actuators is crucial for many applications. Therefore, installing several thin NiTi wires mechanically in parallel is beneficial. To allow air convection between the single wires, a determined distance between the wires needs to be set.

In this work, flat wire bundles, as displayed in Figure 11, are designed and manufactured. They feature installation space for up to seven microwires at a width of 5 mm. This results in a force output of 11 N at 200 MPa combined with short cooling times. The manufacturing process is based on an X-Y stage with two workpiece carriers for the sheet metal substrates. The stage is positioned under the resistance weld head. The adjustable distance between both carriers defines the length of the actuator bundle. The NiTi wire is guided from the reel through a funnel (see Figure 3) and positioned on a specified spot on the steel substrate. After the SMA wire is welded to the first piece of sheet metal, the workpiece holders move sideways and pull wire through the funnel from the reel until the second piece of sheet metal is positioned under the weld head. The wire length is set with a defined prestress, which is then released for the welding process. After the wire is attached on both ends, it is cut, and the next NiTi wire is placed in a defined distance from the first one. The procedure is repeated until the desired number of parallel wires is attached.

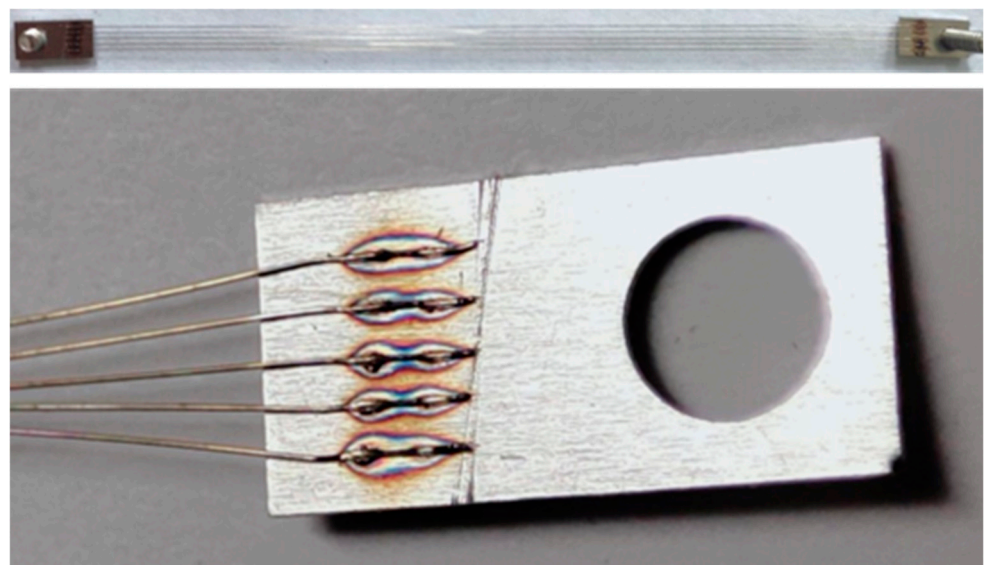


Figure 11. Pictures of a welded SMA wire bundle consisting of five 100 μm wires welded to stainless steel substrates. The upper picture shows a whole bundle with a 105 mm wire length. The bottom picture shows a detailed view of the weld spots.

For evaluating the performance of the bundle, actuator tests to compare a bundle to a single wire with a larger diameter are run. A 200 μm diameter wire features the same accumulated cross-sectional area as four 100 μm wires. Therefore, they feature similar force output at the same material stress level. The experiment is run on the same setup as the fatigue tests. Both actuator samples have a length of 70 mm and are biased with the same spring. The samples are prestressed to 4.15 N (130 MPa) and activated via Joule heating with a constant current pulse of 800 mA for a duration of 2 s. The activation is repeated three times with a cooling time of 8 s in between. The experimental data are displayed in Figure 12. Both samples reach a stroke of 4% and a force of 10.8 N (340 MPa). The crucial part of the data is the time response of both samples. While the single wire heats faster than the bundle, it takes distinctively longer to cool. This is due to the difference in the ratio of the surface to cross-sectional area. The bundle dissipates heat faster via natural convection than the 200 μm wire. The single wire resets by 1% after 1.5 s, and the bundle resets by 3.3%. The bundle reaches 95% reset of stroke after 2.3 s, while the 200 μm wire takes 3.7 s. Also, it takes 7 s for the single wire to reach the initial force value, while the bundle takes only about 50% of that time. It can be assumed that the dynamics do not change when adding more wires to the bundle to increase the force output further.

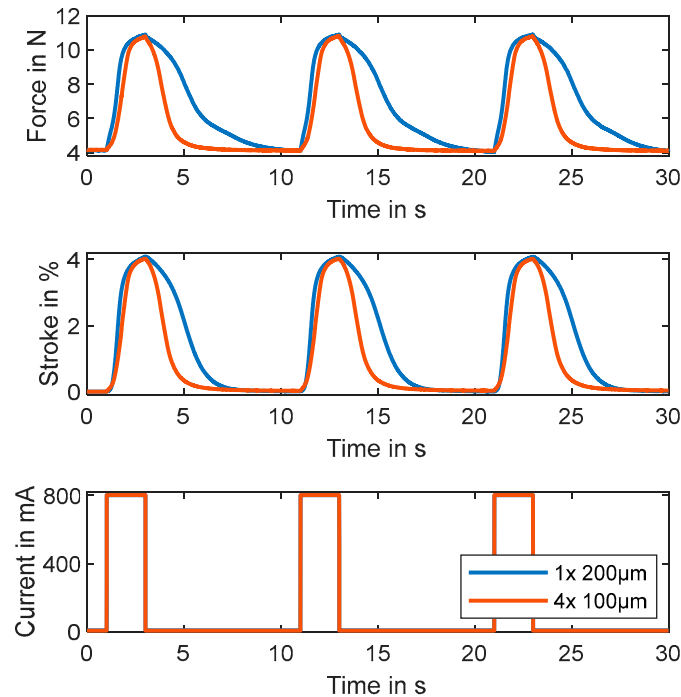


Figure 12. Comparison between bundle of four 100 μm wires and a single 200 μm diameter wire. Displayed are force, stroke and current over time of three consecutive actuation tests.

Compared to the manufacturer's data of a 100 μm SMA wire, the cooling time measured in this experiment is slightly higher [44]. This can be explained by the proximity of the heated wires in the bundle that reduce the heat transfer to the ambient air, as also discussed by Britz et al. [5].

So far, the literature on SMA wire bundles is concentrated on clamped or crimped wires. The welded bundles in this work are more compact, easier to manufacture, need fewer individual parts and prove to be durable as well. Data on welded NiTi bundles with different welding technologies are not yet available. However, the electrode size of the resistance weld head is setting the limits for the distance between the wires, and the manufacturing speed is restricted by the movement of the mechanical parts of the setup. A laser-welding process could be faster and enable to further reduce the installation space. These attributes come with the cost of a more complex and expensive process.

The SMA actuator bundles presented in this work are already used in a variety of different research projects. Scholtes et al. designed different industrial grippers driven by the presented bundles [45–47]. The latest version of a gripper driven by SMA bundles with six wires in parallel was awarded “Hardware Winner” of the “CASmart 4th Design Challenge” at the SMST conference in 2021 [48]. Furthermore, Simone et al. used the developed actuator bundles for their design of a bioinspired gripping system, and Pirritano et al. utilized them to drive a small rotary motor [6,49].

4. Conclusions

Resistance welding represents a valid joining technology for NiTi microwires. The presented work demonstrates the feasibility to join the SMA wires to stainless steel as well as copper alloys without negatively influencing the material properties. The welding results to steel are especially promising. The verified fusion bond leads to high pull-off strength as well as high fatigue strength. Also, peel tests prove to be a useful tool for the parameter identification of resistance welding processes for NiTi wire. Cyclic actuation tests show that the fatigue life is not reduced by the welded joints. The welding process itself is robust, as the parameter identification shows. With the help of resistance welding, automated and reliable bundling processes are possible. The designed bundles are compact and flat, while

showing high performance compared to single wires. The cooling time is 1.4 s faster than a wire with the same accumulated cross-sectional area. The performance of the bundles has already been successfully verified in a variety of technology demonstrations and prototypes. The results of this work are an important step towards industrial manufacturing of high-performance SMA actuators.

The joining of NiTi wires to copper alloys is an open question for future work. Although a welded joint between the two materials can be established, further research to improve the joint strength is needed. Another field that needs to be examined is the design parameters of NiTi wire bundles. The understanding of the influence of wire distance, wire number and geometrical arrangement on the cooling time is important for a further development of the technology.

Author Contributions: Conceptualization, D.S.; methodology, D.S. and R.-K.Z.; software, D.S.; validation, D.S.; formal analysis, D.S.; investigation, D.S.; resources, D.S.; data curation, D.S.; writing—original draft preparation, D.S.; writing—review and editing, P.M.; visualization, D.S.; supervision, P.M., B.F. and S.S.; project administration, P.M.; funding acquisition, P.M. and R.-K.Z. All authors have read and agreed to the published version of the manuscript.

Funding: This work was funded by the European Regional Development Fund (ERDF) and Saarland Government in the project ProForm.

Data Availability Statement: Data are available upon request.

Conflicts of Interest: The authors declare no conflicts of interest.

References

1. Janocha, H.; Bonertz, T.; Pappert, G. *Unkonventionelle Aktoren: Eine Einführung*; Oldenbourg Wissenschaftsverlag: München, Germany, 2013.
2. Prechtel, J.; Seelecke, S.; Motzki, P.; Rizzello, G. Self-Sensing Control of Antagonistic SMA Actuators Based on Resistance-Displacement Hysteresis Compensation. In Proceedings of the ASME 2020 Conference on Smart Materials, Adaptive Structures and Intelligent Systems, SMASIS, Online, 15 September 2020. [[CrossRef](#)]
3. Kirsch, S.-M.; Welsch, F.; Bevilacqua, D.; Naso, D.; Seelecke, S.; Rizzello, G.; Motzki, P. SMA Antagonistic-Micro-Wire Bundle: First Measurement Results. In Proceedings of the ASME 2020 Conference on Smart Materials, Adaptive Structures and Intelligent Systems, Online, 15 September 2020. [[CrossRef](#)]
4. Williams, E.; Elahinia, M.H. An Automotive SMA Mirror Actuator: Modeling, Design, and Experimental Evaluation. *J. Intell. Mater. Syst. Struct.* **2008**, *19*, 1425–1434. [[CrossRef](#)]
5. Britz, R.; Motzki, P. Analysis and evaluation of bundled SMA actuator wires. *Sens. Actuators A Phys.* **2022**, *333*, 113233. [[CrossRef](#)]
6. Simone, F.; Rizzello, G.; Seelecke, S.; Motzki, P. A Soft Five-Fingered Hand Actuated by Shape Memory Alloy Wires: Design, Manufacturing, and Evaluation. *Front. Robot. AI* **2020**, *7*, 608841. [[CrossRef](#)]
7. Buehler, W.J.; Gilfrich, J.V.; Wiley, R.C. Effect of Low-Temperature Phase Changes on the Mechanical Properties of Alloys near Composition TiNi. *J. Appl. Phys.* **1963**, *34*, 1475–1477. [[CrossRef](#)]
8. Buehler, W.J.; Wang, F.E. A summary of recent research on the nitinol alloys and their potential application in ocean engineering. *Ocean Eng.* **1968**, *1*, 105–120. [[CrossRef](#)]
9. Duerig, T.; Pelton, A.; Stöckel, D. An overview of nitinol medical applications. *Mater. Sci. Eng. A* **1999**, *273–275*, 149–160. [[CrossRef](#)]
10. Adler, P.; Yu, W.; Pelton, A.; Zadno, R.; Duerig, T.; Barresi, R. On the tensile and torsional properties of pseudoelastic NiTi. *Scr. Met. et Mater.* **1990**, *24*, 943–947. [[CrossRef](#)]
11. Lagoudas, D.C. *Shape Memory Alloys*; Springer: Boston, MA, USA, 2008; Volume 1. [[CrossRef](#)]
12. Wang, S.; Shi, Y.; Li, Y.; Lin, H.; Fan, K.; Teng, X. Solid-state refrigeration of shape memory alloy-based elastocaloric materials: A review focusing on preparation methods, properties and development. *Renew. Sustain. Energy Rev.* **2023**, *187*, 113762. [[CrossRef](#)]
13. Hou, H.; Simsek, E.; Ma, T.; Johnson, N.S.; Qian, S.; Cissé, C.; Stasak, D.; Al Hasan, N.; Zhou, L.; Hwang, Y.; et al. Fatigue-resistant high-performance elastocaloric materials made by additive manufacturing. *Science* **2019**, *366*, 1116–1121. [[CrossRef](#)]
14. Schmidt, M.; Schütze, A.; Seelecke, S. Scientific test setup for investigation of shape memory alloy based elastocaloric cooling processes. *Int. J. Refrig.* **2015**, *54*, 88–97. [[CrossRef](#)]
15. Bruederlin, F.; Ossmer, H.; Wendler, F.; Miyazaki, S.; Kohl, M. SMA foil-based elastocaloric cooling: From material behavior to device engineering. *J. Phys. D: Appl. Phys.* **2017**, *50*, 424003. [[CrossRef](#)]
16. Curtis, S.M.; Gugat, J.L.; Bumke, L.; Dengiz, D.; Seigner, L.; Schmadel, D.; Lazarus, N.S.; Quandt, E. Thin-Film Superelastic Alloys for Stretchable Electronics. *Shape Mem. Superelasticity* **2023**, *9*, 35–49. [[CrossRef](#)]

17. Dengiz, D.; Goldbeck, H.; Curtis, S.M.; Bumke, L.; Jetter, J.; Quandt, E. Shape Memory Alloy Thin Film Auxetic Structures. *Adv. Mater. Technol.* **2023**, *8*, 2201991. [[CrossRef](#)]
18. Oliveira, J.; Miranda, R.; Fernandes, F.B. Welding and Joining of NiTi Shape Memory Alloys: A Review. *Prog. Mater. Sci.* **2017**, *88*, 412–466. [[CrossRef](#)]
19. Kannan, T.D.B.; Ramesh, T.; Sathiy, P. A Review of Similar and Dissimilar Micro-joining of Nitinol. *JOM* **2016**, *68*, 1227–1245. [[CrossRef](#)]
20. Gugel, H.; Schuermann, A.; Theisen, W. Laser welding of NiTi wires. *Mater. Sci. Eng. A* **2007**, *481–482*, 668–671. [[CrossRef](#)]
21. Gugel, H.; Theisen, W. Laserstrahlschweißen von Mikrodrähten aus Nickel-Titan-Formgedächtnislegierungen und austenitischem Stahl. *Mater. Werkst.* **2007**, *38*, 489–493. [[CrossRef](#)]
22. Zeng, Z.; Pantan, B.; Oliveira, J.P.; Han, A.; Zhou, Y.N. Dissimilar laser welding of NiTi shape memory alloy and copper. *Smart Mater. Struct.* **2015**, *24*, 125036. [[CrossRef](#)]
23. Rodrigues, L.F.A.; Amorim, F.A.; Grassi, E.N.D.; dos Santos, P.L.L.; de Araújo, C.J. TIG spot welding applied to NiTi shape memory wires optimized by factorial design. *Int. J. Adv. Manuf. Technol.* **2022**, *121*, 7749–7762. [[CrossRef](#)]
24. Li, J.; Pantan, B.; Mao, Y.; Vivek, A.; Daehn, G. High strength impact welding of NiTi and stainless steel wires. *Smart Mater. Struct.* **2020**, *29*, 105023. [[CrossRef](#)]
25. Barcellona, A.; Fratini, L.; Palmeri, D.; Maletta, C.; Brandizzi, M. Friction stir processing of Niti shape memory alloy: Microstructural characterization. *Int. J. Mater. Form.* **2010**, *3*, 1047–1050. [[CrossRef](#)]
26. Tam, B.; Pequegnat, A.; Khan, M.I.; Zhou, Y. Resistance Microwelding of Ti-55.8 wt pct Ni Nitinol Wires and the Effects of Pseudoelasticity. *Met. Mater. Trans. A* **2012**, *43*, 2969–2978. [[CrossRef](#)]
27. Shamsolhodaie, A.; GhateiKalashami, A.; Safdel, A.; Midawi, A.; Elbestawi, M.; Peng, P.; Zhou, Y. Resistance spot welding of NiTi shape memory alloy sheets: Microstructural evolution and mechanical properties. *J. Manuf. Process.* **2022**, *81*, 467–475. [[CrossRef](#)]
28. Delobelle, V.; Delobelle, P.; Liu, Y.; Favier, D.; Louche, H. Resistance welding of NiTi shape memory alloy tubes. *J. Mech. Work. Technol.* **2013**, *213*, 1139–1145. [[CrossRef](#)]
29. Zhang, K.; Shamsolhodaie, A.; Ghatei-Kalashami, A.; Oliveira, J.; Zang, C.; Schell, N.; Li, J.; Midawi, A.; Lopes, J.; Yan, J.; et al. Revealing microstructural evolution and mechanical properties of resistance spot welded NiTi-stainless steel with Ni or Nb interlayer. *J. Mater. Sci. Technol.* **2024**, *180*, 160–173. [[CrossRef](#)]
30. Scholtes, D.; Zaeh, R.; Schmidt, M.; Motzki, P.; Faupel, B.; Seelecke, S. Resistance Welding of NiTi Actuator Wires. In Proceedings of the ACTUATOR 2018: 16th International Conference on New Actuators, Bremen, Germany, 25–27 June 2018; pp. 500–504.
31. Mosley, M.J.; Mavroidis, C. Design and Control of a Shape Memory Alloy Wire Bundle Actuator. In Proceedings of the ASME 2000 International Design Engineering Technical Conferences and Computers and Information in Engineering Conference, Volume 7B: 26th Biennial Mechanisms and Robotics Conference, Baltimore, MD, USA, 10–13 September 2000; American Society of Mechanical Engineers: New York, NY, USA, 2000; pp. 973–979. [[CrossRef](#)]
32. Kratz, R.; Stelzer, M.; von Stryk, O. Macroscopic Sma Wire Bundle Actuator/Sensor System: Design, Measurement, Control Approach. *IFAC Proc. Vol.* **2006**, *39*, 1054–1058. [[CrossRef](#)]
33. Britz, R.; Welsch, F.; Kirsch, S.M.; Simone, F.; Schmidt, M.; Motzki, P.; Seelecke, S. SMA Wire Bundles—Mechanical and Electrical Concepts. In Proceedings of the ACTUATOR 2018: 16th International Conference on New Actuators, Bremen, Germany, 25–27 June 2018; pp. 1–4.
34. Pfeifer, M. Manufacturing Process Considerations. In *Materials Enabled Designs*; Elsevier: Amsterdam, The Netherlands, 2009; pp. 115–160. [[CrossRef](#)]
35. SAES Group. SmartFlex Springs and Wires. Available online: <https://www.saesgetters.com/wp-content/uploads/sites/8/2024/01/SmartFlex-wires.pdf> (accessed on 26 September 2024).
36. Amada Miyachi America. Fundamentals of Small Parts Resistance Welding. Available online: <https://www.amadaweldtech.eu/sites/default/files/images/knowledgebase/AMYA%20Fundamentals%20Resistance%20Welding%2003-16.pdf> (accessed on 8 March 2024).
37. Deutsches Kupferinstitut. CuSn6. Available online: <https://kupfer.de/wp-content/uploads/2019/11/CuSn6-1.pdf> (accessed on 8 March 2024).
38. Deutsches Kupferinstitut. CuZn30. Available online: <https://kupfer.de/wp-content/uploads/2019/11/CuZn30-1.pdf> (accessed on 8 March 2024).
39. Jury, A.; Balandraud, X.; Heller, L. Thermal Conductivity and Specific Heat Capacity of Austenite and Stress-Induced Martensite in Superelastic NiTi at Ambient Temperature. *Int. J. Thermophys.* **2023**, *44*, 162. [[CrossRef](#)]
40. Scholtes, D.; Seelecke, S.; Motzki, P. Electro-thermo-mechanical characterization of shape memory alloy wires for actuator and sensor applications—Part 1: The effects of training. *Eng. Rep.* **2024**, e12867. [[CrossRef](#)]
41. Eagar, T.W. Resistance Welding: A Fast, Inexpensive and Deceptively Simple Process. In Proceedings of the 3rd International Conference on Trends in Welding Research, Gatlinburg, TN, USA, 1–5 June 1992; David, S.A., Vitek, J.M., Eds.; ASM International: Gatlinburg, TN, USA, 1992; pp. 347–351.
42. Deng, L.; Li, Y.; Cai, W.; Haselhuhn, A.S.; Carlson, B.E. Simulating Thermoelectric Effect and Its Impact on Asymmetric Weld Nugget Growth in Aluminum Resistance Spot Welding. *J. Manuf. Sci. Eng.* **2020**, *142*, 091001. [[CrossRef](#)]

43. Mayer, J.; Molitor, P.; Goergen, Y.; Motzki, P. Design of a Modular Lifespan Test Bench for Shape Memory Alloy Wires. In Proceedings of the ASME 2022 Conference on Smart Materials, Adaptive Structures and Intelligent Systems, Dearborn, MI, USA, 12–14 September 2022. [[CrossRef](#)]
44. Saes Getters. SmartFlex[®] Wire. Available online: www.saesgroup.com (accessed on 17 April 2024).
45. Scholtes, D.; Seelecke, S.; Rizzello, G.; Motzki, P. Design of a Compliant Industrial Gripper driven by a Bistable Shape Memory Alloy Actuator. In Proceedings of the ASME 2020 Conference on Smart Materials, Adaptive Structures and Intelligent Systems, SMASIS, Online, 15 September 2020. [[CrossRef](#)]
46. Scholtes, D.; Seelecke, S.; Motzki, P. Development of a Bistable SMA Actuated Industrial Gripper Based on a Compliant Design. In Proceedings of the ACTUATOR—International Conference and Exhibition on New Actuator Systems and Applications, Online, 17–19 February 2021; pp. 181–184.
47. Scholtes, D.; Seelecke, S.; Motzki, P. Design of a lightweight SMA driven parallel gripper for collaborative robots. In Proceedings of the SPIE Smart Structures and Materials + Nondestructive Evaluation and Health Monitoring, Active and Passive Smart Structures and Integrated Systems XVII, 124830K, Long Beach, CA, USA, 12–16 March 2023; SPIE: Long Beach, CA, USA, 2023. [[CrossRef](#)]
48. CASMART 4th Design Challenge. Available online: <https://www.casmart.org/home/student-design-challenges/casmart-4th-design-challenge> (accessed on 17 April 2024).
49. Pirritano, C.; Gorges, T.; Britz, R.; Scholtes, D.; Zimmer, L.; Preetz, J.; Goergen, Y.; Motzki, P. Fully Integrated Rotary Motor Based on Antagonistic Shape Memory Alloy Wire Bundles. In Proceedings of the ASME 2023 Conference on Smart Materials, Adaptive Structures and Intelligent Systems, SMASIS, Austin, TX, USA, 11–13 September 2023. [[CrossRef](#)]

Disclaimer/Publisher’s Note: The statements, opinions and data contained in all publications are solely those of the individual author(s) and contributor(s) and not of MDPI and/or the editor(s). MDPI and/or the editor(s) disclaim responsibility for any injury to people or property resulting from any ideas, methods, instructions or products referred to in the content.

3 Fazit und Ausblick

In der Arbeit werden, neben vielen konkreten und für Anwendungen wichtige Daten und Messungen, Methoden erarbeitet und vorgestellt, mit denen sich FGL-Aktordrähte vollumfänglich charakterisieren lassen. Außerdem wird ebenfalls eine Systematik aufgezeigt, um Widerstandsschweißprozesse für FGL-Mikrodrähte zu entwickeln. Daraus resultiert eine neue und vielversprechende Fertigungsmethode für FGL-Drahtbündel.

Das wichtigste Werkzeug zur Charakterisierung der Aktordrähte ist dabei der multifunktionale Prüfstand für FGL Mikrodrähte. Durch dessen besondere Funktionen lassen sich die relevantesten Parameter für Aktor-Sensor-Systeme mit unterschiedlich behandelten FGL-Drähten in Durchmessern bis zu 100 μm ermitteln. Die Methoden, insbesondere die sogenannte „Basic Characterization“ als auch die Aktortests mit unterschiedlichen Vorspannmechanismen, ermöglichen einen Vergleich zwischen unterschiedlichen FGL Drähten (Hersteller, Training, Legierungszusammensetzung, etc.). Somit kann der für eine spezielle Anwendung am besten geeignete Draht und die passende Konditionierung ermittelt werden. Die Erkenntnisse zu Widerstands- und Hochtemperaturverhalten, und wie diese mittels des Trainings und der Last beeinflussbar sind, ermöglichen die Entwicklung von robusteren und vielseitigeren Aktor-Sensor-Systemen.

Mit der Ausarbeitung des gut zu beherrschenden Widerstandsschweißprozesses, lassen sich die entsprechenden Systeme mit Drahtbündeln bestücken, die eine deutlich verbesserte Dynamik im Vergleich zu bisherigen Systemen mit Einzeldrähten in größeren Durchmessern aufweisen. Die flachen und kompakten Bündel können in engsten Bauräumen untergebracht werden und helfen so bei der Miniaturisierung von Antriebssystemen. Mithilfe des Spalt- beziehungsweise Stufenschweißprozesses ist während der Montage nur die Zugänglichkeit von einer Seite notwendig. Somit lassen sich auch Einzeldrähte leichter als mit Klemmungen aus Schrauben oder Crimps in Baugruppen integrieren. Mit der Methode der Schälversuche, anstatt gewöhnlicher Abrissversuche, lassen sich die entsprechenden Parametersätze eindeutig ermitteln. Im Vergleich zum oft untersuchten und weiter verbreiteten Laserschweißen, ist die hier aufgezeigte Verbindungstechnik kosteneffektiver, leichter zu handhaben und einfacher zu automatisieren. Außerdem gibt es prozessbedingt keine Probleme mit der Drahtpositionierung oder -fixierung während des Schweißens.

3.1 Abgeleitete Anwendungen

Die Ergebnisse der Forschungsarbeit haben bereits eine Reihe von Entwicklungen von neuartigen Systemen und Anwendungen mit FGL-Antrieb und -Sensorik ermöglicht. Einige Beispiele hierfür werden im Folgenden vorgestellt. Grundlage für die Entwicklung der Technologiedemonstratoren sind sowohl die Ergebnisse der Charakterisierungsstudie als auch die geschweißten Drahtbündel.

Vor dem Hintergrund, dass ein großer Teil des Energieverbrauchs der produzierenden Industrie der Erzeugung von Druckluft dient, ist die vollständige Elektrifizierung von neuen Produktionsstraßen ein wichtiger Schritt zur Reduzierung des Energieverbrauchs. Damit auf Druckluft verzichtet werden kann, müssen auch die eingesetzten Pneumatikgreifer (siehe Abbildung 1 im Hintergrund), durch elektrisch angetriebene Modelle ersetzt werden. Im Zuge dieses Umbaus wurde, in Zusammenarbeit mit der Firma Bosch (Standort Homburg), der Prototyp eines Industriegreifers mit FGL Antrieb entwickelt [68], [83], [84]. Durch die bistabile Antriebsmechanik, die auf einer vorgespannten, drehbar gelagerten Blattfeder basiert, weist der Prototyp eine hohe Energieeffizienz auf.

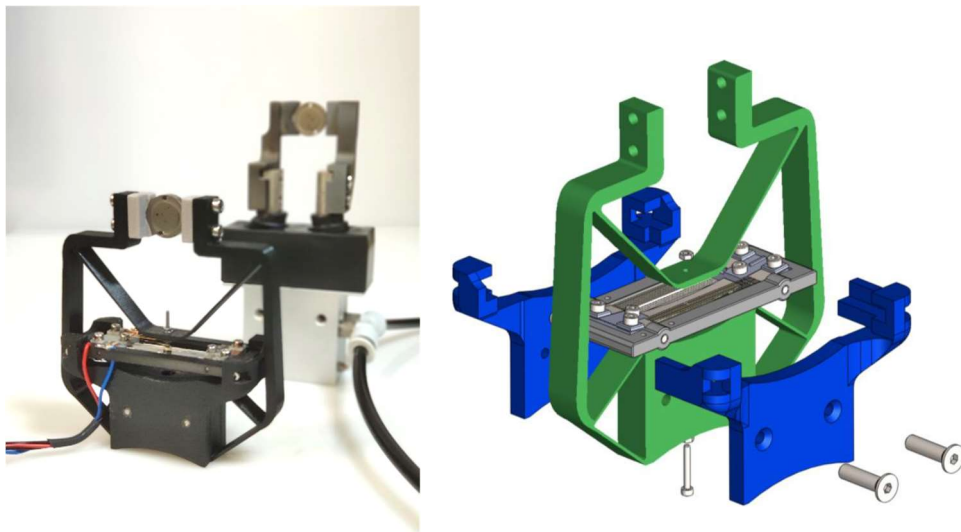


Abbildung 1: links: Fotografie des Prototyps eines Festkörpergelenkgreifers mit bistabilem FGL Antrieb vor einem Pneumatikgreifer, wie er aktuell in der Industrie eingesetzt wird. rechts: Explosionsansicht des CAD Modells des Greifers.

Die geschlossene und offene Position wird selbstständig und energiefrei gehalten. Nur für das Öffnen und Schließen sind kurze Stromimpulse notwendig. Wie in Abbildung 1 zu erkennen, ist die Greiferkinematik mit Festkörpergelenken ausgelegt. Diese haben, im Vergleich zu herkömmlichen Gelenken, die Vorteile, dass sie spielfrei arbeiten und nicht dem Reibungsverschleiß unterliegen. Als Weiterentwicklung dieses Greifers wurde im Rahmen der

„CASMART Student Design Challenge 2021“ ein im Bauraum optimierter, bistabiler Greifer inklusive eines Handling Systems in Form eines Schwenkarms entwickelt. Im Verlaufe des Wettbewerbs wurde das System als Sieger im Bereich „Hardware Design“ gekürt [85]. Die Weiterentwicklungen des Greifers liegen im Bereich des Gehäuses, der Festkörperkinematik sowie der Lagerung der bistabilen Blattfeder. Die bistabile Mechanik in beiden Greifer Modellen wird von insgesamt vier Drahtbündeln, bestehend aus jeweils sechs NiTi-Drähten mit 100 μ m Durchmesser angetrieben. Auch der Schwenkarm, an dem der Greifer, wie in Abbildung 2 zu erkennen, montiert ist, verfügt über zwei stabile Positionen und wird mit geschweißten FGL-Drahtbündeln angetrieben. Die Bistabilität des Arms wird mittels einer exzentrisch angebrachten Zugfeder erreicht.

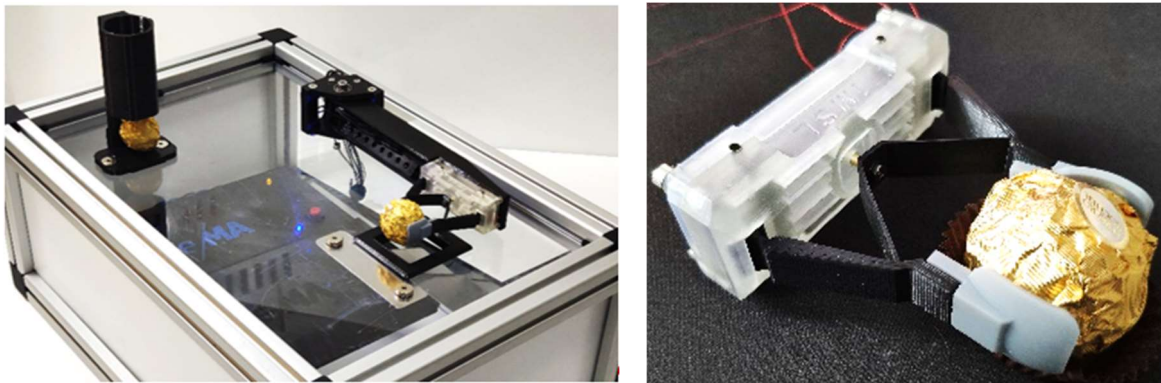


Abbildung 2: FGL-angetriebenes bistabiles Greifsystem „SmartGrip“ als Anwendungsbeispiel für die Lebensmittel Industrie. links: System bestehend aus Schwenkarm, Greifer und Demo-Plattform. rechts: Detailaufnahme des Greifers mit Praline in der Werkstückaufnahme.

Die Auslegung der FGL-Systeme basiert dabei auf den Ergebnissen der Charakterisierungsstudien, vorgestellt in den ersten beiden Veröffentlichungen in dieser Arbeit. Durch den Verzicht auf Druckluft ist das Handling System für die Lebensmittelindustrie prädestiniert. Daher wurde, wie in Abbildung 2 auf der linken Seite zu erkennen, als Beispielanwendung der Transport, bzw. die Zuführung von Pralinen, aus einem Stapelmagazin gewählt.

Bei der Entwicklung von FGL-basierten Antrieben muss oft, zum Beispiel aufgrund des Bauraums, zwischen höherem Kraftabtrieb und höherem Hub abgewogen werden. Um dennoch einen Industriegreifer mit großem Greifbackenhub und hoher Greifkraft bei einer Zykluszeit von einer Sekunde zu erreichen, muss eine große Anzahl an gebündelten Drähten mit einer hohen Hub-Übersetzung kombiniert werden. Umgesetzt wurde dies anhand eines Parallelgreifers zur Anwendung mit kollaborativen Robotern (Cobots), dargestellt in Abbildung 3. Als Antrieb arbeiten in dem Greifer 96 NiTi-Drähte mit einem Durchmesser von

76 μm und einer Länge von 85 mm. Sie setzen sich zusammen aus geschweißten Bündeln mit jeweils sechs Drähten. Durch einen gekoppelten Teleskopmechanismus und eine Übersetzungsmechanik erreicht der Greifer eine maximale Greifkraft von 14 N bei 30 mm Öffnungshub. Durch die integrierte Druckfeder als Vorspannmechanismus für die FGL-Drähte, ist der Greifer „normally closed“. Das bedeutet das Halten der Werkstücke erfolgt energiefrei [67].



Abbildung 3: CAD-Konstruktion (links) und Foto (rechts) des ersten Prototyps eines Leichtbau Parallelgreifers mit FGL-Antrieb zur Anwendung mit kollaborativen Robotern.

Bei einer weiteren Entwicklung wird der Vorteil der Kompaktheit der FGL-Bündel ausgenutzt und die Auslegung geschieht ebenfalls basierend auf den Messungen des multifunktionalen Prüfstandes. Ziel der Entwicklung war ein vollintegrierter, lautloser, leichter und kompakter Rotationsantrieb [56]. Konzipiert ist der Rotationsaktor mit FGL-Bündel Antrieb für den Automotive Bereich, um neue Funktionalitäten in engsten Bauräumen unterzubringen. Die CAD-Konstruktion des Prototyps ist in Abbildung 4 zu sehen. Hier ist die integrierte Steuerplatine, die Zahnstangen- und Zahnradübersetzung sowie eines der beiden antagonistisch arbeitenden FGL-Bündeln zu erkennen.

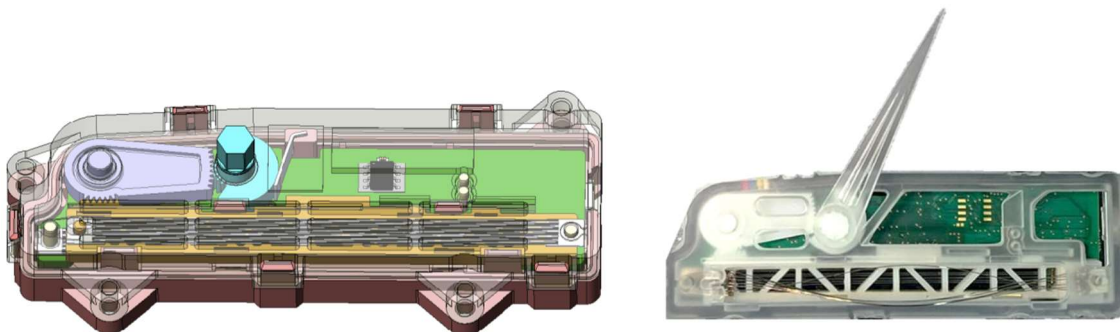


Abbildung 4: links: CAD-Baugruppe des kompakten FGL-Rotationsantriebs mit antagonistisch angeordneten, widerstandsgeschweißten FGL-Bündeln., rechts: Foto des fertig montierten Systems mit Winkelanzeiger.

Durch ihre feine Struktur erinnern FGL-Mikrodrähte an textile Fasern. Daher existieren auch einige Forschungen im Bereich der Textilintegration, um Stoffe mit Hilfe von FGL mit aktiven Funktionen auszustatten [86]–[89]. Hierzu wurde mit FGL-basierten weichen Knöpfen zur Integration in textile Oberflächen ein Beitrag geleistet [66]. Dabei werden beide Aspekte der NiTi-Drähte, nämlich Aktor- und Sensoreigenschaft, genutzt. Die eigentlichen Knöpfe, dargestellt auf der linken Seite in Abbildung 5, bestehen aus flachen, 3D gedruckten TPU Kreuzstrukturen, unter denen dünne FGL-Drähte angebracht sind. Durch die Aktivierung der FGL-Drähte beult das Kreuz nach oben aus und kann als Knopf genutzt werden. Durch Drücken des Knopfes werden die FGL-Drähte gedehnt und ihr Widerstand erhöht sich. Der Widerstand kann in Form eines Spannungssignals ausgelesen werden.

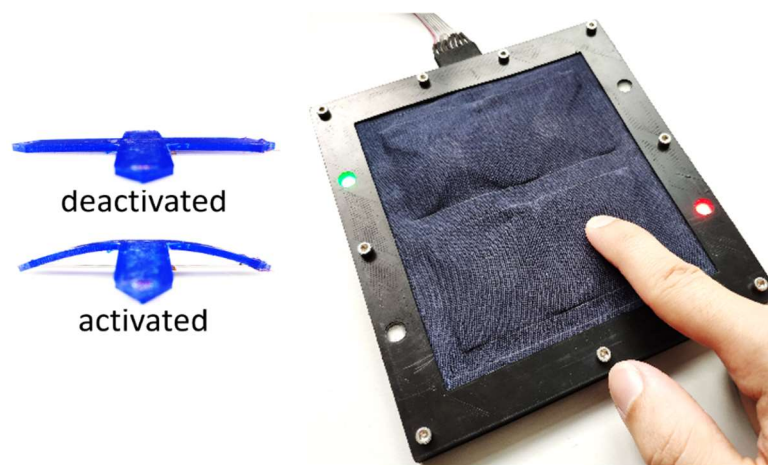


Abbildung 5: Technologiedemonstrator mit aktiven, integrierbaren Knöpfen mit FGL-Sensor und -Aktor Eigenschaft. links: Knopf als TPU Kreuzstruktur mit integriertem FGL-Draht. rechts: Textilintegration der Knöpfe mit kontinuierlichem Signalausgang.

In dem entwickelten Technologiedemonstrator wurden die Knöpfe fast unsichtbar, rasterförmig in ein Textil integriert. Bei Aktivierung der Knöpfe werden diese durch die Wölbung nach oben sichtbar. Mittels farbveränderlicher LEDs wird der Druck auf die Knöpfe visualisiert. Der Farbverlauf ändert sich dabei mit Erhöhen der Druckkraft kontinuierlich von grün zu rot. Entscheidend für die Auslegung des FGL-Systems sowie der Ansteuerungs- und Auswerteelektronik sind dabei die Widerstandsdaten der FGL-Drähte bei Aktivierung und unter Zug, die auf dem Charakterisierungsprüfstand ermittelt wurden.

Auch andere Forscherinnen und Forscher haben bereits unter Zuhilfenahme der, in dieser Dissertation vorgestellten, Forschungsergebnisse neue FGL-Anwendungen entwickelt. Dazu zählen zum Beispiel der Veröffentlichungen von Simone et al. und Goergen et al [82], [90].

3.2 Ausblick

Der entwickelte Prüfstand und die vorgestellten Methoden zur Charakterisierung von FGL-Drähten legen die Grundlage für weitere zukünftige, systematische Untersuchungen der Materialeigenschaften für den Aktor und Sensor Bereich. Beispiele für solche Untersuchungen sind der Einfluss von unterschiedlichen Trainingsparametern und Legierungszusammensetzungen auf die Eigenschaften. Eine erste Studie zum Einfluss unterschiedlicher Trainingsmethoden auf die Lebensdauer der Aktordrähte wurde bereits in Form einer Master-Thesis gestartet. Ein Gebiet, das bei den Untersuchungen zur Materialcharakteristik nicht bearbeitet wurde, ist die Dynamik, beziehungsweise die Abkühlgeschwindigkeit der NiTi-Legierung. Um dies in Zukunft zu ermöglichen, wird die kraftgesteuerte Regelung der Linearachse in derselben Abschlussarbeit optimiert. Damit wird eine schnellere Rückstellung des FGL-Drahtes erreicht und somit kann auch die Dynamik des Aktuators unter unterschiedlichen Vorspannungen und bei erhöhten Umgebungstemperaturen untersucht werden. Die Ergebnisse bis dato haben allerdings schon großes Potenzial aufgrund der neuen Erkenntnisse über das Verhalten der FGL-Drähte die Entwicklung zukünftiger, neuartiger Systeme zu ermöglichen und zu unterstützen.

Die Mikrodrahtbündel, mit unterschiedlichen Drahtdurchmesser, werden aktuell weiterhin in neuen Forschungs- und Entwicklungsprojekten genutzt, um die optimale Funktionalität von FGL-Antrieben auszunutzen. Die Bündelungsmethode mit dem Widerstandsschweißprozess zeigt das Potenzial, demnächst auch in der Serienfertigung von Produkten mit FGL-Antrieb eingesetzt zu werden. Trotzdem wird daran weiter geforscht, um zum Beispiel dickere Drahtdurchmesser oder abgeänderte Geometrien zu verwenden.

Im Bereich der Bündelung besteht des Weiteren noch Forschungsbedarf bei der gegenseitigen Beeinflussung der Drähte bezüglich ihrer Temperatur. Drahtabstand, -durchmesser, -lage und -anzahl sind hier einige beispielhafte Einflussfaktoren auf die Abkühlzeit der Bündel.

Literaturverzeichnis

- [1] T. Wang *et al.*, “Electroactive polymers for sensing,” *Interface Focus*, vol. 6, no. 4, p. 20160026, Aug. 2016, doi: 10.1098/rsfs.2016.0026.
- [2] B. Scrosati, Ed., *Applications of Electroactive Polymers*. Dordrecht: Springer Netherlands, 1993. doi: 10.1007/978-94-011-1568-1.
- [3] S. Gratz-Kelly *et al.*, “A Multi-Mode, Multi-Frequency Dielectric Elastomer Actuator,” *Adv. Funct. Mater.*, vol. 32, no. 34, p. 2201889, Aug. 2022, doi: 10.1002/ADFM.202201889.
- [4] A. York, J. Dunn, and S. Seelecke, “Experimental characterization of the hysteretic and rate-dependent electromechanical behavior of dielectric electro-active polymer actuators,” *Smart Mater. Struct.*, vol. 19, no. 9, p. 094014, Sep. 2010, doi: 10.1088/0964-1726/19/9/094014.
- [5] P. Dineva, D. Gross, R. Müller, and T. Rangelov, “Piezoelectric Materials,” in *Solid Mechanics and its Applications*, Springer, Cham, 2014, pp. 7–32. doi: 10.1007/978-3-319-03961-9_2.
- [6] J. de Vicente, D. J. Klingenberg, and R. Hidalgo-Alvarez, “Magnetorheological fluids: a review,” *Soft Matter*, vol. 7, no. 8, p. 3701, 2011, doi: 10.1039/c0sm01221a.
- [7] H. E. Karaca, I. Karaman, B. Basaran, Y. Ren, Y. I. Chumlyakov, and H. J. Maier, “Magnetic Field-Induced Phase Transformation in NiMnCoIn Magnetic Shape-Memory Alloys—A New Actuation Mechanism with Large Work Output,” *Adv. Funct. Mater.*, vol. 19, no. 7, pp. 983–998, Apr. 2009, doi: 10.1002/ADFM.200801322.
- [8] M. Kohl, M. Gueltig, V. Pinneker, R. Yin, F. Wendler, and B. Krevet, “Magnetic Shape Memory Microactuators,” *Micromachines 2014, Vol. 5, Pages 1135-1160*, vol. 5, no. 4, pp. 1135–1160, Nov. 2014, doi: 10.3390/MI5041135.
- [9] B. Kiefer and D. C. Lagoudas, “Magnetic field-induced martensitic variant reorientation in magnetic shape memory alloys,” *Philos. Mag.*, vol. 85, no. 33–35, pp. 4289–4329, Nov. 2005, doi: 10.1080/14786430500363858.
- [10] B. Minorowicz and A. Milecki, “Design and Control of Magnetic Shape Memory Alloy Actuators,” *Materials (Basel)*, vol. 15, no. 13, p. 4400, Jun. 2022, doi: 10.3390/ma15134400.
- [11] A. Ölander, “An electrochemical investigation of solid cadmium-gold alloys,” *J. Am. Chem. Soc.*, vol. 54, no. 10, pp. 3819–3833, Oct. 1932, doi: 10.1021/ja01349a004.
- [12] W. J. Buehler, J. V. Gilfrich, and R. C. Wiley, “Effect of Low-Temperature Phase

- Changes on the Mechanical Properties of Alloys near Composition TiNi,” *J. Appl. Phys.*, vol. 34, no. 5, pp. 1475–1477, May 1963, doi: 10.1063/1.1729603.
- [13] F. E. Wang, W. J. Buehler, and S. J. Pickart, “Crystal structure and a unique ‘martensitic’ transition of TiNi,” *J. Appl. Phys.*, vol. 36, no. 10, pp. 3232–3239, Oct. 1965, doi: 10.1063/1.1702955.
- [14] W. J. Buehler and F. E. Wang, “A summary of recent research on the nitinol alloys and their potential application in ocean engineering,” *Ocean Eng.*, vol. 1, no. 1, pp. 105–120, Jul. 1968, doi: 10.1016/0029-8018(68)90019-X.
- [15] D. C. Lagoudas, *Shape Memory Alloys*, vol. 1. Boston, MA: Springer US, 2008. doi: 10.1007/978-0-387-47685-8.
- [16] S. Langbein and A. Czechowicz, *Konstruktionspraxis Formgedächtnistechnik*. Wiesbaden: Springer Fachmedien Wiesbaden, 2013. doi: 10.1007/978-3-8348-2343-4.
- [17] R. H. Bricknell, K. N. Melton, and O. Mercier, “The structure of NiTiCu shape memory alloys,” *Metall. Trans. A*, vol. 10, no. 6, pp. 693–697, Jun. 1979, doi: 10.1007/BF02658390.
- [18] O. Benafan *et al.*, “Ultra-High Temperature Shape Memory Behavior in Ni–Ti–Hf Alloys,” *Shape Mem. Superelasticity*, vol. 10, no. 1, pp. 55–69, Mar. 2024, doi: 10.1007/s40830-024-00473-1.
- [19] B. Feng *et al.*, “Endowing low fatigue for elastocaloric effect by refined hierarchical microcomposite in additive manufactured NiTiCuCo alloy,” *Int. J. Extrem. Manuf.*, vol. 6, no. 4, p. 045501, Aug. 2024, doi: 10.1088/2631-7990/ad35ff.
- [20] M. I. Dawson, S. Batool, and R. Nadeem, “Development of Cu-Zn-Al based shape memory alloy,” in *2017 Fifth International Conference on Aerospace Science & Engineering (ICASE)*, Islamabad: IEEE, Nov. 2017, pp. 1–5. doi: 10.1109/ICASE.2017.8374258.
- [21] T. Maruyama and H. Kubo, “Ferrous (Fe-based) shape memory alloys (SMAs): properties, processing and applications,” *Shape Mem. Superelastic Alloy.*, pp. 141–159, Jan. 2011, doi: 10.1533/9780857092625.2.141.
- [22] T. Duerig, A. Pelton, and D. Stöckel, “An overview of nitinol medical applications,” *Mater. Sci. Eng. A*, vol. 273–275, pp. 149–160, Dec. 1999, doi: 10.1016/s0921-5093(99)00294-4.
- [23] H. Janocha, T. Bonertz, and G. Pappert, *Unkonventionelle Aktoren: eine Einführung*. München: Oldenbourg Wissenschaftsverlag, 2013.

- [24] N. B. Morgan, “Medical shape memory alloy applications—the market and its products,” *Mater. Sci. Eng. A*, vol. 378, no. 1–2, pp. 16–23, Jul. 2004, doi: 10.1016/j.msea.2003.10.326.
- [25] Y. Sutou *et al.*, “Development of Medical Guide Wire of Cu-Al-Mn-Base Superelastic Alloy with Functionally Graded Characteristics,” 2004, doi: 10.1002/jbm.b.10079.
- [26] C. Rodriguez and L. C. Brown, “The thermal effect due to stress-induced martensite formation in B-CuAlNi single crystals,” *Metall. Mater. Trans. A*, vol. 11, no. 1, pp. 147–150, Dec. 1980, doi: 10.1007/BF02700450.
- [27] M. Schmidt, “Elastokalorisches Kühlen mit Ni-Ti-basierten Formgedächtnislegierungen: Thermodynamische Analyse, experimentelle Untersuchungen, Prozessoptimierung,” PhD thesis, Saarland University, 2017. doi: 10.2370/9783844052251.
- [28] S. Qian *et al.*, “A review of elastocaloric cooling: Materials, cycles and system integrations,” *Int. J. Refrig.*, vol. 64, pp. 1–19, Apr. 2016, doi: 10.1016/j.ijrefrig.2015.12.001.
- [29] F. Louia, N. Michaelis, A. Schütze, S. Seelecke, and P. Motzki, “A unified approach to thermo-mechano-caloric-characterization of elastocaloric materials,” *J. Phys. Energy*, vol. 5, no. 4, p. 045014, Oct. 2023, doi: 10.1088/2515-7655/ACFB39.
- [30] J. Cui *et al.*, “Demonstration of high efficiency elastocaloric cooling with large Δt using NiTi wires,” *Appl. Phys. Lett.*, vol. 101, no. 7, Aug. 2012, doi: 10.1063/1.4746257/111937.
- [31] S. M. Kirsch *et al.*, “NiTi-Based Elastocaloric Cooling on the Macroscale: From Basic Concepts to Realization,” *Energy Technol.*, vol. 6, no. 8, pp. 1567–1587, Aug. 2018, doi: 10.1002/ENTE.201800152.
- [32] S. Dall’Olio, Ž. Ahčin, A. Žerovnik, P. Kabirifar, M. Brojan, and J. Tušek, “Development of a Tube-Based Elastocaloric Regenerator Loaded in Compression: A Review,” *Shape Mem. Superelasticity*, vol. 1, pp. 1–20, Apr. 2024, doi: 10.1007/s40830-024-00483-z.
- [33] N. Emaikwu, D. Catalini, J. Muehlbauer, Y. Hwang, I. Takeuchi, and R. Radermacher, “Development of a Cascade Elastocaloric Regenerator,” *ASME 2019 13th Int. Conf. Energy Sustain. ES 2019, collocated with ASME 2019 Heat Transf. Summer Conf.*, Dec. 2019, doi: 10.1115/ES2019-3887.
- [34] H. Hou *et al.*, “Fatigue-resistant high-performance elastocaloric materials made by

- additive manufacturing,” *Science* (80-.), vol. 366, no. 6469, pp. 1116–1121, Nov. 2019, doi: 10.1126/science.aax7616.
- [35] S. Nalbach, P. Motzki, and S. Seelecke, “Sma-based hydraulic switching valve,” in *ASME 2015 Conference on Smart Materials, Adaptive Structures and Intelligent Systems, SMASIS 2015*, American Society of Mechanical Engineers, Sep. 2015. doi: 10.1115/SMASIS2015-8901.
- [36] F. Welsch, M. Schmidt, S. M. Kirsch, S. Seelecke, and P. Motzki, “Vacuum gripper system based on bistable SMA actuation,” *ASME 2018 Conf. Smart Mater. Adapt. Struct. Intell. Syst. SMASIS 2018*, vol. 1, no. September 2019, 2018, doi: 10.1115/SMASIS2018-7980.
- [37] C. H. Park and Y. S. Son, “SMA spring-based artificial muscle actuated by hot and cool water using faucet-like valve,” in *Active and Passive Smart Structures and Integrated Systems 2017*, SPIE, Apr. 2017, p. 101640T. doi: 10.1117/12.2257467.
- [38] P. Motzki and S. Seelecke, “Industrial Applications for Shape Memory Alloys,” in *Reference Module in Materials Science and Materials Engineering*, Elsevier, 2019. doi: 10.1016/B978-0-12-803581-8.11723-0.
- [39] H. J. Lee and J. J. Lee, “Evaluation of the characteristics of a shape memory alloy spring actuator,” *Smart Mater. Struct.*, vol. 9, no. 6, pp. 817–823, Dec. 2000, doi: 10.1088/0964-1726/9/6/311.
- [40] W. Wang and S. H. Ahn, “Shape Memory Alloy-Based Soft Gripper with Variable Stiffness for Compliant and Effective Grasping,” *Soft Robot.*, vol. 4, no. 4, pp. 379–389, 2017, doi: 10.1089/soro.2016.0081.
- [41] D. Scholtes, S. Seelecke, and P. Motzki, “Electro-thermo-mechanical characterization of shape memory alloy wires for actuator and sensor applications—Part 1: The effects of training,” *Eng. Reports*, p. e12867, Feb. 2024, doi: 10.1002/ENG2.12867.
- [42] S. Sławski, M. Kciuk, and W. Klein, “Change in Electrical Resistance of SMA (NiTi) Wires during Cyclic Stretching,” *Sensors*, vol. 22, no. 9, 2022, doi: 10.3390/s22093584.
- [43] F. Simone, G. Rizzello, and S. Seelecke, “Metal muscles and nerves - A self-sensing SMA-actuated hand concept,” *Smart Mater. Struct.*, vol. 26, no. 9, 2017, doi: 10.1088/1361-665X/aa7ad5.
- [44] J. Prechtel, S. Seelecke, P. Motzki, and G. Rizzello, “Self-Sensing control of antagonistic sma actuators based on resistance-Displacement hysteresis compensation,” in *ASME 2020 Conference on Smart Materials, Adaptive Structures and Intelligent Systems*,

- SMASIS 2020*, Virtual, Online: ASME, Sep. 2020. doi: 10.1115/SMASIS2020-2224.
- [45] V. Antonucci, G. Faiella, M. Giordano, F. Mennella, and L. Nicolais, “Electrical resistivity study and characterization during NiTi phase transformations,” *Thermochim. Acta*, vol. 462, no. 1–2, pp. 64–69, 2007, doi: 10.1016/j.tca.2007.05.024.
- [46] “Products - Actuator Solutions GmbH.” <https://www.actuatorolutions.de/english/products/> (accessed Aug. 21, 2023).
- [47] “Miga Robotics.” <https://www.migarobotics.com/product-page/miga-t220-nc-sma-actuator> (accessed Feb. 22, 2023).
- [48] “Kinitics Automation Products - Kinitics Automation Limited.” <https://kiniticsautomation.com/products-overview/> (accessed May 06, 2024).
- [49] “Cambridge Mechatronics - Actuators.” <https://www.cambridgemechatronics.com/en/cml-technology/actuators/> (accessed Aug. 21, 2023).
- [50] P. Motzki, T. Gorges, M. Kappel, M. Schmidt, G. Rizzello, and S. Seelecke, “High-speed and high-efficiency shape memory alloy actuation,” *Smart Mater. Struct.*, vol. 27, no. 7, p. 075047, Jul. 2018, doi: 10.1088/1361-665X/aac9e1.
- [51] Saes Getters, “SmartFlex® Wire.” www.saesgroup.com (accessed Apr. 17, 2024).
- [52] R. Britz *et al.*, “SMA Wire Bundles - Mechanical and Electrical Concepts,” in *ACTUATOR 2018: 16th International Conference on New Actuators*, Bremen: VDE, 2018, pp. 514–517.
- [53] S.-M. Kirsch *et al.*, “SMA Antagonistic-Micro-Wire Bundle: First Measurement Results,” in *ASME 2020 Conference on Smart Materials, Adaptive Structures and Intelligent Systems*, Virtual, Online: ASME, Sep. 2020. doi: 10.1115/SMASIS2020-2261.
- [54] R. Kratz, M. Stelzer, and O. Von Stryk, “Macroscopic SMA wire bundle actuator/sensor system: Design, measurement, control approach,” in *IFAC Proceedings Volumes (IFAC-PapersOnline)*, Elsevier, Jan. 2006, pp. 1054–1058. doi: 10.3182/20060912-3-de-2911.00181.
- [55] R. Britz and P. Motzki, “Analysis and evaluation of bundled SMA actuator wires,” *Sensors Actuators A Phys.*, vol. 333, no. 1-2 SPEC. ISS, p. 113233, Jan. 2022, doi: 10.1016/j.sna.2021.113233.
- [56] C. Pirritano *et al.*, “Fully Integrated Rotary Motor Based on Antagonistic Shape Memory Alloy Wire Bundles,” in *Proceedings of ASME 2023 Conference on Smart Materials*,

- Adaptive Structures and Intelligent Systems, SMASIS 2023*, Austin: ASME, Nov. 2023. doi: 10.1115/SMASIS2023-111255.
- [57] T. Ataalla, M. Leary, and A. Subic, “Functional Fatigue of Shape Memory Alloys,” in *Sustainable Automotive Technologies 2012*, Springer, Berlin, Heidelberg, 2012, pp. 39–43. doi: 10.1007/978-3-642-24145-1_6.
- [58] D. C. Lagoudas, D. A. Miller, L. Rong, and P. K. Kumar, “Thermomechanical fatigue of shape memory alloys,” *Smart Mater. Struct.*, vol. 18, no. 8, 2009, doi: 10.1088/0964-1726/18/8/085021.
- [59] F. Auricchio, A. Constantinescu, C. Menna, and G. Scalet, “A shakedown analysis of high cycle fatigue of shape memory alloys,” *Int. J. Fatigue*, vol. 87, pp. 112–123, 2016, doi: 10.1016/j.ijfatigue.2016.01.017.
- [60] W. Kim, B. M. Barnes, J. E. Luntz, and D. E. Brei, “Conglomerate stabilization curve design method for shape memory alloy wire actuators with cyclic shakedown,” *J. Mech. Des.*, vol. 133, no. 11, pp. 1–10, 2011, doi: 10.1115/1.4004460.
- [61] Y. Goergen *et al.*, “Shape Memory Alloys in Continuum and Soft Robotic Applications,” in *ASME 2019 Conference on Smart Materials, Adaptive Structures and Intelligent Systems*, American Society of Mechanical Engineers, Sep. 2019. doi: 10.1115/SMASIS2019-5610.
- [62] R. Britz, G. Rizzello, and P. Motzki, “High-Speed Antagonistic Shape Memory Actuator for High Ambient Temperatures,” *Adv. Eng. Mater.*, vol. 24, no. 9, p. 2200205, Sep. 2022, doi: 10.1002/adem.202200205.
- [63] S.-H. Song, J.-Y. Lee, H. Rodrigue, I.-S. Choi, Y. J. Kang, and S.-H. Ahn, “35 Hz shape memory alloy actuator with bending-twisting mode,” *Sci. Rep.*, vol. 6, no. 1, p. 21118, Feb. 2016, doi: 10.1038/srep21118.
- [64] S. Kennedy, M. R. E. U. Shougat, and E. Perkins, “Robust self-sensing shape memory alloy actuator using a machine learning approach,” *Sensors Actuators A Phys.*, vol. 354, p. 114255, May 2023, doi: 10.1016/j.sna.2023.114255.
- [65] P. Motzki, F. Khelifa, L. Zimmer, M. Schmidt, and S. Seelecke, “Design and Validation of a Reconfigurable Robotic End-effector Based on Shape Memory Alloys,” *IEEE/ASME Trans. Mechatronics*, no. January, 2019, doi: 10.1109/TMECH.2019.2891348.
- [66] D. Scholtes, Y. Goergen, P. Motzki, S. Seelecke, and P. Scheiner, “Soft morphing buttons based on actuator and sensor properties of shape memory alloy wires,” in *ASME*

- 2019 Conference on Smart Materials, Adaptive Structures and Intelligent Systems, SMASIS 2019, Louisville: ASME, Sep. 2019. doi: 10.1115/SMASIS2019-5504.
- [67] D. Scholtes, S. S. Seelecke, and P. Motzki, “Design of a lightweight SMA driven parallel gripper for collaborative robots,” in *Proceedings Volume 12483, Active and Passive Smart Structures and Integrated Systems XVII*, Long Beach: SPIE, Apr. 2023, p. 34. doi: 10.1117/12.2658402.
- [68] D. Scholtes, S. Seelecke, and P. Motzki, “Development of a Bistable SMA Actuated Industrial Gripper Based on a Compliant Design,” in *ACTUATOR; International Conference and Exhibition on New Actuator Systems and Applications 2021*, Virtual, Online: VDE, 2021, pp. 181–184.
- [69] D. A. Miller and D. C. Lagoudas, “Thermomechanical characterization of NiTiCu and NiTi SMA actuators: Influence of plastic strains,” *Smart Mater. Struct.*, vol. 9, no. 5, pp. 640–652, 2000, doi: 10.1088/0964-1726/9/5/308.
- [70] C. B. Churchill and J. A. Shaw, “Shakedown response of conditioned shape memory alloy wire,” *Behav. Mech. Multifunct. Compos. Mater. 2008*, vol. 6929, p. 69291F, 2008, doi: 10.1117/12.778726.
- [71] C. B. Churchill, J. A. Shaw, and M. A. Iadicola, “Tips and Tricks for Characterizing Shape Memory Alloy Wire: Part 1 – Differential Scanning Calorimetry & Basic Phenomena,” *Exp. Tech.*, vol. 33, no. 1, pp. 51–62, Jan. 2009, doi: 10.1111/J.1747-1567.2008.00460.X.
- [72] J. A. Shaw, C. B. Churchill, and M. A. Iadicola, “Tips and Tricks for Characterizing Shape Memory Alloy Wire: Part 2—Fundamental Isothermal Responses,” *Exp. Tech.*, vol. 32, no. 5, pp. 55–62, Sep. 2008, doi: 10.1111/J.1747-1567.2008.00410.X.
- [73] C. B. Churchill, J. A. Shaw, and M. A. Iadicola, “Tips and tricks for characterizing shape memory alloy wire: Part 3-localization and propagation phenomena,” *Exp. Tech.*, vol. 33, no. 5, pp. 70–78, 2009, doi: 10.1111/j.1747-1567.2009.00558.x.
- [74] C. B. Churchill, J. A. Shaw, and M. A. Iadicola, “Tips and tricks for characterizing shape memory alloy wire: Part 4 - Thermo-mechanical coupling: Experimental characterization of active materials series,” *Exp. Tech.*, vol. 34, no. 2, pp. 63–80, 2010, doi: 10.1111/j.1747-1567.2010.00619.x.
- [75] H. Gugel, A. Schuermann, and W. Theisen, “Laser welding of NiTi wires,” *Mater. Sci. Eng. A*, vol. 481–482, no. 1-2 C, pp. 668–671, May 2008, doi: 10.1016/j.msea.2006.11.179.

- [76] W. Wang, “Microstructure Change in Welded TiNi Alloys,” *J. Phys. Conf. Ser.*, vol. 1676, no. 1, p. 012023, Nov. 2020, doi: 10.1088/1742-6596/1676/1/012023.
- [77] A. Falvo, F. M. Furgiuele, and C. Maletta, “Functional behaviour of a NiTi-welded joint: Two-way shape memory effect,” *Mater. Sci. Eng. A*, vol. 481–482, no. 1-2 C, pp. 647–650, 2008, doi: 10.1016/j.msea.2006.11.178.
- [78] Z. Zeng, B. Panton, J. P. Oliveira, A. Han, and Y. N. Zhou, “Dissimilar laser welding of NiTi shape memory alloy and copper,” *Smart Mater. Struct.*, vol. 24, no. 12, Dec. 2015, doi: 10.1088/0964-1726/24/12/125036.
- [79] M. Mehrpouya, A. Gisario, M. Barletta, S. Natali, and F. Veniali, “Dissimilar Laser Welding of NiTi Wires,” *Lasers Manuf. Mater. Process.*, vol. 6, no. 2, pp. 99–112, Jun. 2019, doi: 10.1007/s40516-019-00084-0.
- [80] C. B. Churchill and J. A. Shaw, “Thermo-Electro-Mechanical Shakedown Response of Conditioned Shape Memory Alloy Wires,” in *Volume 1: Active Materials, Mechanics and Behavior; Modeling, Simulation and Control*, Oxnard: ASMEDC, Jan. 2009, pp. 137–148. doi: 10.1115/SMASIS2009-1306.
- [81] M. A. Mandolino, D. Scholtes, F. Ferrante, and G. Rizzello, “A Physics-Based Hybrid Dynamical Model of Hysteresis in Polycrystalline Shape Memory Alloy Wire Transducers,” *IEEE/ASME Trans. Mechatronics*, 2023, doi: 10.1109/TMECH.2023.3253250.
- [82] Y. Goergen, G. Rizzello, and P. Motzki, “Systematic Methodology for an Optimized Design of Shape Memory Alloy-Driven Continuum Robots,” *Adv. Eng. Mater.*, p. 2301502, Dec. 2023, doi: 10.1002/ADEM.202301502.
- [83] D. Scholtes, S. Seelecke, G. Rizzello, and P. Motzki, “Design of A compliant industrial gripper driven by A bistable shape memory alloy actuator,” in *ASME 2020 Conference on Smart Materials, Adaptive Structures and Intelligent Systems, SMASIS 2020*, Virtual, Online: ASME, Nov. 2020. doi: 10.1115/SMASIS2020-2204.
- [84] D. Scholtes, S. Seelecke, and P. Motzki, “Konstruktion eines Festkörpergelenkgreifers mit bistabiler Formgedächtnisaktuatorik,” in *Digital-Fachtagung Mechatronik 2021*, Darmstadt: TUprints, 2021, pp. 170–174. doi: 10.26083/tuprints-00018615.
- [85] “CASmart 4th Design Challenge.” <https://www.casmart.org/home/student-design-challenges/casmart-4th-design-challenge> (accessed Apr. 17, 2024).
- [86] J. Pilch, L. Heller, and P. Sittner, “Final thermomechanical treatment of thin NiTi filaments for textile applications by electric current,” in *ESOMAT 2009 - 8th European*

- Symposium on Martensitic Transformations*, Praha: EDP Sciences, Sep. 2009, pp. 232–237. doi: 10.1051/esomat/200905024.
- [87] L. Heller, K. Janouchová, P. Šittner, and D. Vokoun, “Functional textiles driven by transforming NiTi wires,” in *ESOMAT 2015 – 10th European Symposium on Martensitic Transformations*, Antwerp: EDP Sciences, Dec. 2015, p. 03010. doi: 10.1051/mateconf/20153303010.
- [88] M. O. Gök, M. Z. Bilir, and B. H. Gürcüm, “Shape-Memory Applications in Textile Design,” *Procedia - Soc. Behav. Sci.*, vol. 195, pp. 2160–2169, Jul. 2015, doi: 10.1016/j.sbspro.2015.06.283.
- [89] J. Shin, Y.-J. Han, J.-H. Lee, and M.-W. Han, “Shape Memory Alloys in Textile Platform: Smart Textile-Composite Actuator and Its Application to Soft Grippers,” *Sensors*, vol. 23, no. 3, p. 1518, Jan. 2023, doi: 10.3390/s23031518.
- [90] F. Simone, G. Rizzello, S. Seelecke, and P. Motzki, “A Soft Five-Fingered Hand Actuated by Shape Memory Alloy Wires: Design, Manufacturing, and Evaluation,” *Front. Robot. AI*, vol. 7, no. December, 2020, doi: 10.3389/frobt.2020.608841.

Anhang

Ergänzende Messdaten zu Veröffentlichungen

Zu der Veröffentlichung “Electro-Thermo-Mechanical Characterization of Shape Memory Alloy Wires for Actuator and Sensor Applications – Part 1: The Effects of Training” sind ergänzende Daten veröffentlicht, welche den zeitlichen Verlauf der Messdaten für alle Messungen darstellen. Diese unterstützenden Informationen sind im Folgenden im Original abgedruckt.

Supporting Information:

For comprehensiveness, the timings of the basic characterization and all actuation tests in sections 3.3 and 3.4 are displayed in the following.

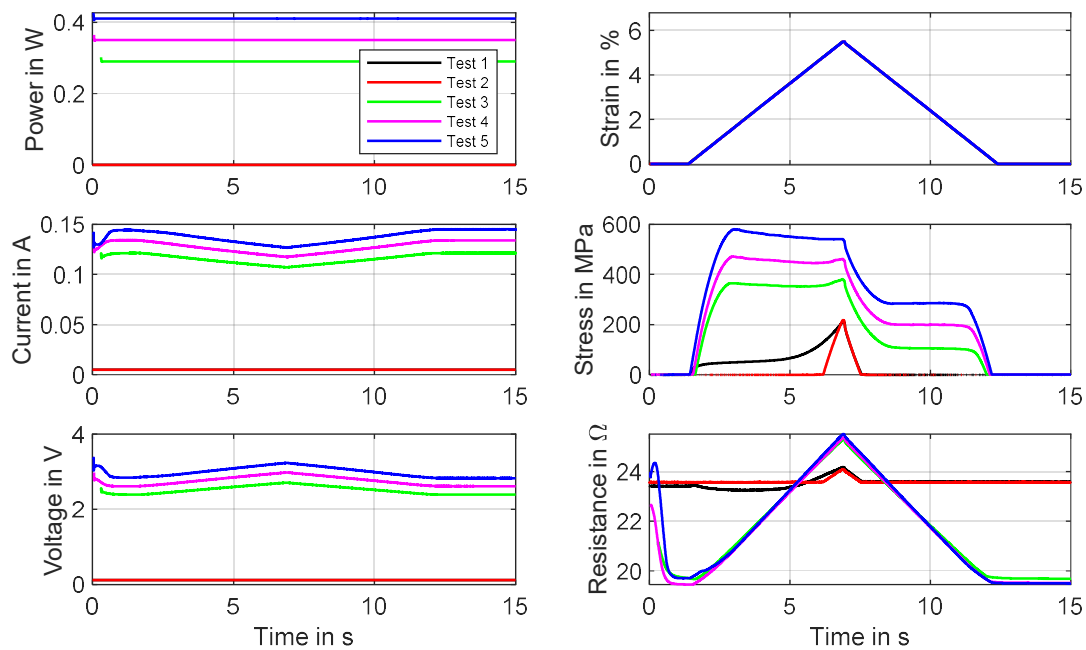


Figure S1: Timing of the **tensile experiment** with the **untreated wire** sample discussed in section 3.3. Displayed are the results of five experiments with varying heating power and a strain rate of 0.05s^{-1} .

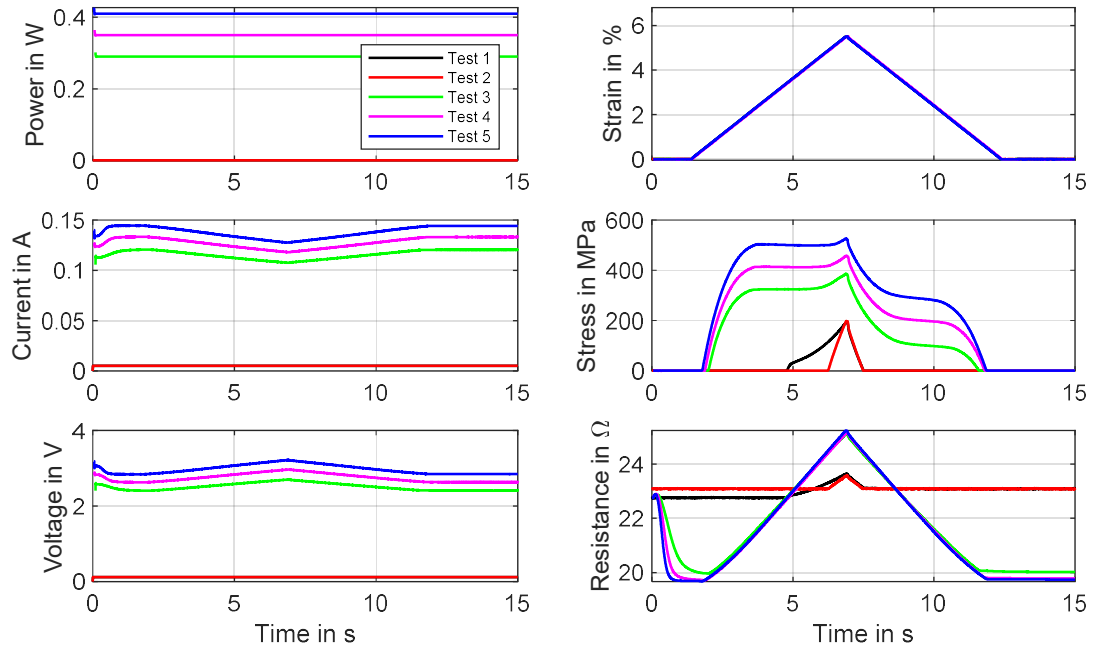


Figure S2: Timing of the **tensile experiment** with the **mechanically trained** wire sample discussed in section 3.3. Displayed are the results of five experiments with varying heating power and a strain rate of 0.05s^{-1} .

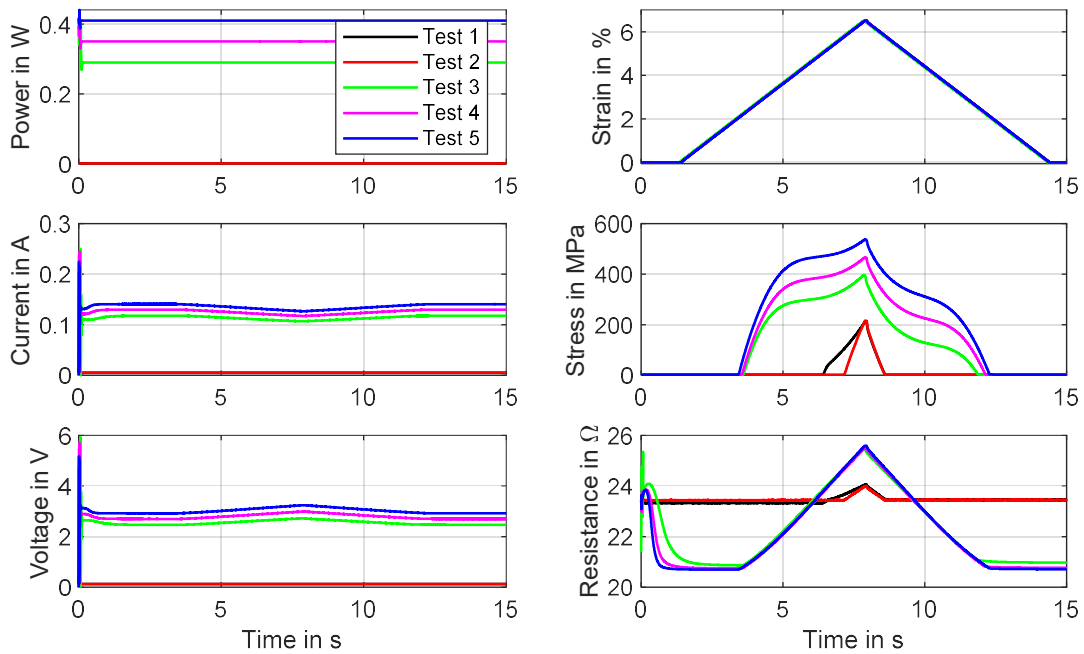


Figure S3: Timing of the **tensile experiment** with the **thermally trained** wire sample discussed in section 3.3. Displayed are the results of five experiments with varying heating power and a strain rate of 0.05s^{-1} .

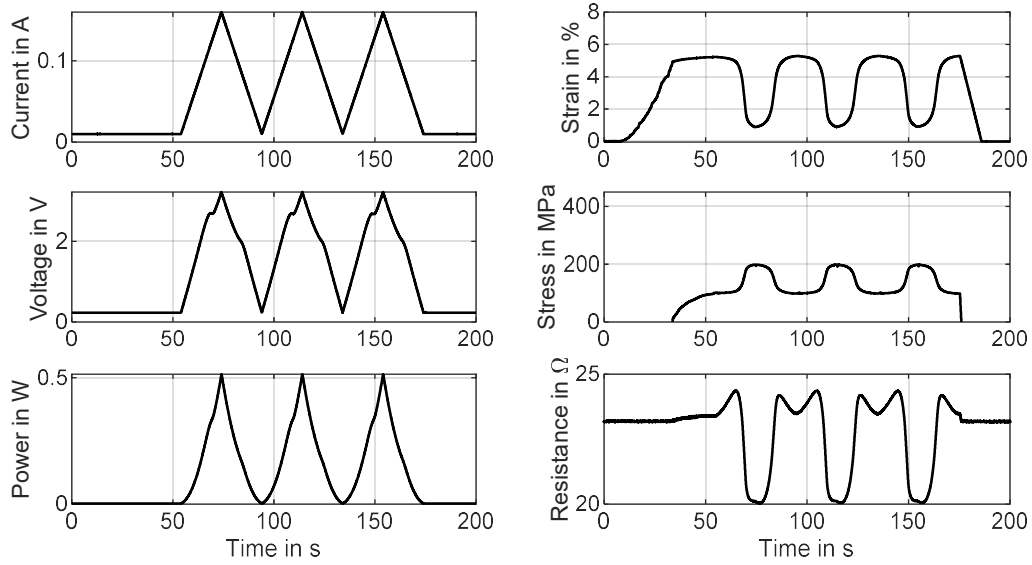


Figure S4: Actuator experiment with **mechanically trained** wire and a **linear spring** load corresponding **100 MPa of prestress** and 200 MPa maximum load. The plots display the timing of the experiment discussed in section 3.4.1.

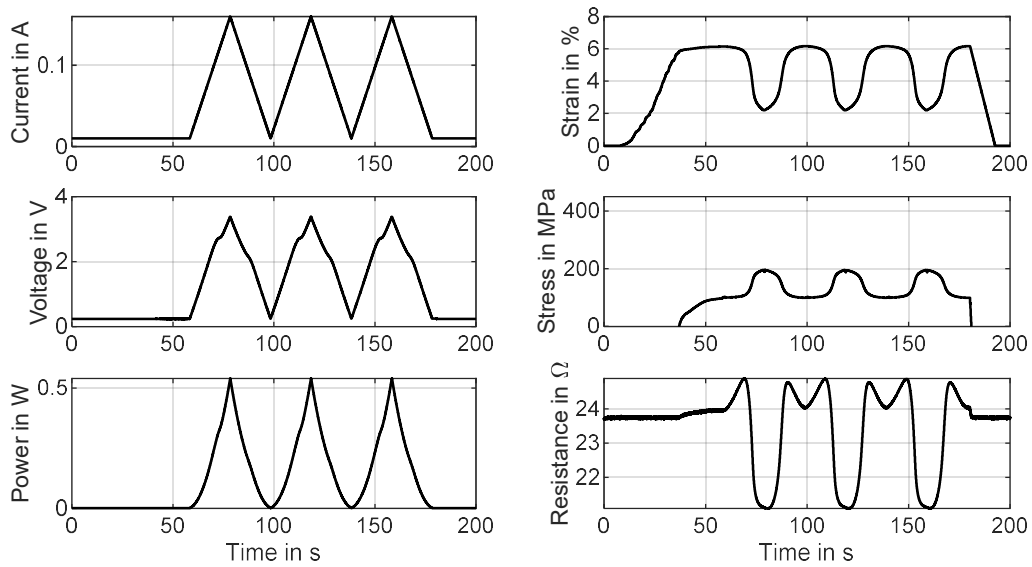


Figure S5: Actuator experiment with **thermally trained** wire and a **linear spring** load corresponding **100 MPa of prestress** and 200 MPa maximum load. The plots display the timing of the experiment discussed in section 3.4.1.

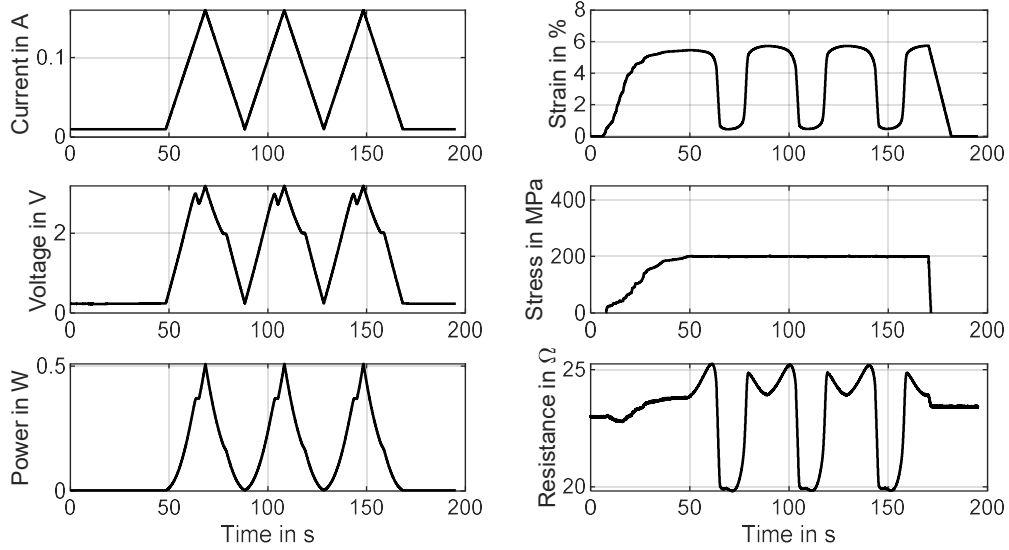


Figure S6: Actuator experiment with **untreated** wire and a constant load corresponding to **200 MPa** of stress. The plots display the timing of the experiment discussed in section 3.4.2.

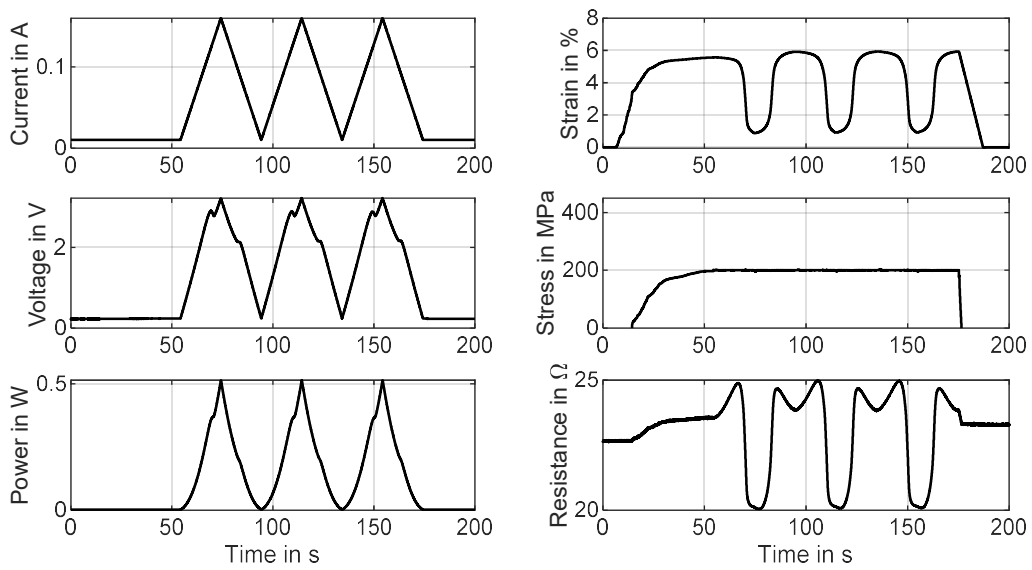


Figure S7: Actuator experiment with **mechanically trained** wire and a constant load corresponding to **200 MPa** of stress. The plots display the timing of the experiment discussed in section 3.4.2.

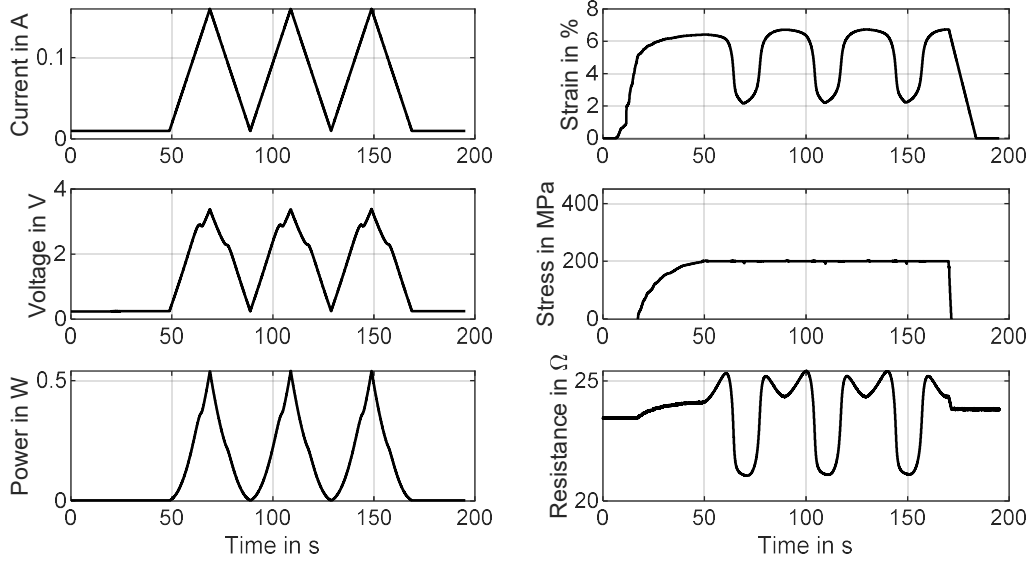


Figure S8: Actuator experiment with **thermally trained** wire and a constant load corresponding to **200 MPa** of stress. The plots display the timing of the experiment discussed in section 3.4.2.

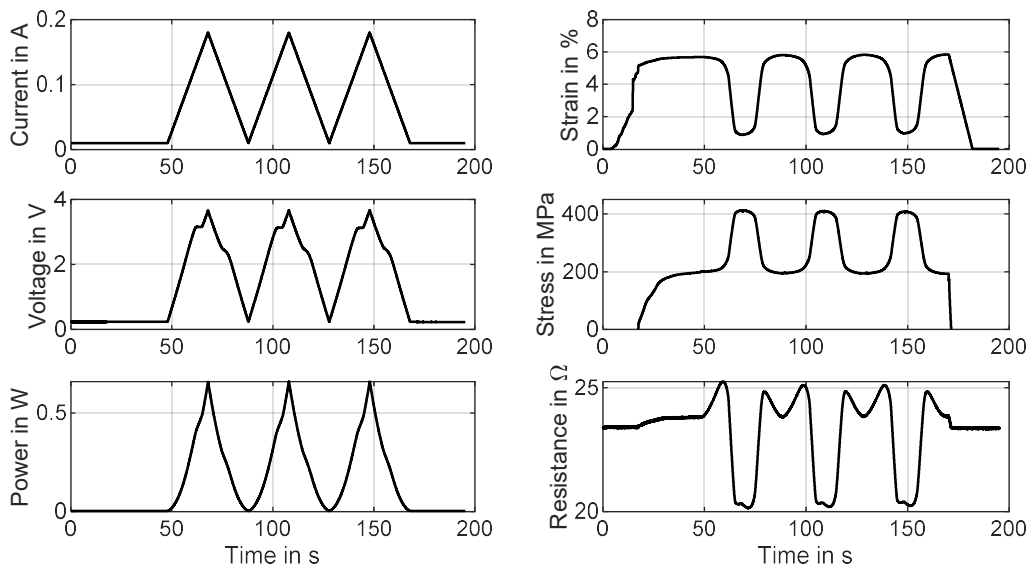


Figure S9: Actuator experiment with **untreated** wire and a **linear spring** load corresponding **200 MPa** of prestress and 400 MPa maximum load. The plots display the timing of the experiment discussed in section 3.4.3.

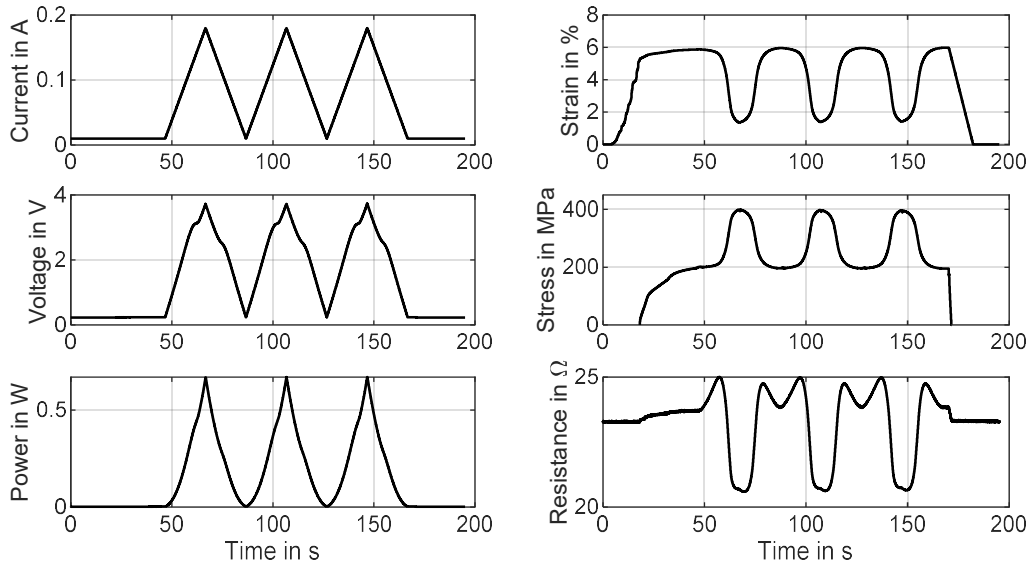


Figure S10: Actuator experiment with **mechanically trained** wire and a **linear spring** load corresponding **200 MPa of prestress** and 400 MPa maximum load. The plots display the timing of the experiment discussed in section 3.4.3.

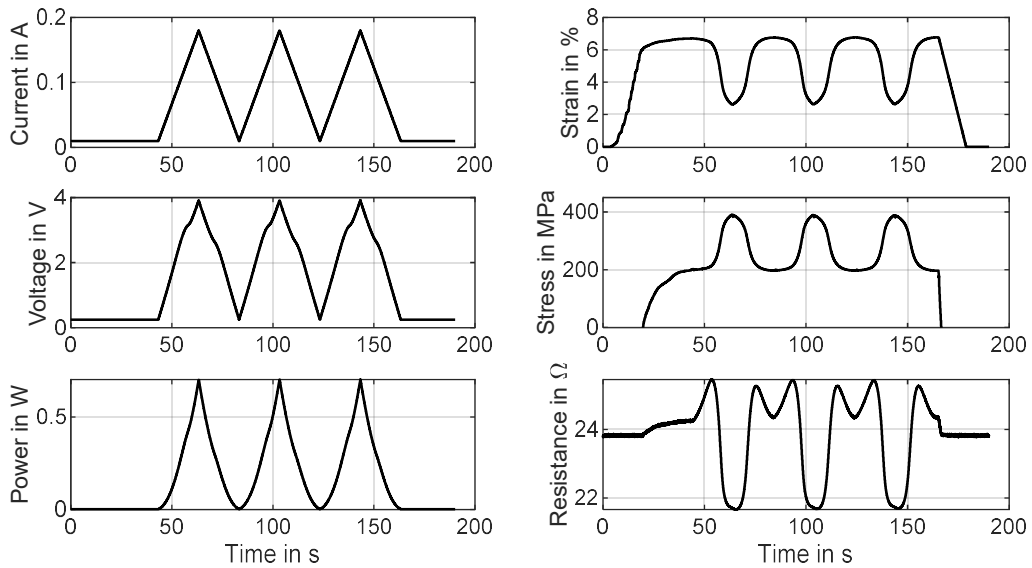


Figure S11: Actuator experiment with **thermally trained** wire and a **linear spring** load corresponding **200 MPa of prestress** and 400 MPa maximum load. The plots display the timing of the experiment discussed in section 3.4.4.

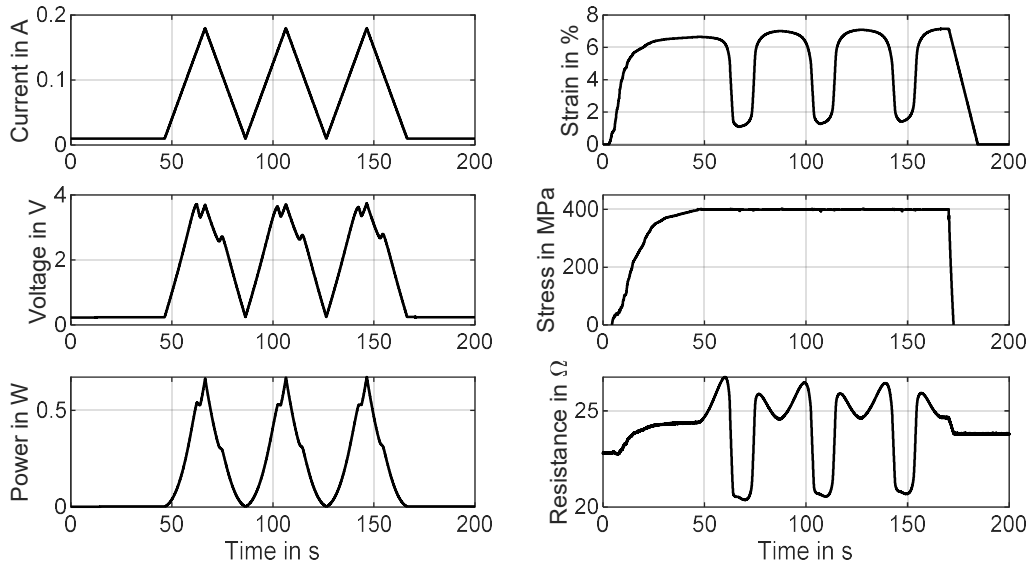


Figure S12: Actuator experiment with **untreated** wire and a constant load corresponding to **400 MPa** of stress. The plots display the timing of the experiment discussed in section 3.4.4.

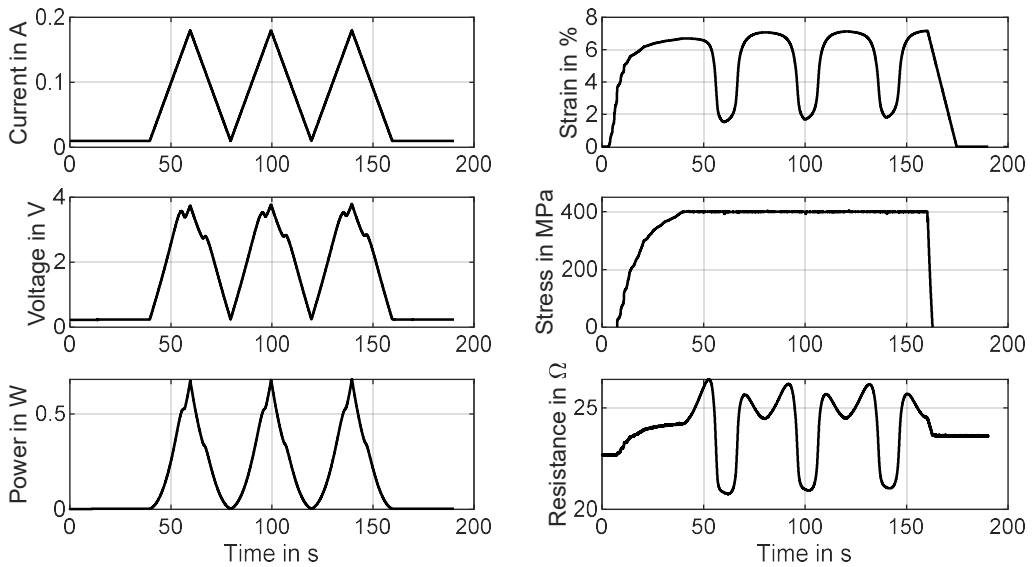


Figure S13: Actuator experiment with **mechanically trained** wire and a constant load corresponding to **400 MPa** of stress. The plots display the timing of the experiment discussed in section 3.4.4.

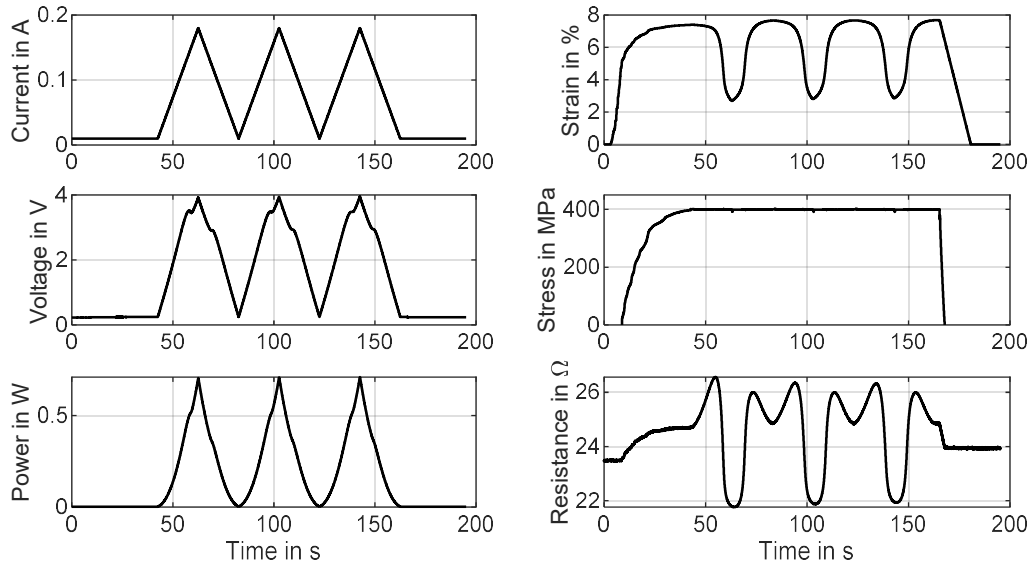


Figure S14: Actuator experiment with **thermally trained** wire and a constant load corresponding to **400 MPa** of stress. The plots display the timing of the experiment discussed in section 3.4.4.

Beitragsberichte zu den eingebundenen Veröffentlichungen

Hier werden die einzelnen Beiträge aller Autoren zu den jeweiligen Veröffentlichungen erläutert. Außerdem wird der Status, die Qualität und die Art der Begutachtung der Publikationen dargestellt.

A Multifunctional Characterization Test Bench for Shape Memory Alloy Micro-Wires – Design, Implementation and Validation

Journal: Materials (2022 Impact Factor: 3.4)

Verlag: MDPI

Qualität: Forschungsartikel

Status: Veröffentlicht am 4. Juli 2024 nach Peer-Review Begutachtung.

Dominik Scholtes hat die Versuche und Messungen geplant, durchgeführt und ausgewertet. Außerdem hat er Optimierungen an der Prüfstands Konstruktion, der elektrischen Ansteuerung sowie der Programmierumgebung vorgenommen. Er hat das Manuskript verfasst und die Abbildungen erstellt.

Marvin Schmidt hat den Prüfstand entworfen und in Betrieb genommen. Er hat die Steuerung für den Prüfstand entwickelt und programmiert.

Philipp Linnebach war für die mechanische Konstruktion des Prüfstands, insbesondere der Drahtklemmen, verantwortlich.

Stefan Seelecke war in beratender und leitender Funktion tätig.

Paul Motzki hat das Manuskript Korrektur gelesen und war in beratender Funktion tätig.

Electro-Thermo-Mechanical Characterization of Shape Memory Alloy Wires for Actuator and Sensor Applications – Part 1: The Effects of Training

Journal: Engineering Reports (2022 Impact Factor: 2.0)

Verlag: John Wiley & Sons

Qualität: Forschungsartikel

Status: Veröffentlicht am 18. Februar 2024 nach Peer-Review Begutachtung.

Dominik Scholtes hat die Veröffentlichung verfasst, formatiert und alle Abbildungen erstellt. Er hat die Experimente geplant, durchgeführt und ausgewertet. Er war für die Interpretation der Ergebnisse und die vorrangigere Recherche verantwortlich

Stefan Seelecke war in beratender und leitender Funktion tätig.

Paul Motzki hat das Manuskript Korrektur gelesen und war in beratender und leitender Funktion tätig.

Electro-Thermo-Mechanical Characterization of Shape Memory Alloy Wires for Actuator and Sensor Applications – Part 2: High Ambient Temperature Behavior

Journal: Advanced Engineering Materials (2022 Impact Factor: 3.6)
Verlag: John Wiley & Sons
Qualität: Forschungsartikel
Status: Veröffentlicht am 11. April 2024 nach Peer-Review Begutachtung.

Dominik Scholtes hat die Veröffentlichung verfasst und alle Abbildungen erstellt. Er hat die Versuche geplant, durchgeführt und ausgewertet. Er war für die Interpretation der der Ergebnisse und die vorrangigere Recherche verantwortlich

Stefan Seelecke war in beratender und leitender Funktion tätig.

Paul Motzki hat das Manuskript Korrektur gelesen und war in beratender und leitender Funktion tätig.

Dissimilar Resistance Welding of NiTi Microwires for High Performance SMA Bundle Actuators

Journal: Actuators (2023 Impact Factor: 2.2)

Verlag: MDPI

Qualität: Forschungsartikel

Status: Veröffentlicht am 05. Oktober 2024 nach Peer-Review Begutachtung.

Dominik Scholtes hat das Manuskript verfasst, formatiert und die Abbildungen erstellt. Er hat die Versuche und Messungen geplant, durchgeführt und ausgewertet. Er war für die Interpretation der Ergebnisse und die Recherche verantwortlich. Er hat die Schweißparameter und den Bündelungsprozess entwickelt und ausgearbeitet. Außerdem hat er den Prüfstand für die Abrissversuche entwickelt und aufgebaut.

Ralf-Kilian Zäh hat die Schweißumgebung mit Positioniereinheit zum teilautomatisierten Schweißen entwickelt und aufgebaut sowie die mikroskopischen Untersuchungen geleitet.

Benedikt Faupel war in beratender und leitender Funktion tätig.

Stefan Seelecke war in beratender und leitender Funktion tätig.

Paul Motzki hat war in beratender Funktion tätig.

